Exploring the Reactions and Presence of Munitions Compounds and Insecticides in Aquatic Systems

A DISSERTATION

SUBMITTED TO THE FACULTY OF

UNIVERSITY OF MINNESOTA

BY

Matthew John Berens

IN PARTIAL FULFILLMENT OF THE REQUIREMENTS
FOR THE DEGREE OF
DOCTOR OF PHILOSOPHY

William A. Arnold

September 2020

Acknowledgements

I thank Bill for being my advisor and guide and for allowing me the flexibility to pursue my personal interests during my graduate career.

I gratefully acknowledge Thomas Hofstetter and Paul Capel for serving as secondary advisors and for their support as they introduced me to their respective fields of expertise and answered my many questions.

I thank Jennifer Strehlau for being an invaluable mentor during the first two years of my graduate career. She displayed incredible patience as she taught me how to be a proficient, careful, and thorough researcher. I credit her the amount of progress I achieved throughout my entire career

I thank my many colleagues who helped conduct experiments, interpret data, and answer my questions throughout this work: Bridget Ulrich, Jakov Bolotin, Yiran Tong, Sarah Pati, Stephen Todey, Adel Soroush, Priya Hora, Sam Lombardo, Kolton Kitterman, Makenzie Pillsbury, and Huan He. I also thank my many collaborators who assisted in field sample collection: John Manske, John Barry, Lee Ganske, O'Niell Tedrow, Marcus Langevin, Michael MacDonald, Danni Halvorson, Tony Dingmann, Dave Tollefson, Adam Sealock, and Dylan Timm.

I acknowledge my funding sources for making this work possible: the Department of Defense Strategic Environmental Research and Development Program (SERDP; ER2618), the Minnesota Environment and Natural Resources Trust Fund as recommended by the Legislative Citizen Commission on Minnesota Resources (LCCMR; 048-B). The liquid chromatograph-tandem mass spectrometer was housed at the Analytical Biochemistry facility within the University of Minnesota Masonic Cancer Center.

I thank Kevin for being a brother and friend and for his innumerable and unknowing positive impacts throughout my life.

I am forever indebted to my parents for their unending support and for instilling in me the passion to pursue science and to appreciate the natural world.

Dedication

For Mom, Dad, and Kevin.

Abstract

Organic chemicals are ubiquitous in the environment and are responsible for the widespread pollution of many natural and engineered ecosystems including surface and groundwater, soils and sediments, and municipal water systems. In the environment, these chemicals are toxic to many species of plants, animals, and humans. There is still much to be understood, however, about the occurrence and fate of chemical pollutants and what approaches can be taken to mitigate their environmental impacts. In this dissertation, two classes of chemical pollutants, nitroaromatic compounds (NACs) and neonicotinoid insecticides, were investigated to address these knowledge gaps.

An analytical technique was developed to better quantify the extent of degradation of the novel munitions compound, 2,4-dinitroanisole (DNAN), by naturally occurring iron oxide minerals across a wide range of environmental conditions. This research incorporated the use of compound specific isotope analysis (CSIA) and revealed that stable isotope ratios of nitrogen and carbon during DNAN reduction are not affected by the type of iron oxide mineral, the presence of natural organic matter, and repeated exposures to a pollutant. Across all experiments, N-isotope enrichment factors (ε_N), ranged from -11.1 ± 4.3‰ to -21.5 ± 2.6‰ with an overall average of -14.9 ± 1.3‰. These values resulted in N and C apparent kinetic isotope effects (AKIEs) of ^{15}N-AKIE = 1.0317 ± 0.0064 and ^{13}C = 1.0008 ± 0.0005 that are typical for abiotic nitro-group reduction of NACs by iron-bearing minerals (^{15}N-AKIE = 1.030–1.045 and ^{13}C ~ 1.000). The results of CSIA were then used to generate a model to estimate the extent of DNAN

degradation from measured N-isotope ratios. The model produced accurate predictions with an average error in predicted vs. actual values of 0.091 ± 0.063 as c/c_0.

Neonicotinoid concentrations were measured in water samples collected from lakes, rivers, streams, groundwater wells, and treated wastewater effluents throughout the state of Minnesota. These results showed that neonicotinoid concentrations were predominantly affected by the type of land use and the time of year for which they were applied. Neonicotinoid concentrations were the highest in agricultural watersheds (median = 12 ng/L) followed by urban (2.9 ng/L) and undeveloped watersheds (1.9 ng/L). Clothianidin was the most frequently detected neonicotinoid in agricultural areas, and imidacloprid was most frequently detected in urban waters. In addition, concentrations were typically greatest at the beginning of the year and decreased thereafter. The potential impacts of neonicotinoids on several planktonic assemblages were assessed, but no significant correlations were observed between neonicotinoid concentrations and plankton population sizes. The overall results of this dissertation showed that while there are many factors that drive environmental pollution, measurements, and predictions of the extent of contamination will continue to improve.

Table of Contents

List of Tables

List of Figures

List of Key Abbreviations

BET	Brunauer-Emmett-Teller
CSIA	compound specific isotope analysis
DAAN	2,4-Diaminoanisole
DNAN	2,4-Dinitrianisole
2,4-DNT	2,4-Dinitrotoluene
EPPS	3-[4-(2-Hydroxyethyl)piperazin-1-yl]propane-1-sulfonic acid
ESHA	Elliot Soil humic acid
GC	gas chromatography
Gth	goethite
HPLC	high performance liquid chromatography
IHSS	International Humic Substances Society
IRMS	isotope ratio mass spectrometry
LC-MS/MS	liquid chromatography-tandem mass spectrometry
Mag	magnetite
MENA	2-methoxy-5-nitroanisole
Mkw	mackinawite
MOPS	3-(N-morpholino)propanesulfonic acid
NAC	nitroaromatic compound
NOM	natural organic matter
OC	organic carbon
PDF	powder diffraction file
ppm	parts per million
RDX	hexahydrotrinitrotrazine
SPME	solid phase micro extraction
TNT	2,4,6-Trinitrotoluene
UV-vis	ultra violet–visible
XRD	X-ray diffraction

List of Symbols

$\Lambda^{N/C}$	correlated N and C isotope fractionation
ε_E	bulk isotope enrichment factor for element E
$\varepsilon_{E,\text{reactive position}}$	position-specific isotope enrichment factor for element E
E	element (e.g., C, N)
$\delta^h E$	current isotope signature for element E
$\delta^h E_0$	initial isotope signature for element E
$\Delta^h E$	change in isotope signature relative to initial value for element E
^{h}E-AKIE	apparent kinetic isotope effect for element E
c	current concentration
c_0	initial concentration
e^-	electron
E_H	one-electron reduction potential
h	atomic weight of heavy isotope of element E
k_{obs}	pseudo-first-order rate constant
^{h}E-KIE	kinetic isotope effect for element E

Chapter 1. Introduction

1.1 Chemicals in the environment

Technological advancements have caused marked improvements in many facets of science and engineering aimed at increasing human productivity. From agriculture to military activities, advancements have included the development of novel chemical compounds aimed at increasing workplace safety, improving agricultural yields, and eradicating noxious species and diseases. In the environment, these compounds evoke unintended effects, such as acute toxicity and developmental defects, that are often more hazardous than their original intent. Thus, the ability to accurately monitor pollutants and understand the relevant transformation processes is imperative to supporting a future of environmental preservation and stewardship.

The focus of this dissertation is on two classes of synthetic chemicals: nitroaromatic compounds (NACs) and neonicotinoid insecticides. NACs are a class of industrial chemicals that have a wide range of uses including explosives and agrochemicals. This has caused widespread pollution to large areas of land and water for decades. NACs have long been the focus of remediation projects and recent attention has been given to the replacement of traditional NACs with safer alternatives. Neonicotinoid insecticides were first produced in the 1990s and are applied in both agricultural and domestic settings. For example, neonicotinoids are used to dispel chewing insects on corn and soybeans in addition to fleas and ticks on pets. Despite the exceptional efficacy of neonicotinoids to mitigate pest insects, they are easily mobilized in the environment and are potentially

toxic to non-target organisms, such as honeybees, aquatic invertebrates, birds, and some mammals.

1.2 Nitroaromatic compounds

NACs are a class of chemicals commonly used as explosives, solvents, chemical intermediates, and dyes.[1] Their widespread use in many industrial processes has caused NACs to be ubiquitous pollutants in the environment. The route for NACs to enter the environment depends on the intended use. For example, NACs in explosives can enter the environment during military training exercises while those used as dyes are released into wastewater streams from textile manufacturing facilities.

Nitroaromatic compounds are defined as chemicals with one or more nitro groups (-NO_2) attached to an aromatic ring (e.g., benzene). The simplest NAC is nitrobenzene (Figure 1-1, **(1)**), which contains a single -NO_2 functional group attached to a benzene molecule. Other examples include 2-nitrophenol (Figure 1-1, **(2)**), a precursor of dye synthesis, and the explosives 2,4,6-trinotoluene (TNT; Figure 1-1, **(3)**) and 2,4-dinitroanisole (DNAN; Figure 1-1, **(4)**).

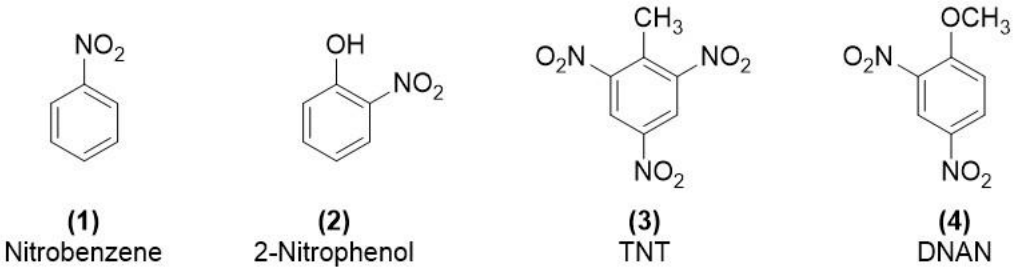

Figure 1-1. Chemical structures of four NACs: **(1)** nitrobenzene, **(2)** 2-nitrophenol, **(3)** TNT, and **(4)** DNAN.

In the environment, NACs exhibit a wide range of solubility, sediment-partitioning behavior, and ecotoxicity.[2] Moreover, as NACs are degraded by one or more environmental processes, such as decomposition by bacteria and reduction by iron-rich minerals, the products that form are often more harmful than the original compound. Such observations emphasize the need to fully understand the relevant fate and transport processes of NACs in land, water, and the subsurface.[2]

The scope of Chapters 2 and 3 of this dissertation encompasses the fate of NACs that are used as explosives, propellants, and munitions. Energetic materials containing NACs contaminate large areas of soil, sediment, and water at military installations worldwide where they enter the environment through improper handling (e.g., production, handling, disposal) and incomplete or unintended detonations.[3,4] Several studies have assessed the fate of common NACs, such as TNT (Figure 1-1, **(3)**) and isomers of dinitrobenzene (e.g., 1,3–DNB, 1,4–DNB) and reveal the tendency for NACs to persist over long periods of time and elicit toxic effects that are enhanced following partial or complete degradation.[1,5] There is a lack of knowledge, however, about how new classes of

energetic materials will respond to different environmental conditions and remediation attempts.

Insensitive munitions are one new class of energetic materials that have recently caused concern for the potential to cause significant environmental contamination.[3] Insensitive munitions were developed as safer alternatives to conventional energetic materials and are less sensitive to shock and high temperature and are designed to improve stability during storage and handling.[3] Their decreased reactivities, however, increase the likelihood of incomplete detonations and the potential to cause undetonated munitions fragments to scatter and accumulate in land and water. This can lead to their mobilization in surface water or infiltration into soils, sediments, and groundwater systems.

DNAN is a NAC that replaces TNT as a constituent of two insensitive munitions formulations currently in production by the U.S. military (IMX-101 and IMX-104). The structural similarity of DNAN to other NACs suggests that the potential toxicity and environmental persistence of DNAN may be similar to traditional NACs. While there are several studies that investigated microbial assemblages that degrade DNAN,[6–10] there has been limited attention to abiotic remediation pathways.[11,12] There is a particular lack of research into the efficacy of iron-rich minerals to abiotically reduce DNAN and how to enhance and better monitor the extent of DNAN degradation.

Iron-rich minerals promote the reduction of NACs by donating electrons from the mineral structure to NACs to convert $-NO_2$ functional groups to amines ($-NH_2$; Figure 1-2). The electrons originate from dissolved ferrous iron (Fe(II)) that binds to hydroxyl

groups associated with Fe(III) on iron oxide, iron (oxy)hydroxide, and sulfide-bearing mineral surfaces. Because Fe(II) oxidizes to Fe(III) in the presence of oxygen, anoxic conditions (< 0.5 ppm O_2) are required to maintain enough dissolved Fe(II) for NAC reduction. When an electron is transferred from mineral-bound Fe(II) to a pollutant, Fe(II) is regenerated either from the dissolved pool of Fe(II) or by Fe(III)-reducing microorganisms,[8,13–17] thus allowing pollutant reduction to continue.

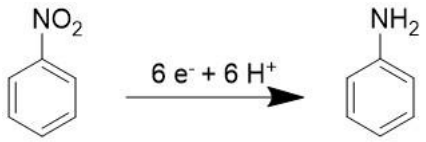

Figure 1-2. Reduction of the nitrobenzene to nitroaniline. Electrons are provided to nitrobenzene to reduce the NO_2-functional group to a NH_2-group,

Assessing the extent of NAC degradation in the environment is difficult because of the possibility of several simultaneous (and potentially competing) transformation and transport processes.[16] For example, the traditional approach to monitor remediation effectiveness is to regularly collect field samples and measure the pollutant concentration and, if possible, reaction products. This method does not necessarily allow for the distinction between multiple reaction pathways (e.g., abiotic vs. biotic) or account for processes which ostensibly reduce pollutant concentrations but do not cause degradation of the compound of interest. For example, dilution along a groundwater plume will decrease the measured concentration of a contaminant at a location over time or distance, but in reality, the total mass of contaminant has only been dispersed throughout a larger volume and no pollutant degradation has occurred. Because NACs in the subsurface

occur in different environmental matrices[18,19] (e.g., soil, sediment, water, air), sorption to surfaces and volatilization into the gas phase also render the interpretation of pollutant concentration dynamics difficult.[20,21]

Compound specific isotope analysis (CSIA) is a valuable tool for monitoring NAC (bio)transformations in that it does not require the direct measurement of analyte concentrations.[22] CSIA, therefore decreases interferences from environmental matrices as described above. CSIA uses stable isotope in parent and/or daughter compounds to quantitively describe the extent of transformation of a compound. All compounds that contain elements with stable (non-radioactive) isotopes (e.g., N, C, H, O) have isotope ratios (e.g., $^{15}N/^{14}N$, $^{13}C/^{12}C$, $^{2}H/^{1}H$, $^{18}O/^{16}O$) present in the compound. Throughout the course of pollutant degradation, stable isotope ratios change if the rate limiting step is a bond breakage at an element with stable isotopes. This change is quantitatively measured against an internationally accepted reference standard. The change in the isotope ratios is called isotope fractionation and is calculated by eq. 1-1.

$$\delta^{h}E = \left(\frac{{}^{h}E/\,{}^{l}E_{sample}}{{}^{h}E/\,{}^{l}E_{reference}} - 1 \right) * 1000‰ \qquad (1-1)$$

where $^{h}E/^{l}E$ is the isotope ratio in the sample and reference material for an arbitrary element, E; $\delta^{h}E$ is termed the bulk isotope signature.[23–25] Permil notation (‰) is used to describe values of $\delta^{h}E$ because of the low natural abundance of most heavy isotopes (e.g., $^{15}N/^{14}N_{reference} = 0.00366 = 3.66‰$).[22]

Isotope fractionation occurs because chemical bonds involving heavy isotopes are stronger than those containing isotopically lighter atoms and react slower and less

favorably during contaminant degradation.[22] The unreacted substrate thus becomes enriched in heavy isotopes (more positive $\delta^{h}E$) while the reaction products are enriched in the lighter isotope (more negative $\delta^{h}E$). Figure 1-3 provides a graphic representation of this phenomenon; A pollutant is degraded (Figure 1-3 circles), molecules that contain lighter isotopes preferentially react and cause an increase in the isotope ratio of the residual molecules (Figure 1-3 triangles) as more molecules with heavier isotopes remain.

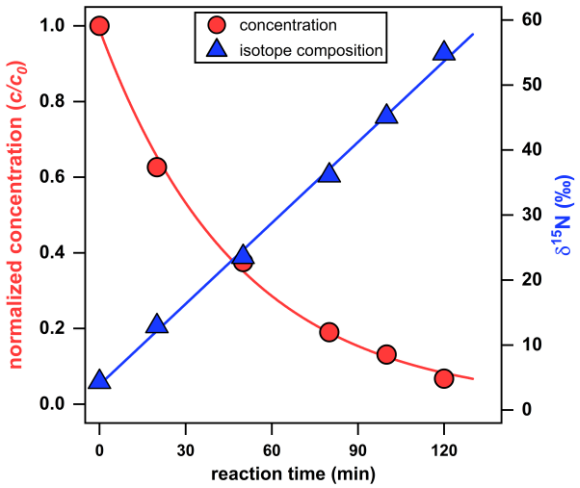

Figure 1-3. Correlation of the extent of a chemical reaction (c/c_0, circles) with N-isotope ratios ($\delta^{15}N$, triangles).

The extent of isotope fractionation is unique for a specific reaction pathway, and the amount that occurs during a reaction is described by the isotope enrichment factor (ε_E, eq. 1-2):

$$\frac{\delta^{h}E+1}{\delta^{h}E_0+1}=\left(\frac{c}{c_0}\right)^{\varepsilon_E} \qquad (1-2)$$

where $\delta^{h}E_0$ is the isotope ratio of the unreacted compound and c/c_0 is the fraction of remaining substrate. Based on eq. 1-2, a more negative ε_E occurs in substrates that are more enriched in heavier isotopes and less degradation has occurred. This approach also eliminates the need to quantify reaction products, which may be not amenable to detection, further degraded, bound to organic matter, or sorbed to the matrix.[26,27]

The different reaction rate constants of molecules containing heavy (^{h}k) and light (^{l}k) isotopes are also reflected by kinetic isotope effects ($KIE_E = {}^{l}k/{}^{h}k$) which are controlled by changes in bonding at a reaction center during the rate-limiting step. Kinetic isotope effects are *normal* ($KIE_E > 1$) if bonds are broken or weakened during a reaction and *inverse* ($KIE_E < 1$) if bonds are formed or strengthened.[22] Kinetic isotope effects are also a bulk property (i.e., considers all isotopes of an element in a compound) and are transformed to *apparent* kinetic isotope effects (AKIEs, eq. 1-3) to describe enrichment at a specific reactive position ($\varepsilon_{\text{reactive position}}$):

$$^{h}\text{E-AKIE} = \frac{1}{1+n \times \varepsilon_{\text{reactive position}}/1000} \qquad (1-3)$$

where n is the number of competing reactive sites. The dependence of isotope fractionation on reaction mechanisms results in unique KIEs for specific reaction pathways. For example, the abiotic reduction of NACs produces large ^{15}N-AKIEs and small ^{13}C-AKIEs because cleavage of the first N–O bond is the rate-limiting step (i.e., ^{15}N-AKIEs are primary). The opposite is true for reactions of NACs which occur primarily at carbon atoms (e.g., enzymatic and alkaline hydrolysis).[12] Simultaneous monitoring of $\delta^{h}E$ values for multiple atoms is performed to differentiate between two or more reaction mechanisms. The dual-element correlation slope ($\Lambda_{N/C} = \Delta^{15}N/\Delta^{13}C$)[28] is,

thus, <1 for the enzymatic and alkaline hydrolysis of NACs and >>1 for abiotic reduction.[12,29–31] The discussion above illustrates how CSIA can be performed in the laboratory to establish isotope fractionation patterns that can be applied to contaminated field sites. Such data may allow for the extent of pollutant degradation to be estimated without the need for direct measurement of contaminant concentrations which is often significantly hampered by environmental conditions and matrix effects.

The goal of this research was to use CSIA to characterize the transformation of NACs during abiotic reduction by Fe(II) associated with Fe-bearing mineral surfaces. First, the isotope fractionation behavior was assessed for DNAN reduction by synthetic Fe-bearing minerals in response to conditions typically encountered in the environment (Chapter 2). These experiments were then extended to include natural sediment materials extracted from two military installations: the Twin Cities Army Ammunition Plant (TCAAP) in Arden Hills, MN and the Tinker Air Force Base (Tinker AFB) in Oklahoma City, OK (Chapter 3).

1.3 Neonicotinoid insecticides

Neonicotinoid insecticides (Figure 1-4) are the most widely used class of insecticides in the world.[32–34] Due in part to their broad range of uses in both agricultural and urban environments, neonicotinoids currently represent approximately 25% of the global insecticide market.[35] Despite their success in mitigating pest insects, they may cause irreparable harm to non-target organisms and ecosystem functioning.[36–40] Moreover, the increasing use of neonicotinoids has caused widespread pollution of U.S. waters and

presents an urgent need to better understand their harmful effects and develop safe use strategies.[41–44]

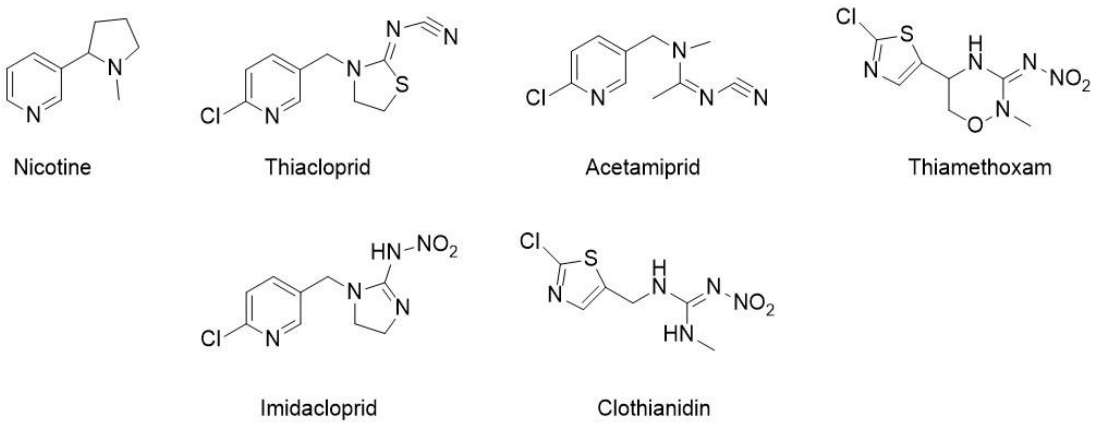

Figure 1-4. Chemical structures of nicotine and several common neonicotinoid insecticides.

Neonicotinoids first entered the insecticide market in 1991 when imidacloprid, produced by Bayer CropScience, was registered for use in the U.S.[35] Over the following decades, several other compounds were approved for use including clothianidin, acetamiprid, thiamethoxam, and thiacloprid (Figure 1-4). Neonicotinoid development was motivated by concerns over the toxicity and environmental impacts of conventional insecticides (e.g., organophosphates and carbamates) and from a growing degree of insect resistance and an awareness of their potential toxicity to mammals and birds.[33,35–40,45] Studies have also shown the potential for neonicotinoids to harm zooplankton taxa, many of which are important algal grazers and indirectly affect the formation of harmful algal blooms.[46,47] Thus, like NACs, neonicotinoids are widespread and have potential adverse impacts.

The most commonly used neonicotinoids are acetamiprid, thiacloprid, imidacloprid, clothianidin, and thiamethoxam. As shown in Figure 1-4, neonicotinoids are structurally similar to nicotine and thus share a common mode of action by inhibiting nicotinic acetylcholine receptors (nAChR) in the central nervous system of insects.[48] They are especially effective as insecticides because these nAChR channels are present in all insects.[49] Neonicotinoids are also systemic, which means that they are incorporated into plants through the roots, dispersed outwards to the terminal structures, and impart toxicity throughout the whole plant (above and below ground). Insects are then exposed to the chemicals when they interact with and feed on treated plants and surfaces.

In agriculture, neonicotinoids are often applied as coatings on seeds (e.g., maize, soybeans, cotton) before sowing.[44] While this decreases the need for airborne sprays and solid granular amendments, it is estimated that only a minor fraction (< 20%) of the coatings are absorbed by the plant,[50,51] leaving the rest to be potentially released into the environment. Traditional application methods, such as foliar sprays and solid granules are still used at many agricultural facilities. The latter create a more direct route for neonicotinoids to pollute the surrounding environment and have caused neonicotinoids to be found in wildflowers surrounding agricultural fields.[52]

In urban areas, most neonicotinoid products are still applied as sprays, granules, and topical treatments on lawns, gardens, and household plants.[33,53] Tree injections are also used to control for the emerald ash borer[54] and some are used in flea medications for

household pets.[33] While neonicotinoids runoff directly into surface and groundwaters, urban applications also enter the environment through stormwater and wastewater collection systems.[55,56] For example, imidacloprid has been detected in urban stormwater at a greater frequency and in higher concentrations than both urban and agricultural streams.[44,55] Urban and agricultural areas also differ in the specific neonicotinoids that are used. Clothianidin, imidacloprid, and thiamethoxam are all commonly detected in agricultural areas while imidacloprid is often the predominant compound found in urban areas.[44]

The physical and chemical properties of neonicotinoids make them highly persistent and mobile in aquatic systems.[57,58] Examples of these properties include high aqueous solubilities (~10^2–10^3 mg/L), low hydrophobicities (log K_{ow} 0.55–1.26, log K_{oc} 1.4–2.3), low volatilities, and modest dissipation half-lives (4.7–40.3 d in water, 3 to >1000 d in soil).[57,59,60] Moreover, as neonicotinoids are transported from their point of application, they are subject to various transformation processes which can produce a number of degradation products of equal or greater toxicity than the parent compound.[61,62] Analytical methods have been developed to detect low concentrations of neonicotinoids in the environment, but a significant gap remains in the application of such methods to neonicotinoid breakdown products.[63,64]

There were two main goals associated with this research. The first goal was to determine how the type of water body (e.g., lake, river, groundwater, treated wastewater effluent) and land use (e.g., agricultural, urban, undeveloped) affected the amount and identity of detected neonicotinoids. In addition, the occurrence of neonicotinoid

transformation products, some of which are of concern to mammals and are known to form during conventional drinking water treatment, was also investigated.[65–67] This aim was approached by collecting water samples from a variety of environmental regimes throughout the state of Minnesota during 2019. The samples were processed using solid phase extraction (SPE) to increase the concentration of each compound and decrease the amount of impurities introduced by the environmental matrix. The analyte concentrations were measured by liquid chromatography-tandem mass spectrometry (LC-MS/MS)[63,64] which separates the components of a mixture based on their individual chemical structure and properties.

The second goal of this research was to investigate any influences of neonicotinoids on the health of non-target organisms, such as zooplankton, aquatic insects, and primary producers. Using the samples collected from lake surface waters, the taxonomic abundance and distribution of several phytoplankton and zooplankton assemblages were quantified. Correlations between planktonic concentrations at several points throughout 2019 and neonicotinoid concentrations were assessed. The combined results from the two research goals will have a direct impact on further understanding the effects of neonicotinoid use (described in Chapter 4) and guiding future management decisions.

Chapter 2. Mineral identity, natural organic matter, and repeated contaminant exposures do not affect the carbon and nitrogen isotope fractionation of 2,4-dinitrianisole during abiotic reduction

This chapter has been published in the journal *Environmental Science: Processes & Impacts* and is reproduced with permission.

Berens, M.J.; Ulrich, B.A.; Strehlau, J.H.; Hofstetter, T.B.; Arnold, W.A. *Environmental Science: Processes and Impacts*. **2019**, *21*, 51–62. doi: 10.1039/C8EM00381E

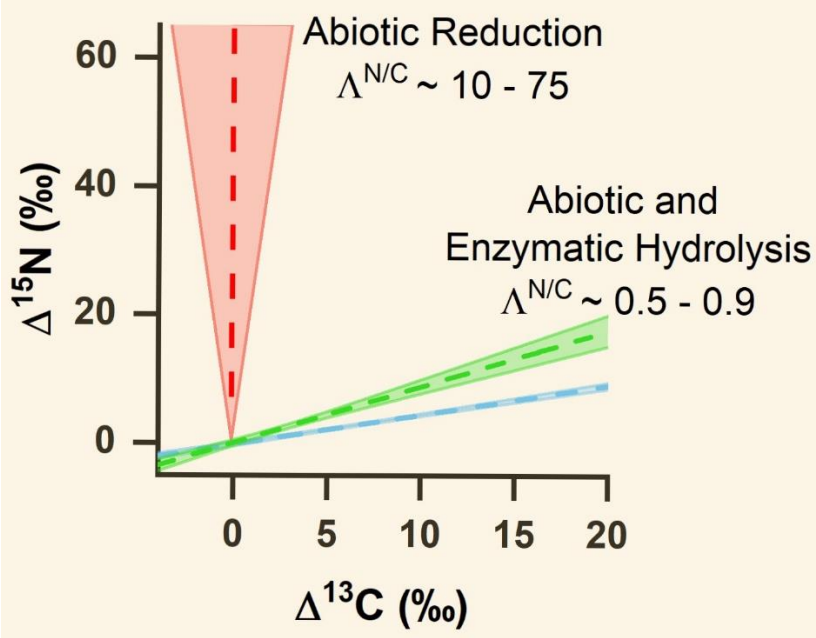

2.1 Overview

The recent development of insensitive munitions, such as 2,4-dinitroanisole (DNAN), as components of military explosives has generated concern for potential subsurface contamination and created a need to fully characterize their transformation processes. Compound specific isotope analysis (CSIA) has proven to be a useful means of assessing transformation pathways according to characteristic stable isotope fractionation patterns. The C and N isotope fractionation of DNAN associated with abiotic and enzymatic

hydrolysis was recently assessed. The extent to which DNAN isotope fractionation will be affected by other potentially competing transformation pathways known for nitroaromatic compounds (e.g., reduction) and if previous knowledge can be extrapolated to other environmental matrices remains to be understood. Here, we investigated the C and N isotope fractionation and reaction rate constants of DNAN during abiotic reduction mediated by mineral-associated Fe(II) species as a function of mineral type, natural organic matter presence, and repeated exposures to DNAN. Though rate constants varied, N and C apparent kinetic isotope effects (AKIEs) remained consistent across all experiments (averaged values of ^{15}N-AKIE = 1.0317 ± 0.0064 and ^{13}C-AKIE = 1.0008 ± 0.0005) and revealed significant ^{15}N- and minimal ^{13}C- enrichment in agreement with previous work on nitroaromatic compounds. Moreover, the observed fractionation was clearly distinct from trends for abiotic and enzymatic hydrolysis. This study provides a strengthened basis for the use of compound specific isotope analysis as a robust tool for monitoring DNAN degradation in complex environmental matrices as a component of future remediation efforts.

2.2 Introduction

Insensitive munitions have emerged as safer alternatives to traditional explosives such as 2,4,6-trinitrotoluene (TNT) and hexahydro-1,3,5-trinitro-1,3,5-triazine (RDX). The U.S. military has recently begun development of two insensitive munitions formulations (IMX-101 and IMX-104) containing 2,4-dinitroanisole (DNAN).[3] These formulations exhibit a decreased sensitivity to shock and high temperatures relative to traditional

munitions and are designed to minimize the risk of accidental detonations during handling and storage.[68,69] Previous contamination by traditional munitions at military installations has caused concern for future contamination by insensitive munitions, motivating considerable effort towards understanding their subsurface fate and transport properties. Limited data, however, is available concerning the fate and transport of these new energetic materials.[16,70] Moreover, the toxicity and sediment-water partitioning behavior of DNAN and its transformation products have shown to be similar to that of TNT.[1,3,18] A better understanding of the relevant natural attenuation processes for DNAN in subsurface environments is therefore needed.

The degradation of DNAN in the environment occurs through several abiotic transformation pathways including alkaline hydrolysis[9,71], photolysis,[72,73] and also reduction in systems containing zero valent iron or other iron-bearing mineral species.[74,75] Previous work has shown that ferrous iron associated with iron oxides, iron (oxy)hydroxides, and sulfide-bearing minerals mediates the abiotic transformation of nitroaromatic compounds (NACs) under anoxic conditions,[5,76–78] reducing NACs to the corresponding substituted anilines (e.g., Scheme 2-1).[79,80] Such pathways have been observed for DNAN and can be attributed to mineral-bound Fe(II) species as well as electron-donating functional groups of natural organic matter.[5,17] Substituted anilines may also form during biotic processes facilitated by Fe(III)-reducing microorganisms and other concomitant suites of aerobic and anaerobic microbiota.[8,13–17] Complete reduction of DNAN in subsurface environments is often achieved through coupled abiotic-biotic transformation mechanisms. For example, Niedźwiecka et al.[81] observed rapid DNAN

reduction in microcosms containing Fe(III) following reduction of Fe(III) to Fe(II) by *Geobacter metallireducens*, compared to microcosms without ferric iron.

Scheme 2-1.Reductive transformation pathway of DNAN, with one N atom at which the reduction reaction can occur highlighted. The pathway is initiated by the formation of a nitroso-moiety (2) from a NO_2 group,[17,75,82] followed by formation of hydroxylamine (3) and subsequently an amine derivative (e.g., 2-methoxy-5-nitroaniline (MENA) (4)). The mechanism of aromatic NO_2 reduction is shown here arbitrarily for the *ortho*-substituent and does not imply preferential formation of MENA. However, most current studies are in agreement that reduction is initiated at the *ortho* substituent.[17,82,83] In the presence of sufficient reductant, this process continues through other intermediates before reducing the second NO_2-group to generate 2,4-diaminoanisole (DAAN) (5).[5]

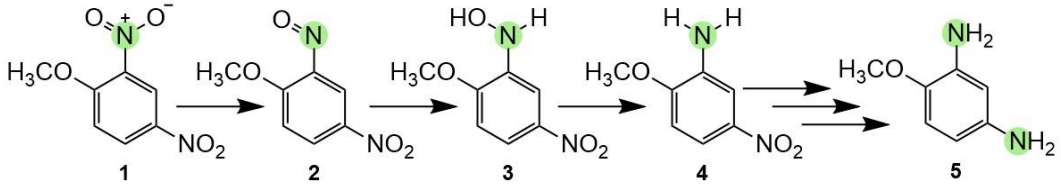

Assessing the transformation of NACs in the environment is complicated by the possibility of several simultaneous (and potentially competing) transformation and transport processes (e.g., sorption, volatilization, (bio)degradation).[16] Likewise, NACs in the subsurface may be present in different phases[18,19] and exhibit high soil and sediment sorption, rendering the interpretation of concentration dynamics difficult.[20,21] Compound specific isotope analysis (CSIA) has proven useful for assessing degradation processes of NACs in such complex environmental systems with potentially competing attenuation processes.[84,85] CSIA of NAC (bio)transformations is based on characteristic changes in stable isotope ratios (e.g., $^{15}N/^{14}N$, $^{13}C/^{12}C$) that are indicative of a specific pathway.[23,86] Thus, it is possible to use CSIA to determine the reaction process occurring without the need to detect reaction products, which may be not be amenable to detection, further

degraded, bind to organic matter, or sorb to the matrix.[26,27] These so-called isotope fractionation patterns arise from apparent kinetic isotope effects (AKIEs) controlled by changes in the bonding environment at the reactive position during the initial stages of NAC transformation.[87] Indeed, AKIEs have been well-characterized for the abiotic reduction of several NACs including chloro- and methyl-substituted nitrobenzenes, dinitrobenzene isomers, and 2,4,6-trinitrotoluene (^{15}N-AKIE ~ 1.03–1.04, ^{13}C-AKIE ~ 1.001).[29–31,88]

Abiotic reductions of NACs (Scheme 2-1) result in large primary ^{15}N-AKIEs, for which cleavage of the first N—O bond to form a nitroso intermediate is the rate-limiting step and thus dictates shifts in the isotope signature. In contrast, the corresponding ^{13}C-AKIEs are typically small because C atoms are not directly involved in the rate-limiting step (i.e., secondary AKIEs).[29–31] Whereas Ulrich et al.[12] recently assessed ^{13}C and ^{15}N fractionation during the abiotic (i.e., alkaline) and enzymatic hydrolysis of DNAN, the isotope fractionation that arises from reductive transformation of DNAN remains to be assessed. Previous work on the abiotic reduction of NACs by Fe(II) associated with the surfaces of iron oxides and clay minerals suggests that DNAN will display similar isotopic fractionation behavior.[29–31,88] Those studies, however, focused on isomers of chloro- and methyl-substituted compounds and on a limited set of minerals (i.e., Fe(II) associated with goethite and structural Fe(II) in magnetite and ferruginous smectite). Showing that fractionation is independent of environmental matrix conditions is imperative for accurately quantifying the extent of pollutant degradation at contaminated field sites where the subsurface composition may be complex, changing, or unknown.

Potential matrix conditions could include the presence of different minerals with different reactivity towards NACs, interferences of natural organic matter (NOM) through association with the mineral surface, and the transformation of Fe minerals after repeated exposure to NACs. Previous work has revealed that transformation rates of NACs may span orders of magnitude depending on the type of mineral involved owing to modulations in the electrochemical potential (E_H) of the oxide-associated Fe(II) system.[76,77,89–91] The presence of NOM may also impact reaction rates through the formation of Fe(II)-NOM complexes.[92] NOM may also alter particle dispersion or change the availability of reactive sites.[93–96] Repeated contaminant exposure may induce evolution of the mineral structure, potentially interfering with Fe(II) uptake or developing a new surface oxide.[96,97] Because the magnitude of isotope fractionation during the reduction of NACs was proposed to be determined by changes of bonding in the aromatic NO_2 substituent(s) regardless of the rate of transformation (i.e., reduction of a nitro-group to form a nitroso-moiety), we hypothesize isotope fractionation associated with the reduction of new potential contaminants such as DNAN in the environment will be consistent with previously determined AKIE-values as well as independent of matrix conditions discussed above.[29,31,84,88,98,99]

The goal of this study was to investigate the effects of matrix conditions that could be encountered in environmental systems on the reaction kinetics and C and N isotope fractionation associated with abiotic DNAN reduction, thereby evaluating the robustness of AKIEs and the associated isotope enrichment factors for the application of CSIA for assessing reductive transformations of DNAN. To this end, we characterized the pseudo-

first-order kinetics and the C and N isotope fractionation during abiotic DNAN reduction as a function of (1) the type of mineral (goethite, magnetite, or mackinawite), (2) the presence of natural organic matter (NOM), and (3) repeated exposures to DNAN. Measured C and N isotope signatures ($\delta^{13}C$ and $\delta^{15}N$) as a function of reaction extent were used to derive the corresponding isotope enrichment factors (ε_C and ε_N) and apparent kinetic isotope effects (^{13}C-AKIE and ^{15}N-AKIE). These values were compared to previous evidence on isotope effects associated with NAC reduction as well as to those recently established for alkaline and enzymatic hydrolysis[12] to confirm the efficacy of CSIA to distinguish between the most likely environmental DNAN degradation reactions. The findings of this work provide a strengthened basis for identifying and assessing these processes in subsurface environments by CSIA, a result that will be of particular significance to potential future efforts to monitor and remediate DNAN-contaminated subsurface environments.

2.3 Methods

2.3.1 Chemicals

Detailed chemical information is provided in Appendix A. Fresh Fe(II) and DNAN stock solutions were prepared prior to each reduction experiment. Aqueous Fe(II) stock solutions were prepared by adding 0.44 g $FeCl_2 \cdot 6H_2O$ to 0.4 mL of 1 M HCl and enough deoxygenated ultrapure water to achieve a final concentration of 175 mM. DNAN (Alfa Aesar, 98%, CAS# 119-27-7) stock solutions were similarly prepared in deoxygenated methanol. It should be noted that DNAN was purchased in 2016 and is no longer

available from Alfa Aesar in the United States. DNAN transformation products 2-methoxy-5-nitroaniline (MENA, 98%, CAS# 99-59-2) and 2,4-diaminoanisole (DAAN, ≥98%, CAS# 615-05-4) were purchased from Fisher Scientific. Elliot Soil humic acid (ESHA) was purchased from the International Humic Substances Society (IHSS, St. Paul, MN). With the exception of goethite synthesis and storage, all experiments were performed inside an anaerobic chamber (Coy, 95% N_2/5% H_2).

2.3.2 Mineral Synthesis

Detailed mineral synthesis and analysis procedures are provided in Appendix A. Mackinawite was precipitated using the method of Butler and Hayes[100] and particles were stored in suspension in the anaerobic chamber at room temperature and pH 7. Synthetic goethite was prepared according to Anschutz and Penn[101] and stored in suspension outside the anaerobic chamber at pH 4 and 4 °C. Magnetite synthesis was adapted from Schwertmann and Cornell.[102] Synthetic magnetite was dried and stored as a powder inside the chamber. Magnetite stoichiometry (x = Fe(II)/Fe(III)) was determined by acid dissolution in 3 M HCl (Sigma, trace metals) as x = 0.50. Total Fe(II) and Fe(III) content was quantified using the ferrozine colorimetric assay (Appendix A).[103] Each mineral was characterized by X-ray diffraction (XRD) and compared to reference patterns to support the presence of each desired mineral phase (Figure A-1). The XRD results for synthetic magnetite and goethite indicated the presence of only the desired phases. The pattern collected from mackinawite contained peaks consistent with mackinawite and greigite (Fe_3S_4, PDF No. 16-0713). Previous work has reported rapid phase transformation of

mackinawite to greigite under oxic conditions at room temperature, which may suggest the presence of greigite as an artifact of sample preparation.[104]

Mineral surface areas were determined by nitrogen adsorption analysis using the Brunauer-Emmett-Teller (BET) adsorption model[105] as 103.8 m^2/g and 17.8 m^2/g for goethite and magnetite, respectively. Mackinawite decomposed under high vacuum and temperature during outgassing and an accurate surface area measurement could not be obtained. Mass loading experiments were performed and the particle concentrations in goethite and mackinawite suspensions were approximately 10 g/L and 33 g/L, respectively.

2.3.3 Batch Reactions

Batch experiments to assess reaction kinetics were performed in triplicate in 50 mL borosilicate serum bottles capped with Teflon-lined butyl rubber septa. All reactors contained a mineral suspension in $NaHCO_3$ buffer (10 mM, pH 7.0). Mineral loadings were 2.0 g/L for magnetite, 1.5 g/L for mackinawite, and 1.0 g/L for goethite. Aqueous Fe(II) was added to goethite and magnetite reactors at a concentration of 1 mM and equilibrated overnight by rotating on an end-over-end rotator (Glas-Col, 40 rpm). No Fe(II) was added to mackinawite reactors and only a 1 h equilibration was performed. For the subset of reactions containing NOM, ESHA was added at 5 mg C/L prior to equilibration. The pH was then measured and Fe(II) concentrations were determined using the ferrozine method.[103] If necessary, the pH was adjusted back to 7.0 with 1 M HCl or 1 M NaOH (Fisher, ACS grade) and the Fe(II) was augmented to 1 mM in the

magnetite and goethite reactors. Reactions were initiated by spiking DNAN from the methanolic stock solution to a concentration of 0.20 mM and returning reactors to the rotator. The DNAN concentration was selected to ensure that a sufficient concentration remained in solution to allow detection by CSIA after achieving our target of 95% reduction. Every hour, the pH and Fe(II) in the reactors were determined and adjusted to pH 7 and 1 mM, respectively. This was necessary because the initial 1 mM Fe(II) is not sufficient to completely reduce the 0.20 mM DNAN (a minimum of 2.4 mM e^- is needed to reduce both $–NO_2$ moieties to $–NH_2$), and it allows for the assumption of pseudo-first-order kinetics by maintaining a high Fe(II) concentration. At appropriate time points, an aliquot from each reactor was removed and filtered with a 0.2 μm PTFE syringe filter. Aqueous DNAN, MENA, and DAAN concentrations were quantified at a wavelength of 230 nm using an Agilent 1200 series high pressure liquid chromatograph (HPLC, method in Appendix A). Pseudo-first-order rate constants were determined by regression using a log-linear relationship of $\ln(c/c_0)$ versus time.

To perform batch experiments for CSIA, eight replicate reactors were assembled as described above for each set of reaction conditions. At each sampling point, the entire contents of one reactor were removed, filtered, and stabilized by adjusting the pH to < 4 with 1 M HCl (Sigma, trace metals). Approximately 14 mL of acidified filtrate were transferred to a clean 20 mL glass vial, fitted with a butyl rubber plug (Fisher, 20 mm) and crimp cap, and stored at 4 °C until isotope analysis (method described below).

To assess the baseline reactivity of each mineral suspension for DNAN transformation, reactors were assembled containing only mineral, buffer, Fe(II) (for iron

oxides), and DNAN. A control was performed with Fe(II) alone in $NaHCO_3$ buffer, in which no reaction was observed over 21 days (Figure A-2). To perform repeated contaminant exposure experiments, batch reactors were assembled in triplicate as described above. The first spike was initiated by injecting DNAN to a concentration of 0.20 mM. The Fe(II) content was determined in goethite and magnetite reactors after 1 h of reaction and adjusted accordingly to return each reactor to 1 mM Fe(II). A single aliquot (~0.20 mL) was removed for analysis by HPLC after approximately 8 h to confirm complete DNAN transformation (<0.001 mM). Subsequently, to avoid the formation and accumulation of products over multiple reaction cycles, the aqueous solution from each reactor was removed and replaced with fresh buffer solution at the end of each reduction cycle. Suspensions were settled for at least 12 h or, in the case of magnetite, particles were isolated by using a neodymium magnet and discarding the supernatant. Fresh Fe(II) (1 mM) was added to goethite and magnetite reactors and the reactors were then equilibrated as described above. The pH was adjusted back to 7.0 in all reactors and a second DNAN spike was initiated and the reaction performed as described above. This procedure was carried out for five cycles, with concentrations measured as a function of time in triplicate during the desired cycle. For CSIA, a reactor was sacrificed at each time point during the fifth cycle and prepared for isotope analysis as described above.

2.3.4 Compound Specific Isotope Analysis

Isotopic analysis of DNAN was conducted by gas chromatography isotope ratio mass spectrometry (GC/IRMS). DNAN was concentrated by solid phase micro extraction (SPME) prior to isotopic analysis. A method was modified from established SPME procedures[12,106] using the PAL SPME Arrow (DVB/PDMS sorption phase, 120 µm phase thickness, 1.1 mm diameter) instead of a normal SPME fiber, such that improved sensitivity could be obtained with a larger sorption phase.[107] Automated SPME was carried out using a PAL autosampler equipped with a PAL SPME Arrow Tool and a Heatex Stirrer. All samples were initially diluted with 10 mM phosphate buffer (pH 7, prepared with nanopure water) to obtain concentrations within a range of linear response, and sodium chloride (100 g/L) was added to maximize extraction efficiency. Following equilibration at 50 °C for 10 min, the SPME Arrow was immersed in the sample for 70 minutes at 50 °C (600 RPM stir rate), and then DNAN was thermally desorbed from the arrow in an injector equipped with a deactivated liner (270 °C, 6 minutes).

DNAN $^{15}N/^{14}N$ and $^{13}C/^{12}C$ ratios were determined using a Trace GC (Thermo Electron Corp.) coupled to an IRMS (DeltaPLUS XL, Thermo Electron Corp.) via a combustion interface (GC Combustion III, Thermo) equipped with a custom-made Ni/Pt reactor. The GC contained an Rtx-5MS capillary column (0.32 mm ID, 1 µm film thickness, 30 m length) and was operated in splitless mode (splitless time 6 minutes, purge flow 50 ml/min) with the following temperature program: 50 °C for 1 minute, ramp 10 °C/min to 250 °C, hold for 5 minutes. During $\delta^{15}N$ analysis a liquid nitrogen trap was used to trap CO_2 produced from combustion. The oxidation reactor was operated as

described previously.[108] Method quantification limits (MQLs) for $\delta^{13}C$ and $\delta^{15}N$ according to the moving mean procedure were 0.2 µM and 1 µM, respectively.[109]

Isotope ratios were references against standard laboratory gases as well as DNAN of known isotopic composition ($\delta^{13}C$ = 37.3 ± 0.1 ‰ and $\delta^{15}N$ = -2.4 ± 0.1 ‰ as determined by an elemental analyzer) using standard bracketing procedures.[28] Carbon and nitrogen isotope enrichment factors (ε_C and ε_N) were derived according to methods described by Pati et al.[28] Linear regression analyses of the isotope signature data were carried out using the log-linearized form of eq. 1-1:

$$\frac{\delta^{h}E+1}{\delta^{h}E_0+1}=\left(\frac{c}{c_0}\right)^{\varepsilon_E} \qquad (1-1)$$

where $\delta^{h}E_0$ is the C or N isotope signature of unreacted DNAN and c/c_0 is the fraction of remaining substrate (detailed calculations in Appendix A).[110] Apparent kinetic isotope effects (^{13}C-AKIE and ^{15}N-AKIE) were then derived from the calculated ε_E values using eq. 1-2.[85]

$$^{h}E\text{-AKIE}=\frac{1}{1+z\times\varepsilon_E/1000} \qquad (1-2)$$

where z is the number of competing reactive sites (i.e., z = 2 for N and z = 1 for C in DNAN).[22] Combined AKIEs were calculated for all three sets of conditions for each mineral phase (i.e., mineral alone, presence of NOM, repeated contaminant exposures) according to the method of Scott et al.[111] using the Pitman estimator. Additional details for isotope analysis are provided in Appendix A.

2.4 Results and Discussion

2.4.1 Kinetic Experiments

Pseudo-first-order rate constants (k_{obs}) from triplicate reactors were calculated for all conditions tested (Table 2-1). The only reaction products observed were MENA and DAAN. Aqueous concentrations of DNAN and its transformation products are highlighted in Figure 2-1. Mass balances were ~80%, and given the high initial concentration, the incomplete mass balance could be due to formation of coupling products between hydroxylamine and nitroso intermediates.[112,113] The limited accumulation of DAAN is likely due to lower reactivity of MENA compared to DNAN, because Fe(II) was maintained at 1 mM throughout the experiments with goethite and magnetite. The greater accumulation of MENA with mackinawite may be due to changing mineralogy (see below). Because the focus of CSIA analysis was on DNAN, monitoring the reaction to complete conversion to DAAN was not necessary. The highest transformation rates were observed for the first contaminant exposure (i.e., Spike 1) in Fe(II)/goethite suspensions followed by mackinawite and Fe(II)/magnetite, respectively. Aqueous Fe(II) was supplemented (and added throughout the experiment to maintain a 1 mM concentration) into goethite and magnetite suspensions because these minerals contain little to no inherent surface associated Fe(II) reactive sites. In contrast, mackinawite is an Fe(II)-bearing mineral known to directly participate in reduction reactions.[100,114,115] Mineral concentrations in batch reactors decreased in the order of magnetite (2.0 g/L), mackinawite (1.5 g/L), and goethite (1.0 g/L), resulting in the same order of increasing k_{obs} when normalized to mineral loadings. Mineral concentrations

were selected such that DNAN reduction experiments occurred within a similar experimental time frame. Organic matter (5 mg C/L from ESHA) had no effect on k_{obs} in all samples tested. Previous work has shown that organic matter decreases reduction rates of NACs, likely via competitive adsorption with Fe(II) or blocking of reactive sites at the mineral surface.[96] One possible explanation for these differences is that our work uses higher mineral loadings and a constant supply of Fe(II), thus increasing the abundance of Fe(II) and mineral reactive sites while decreasing the competition for each. Alternatively, higher mineral loadings and Fe(II) content may overcome any increases in E_H imposed by NOM functional groups which have been linked to decreased rates of contaminant reduction.[91]

Table 2-1.Pseudo-first-order rate constants, k_{obs}, for DNAN reduction.[a,b] Rate constants were calculated in systems containing the mineral alone (Spike 1), the addition of NOM (ESHA), and during the fifth sequential contaminant exposures (Spike 5).

	k_{obs} (h^{-1})		
System	Mackinawite	Goethite	Magnetite
Spike 1	1.15 ± 0.12	2.55 ± 0.14	0.79 ± 0.05
ESHA	1.16 ± 0.09	2.49 ± 0.18	0.82 ± 0.04
Spike 5	0.19 ± 0.04	2.52 ± 0.11	0.81 ± 0.07

[a]Rate constants obtained from linear regression of natural log of concentration versus time data. [b]Uncertainties represent standard deviations of triplicate reactors.

Rate constants calculated during repeated contaminant exposure experiments revealed that reaction kinetics were independent of previous contaminant exposure in reactors containing goethite and magnetite. This is consistent with previous work with iron oxides, confirming that minimal variation in the rate constant can be expected if pH is carefully maintained over multiple contaminant exposures.[96] Moreover, these results

suggest that any mineral transformations that may have occurred during repeated exposures did not significantly affect the reduction potential of the oxide-bound Fe(II) in each system.[91]

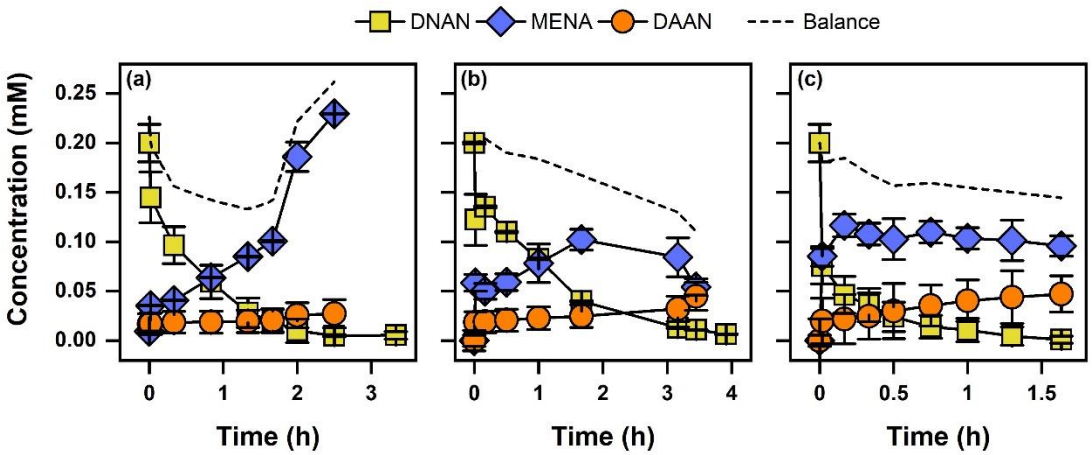

Figure 2-1. Aqueous concentrations of DNAN, MENA, and DAAN during DNAN kinetics experiments in suspensions of (a) mackinawite (1.5 g/L), (b) magnetite (2 g/L), and (c) goethite (1.0 g/L). Reactions were performed at pH 7 with 1 mM Fe(II) and are for the first spike of DNAN. Error bars represent standard deviations of triplicate reactors. Dotted lines represent mass balances (moles) of the three compounds.

In contrast to goethite and magnetite, the observed pseudo-first order reaction rate constant for mackinawite decreased with each exposure to DNAN (Figure 2-2a). This observation could be attributed to the development of lepidocrocite (γ-FeOOH, PDF No. 44-1415) over the course of five contaminant spikes (Figure 2-2b). While it is likely the rate constant was changing over the course of each contaminant exposure, a pseudo-first order model adequately fits the data for each spike and allows quantification of the loss of reactivity over time (Figure 2-2a). Lepidocrocite is a polymorph of goethite and could

be expected to exhibit similar reactive properties to goethite if sufficient Fe(II) was available,[89] which it likely is not in this system given that none was added.

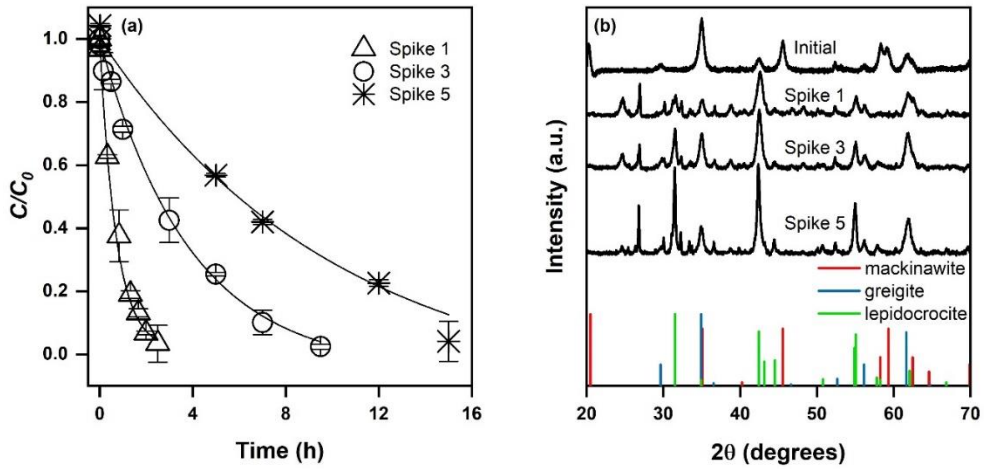

Figure 2-2. (a) Kinetic profiles and (b) XRD patterns of mackinawite reactions during repeated exposures to DNAN. Error bars represent standard deviations of triplicate reactors, and lines are pseudo-first order fits to the data.

Therefore, the observation that k_{obs} decreases during lepidocrocite formation is supported by the observation that lepidocrocite has a lower k_{obs} for NAC transformation and the requirement of Fe(II) supplementation for reaction to occur on Fe(III)-oxides.[76] These results highlight the importance of understanding the effects of phase evolution on reaction kinetics at highly contaminated sites.

2.4.2 CSIA of DNAN reduction

The transformation of DNAN in suspensions of mackinawite, Fe(II)/goethite, and Fe(II)/magnetite was associated with strong enrichment of ^{15}N of up to 60‰ in the remaining substrate whereas enrichment of ^{13}C was minimal (below 2.4‰) in agreement with previous work on the reductive transformation of other NACs.[23,31,86–88] The extent of

DNAN degradation was related to isotope fractionation by eq. 1-1. Average ε_N-values for the reduction of DNAN derived after the first vs. fifth spike to the mineral suspension decreased by 1‰ to 5‰ as shown in Table 2-2 (e.g., -19 ± 1‰ in mackinawite experiment spike 1 vs. -16 ± 2‰ for spike 5). All changes, however, were within the uncertainty (95% confidence intervals). Variations of ε_C were much smaller (with errors of the same magnitude as the measurements) and did not show a discernable trend (Figure 2-3b). The minimum and maximum ^{15}N-AKIE-values derived from ε_N (eq. 1-2) ranged from 1.018 ± 0.002 (magnetite, spike 5) to 1.039 ± 0.001 (mackinawite, spike 1) and fall within the range of data reported for the abiotic reduction of substituted mono-, di-, and trinitroaromatic compounds by mineral-bound Fe(II) reported previously.[23,31,86–88] Whereas large ^{15}N-AKIEs are due to the rate-limiting cleavage of the first N–O bond of the aromatic NO_2 groups, ^{13}C-AKIE are small (i.e., secondary) vary between 1.000 and 1.002 (Table 2-2) because no changes in bonds to C occur. Identical observations were made with experiments where DNAN was reduced in mineral suspension in the presence of ESHA in that ^{15}N- and ^{13}C-AKIE were identical within experimental error to experiments without humic acids.

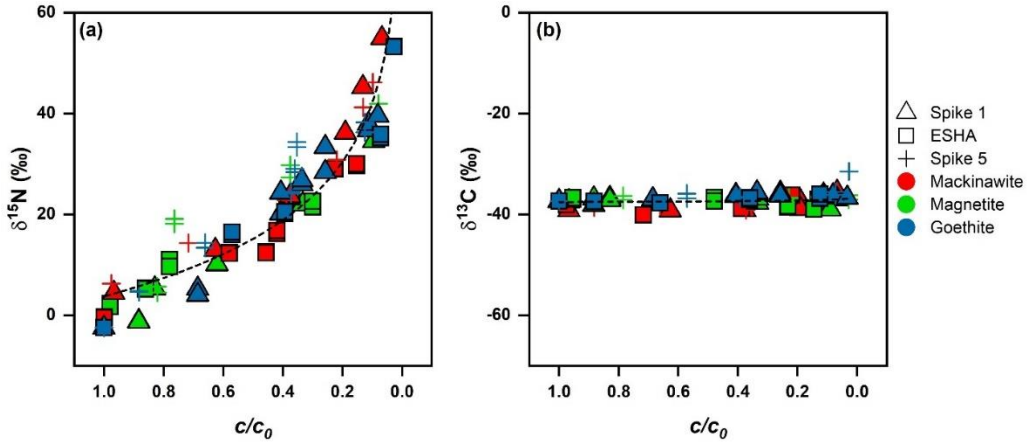

Figure 2-3. Nitrogen and carbon isotope fractionation of DNAN during abiotic reduction. (a) $\delta^{15}N$ and (b) $\delta^{13}C$ vs. fraction of remaining substrate (c/c_0) with dotted lines provided to guide the eye along the data. Detailed N and C enrichment values are provided in Table 2-2 (see Figure A-3 for $\delta^{15}N$ and $\delta^{13}C$ vs. c/c_0 data separated by reaction condition).

Slight decreases in fractionation were observed during repeated contaminant exposure in Fe(II)/goethite and Fe(II)/magnetite systems (Table 2-2). This suggests that morphological changes (e.g., phase evolution and growth) occurring on the mineral structure during repeated surface oxidation and Fe(II) exposure may have limited the accessibility of reactive Fe(II) and thus slightly masked the isotope fractionation (Figure A-4). These changes were within experimental error of the initial spike experiment (ε_N = -17 ± 3‰ to -11 ± 1‰ and -15 ± 3‰ to -9 ± 2‰ between the single and multiple spike experiments for goethite and magnetite, respectively).

Table 2-2. N and C bulk isotope enrichment factors (ε_N, ε_C)[a,b,c] and apparent kinetic isotope effects (^{15}N-AKIE, ^{13}C-AKIE)[b,c] during the reduction of DNAN in different mineral systems.

System	ε_N (‰)	ε_C (‰)	^{15}N-AKIE (-)	^{13}C-AKIE (-)
Mackinawite				
Spike 1	-19 ± 1	-0.8 ± 0.6	1.039 ± 0.001	1.0008 ± 0.0008
ESHA	-16 ± 1	-0.7 ± 1.4	1.034 ± 0.001	1.0007 ± 0.0014
Spike 5	-16 ± 2	-1.5 ± 1.2	1.034 ± 0.002	1.0015 ± 0.0012
Average	-19 ± 2	-0.3 ± 0.6	1.039 ± 0.004	1.0003 ± 0.0006
Goethite				
Spike 1	-17 ± 3	-0.1 ± 0.3	1.035 ± 0.003	1.0000 ± 0.0003
ESHA	-16 ± 5	-0.6 ± 0.4	1.034 ± 0.005	1.0006 ± 0.0004
Spike 5	-11 ± 1	-1.2 ± 0.9	1.022 ± 0.001	1.0012 ± 0.0009
Average	-16 ± 3	-0.5 ± 0.3	1.033 ± 0.007	1.0005 ± 0.0003
Magnetite				
Spike 1	-15 ± 3	-0.7 ± 0.6	1.031 ± 0.003	1.0007 ± 0.0006
ESHA	-17 ± 3	-1.3 ± 0.2	1.036 ± 0.003	1.0013 ± 0.0005
Spike 5	-9 ± 2	-0.1 ± 0.2	1.018 ± 0.002	1.0000 ± 0.0002
Average	-17 ± 3	-0.3 ± 0.5	1.035 ± 0.006	1.0000 ± 0.0005
Alkaline Hydrolysis[d]	-2.7 ± 0.4	-6.0 ± 0.5	1.0027 ± 0.0004	1.0445 ± 0.0028
Enzymatic hydrolysis by O-demethylase[d]	-3.2 ± 0.1	-3.7 ± 0.1	1.0032 ± 0.0003	1.0269 ± 0.0053

[a]Values derived from log-linear regression analysis of eq. 1-1.
[b]Uncertainties represent 95% confidence intervals.
[c]Averaged values according to the methods of Scott et al.[111] using the Pitman estimator.
[d]Data from Ulrich et al.[12] and references therein.[23,29–31,106]

The collective C and N isotope fractionation data from all DNAN reduction experiments is plotted in Figure 2-3. Plots separated by mineral are in Figure A-3. The values of δ^{15}N follow the general trend of ε_N values between -19 ± 1‰ to -9 ± 2‰ from

individual DNAN reduction experiments. The scatter of $\delta^{15}N$ values illustrates that experimental and analytical uncertainties are larger in experiments with ESHA and after repeated spikes of DNAN. We conclude that those uncertainties are primarily responsible for the observed variations of ε_N values from the individual experiments as well as for the large confidence intervals (typically <0.5‰).[28] Based on this interpretation, we derived average ^{15}N-AKIE for DNAN reduction by each mineral, that is 1.039 ± 0.004, 1.033 ± 0.007, and 1.035 ± 0.005 for mackinawite, goethite, and magnetite, respectively (Table 2-2) which are again identical within uncertainty.

An analysis of eqs. 1-1 and 1-2 illustrates that a variation of ε_N for DNAN by ± 2.8‰, that is variations of ^{15}N-AKIE of ± 0.006 as observed in the average uncertainty of ^{15}N-AKIEs in this study, will introduce uncertainty in estimating the extent of transformation (i.e., 100 × (1-c/c_0)). This uncertainty will be higher when the observed N isotope fractionation is small (e.g., 15% for $\Delta^{15}N$ of 5‰) and level off as the N isotope fractionation increases (e.g., <7.5% at $\Delta^{15}N$ of 25‰[84] see Figure 2-4). Given the large magnitude of ^{15}N-AKIEs observed here, the extent of DNAN reduction has to exceed only approximately 12% to generate N isotope fractionation beyond the typical total uncertainties of N isotope ratio measurements of ±1‰[86] based on an average ε_N value of --16‰.

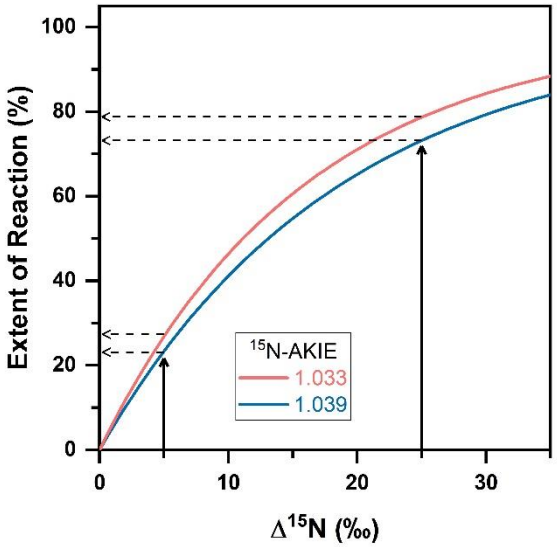

Figure 2-4. Changes in N isotope ratios ($\Delta^{15}N = \delta^{15}N - \delta^{15}N_0$) vs the extent of DNAN reaction ($100 \times (1\text{-}c/c_0)$). Equations 1-1 and 1-2 were used to illustrate variations in the extent of reaction given uncertainties in calculated AKIEs. Isotope fractionation profiles were generated using ε_N values of -16.0‰ (red) and -18.8‰ (blue), values typical for abiotic reductions of NACs but also within the range of isotope effects derived for the reduction of other NACs by other minerals. These ε_N values represent the extrema observed in this work. Dotted lines represent uncertainties in calculating the extent of reaction from uncertainties in ^{15}N–AKIEs.

The N isotope fractionation data for DNAN reduction reveal two important findings. First, abiotic reduction of DNAN will give rise to similar isotope enrichment factors across a variety of reaction conditions (i.e., regardless of the presence of NOM and previous contaminant exposures). Moreover, it is notable that ^{15}N-AKIE and ε_N values calculated in this study closely agree with those observed for the reduction of other model NACs by Fe-bearing mineral phases.[29–31,88] This comparison confirms our hypothesis that previous N isotope fractionation data for the abiotic reduction of NACs by Fe(II) bearing minerals can be extrapolated to new contaminants such as DNAN. This observation also indicates that N isotope fractionation is a robust indicator for monitoring the extent of

reduction of DNAN and other NACs in complex environmental matrices, even in the absence of knowledge relating to reaction kinetics and product formation. Indeed, this technique has previously been employed to provide quantitative estimates of the extent of organic contaminant transformations at contaminated field sites.[116] Our work, therefore, serves to qualify the prospective use of CSIA to assess the abiotic reduction of novel insensitive munitions in the environment.[84,117]

The combined C and N isotope analysis for DNAN reduction derived here is compared to the data for alkaline hydrolysis and aerobic biodegradation from Ulrich et al.[12] in Figure 2-5 and confirms that the different transformation pathways can also be discerned by CSIA. These data support the claim that N fractionation of DNAN during abiotic reduction is distinct from the isotopic fractionation observed in alkaline hydrolysis (nucleophilic aromatic substitution) and enzymatic hydrolysis (nucleophilic aliphatic substitution). Due to the vertical nature of the $\Lambda^{N/C}$ for the abiotic reduction data, a standard linear regression failed. Thus, the slope was found by plotting all of the $\Delta^{13}C$ vs $\Delta^{15}N$ data, finding the slope, and then taking the inverse of this value. The $\Lambda^{N/C}$ calculated via this method for abiotic reduction was 50.5 ± 23.2 (shown as the dotted line in Figure 2-5) in contrast to 0.46 ± 0.04 and 0.87 ± 0.18 for alkaline hydrolysis and biodegradation, respectively.[12] These results therefore suggest that an identification of those DNAN reaction pathways and their respective contributions in the environment would be possible.[118] Abiotic and biotic transformations of NACs typically elicit variable degree of ^{15}N, ^{13}C, and ^{2}H enrichment, [23,30,119] so that the observable isotope fractionation of processes occurring simultaneously can, in principle, be described by linear

combinations of the enrichment factors pertinent to the individual, contributing processes.[98,118] Such dual or triple isotope analysis[84] can also circumvent masking interferences, which so far, have been reported primarily for oxidative NAC degradation processes[120–122].[85,119,123]

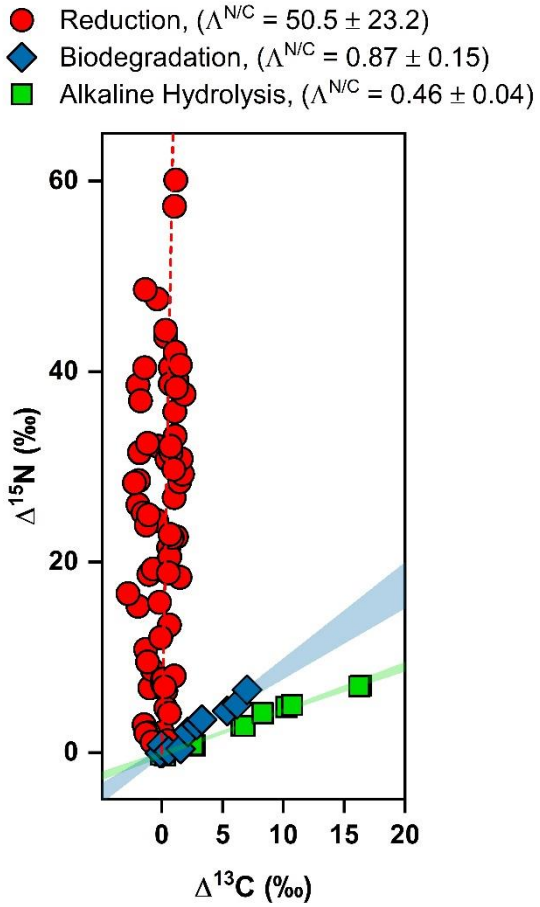

Figure 2-5. Two-dimensional isotope analysis for reductive and oxidative DNAN transformation pathways. Changes in $\delta^{13}C$ and $\delta^{15}N$ values were monitored during abiotic reduction (circles), alkaline hydrolysis (squares), and biodegradation (diamonds). Alkaline hydrolysis and biodegradation data were reproduced with permission from Ulrich et al.[12] Reduction data separated by mineral type are provided in Figure A-5. The dotted line along the reduction data is provided simply to guide the eye. Moreover, any apparent inverse fractionation is an artifact of uncertainties in ^{13}C-AKIEs that are close to 1.

2.5 Conclusion

Knowledge of the stable isotope fractionation associated with DNAN reduction will allow for stakeholders to make quantitative estimates of the extent of DNAN degradation from measured $\delta^{15}N$ and $\delta^{13}C$ values of DNAN at contaminated sites. Our findings revealed that N and C isotope fractionation during the mineral-mediated reduction of DNAN is consistent despite the presence of different minerals, NOM, and repeated contaminant exposures while remaining independent of reaction kinetics. The potential, changes of N isotope enrichment factors with repetitive exposure merit further investigation, especially considering that surface modification on natural minerals may be different than those for synthetic materials while those effects do not affect the interpretation of dual isotope analysis. Moreover, we showed that isotope fractionation during DNAN reduction will elicit $\Lambda^{N/C}$ values that are distinct from transformation pathways initiated by oxidation and substitution reactions.[38] By showing that our data reflects previous results for reductions of other NACs[30,33,34,36,38], this work illustrates how predictive comparisons can be made to assess the extent of pollutant transformation from existing data. Such practices provide a strengthened basis for CSIA to serve as a reliable tool for validating future remediation efforts.

2.6 Acknowledgements

This work was supported by the Strategic Environmental Research and Development Program (SERDP, Project No. ER2618). We thank Lee Penn (University of Minnesota) for providing access to XRD instrumentation. In addition, acknowledgments are given to

the laboratories of Andreas Stein and Marc Hillmyer (University of Minnesota) for allowing the use of instrumentation for nitrogen adsorption analysis.

Chapter 3. Assessment of 2,4-dinitroanisole transformation using compound-specific isotope analysis after in situ chemical reduction of iron oxides

This chapter has been published in the journal *Environmental Science & Technology* and is reproduced with permission.

Berens, M.J.; Hofstetter, T.B.; Bolotin, J.; Arnold, W.A. *Environmental Science & Technology*. **2020**, *54*, 5520-5531. doi: 10.1021/acs.est.9b07616

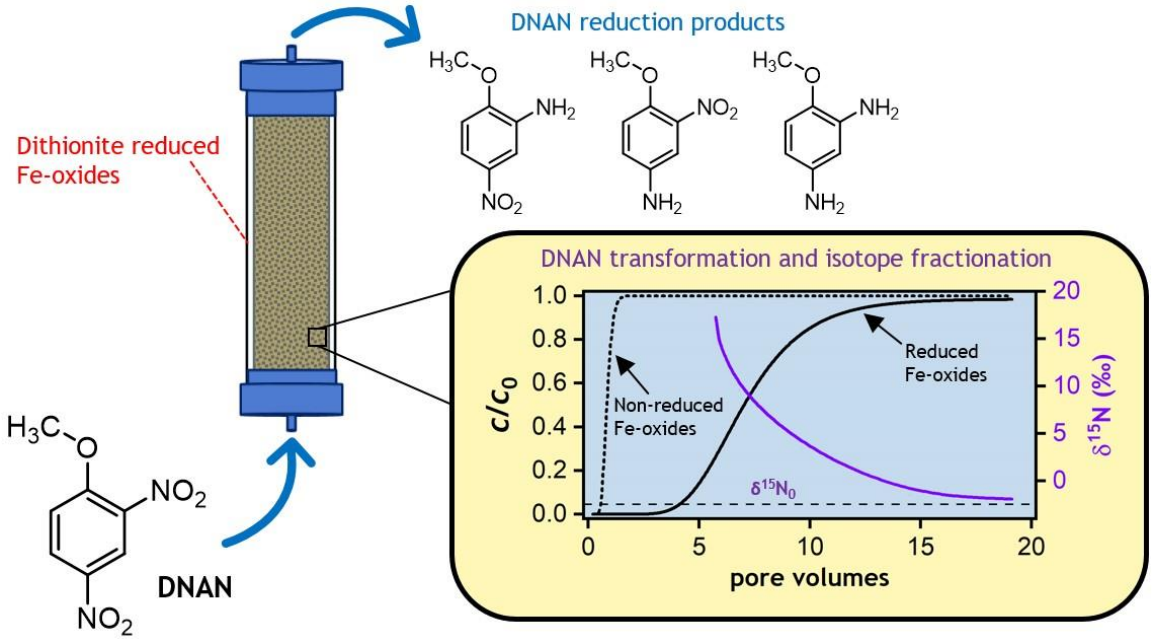

3.1 Overview

Ferrous iron-bearing minerals are important reductants in the contaminated subsurface but their availability for the reduction of anthropogenic pollutants is often limited by competition with other electron acceptors including microorganisms and poor accessibility to Fe(II) in complex hydrogeologic settings. The supply of external electron donors through *in situ* chemical reduction (ISCR) has been proposed as one remediation

approach but the quantification of pollutant transformation is complicated by the perturbations introduced to the subsurface by ISCR. Here, we evaluate the application of compound specific isotope analysis (CSIA) for monitoring the reduction of 2,4-dinitroanisole (DNAN), a component of insensitive munitions formulations, by mineral-bound Fe(II) generated through ISCR of subsurface material from two field sites. Electron balances from laboratory experiments in batch and column reactors showed that 3.6% to 11% of the total Fe in the sediments was available for the reduction of DNAN and its partially reduced intermediates after dithionite treatment. The extent of DNAN reduction was successfully quantified from its N isotope fractionation measured in the column effluent based on the derivation of a N isotope enrichment factor, ε_N, derived from a comprehensive series of isotope fractionation experiments with numerous Fe(II)-bearing minerals as well as dithionite-reduced subsurface materials. Our observations illustrate the utility of CSIA as a robust approach to evaluate the success of *in situ* remediation through abiotic contaminant reduction.

3.2 Introduction

Ferrous iron (Fe(II)) associated with Fe-bearing minerals (e.g., iron (oxyhydr)oxides, clays, sulfide minerals) is an important reductant of many subsurface pollutants.[5,100,124–127] Despite an abundance of Fe(II) in the anoxic subsurface, pollutant reduction is often limited through competition with other potential electron acceptors and restricted pollutant transport and accessibility to reactive Fe(II)-bearing minerals in response to local hydrogeologic conditions. Several approaches have been evaluated to enhance the

availability of reactive Fe(II) including biostimulation,[128,129] bioaugmentation,[130,131] additions of external electron donors (i.e., *in situ* chemical reduction; ISCR) including dithionite, [132,133] polysulfides,[134] and (sulfidized) ZVI,[135,136] and combinations thereof.[13] To date, several of these strategies have been successfully applied to a number of environmental contaminants including heavy metals[133,137,138] and chlorinated solvents.[59,135,139]

One major challenge when applying an *in situ* (bio)remediation technique is providing a reliable evaluation of performance; it is difficult to quantify the amount of transformed contaminants from concentration measurements alone.[140–142] For example, the need to (repeatedly) inject aqueous solutions containing electron donors into the subsurface introduces perturbations that may lead to pollutant dilution without degradation. Moreover, reduction of Fe(III) induces partial reductive dissolution and transformation of reactive Fe minerals and could mobilize solid-bound contaminants.[137,143–145]

Compound specific isotope analysis (CSIA) is used to evaluate the extent of contaminant remediation by quantifying isotope enrichment of one or more elements in the residual pollutant.[84,110,116,146–148] Because changes in stable isotope ratios (e.g., $^{15}N/^{14}N$, $^{13}C/^{12}C$) reflect reactions in which bond-cleavage occurs, isotope fractionation is minimally affected by non-degradative processes (e.g., sorption, dilution, phase transfer), thus circumventing many of the challenges associated with monitoring pollutant removal by concentration measurements alone.[22,149] Despite the incorporation of CSIA into published monitored natural attenuation protocols, the majority of efforts have focused on biodegradation.[84,99,116,140,150,151]

The recent emergence of 2,4-dinitroanisole (DNAN) in insensitive munitions formulations has caused concern because of its potential to contaminate large areas of land and water.[1,3] We previously provided the first assessment of C and N isotope fractionation during abiotic DNAN reduction[152] but did not consider reductants beyond synthetic Fe-minerals. The Fe(II)-mediated reduction of DNAN generated isotope fractionation patterns that were indicative of certain reaction pathways yet independent of DNAN reaction rates and solution chemistry (e.g., organic matter).[152] Given the heterogeneity of natural soils and sediments and the crystallographic diversity of Fe-minerals, however, it remains to be understood if DNAN isotope fractionation during reduction by Fe(II) of natural minerals deviates from that observed with synthetic analogs. Because multiple amendments of a given reductant are often required to achieve remediation targets with ISCR,[133,153,154] it is similarly unknown how multiple redox cycles will affect the interpretation of CSIA results. Our findings suggest that because DNAN reduction by mineral-associated Fe(II) follows a common reaction pathway (i.e., abiotic nitro-group reduction[29–31,84,99,152]), the associated isotope fractionation will not be affected despite the use of synthetic minerals or naturally collected ferruginous soils and sediments. This understanding could allow for DNAN to be a surrogate for other nitroaromatic compounds (NACs) including 2,4,6-trinitrotoluene (TNT) and analogs of nitrobenzene in the subsurface[4] and is important given the continuing need for *in situ* remediation techniques.[70] Numerous studies have indeed reported similar isotope enrichment factors from the abiotic reduction of several NACs in a range of experimental laboratory systems.[29–31]

In this study, we explored the application of CSIA for monitoring DNAN reduction during dithionite-based ISCR schemes. Sodium dithionite ($Na_2S_2O_4$) was chosen as the reductant because of its previous success for pollutant remediation in contaminated aquifers.[132,139,153,155] We tested the reactivity of several Fe-bearing minerals and Fe-mineral containing sediments to promote DNAN reduction in batch reactors receiving amendments of aqueous Fe(II) and those receiving ISCR and used the distributions of reaction products to track the number of reduction equivalents transferred. The N and C isotope fractionation was measured during batch experiments to determine the bulk isotope enrichment factors (ε_N and ε_C) and apparent kinetic isotope effects (^{15}N-AKIE and ^{13}C-AKIE) associated with DNAN reduction. To simulate reducing environmental conditions, subsurface materials collected from two field sites were exposed to DNAN following ISCR in continuous-flow column reactors. A modified Rayleigh equation was used to make quantitative estimates of DNAN degradation from N isotope ratios (δ^{15}N) measured during each experiment. The accuracy of this approach was evaluated by conducting statistical comparisons of predicted versus observed extent of DNAN degradation.

3.3 Materials and Methods

A complete list of chemicals used in this study is provided in the Supporting Information (Appendix B).

3.3.1 *Laboratory conditions*

All syntheses and batch experiments were performed in an anaerobic chamber (Coy Laboratory Products Inc.) with a 95% N_2/5% H_2 atmosphere. Column experiments were performed in a NexGen anaerobic glovebox (Vacuum Atmospheres Company) maintained at <1 ppm O_2 with N_2 balance. Ultrapure water (≥18.2 MΩ•cm) was generated by a Milli-Q Academic system (MilliporeSigma) and used to prepare all aqueous solutions. The ultrapure water was purged with N_2 gas (99.99%, Matheson) for at least 2 h prior to transfer into the chamber. Methanolic stock solutions were similarly prepared in deoxygenated methanol (ACS grade, MilliporeSigma). Laboratory equipment and reagents were evacuated in the exchange chamber and equilibrated overnight in the glovebag before use.

3.3.2 Material preparation and characterization

Subsurface materials were collected from the Twin Cities Army Ammunition Plant (TCAAP; Arden Hills, MN) and the Tinker Air Force Base (Tinker AFB; Oklahoma City, OK). Both sites have a history of contamination by organic pollutants and have required remediation efforts.[124,156] Aquifer material from TCAAP was collected from the saturated zone by sonic drilling to a depth of 41–45 m. The material was dried, purged with N_2 gas, and stored inside the anaerobic chamber. Shallow sediment collected from Tinker AFB was dried at 100 °C and stored in an amber jar under laboratory atmosphere. Both TCAAP and Tinker AFB materials were sieved by particle size to 350–425 μm before use. Synthetic magnetite nanoparticles were obtained from our previous work[152]

and a suspension of rhombohedral hematite in deoxygenated, ultrapure water (~15 g/mL) was acquired from Voelz et al.[157]

Each material was characterized by X-ray diffraction (XRD; Figure B-1) to evaluate the purity (synthetic minerals) and bulk mineralogy (natural materials). No additional peaks were detected in patterns collected from synthetic minerals. The primary Fe-bearing phase as detectable by XRD in natural materials was magnetite (Fe_3O_4; TCAAP)[124,158] and hematite (Fe_2O_3; Tinker AFB). Quartz (SiO_2; PDF #46-1045) was detected in each collected material as expected for highly weathered systems.

The total iron content (Fe_T) of TCAAP and Tinker AFB materials was quantified by inductively coupled plasma optical emission spectroscopy (ICP-OES). The ratio of Fe(II)/Fe(III) was estimated by acid dissolution in 3 M HCl[159,160] and quantification by the ferrozine method[103] (Appendix B). The amount of ion-exchangeable Fe(II) was estimated by saturating each material in 1 M $CaCl_2$ for 7 d and was below the limit of quantification in all samples (data not shown).[161] The magnetic portion of the TCAAP sediment (hereafter termed "TCAAP extract") was separated from the bulk material with a neodymium magnet as described by Strehlau et al.[158] and characterized by the same analyses. A summary of the relevant chemical and physical properties of all materials is provided in Table B-1. Additional characterizations of hematite[157] and magnetite[158] are reported elsewhere.

3.3.3 In situ chemical reduction

For batch experiments receiving ISCR treatment, Fe-bearing materials were suspended in a solution of $K_2CO_3/S_2O_4^{2-}$ (2:1 mol/mol) and rotated for 24 h, at which point the suspension was separated via centrifugation and the supernatant discarded. The dithionite concentrations were selected so that enough dithionite was added to theoretically reduce one-tenth of the total Fe present (i.e., 1 mol $S_2O_4^{2-}$:20 mol Fe_T; see eq 3-1). The $K_2CO_3/S_2O_4^{2-}$ ratio was chosen to buffer the 4 moles of H^+ released per 1 mole of dithionite consumed during iron reduction (eq 3-1).

$$S_2O_4^{2-} + 2Fe^{3+} + 2H_2O \rightarrow 2Fe^{2+} + 2SO_3^{2-} + 4H^+ \qquad (3-1)$$

The treated materials were then washed three times with carbonate buffer (10 mM, pH 7) by centrifugation to remove excess dithionite and its reaction products (e.g., sulfate, sulfite, thiosulfate),[132] suspended in carbonate buffer, and immediately used for DNAN reduction experiments in batch reactors. The Fe(II) content of each reduced material after ISCR was determined by acid dissolution as described above.

For column experiments, the materials were conditioned before adding dithionite by passing carbonate buffer (10 mM, pH 7.0) upwards through the column at 0.5 mL/min for 5 pore volumes. An aqueous solution of 1.25 mM sodium dithionite and 2.50 mM K_2CO_3 (pH 8–9) was then fed upward to the column at 0.25 mL/min for ~18–20 h. The low flow rate and long run (~30 pore volumes) time were used to allow enough time for the reaction to occur. Columns were flushed with ~10 pore volumes of carbonate buffer to remove unreacted dithionite and any oxidized sulfur species. The exact amounts of pore volumes were chosen so that the same total amount of dithionite:Fe was introduced to

each system (see eq 3-1). The total amount of iron in each column was in 20-fold excess to the dithionite added (i.e., 1 mol $S_2O_4^{2-}$:20 mol Fe_T) to target a reduction of one-tenth of Fe_T. Anoxic dithionite-buffer solutions were prepared fresh before each experiment to avoid loss of dithionite by aqueous disproportion; the rate of dithionite loss by aqueous disproportionation, however, has shown to be slower than Fe(III) reduction by dithionite.[139]

3.3.4 Batch experiments

Batch reactors were prepared in 35 mL borosilicate serum bottles according to previously described procedures.[152] First, a suspension of an untreated or dithionite-reduced Fe-bearing mineral in 10 mM carbonate buffer (pH 7.0) was added to each reactor. Solid loadings were varied from 1.0 g/L (hematite) to 143 g/L (TCAAP) such that DNAN transformation occurred in a similar time period. Aqueous Fe(II) was added to a concentration of 1 mM in reactors containing untreated materials. The dithionite-reduced materials did not receive amendments of Fe(II). Reactors were equilibrated for 21–24 h on an end-over-end rotator (Glas-col) at 40 rpm at which point the pH and aqueous Fe(II) concentration (via the Ferrozine assay;[103] Appendix B) were measured. If necessary, the pH was adjusted back to 7.0 with 1 M HCl or 1 M NaOH and the aqueous Fe(II) content was restored to 1 mM in the reactors to which Fe(II) was added. Reactions were initiated by spiking DNAN from a methanolic stock solution to an initial concentration of 200 μM. Reactors were placed on the rotator (40 rpm) and sacrificed at appropriate time points for concentration and stable isotope analyses. The pH (all

reactors) and Fe(II) concentrations (Fe(II) amended reactors only) were closely monitored during reactions and maintained at 7.0 and 1 mM, respectively. Reactions were quenched by filtration through a 0.2 µm nylon syringe filter (Chrom Tech) and stabilized with 1 M HCl (trace metals grade, MilliporeSigma) to pH<4 to prevent iron precipitation; DNAN did not react with aqueous Fe(II) under these conditions (data not shown). A portion (~1 mL) of each sample was analyzed for DNAN and intermediate/product concentrations by high pressure liquid chromatography (HPLC; method in Appendix B) and the remaining sample (~18 mL) was stored at 4 °C for CSIA of DNAN.

The quantity of reduction equivalents transferred to DNAN from each reduced material was calculated with the assumption that 6 moles of electrons are required to reduce one nitro-moiety to the corresponding amine (see Scheme B-1). The reduced products typically generated during abiotic DNAN reduction are 2-amino-4-nitroanisole (2-ANAN), 4-amino-2-nitroanisole (4-ANAN), and 2,4-diaminoanisole (DAAN). Thus, 6 and 12 electrons are required for each mole of 2/4-ANAN and DAAN formed during DNAN reduction, respectively (Appendix B and eq B-1).

3.3.5 Reactions in sediment columns.

Borosilicate glass columns (Kimble FLEX-COLUMNS®; 2.5 cm I.D., 10 cm length) were packed with each natural material to uniform bulk (ρ_b = 1.66 ± 0.04 g/cm^3) and particle densities (ρ_p = 2.68 ± 0.05 g/cm^3). The mean porosity of sediment columns was 0.44 ± 0.05 (see Table B-2). A flow adapter (Kimble) with fluorinated ethylene propylene

(FEP) tubing was secured to the column inlet to prevent sediment migration and facilitate accurate bed height calculations. A polypropylene end cap was fixed at the column outlet. All feed solutions were amended with 10 mM NaCl to prevent the precipitation of insoluble species which may cause changes to flow characteristics. Pore volume and porosity were determined by saturating with 10 mM NaCl and a step input conservative tracer (100 mM NaBr) was used to characterize column flow and estimate the dispersion coefficient (Table B-2; fitting details in Appendix B). Bromide concentrations at the column outlet were measured with a conductivity probe (Oakton). Dispersion coefficients prior to experiments were 2.38 ± 0.24 and 2.53 ± 0.12 $cm^2 s^{-1}$ for TCAAP and Tinker AFB columns, respectively, at a flow rate of 0.5 mL/min. All column materials were then reduced by sodium dithionite before experiments using DNAN.

Columns were equilibrated prior to DNAN reduction experiments by upward flow (0.5 mL/min) with 10 mM, pH 7.0 carbonate buffer including 10 mM NaCl for 5 pore volumes. Reactions were initiated by adding DNAN (200 μM) to the feed solution and collecting effluent samples with an automated fraction collector (Bio-Rad Laboratories Inc). Experiments were terminated once the effluent concentration was equal to that of the feed solution. Columns were then flushed with carbonate buffer for several pore volumes to remove residual DNAN and any reaction products. The column materials were then reduced again by sodium dithionite according to the method described above before further experiments using DNAN. The total number of reduction equivalents transferred to DNAN were calculated by integrating the concentrations of 2/4-ANAN and DAAN measured in the effluent (eq B-2).

3.3.6 Compound specific isotope analysis.

$^{13}C/^{12}C$ and $^{15}N/^{14}N$ isotope ratios of DNAN were measured following previously established procedures for gas chromatography / isotope ratio mass spectrometry (GC/IRMS) and solid phase micro extraction (SPME arrow) and are detailed in Appendix B.[12,28,106,107,152] Isotope signatures were calculated from isotope ratios according to eq B-4 relative to Vienna PeeDee Belemnite ($\delta^{13}C_{VPDB}$) and air ($\delta^{15}N_{air}$) reference standards.[162] Carbon and nitrogen isotope enrichment factors (ε_C, ε_N) were calculated by non-linear regression of C and N isotope signatures ($\delta^{13}C$, $\delta^{15}N$) vs the fraction of remaining substrate (c/c_0) as shown in eq 1-2.[28]

$$\frac{\delta^h E+1}{\delta^h E_0+1} = \left(\frac{c}{c_0}\right)^{\varepsilon_E} \qquad (1-2)$$

where $\delta^h E_0$ is the initial isotope ratios of DNAN ($\delta^{13}C_0$ = -37.4 ± 0.1‰, $\delta^{15}N_0$ = -2.4 ± 0.1‰) as evaluated by elemental analysis (EA)/IRMS. Apparent kinetic isotope effects (^{13}C-AKIE, ^{15}N-AKIE) were determined from eq 1-3 based on the methods outlined by Elsner et al.[85]

$$^h\text{E-AKIE} = \frac{1}{1+n \times \varepsilon_E} \qquad (1-3)$$

where n is a correction for isotopic dilution (n = 2 for primary ^{15}N-AKIEs and n = 1 for secondary ^{13}C-AKIEs). A linear regression of N and C isotope signatures was used to evaluate two-dimensional isotope fractionation trends. The slope of this regression ($\Lambda^{N/C}$) was calculated using both a simple linear regression model and the York method described by Ojeda et al.[163] and is approximately equal to the ratio of the bulk isotope

enrichment factors ($\varepsilon_N/\varepsilon_C$). Because values of $\Lambda^{N/C}$ from our previous work[152] were calculated by simple linear regression, in this report the result of the York method is provided as an additional reference.

To estimate the extent of DNAN transformation (*F*) during column experiments, measurements of $\delta^{15}N$ at the breakthrough front were applied to a modified form of the Rayleigh fractionation equation (eq 3-2)[116] using an ε_N that was calculated based on the results of multiple datasets. This combined ε_N value (ε_N^*) was obtained by plotting all $\delta^{15}N$ measurements (n = 122) from batch experiments of DNAN reduction in this study and in Berens et al. [152] and performing a non-linear regression of the combined data according to eq 1-2. The extent of DNAN reduction was calculated with eq 3-2 from the deviation of measured $\delta^{15}N$ values from $\delta^{15}N_0$. using the combined ε_N^* value. Note that eq 3-2 is the result of a reorganization of eq 1-2 to account for ε_N^*. We evaluated the accuracy of our estimates by performing a linear regression of the predicted vs measured values of c/c_0 and calculating the mean absolute error (MAE) of the predictions (eq 3-1).

$$1 - F = \frac{c}{c_0} = \left(\frac{\delta^{15}N + 1}{\delta^{15}N_0 + 1}\right)^{1/\varepsilon_N^*} \qquad (3-2)$$

$$MAE = \frac{\sum_{i=1}^{n} \left| \left(c/c_{0,\,measured}\right)_i - \left(c/c_{0,\,predicted}\right)_i \right|}{n} \qquad (3-3)$$

3.4 Results and Discussion

3.4.1 Kinetic studies in batch reactors.

Reduction of DNAN occurred in all reactors receiving amendments of aqueous Fe(II) (Figure 3-1a, open symbols) or ISCR by sodium dithionite (Figure 3-1a, closed symbols).

DNAN reduction was not observed in reactors containing only untreated minerals or aqueous Fe(II) alone (Figure B-2). This supports the current understanding that Fe(II)-surface associations are required to mediate contaminant,[5,76,77,164–166] and in particular DNAN,[152] reduction. The transformation products detected during DNAN reduction were 2-ANAN, 4-ANAN, and DAAN (Figure 3-1b). X-ray diffraction (XRD) patterns collected before and after ISCR showed no detectable changes in mineral composition following the treatments (Figure B-1) which suggests that the primary effect of ISCR on the structures of hematite and magnetite was the generation of surface-associated Fe(II) from oxide-Fe(III).

When aqueous Fe(II) was maintained (1 mM) throughout the batch experiments, all of the added DNAN was reduced to 2/4-ANAN or subsequently DAAN by each of the untreated minerals (Figure 3-1a, open symbols). In reactors receiving ISCR, only a portion of the DNAN was removed (Figure 3-1a, closed symbols), likely because of a limited supply of available electron equivalents (i.e., mineral-associated Fe(II)) generated during ISCR. To understand the extent of DNAN reduction in systems receiving ISCR, an electron balance was computed for each set of reactions (Figure 3-1b, dashed line). Accounting for the number of electrons transferred to DNAN as a function of the mineral-associated Fe(II) (i.e., mol e^-/mol Fe(II)) allowed for an evaluation of the efficiency of ISCR to generate reactive Fe(II).

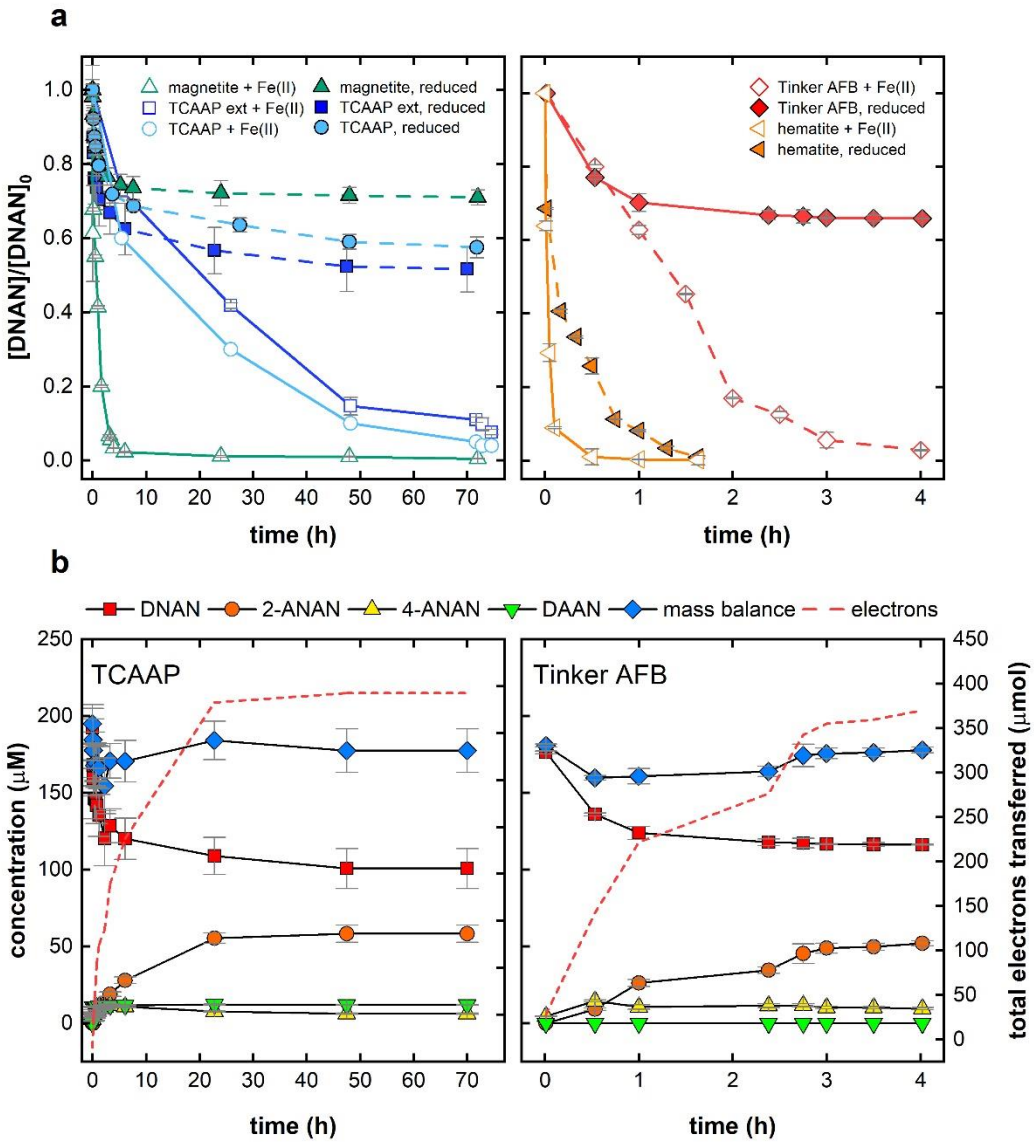

Figure 3-1. (a) Concentrations of DNAN during abiotic reduction by natural (TCAAP and Tinker AFB) and synthetic Fe-bearing (magnetite and hematite) materials. Experiments were performed with either untreated materials in the presence of 1 mM aqueous Fe(II) (open symbols) or with dithionite-reduced materials without additional Fe(II) (closed symbols). (b) Concentrations of DNAN, 2-ANAN, 4-ANAN, DAAN, and the cumulative number of electrons transferred during DNAN reduction by reduced TCAAP (left) and Tinker AFB (right) materials. All error bars represent standard deviations of triplicate reactors. Note the difference in time scales.

Dithionite-reduced magnetite, TCAAP extract, and hematite promoted DNAN reduction with extents of electron transfer ranging from 0.359–0.603 mol e^-/mol Fe(II) (Table 3-1). These results suggest that not all available iron (Fe_T) was reduced to reaction-accessible Fe(II)[167] during ISCR. The washing of materials following dithionite treatments may have caused the release of Fe(II) that was not retained on mineral surfaces. It is also possible that potentially reducible oxide-Fe(III) was inaccessible to dithionite.[168–171]

The lower standard reduction potential (E_H^0) of hematite/Fe(II) (+0.793 V) versus magnetite/Fe(II) (+1.053 V)[172] may further explain the difference in electron transfer between the two systems. The reactivity of Fe-bearing minerals for pollutant reduction increases with lower E_H values as evidenced by hematite experiments. Moreover, magnetite stoichiometry (x = Fe(II)/Fe(III)) directly correlates with its intrinsic E_H values[88] and reactivity towards NAC reduction.[173] The magnetite used in this study ranged from partially oxidized (x = 0.1, TCAAP extract) to fully reduced, stoichiometric (x = 0.5, synthetic magnetite) materials. Low stoichiometry magnetite is a better oxidant and was thus more easily reduced by dithionite than the high stoichiometry magnetite (Table B-1). These results emphasize the potential benefits of ISCR to magnetite-bearing soils and sediments in which partially oxidized magnetite is common and may be amenable to ISCR leading to more stoichiometric and thus reactive magnetite.[174,175]

Table 3-1. Total iron (Fe_T) and Fe(II) content of materials after dithionite treatments, and the cumulative number electrons transferred during DNAN reduction experiments.

system	Fe_T (μmol)	Fe(II) (μmol)[c]	total e^- transferred (μmol)[d,e]	mol e^-/mol Fe(II)[e]
batch				
TCAAP	3430[a]	170	393 ± 1	2.31 ± 0.01
TCAAP extract	865[a]	432	232 ± 1	0.536 ± 0.003
magnetite	903[b]	451	162 ± 0.3	0.359 ± 0.001
Tinker AFB	2180[a]	79.1	370 ± 0.4	4.68 ± 0.01
hematite	439[b]	219	132 ± 1	0.603 ± 0.006
column				
TCAAP	25800[a]	1280	183 ± 30	0.143 ± 0.022
Tinker AFB	17000[a]	616	109 ± 10	0.176 ± 0.020

[a]Determined by ICP-OES.
[b]Calculated from structural formulas of pure minerals.
[c]Calculated by acid dissolution and quantification by the ferrozine method.[103]
[d]Calculated using eqs B-1 and B-2.
[e]Uncertainties represent standard deviations of triplicate reactors.

The number of reduction equivalents transferred to DNAN from dithionite-reduced TCAAP (2.31 ± 0.01 mol e^-/mol Fe(II)) and Tinker AFB (4.68 ± 0.01 mol e^-/mol Fe(II)) materials exceeded the initial amount of Fe(II) present after dithionite treatments (Table 3-1). Despite targeted dithionite dosages to reduce one-tenth of the Fe_T, the calculated reduction efficiencies (i.e., Fe(II)/Fe_T from data in Table 3-1) of TCAAP and Tinker AFB materials during ISCR were only 4.95% and 3.62%, respectively. The low reduction efficiencies suggest that other reducible moieties were present in the natural materials which were reduced by dithionite and subsequently provided reducing equivalents for DNAN reduction.[176,177] For example, the reversible transfer of electrons in the environment is often mediated by natural organic matter and humic substances,

specifically those containing quinone moeities[178–181], and the TCAAP and Tinker materials contained 0.46% (w/w) and 0.88% (w/w) organic matter, respectively. The electron-carrying capacity of these species plays a key role in both the reduction of substituted nitrobenzenes[182] and ferric iron.[183] Another possibility is that acid digestion of the materials to determine Fe(II) was incomplete. This is especially likely in materials with high Si content, such as phyllosilicates, because the Fe(III) is easily reduced by dithionite but Fe(II) extraction requires a rigorous treatment with H_2SO_4 and HF.[167,184,185] This fraction of Fe(II) is a known strong reductant of NACs.[125,186] The prominence of SiO_2 (Figure B-1) and low Fe_T content of TCAAP and Tinker AFB materials (Table B-1) suggests that a large share of Fe_T was associated with silicates.

3.4.2 Reactions in packed columns.

To probe for the availability of reduction equivalents in flow-through systems, DNAN (200 μM) was introduced to column reactors containing dithionite-reduced TCAAP or Tinker AFB materials for five cycles of Fe(III) reduction by dithionite followed by DNAN exposure (Figure 3-2a-b). As shown in Figure 3-2c-d, ISCR in column reactors generated reaction-accessible electron equivalents in natural materials and promoted the reductive transformation of DNAN with a similar product distribution to the batch experiments (Figure 3-1c-d, Figure B-3). It should be noted that DAAN concentrations exceeded the input DNAN concentration (up to 150%) during the early stages of experiments. To assess this phenomenon, the cumulative amount of DAAN measured in the column effluent was compared to the total amount of DNAN introduced. We found

that the amount of DAAN in the peaks did not exceed the total amount of DNAN introduced to the columns. This indicated that DAAN was either associated with or retained on mineral surfaces and was then displaced by another solute, namely DNAN or 2/4-ANAN. The initial rapid production of DAAN leading to high concentration may have driven this interaction, and as aqueous concentrations dropped, other components in the solution displaced DAAN from the surface. Such competition and effluent concentrations exceeding influents have been observed for ion sorption on activated carbon.[187] Another possible explanation is that a reaction intermediate (e.g., a hydroxylamine) is more strongly retained by the solid phase, as previously observed during the reduction of cyanonitrobenzene,[188] and the excess DAAN observed occurs once this intermediate has been reduced and released.

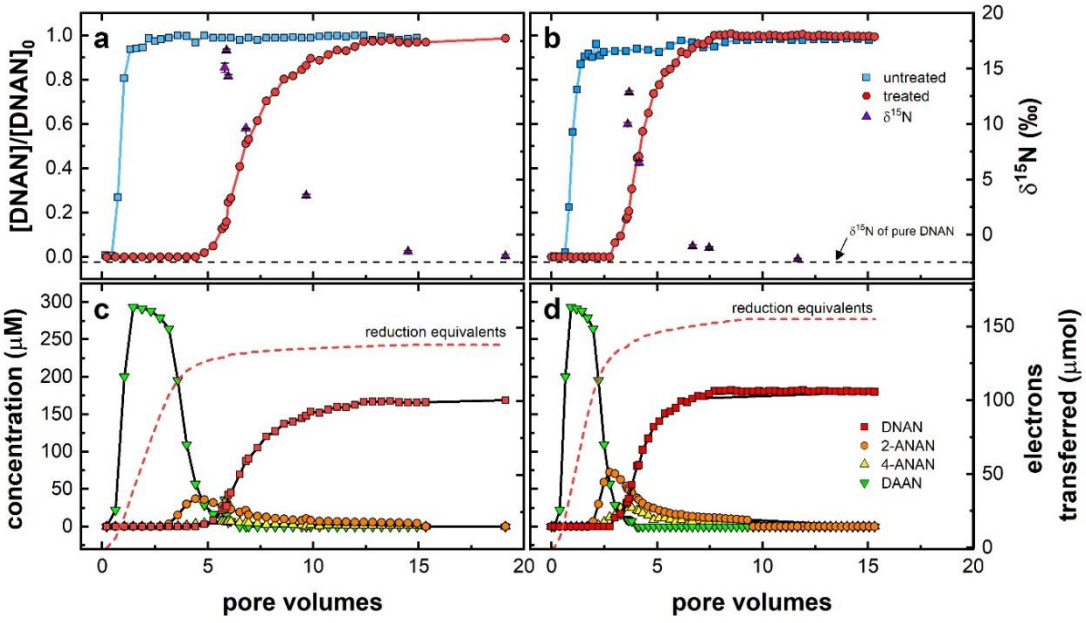

Figure 3-2. Breakthrough curves for 200 μM DNAN in (a) TCAAP and (b) Tinker AFB packed columns before (squares) and after (circles) receiving ISCR. Triangles denote measurements of $\delta^{15}N$ of DNAN in the effluent from treated columns. Error bars denote standard deviations from five sequential breakthrough experiments. Aqueous concentrations of DNAN (circles), 2-ANAN (squares), 4-ANAN (triangles), and DAAN (diamonds) during DNAN exposure to (c) TCAAP and (d) Tinker AFB columns. Dashed lines represent the cumulative number of reduction equivalents transferred to DNAN during experiments. The data provided in panels c and d are a representation of one of the reduction-reaction cycles shown in panels a and b, respectively. Individual cycles are shown in Figure B-3.

Despite ISCR targets that were equivalent to batch experiments (i.e., 10% reduction of Fe_T), the extent of electron transfer to DNAN from the reduced materials was markedly lower in columns than in batch experiments (0.143 ± 0.022 and 0.176 ± 0.020 mol e^-/mol Fe(II) for TCAAP and Tinker AFB columns, respectively; Table 3-1). This suggests that either (i) reactive Fe(II) was removed from the column, (ii) the transport of dithionite or DNAN to mineral surfaces was restricted by conditions within the column, or (iii) the extent of mineral reduction was affected by the rate of dithionite decomposition.

Flow-through systems introduce the potential for newly generated Fe(II) or other reducible species to be removed from the column before association with mineral surfaces or pollutant reduction occurs. Monitoring aqueous Fe(II) in column effluents, however, negligible losses of Fe(II) from the column were observed during and after exposure to dithionite (Figure B-4). Only 1.6 and 5.3 μmol Fe(II) in TCAAP columns and 2.6 and 4.0 μmol Fe(II) in Tinker AFB columns were removed during the first and fifth exposures to dithionite, respectively, corresponding to 0.06–0.20% (w/w) of Fe_T. This suggests that Fe(II) generated during ISCR was mostly retained within the column either because it was not released from the mineral surfaces or it was effectively adsorbed

by or bound within the materials within the column. The presence of silicates may also indicate a portion of Fe(II) that is not readily removed from natural soils and sediments. The consistency of breakthrough curves during the five cycles of ISCR and DNAN exposure (Figure B-3) indicates that the removal of reduction equivalents by column flow likely did not affect the potential for contaminant reduction.

It is also possible that the transport of reducing equivalents or pollutants to mineral surfaces is restricted in confined systems composed of heterogenous media.[189] Moreover, the iron content of natural sediments can be distributed throughout the bulk mineral as opposed to being concentrated at singly-coordinated oxygen atoms on mineral surfaces, leaving Fe(III) inaccessible to dithionite. To account for these potential limitations, the columns in this study were packed to a uniform porosity (0.44 ± 0.05), bulk density (1.66 ± 0.04 g cm^{-3}), and particle density (2.68 ± 0.05 g cm^{-3}) to resemble typical subsurface conditions in sandy soils similar to the TCAAP and Tinker AFB (Table B-2).[168] The dispersion coefficients in TCAAP (2.37 ± 0.22 cm^2 s^{-1}) and Tinker AFB (2.53 ± 12 cm^{-2} s^{-1}) columns were also determined and indicated advection-dominated regimes with negligible effects from flow retardation.[190] Column porosities and dispersion coefficients were remeasured following all experiments and were not appreciably different from the initial values (Table B-2), indicating that ISCR did not affect the physical properties of columns or restrict material transport.

Lastly, the decomposition of dithionite can unevenly distribute iron reduction by ISCR in columns. In batch reactors, the entire supply of dithionite was simultaneously exposed to all of the solid material in a well-mixed heterogenous suspension, whereas, in columns

only the materials located immediately following the inlet were exposed to unreacted dithionite. Because dithionite undergoes rapid disproportionation in aqueous media, the combination of Fe(III) reduction and dithionite decomposition limits mineral reduction at locations away from the point of application.[132,155] These differences explain the difference between the batch and column experiments and provide an explanation for the lower extent of DNAN reduction in the column.

3.4.3 ^{15}N fractionation during DNAN reduction.

DNAN reduction in batch reactors introduced strong ^{15}N enrichment in the remaining contaminant with variations in magnitude comparable to those observed in earlier studies (Figure 3-3). ^{15}N isotope enrichment factors, ε_N, ranged from -11.1 ± 4.3‰ to -21.5 ± 2.6‰ corresponding to ^{15}N-AKIEs of 1.023 ± 0.009 to 1.045 ± 0.005 (eq 3-3). Because no bonds to C atoms are involved during the reactions leading to nitro-group reduction, C isotope fractionation was small and resulted in secondary ^{13}C-AKIE values (1.0005 ± 0.0002). These results are typical for nitro-group reduction on NACs by Fe(II) species associated with minerals (i.e., large ^{15}N-AKIE = 1.030–1.045 and ^{13}C-AKIE close to unity).[29–31,88] The variability of isotope effects is related to uncertainties associated with experimental and data evaluation procedures such as a different number of samples with variable extent of reactant conversion included in the regression analysis.[28] We postulate these effects as the likely the sources of variation in ε_N values reported for experiments with reduced sediments (Figure 3-3). In fact, our previous report of DNAN reduction by iron (oxyhydr)oxides revealed ε_N values between -9 ± 2‰ and -19 ± 1‰ corresponding

to ^{15}N-AKIEs of 1.018 ± 0.002 and 1.039 ± 0.001, respectively, as well as the small ε_C and ^{13}C-AKIE values that are consistent with previous studies.[152] The kinetics of electron and proton transfers preceding the isotope sensitive step of aromatic nitro-group reduction could also lead to variation of ^{15}N-AKIE through partially masking of the isotopically sensitive bond cleavage reaction(s)[31,88,91] and smaller ^{15}N-AKIEs were found with increasing rates of NAC reduction.[31] However, no such trends were observed in our studies with DNAN (Table B-3) and further investigation of this phenomenon is beyond the scope of this work.

The agreement in combined ^{15}N- and ^{13}C-AKIEs between this and other reports of abiotic NAC reduction[29–31] suggests that DNAN reduction followed the same reaction mechanism (i.e., nitro-group reduction) in the presence of Fe(II)-amended synthetic and natural materials and with the naturally collected materials after ISCR. Dual-element isotope analysis (δ^{15}N vs δ^{13}C) was used to support this interpretation by illustrating the distinction of our results from other known DNAN transformation pathways (Figure B-5).[12] For example, the correlation slope ($\Lambda^{N/C}$) calculated from this study was 43.8 ± 28.6 (38.9 ± 4.3 calculated based on Ojeda et al.[163]) which is in clear contrast with independent evidence from biodegradation ($\Lambda^{N/C}$ = 0.87 ± 0.15) and alkaline hydrolysis ($\Lambda^{N/C}$ = 0.46 ± 0.04) experiments.[12] We previously reported a similar $\Lambda^{N/C}$ of 50.5 ± 23.2 during Fe(II)-mediated DNAN reduction by synthetic iron (oxyhydr)oxides (Chapter 2).[152]

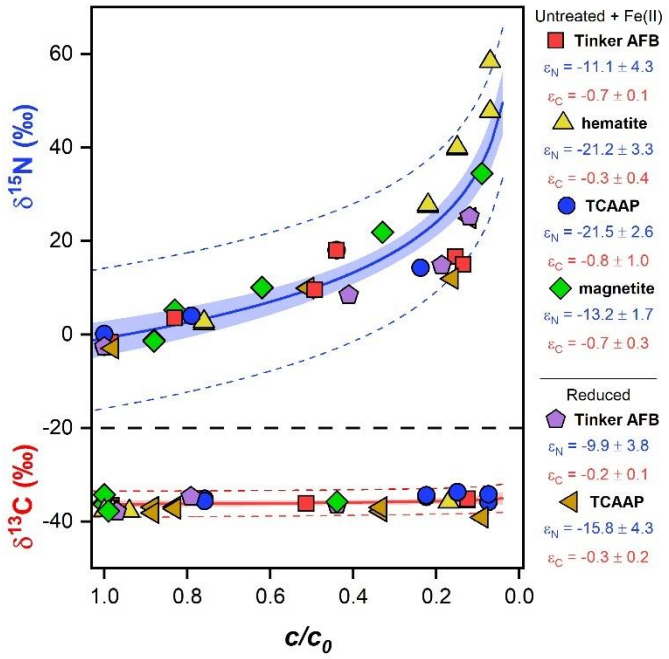

Figure 3-3. Nitrogen ($\delta^{15}N$) and carbon ($\delta^{13}C$) isotope signatures vs fraction of remaining substrate (c/c_0) during DNAN reduction by iron-bearing minerals. Solid lines represent fits from nonlinear regression with shaded portions indicating the 95% confidence intervals. Dashed lines designate 95% prediction intervals. N and C isotope enrichment factors (ε_N, ε_C) were determined from non-linear regression of the data points for each mineral type. Data are shown for untreated materials in the presence of Fe(II) and dithionite-treated materials.

3.4.4 Quantifying DNAN transformation from ^{15}N enrichment in the residual contaminant.

As shown in Figure 3-2a-b, $\delta^{15}N$ values of DNAN at the breakthrough front (~5 pore volumes) were isotopically enriched in ^{15}N corresponding to an increase of $\delta^{15}N$ by 15–20‰. Measured values subsequently decreased and approached the value for unreacted DNAN (-2.4 ± 0.1‰) as the effluent concentrations approached the input level. This trend of $\delta^{15}N$ is consistent with the elution of an increasing share of DNAN that has not been reduced by surface-associated Fe(II). While the data provide evidence that ISCR

promoted DNAN reduction, it should be noted that $\delta^{15}N$ values were not fully restored to the input $\delta^{15}N$ value (–1.9 ± 0.1‰ and -2.2 ± 0.1‰ in columns with TCAAP and Tinker AFB sediment, respectively) suggesting the retention and slow release of enough residual ^{15}N-enriched DNAN from the mineral surfaces to influence the $\delta^{15}N$ after the reaction capacity was exhausted or residual, low level transformation activity.[191–193]

Based on the above reasoning for the variability of N isotope fractionation associated with NAC reduction, we aggregated all of our current data[152] for isotope fractionation during Fe(II)-catalyzed DNAN reduction in batch experiments. The combined N isotope ratio measurements resulted in an averaged ε_N^* value of -14.9 ± 1.3‰, which is based on one of the most comprehensive data sets for the stable N isotope fractionation related to the transformation of a single nitroaromatic contaminant (Figure B-6a). This value was used to establish a quantitative relationship of c/c_0 vs $\Delta^{15}N$ (Figure B-6b) to estimate the amount of DNAN degradation from $\delta^{15}N$ measurements made during column experiments (Figure 3-2a-b). Values of ε_N calculated from TCAAP (-8.6 ± 1.8‰) and Tinker AFB (-7.2 ± 0.8‰) column experiments were lower than batch experiments which could indicate longitudinal mixing with unreacted DNAN in the feed solution. This interpretation agrees with systematic evaluations of the applicability of eq 3-2 to assess contaminant transformation in groundwater plumes,[194] where physical heterogeneity, geometry of the contaminant plume, and the extent of degradation can lead to an underestimation of isotope enrichment factors.

Application of the higher average ε_N^* value of -14.9 ± 1.3‰ from batch experiments for the evaluation of the extent of DNAN reduction in the sediment columns from the

$\delta^{15}N$ of DNAN leads to an underestimation of the actual extent of conversion. A linear regression of predicted versus measured quantities showed a correlation slope of 1.27 ± 0.18 (r^2 = 0.96) with a mean absolute error (MAE) of 0.091 ± 0.063 in c/c_0 which would point to an underestimation of DNAN reduction by approximately 22%. (Figure 3-4). However, the maximum (0.38 ± 0.22, observed at c/c_0 = 0.16 in TCAAP reactor) and minimum (0.96 ± 0.02, observed at c/c_0 = 0.98 in TCAAP reactor) errors in c/c_0 associated with the predictions further illustrate that in our laboratory model system, the accuracy of our assessment if degradation decreased with increasing turnover of the contaminant.

While a number of additional factors pertinent to the hydrology of the contaminated subsurface will contribute to the successful application of CSIA,[195] the linearity of the regression in Figure 3-4 and the low MAE illustrate the degree of consistency between batch and column systems and provides the basis for using the N isotope fractionation of DNAN as a proxy of transformation in the field. To confirm the specificity of our model to N isotope fractionation associated with DNAN reduction, we also measured the accompanying $\delta^{13}C$ values of DNAN to the $\delta^{15}N$ data shown in Figure 3-2a-b. The observed minimal C isotope fractionation of DNAN at the breakthrough front ($\Delta^{13}C$ < ~3‰; data in Figure B-7) is in agreement with the postulated reduction reaction. Because this C isotope fractionation was not observable after 6-7 pore volumes where N isotope fractionation continued, we also consider it unlikely that another reaction such as concurrent (bio)degradation processes contributed to our observations where C isotope fractionation would be more substantial based on the reported ε_C of –3‰ vs. –0.3‰

shown in Figure 3-3.[12] The distribution of $\delta^{13}C$ against $\delta^{15}N$ from column experiments also reflected the batch systems (Figure 3-3 and Figure B-5) and supports that, in both cases, abiotic reduction was the primary reactive pathway. While we cannot exclude small contributions of sorption processes to the observed DNAN isotope fractionation in dithionite treated columns, data with untreated sediment (Figure B-2) suggest that this process is of minor importance.

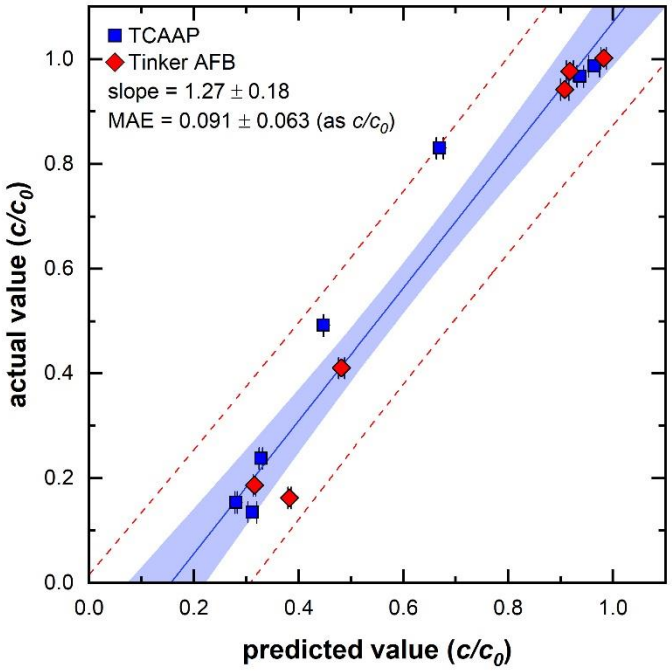

Figure 3-4. Predicted versus measured values of DNAN transformation by chemically reduced TCAAP and Tinker AFB materials in column reactors. Predictions were made according to eq 3-2 using an ε_N* value of -14.9 ‰. The solid line indicates the calculated fit by linear regression. Shaded portions indicate 95% confidence intervals of linear regressions and dashed lines represent the 95% prediction intervals.

3.4.5 Environmental significance.

Our study investigated laboratory conditions and future work should address direct applications of CSIA to contaminated field sites receiving ISCR. In addition, to assess the efficiency of sediment reduction with external electron donors such as dithionite, these analyses will have to include critical phenomena which we were not able to evaluate in a laboratory model system. Several studies have shown that mass transport related processes including diffusive isotope fractionation, hydrodynamic dispersion, multiple contaminant sources, and the quality of stable isotope ratio measurements can lead to both over- and underestimations of the extent of contaminant degradation.[195–198] For ISCR, the understanding of the local hydrogeology will be necessary to accurately estimate the extent of contaminant (bio)degradation with CSIA.

As remediation strategies are implemented, the adaptation of CSIA for pollutant monitoring in treated soil, sediment, and groundwater is critical for its successful integration into protocols for monitored natural attenuation and active remediation. To an extent, this has been accomplished for the assessment of biodegradation of nitroaromatic explosives in soil.[84] In this work, we reported CSIA as a robust technique to quantify abiotic DNAN reduction in systems receiving repeated dithionite treatments, but future work should include a survey of other *in situ* abiotic remediation strategies (e.g., calcium polysulfides,[134] sodium persulfate[199]). The observation that isotope fractionation is unaffected by natural subsurface materials and ISCR can be leveraged to generate accurate estimates of contaminant removal strengthen our findings. Moreover, it provides strong support for the compulsory lines of evidence set by the US Environmental

Protection Agency for evaluating the progress of natural attenuation.[116] Considering DNAN as a surrogate for other NACs allows for this approach to be applied to a wide range of environmental pollutants.

3.5 Acknowledgements

This work was supported by the Strategic Environmental Research and Development Program (SERDP, Project No. ER2618). Thanks to Lee Penn (UMN, Department of Chemistry) for allowing use of the X-ray diffractometer and to Jeanette L. Voelz (UMN, Department of Chemistry) for providing the hematite nanoparticles used in this study. ICP-OES analyses were performed by Clare Johnston (UMN, Department of Chemistry).

3.6 Associated content

A detailed report of additional analytical methods, materials synthesis and characterization techniques, batch reaction procedures, CSIA calculations, and further kinetics and isotope results. The files are provided in Appendix B

Chapter 4. Neonicotinoid Insecticides in Surface Water, Groundwater, and Wastewater across Land Use Gradients and Potential Effects

This chapter has been submitted for publication in the journal *Environmental Toxicology & Chemistry*

4.1 Overview

Neonicotinoid insecticides cause adverse effects on non-target organisms, but more information about their occurrence in surface and groundwater is needed across a range of land use. Sixty-five sites in Minnesota U.S., representing rivers and streams, lakes, groundwater, and treated wastewater, were monitored via collection of 157 water samples to determine the variability in spatiotemporal neonicotinoid concentrations. The data were used to assess relations to land use, to hydrogeologic condition, and potential effects on aquatic life. Results showed total neonicotinoid concentrations were highest in agricultural watersheds (median=12 ng/L) followed by urban (2.9 ng/L) and undeveloped watersheds (1.9 ng/L). Clothianidin was most frequently detected in agricultural areas (detection frequency = 100%) and imidacloprid most often in urban waters (detection frequency = 97%). The seasonal trend of neonicotinoid concentrations in rivers, streams, and lakes showed that their highest concentrations coincided with spring planting and elevated streamflow. Consistently low neonicotinoid concentrations were found in shallow groundwater in agricultural regions (<1.2–16 ng/L, median = 1.4 ng/L). Treated municipal wastewater had the highest concentrations across all hydrologic compartments (12–48 ng/L, median = 19 ng/L) , but neonicotinoid loads from rivers and streams (median = 4100 mg/d) were greater than in treated wastewater (700 mg/d). No concentrations exceeded aquatic-life benchmarks, but increasing use and sublethal effects

create potential risks. This the first study of its size in Minnesota and is critical to better understanding the drivers of widescale environmental contamination by neonicotinoids where urban, agricultural, and undeveloped lands are present.

4.2 Introduction

Neonicotinoids are the most widely used class of insecticides worldwide and make up over 25% of the global insecticide market.[32–34] Neonicotinoids were introduced in the 1990s to replace the harmful carbamate and organophosphate insecticides. As of 2016, their use has grown to include over 500 commercial and domestic products in the United States (U.S.).[33,48,200–202] Neonicotinoids are effective because they share a common mode of action towards many agricultural, urban, and household pests (e.g., aphids, coleopterans, whiteflies, mites)[203] and were originally thought to be safer to wildlife and humans.[204] Because neonicotinoids act non-selectively against most insects, there is a risk that non-target organisms that consume plants or contact surfaces treated with neonicotinoids will be adversely affected.[59]

Neonicotinoids are water soluble and exhibit slow dissipation rates (half-life = 0.5–0.7 yr[205]) in the environment.[41,57,59,60,206,207] Thus, they are relatively persistent, mobile, and readily transported from their point of application via surface and groundwater.[59] Current research to investigate the spatiotemporal drivers of neonicotinoid occurrence have reported year-round detections in numerous surface and groundwaters in addition to water treatment facilities in both agricultural and urban watersheds.[33,48,57,200–202] In one study, Hladik et al.[207] detected neonicotinoids in soil and water at corn and soybean fields more than 3 years after neonicotinoid treatments had ended. Neonicotinoid

concentrations in the environment are influenced by hydrogeology, land-use, rates of transformation, and use patterns.[33,44,208]

Most commercial neonicotinoid products (> 99%) are composed of imidacloprid, clothianidin, acetamiprid, and thiamethoxam either individually or in mixtures.[41,202,209,210] Neonicotinoids also undergo many biotic and abiotic processes that produce transformation products which can be more toxic than the parent compounds.[48,57] Interactive effects between co-occurring pesticides or their transformation products in turn cause either synergistic or antagonistic effects depending on the compound and affected organism.[211,212] It is therefore important to understand the distribution of neonicotinoids and their transformation products in aquatic systems.

The use of neonicotinoids in agricultural (seed coating, foliar spray, soil injection) and urbanized (home and garden sprays, nurseries, flea and tick medications, tree injections, bedbug treatments) areas has led to the contamination of non-target ecosystems.[40,48,213,214] Adverse effects against many non-target pollinators (e.g., honeybees, Lepidoptera), insects (e.g., Ephemeroptera, Trichoptera), and plankton (e.g. Copepods, *Daphnia*) have been reported with median lethal concentrations (LC50s) for acute exposure between 1 to 10,000 μg/L in a waterbody.[215] Neonicotinoids also cause (sub)lethal effects on freshwater vertebrates and macrophytes, but at much higher concentrations (acute LC50s ≥100,000 μg/L).[216]

The state of Minnesota presents a significant concern for environmental contamination by neonicotinoids because it contains almost 20,000 km^2 of surface fresh water (8% by area)[217] and uses large amounts of neonicotinoid insecticide in both urban and agricultural settings. From 2006 to 2016, the estimated use of imidacloprid,

thiamethoxam, clothianidin, and acetamiprid in Minnesota was 86,000 kg, 91,000 kg, 14,000 kg, and 1,200 kg, respectively.[218,219] The purpose of the present study is to understand the occurrence of neonicotinoids in water bodies within various land-use (urban, agricultural, undeveloped) and various hydrogeologic settings. Five neonicotinoids (imidacloprid, clothianidin, thiamethoxam, thiacloprid, acetamiprid) and five neonicotinoid transformation products (imidacloprid-olefin, imidacloprid-urea, desnitro-imidacloprid, thiacloprid-amide, acetamiprid-N-desmethyl) were studied in 11 rivers and streams, 11 lakes, 35 groundwater wells, and 8 wastewater treatment plant (WWTP) effluents in Minnesota during the 2019 growing season. These data create a better understanding of the effects of watershed characteristics and seasonality on neonicotinoid concentrations. The potential risks to non-target aquatic communities were also examined by exploring potential correlations between neonicotinoid concentrations and planktonic abundance. New data that documents the baseline occurrence of neonicotinoids in natural and engineered waters is essential to determine their potential effects and to inform the development of safe use guidelines. This is the first study of its scale to assess the occurrence and effects of neonicotinoids across spatiotemporal and hydrogeologic gradients in Minnesota.

4.3 Materials and methods

4.3.1 Chemicals and reagents

Optima™ grade acetonitrile (99.9%), water, and formic acid (99.0%) were used (Fisher Scientific). The CAS number, manufacturer, and purity of all analytical standards

are provided in the Supporting Information (Appendix C). Stock solutions of each analyte were prepared in Optima grade acetonitrile and stored at -20 °C.

4.3.2 Study area

A total of 157 samples were collected between April and October 2019 from a total of 65 surface water, groundwater, and WWTP sites in Minnesota, U.S. (Figure 4-1, Table C-2–Table C-5). Samples were collected from rivers and streams (n = 11), lakes (n = 11), groundwater wells (n = 35), and wastewater treatment plant effluents (n = 8) which represented 31 predominantly urban (48% of total watersheds), 21 (32%) predominantly agricultural, and 13 (20%) predominantly undeveloped watersheds. Drainage areas ranged from 0.1 to 10,000 km^2. When possible, sample collection was coordinated with a public or private organization as part of an ongoing monitoring program. Complete descriptions of sampling locations and site-specific information are provided in Appendix C.

4.3.3 Sample collection

All samples were collected into cleaned 1 L polycarbonate bottles (see Appendix C) which were then placed on ice and immediately transported to the laboratory. All samples were filtered through a pre-baked glass fiber filter (≤0.7 μm, MilliporeSigma, GF/F, 1 filter/sample). The samples were stored at 4 °C until extraction.

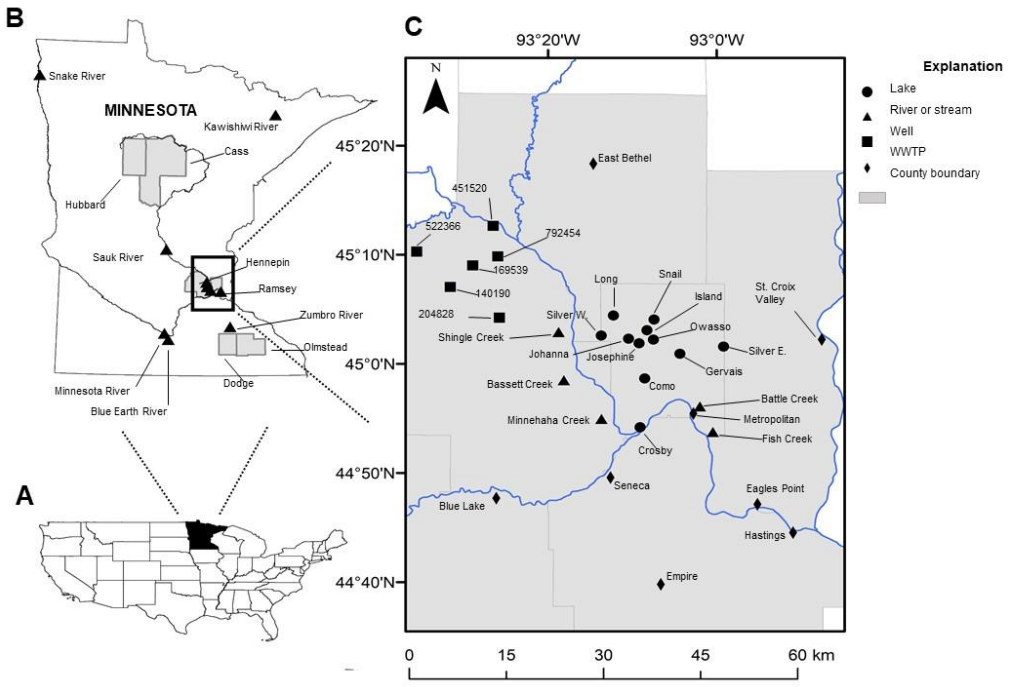

Figure 4-1. Sampling locations for 2019. Extent of locations (A) in the U.S., (B) the State of Minnesota (shaded areas indicate counties where groundwater samples were collected), and (C) the Minneapolis-St. Paul metropolitan area (mainly Hennepin and Ramsey counties). The state of Minnesota is represented by the shaded portion in the (A) U.S. map.

Grab samples from rivers and streams were collected by wading or from a nearby structure with a dipper pole, weighted bucket, or Van Dorn sampler (Table C-2). Sample collection began in May 2019 and one sample was collected in May, July, and August (3 total samples). The Blue Earth River (n =15 total samples, predominately an agricultural watershed; Figure C-1) and Shingle Creek (n=14, predominately an urbanized watershed; Figure C-1) were selected as high-frequency monitoring sites and sampled every 1–2 weeks between April–October. When possible, samples were taken at or near active U.S. Geological Survey (USGS) gauging stations to provide streamflow information. The sampling of rivers and streams was performed in conjunction with the Minnesota Department of Agriculture (MDA), Minnesota Pollution Control Agency (MPCA),

International Water Institute (IWI), and the Vermillion Community College (VCC) Watershed Science program.

All of the lakes are in moderate to highly urbanized portions of Ramsey County, MN (Figure 4-1, Figure C-1 and Figure C-2). One 2 m deep integrated surface water sample was collected from approximately the same location within each lake during June, July, and September, using a 2 m PVC tube with a check valve on one end. This timing of sampling was designed to preclude, co-occur with, and follow the senescence of potentially harmful algal blooms. Como Lake was sampled differently because of its accessibility, urban landscape, and extensive monitoring data record. Here, samples were collected at approximately 2 week intervals from June to October. The samples were collected from the same location in the lake with a Van Dorn sampler at the surface, 2 m depth, and just above the bottom (typically 4.2 to 4.9 m). Additional samples were collected from 8 of the lakes to assess the community composition of several planktonic taxa (details in Appendix C). Lake sampling was coordinated with the Ramsey County Environmental Services (RCES), Lakes Management division.

Groundwater samples were collected from wells in Cass (n = 6; August–September 2018), Hennepin (n = 6; May–June 2019), Hubbard (n = 6; May 2019), Dodge (n = 6; August 2019), and Olmstead (n = 11; September–October 2019) counties (Figure 4-1). One sample was collected from each well. Samples were pumped from wells through a filter attached to the end of a 1 inch tube (polyvinyl chloride, UDP). The pump was operated for at least 5 minutes before sample collection to ensure stabilization of the groundwater chemistry. Well samples were obtained as part of the Minnesota Department of Natural Resources (MN DNR) County Geologic Atlas (CGA) program.

Wastewater treatment plant (WWTP) effluents were sampled from the 8 WWTPs operated by the Minnesota Metropolitan Council Environmental Services (MCES). Samples were taken as a 24 to 48 h composite during 20 to 24 June 2019.

4.3.4 Sample preparation and analysis

Extraction of water samples. Samples were concentrated by solid-phase extraction (SPE) following previously established methods.[64] Extractions were performed using Oasis HLB SPE cartridges (500 mg, 6 cc, Waters) that were conditioned with 5 mL dichloromethane, 5 mL acetone, and 10 mL water. Water samples were spiked with 10 ng of imidacloprid-d_4 and clothianidin-d_3 in acetonitrile as the surrogate standards and loaded onto HLB cartridges under vacuum flow at a rate of ≤ 10 mL/min. The cartridges were then dried completely under continued vacuum. The cartridges were eluted with 10 mL of a dichloromethane and acetone solution (50:50, v/v) and the eluent was evaporated to dryness under a gentle stream of nitrogen gas (99.99%, Matheson). The sample extracts were reconstituted in 1 mL of Optima grade water and spiked with 50 ng of a 2.55 mg/L solution of caffeine-$^{13}C_3$ in acetonitrile, as the internal standard. The acetonitrile was used to ensure that the final sample matrix matched the initial mobile phase during liquid chromatography.

4.3.5 Liquid chromatography tandem mass spectrometry

The neonicotinoids were measured by liquid chromatography with tandem mass spectrometry (LC-MS/MS). Separations were performed by reverse-phase liquid chromatography using a Dionex UltiMate 3000 RSLCnano Ultra Performance Liquid

Chromatography (UPLC) system (Thermo Fisher Scientific) equipped with a Thermo Scientific Hypersil GOLD C18 column (100 mm × 2.1 mm; 1.9 μm particle size) maintained at 40 °C. A binary gradient of 0.1% formic acid in water and acetonitrile was used at a constant flow rate of 15 μL/min. The sample injection volume was 5 μL. The initial mobile phase was 10% acetonitrile and increased at a rate of 3% per min for 13 min followed by a ramp of 8% per min for 5 min and then held at 90% for 3 min. At 24 min, the mobile phase was abruptly decreased to 10% acetonitrile and held for 5 min before the next injection (29 min total analysis time). Detection and quantification were performed using a Thermo Scientific TSQ Vantage triple quadrupole mass spectrometer in electrospray ionization positive (ESI+) mode with full scan acquisition (m/z = 50-400, resolution = 70000). The two most abundant ion transitions were simultaneously monitored via multiple reaction monitoring. The MS mass transitions, collision energies, and LC retention times for all compounds are provided in Appendix C.

4.3.6 Quality assurance

The method detection limits (MDLs) were determined according to the protocol established by the EPA.[220] They are the minimum concentrations that can be reported with 99% confidence as being distinguishable from the method blanks. Seven replicate solutions containing 10 μg/L of each analyte were processed through the entire analytical procedure and analyzed by LC-MS/MS. The analyte-specific MDLs for compound *i* were calculated from eq 4-1.

$$MDL_i = t_{(n-1,1-\alpha=0.99)} S_i \qquad (4-1)$$

where t is the t-value of a single-tailed t-test with (n – 1) degrees of freedom at the 99% confidence level and S is the standard deviation in neonicotinoid concentrations determined from the replicate injections for a given neonicotinoid, *i*. Measurements below the MDL were indicated by < followed by the corresponding MDL. The lower reporting limit (LRL) was set at twice the MDL. Neonicotinoid concentrations beyond the upper calibration range or between the LRL and MDL were considered estimated detections (indicated by < or > followed by the corresponding LRL) and were not included in the data analyses. The detection frequency of each analyte was defined as the proportion of calculated concentrations > MDL. For samples in which no neonicotinoids were observed > MDL, the entry was indicated with "<" and the corresponding MDL (see Table C-8).

Quality assurance measures were based on method blanks, field blanks, equipment blanks, duplicate field samples, and recovery spikes into Optima-grade and field collected water. Field blanks were obtained by exposing a bottle with Optima-grade water to the field atmosphere for at least 10 min. Equipment blanks were collected by processing Optima-grade water through the sampling equipment during sampling. A summary of MDLs and LRLs is shown in Table C-8.

Mean relative recoveries of the surrogate standards were 94 ± 10% (imidacloprid-d_4) and 86 ± 17% (clothianidin-d_3). The measured neonicotinoid concentrations were not recovery corrected. Relative percent differences (RPDs) of duplicate samples (n = 20 total samples) ranged from 1 to 57% with a mean (± SD) of 15 ± 13%. Of the samples used for recovery spike experiments (n = 14 total samples), percent recoveries ranged from 19 to 128% with a mean (± SD) of 75 ± 24% across all neonicotinoids. See

Appendix C for a description of the procedures and calculations used for quality assurance.

4.3.7 Data analysis

Statistical comparisons. All data were analyzed using R (R Core Team, Version 3.6.1) in RStudio (RStudio, Inc., Version 1.2.5033). Data manipulations and descriptive statistics were determined with the dplyr (Version 0.8.5), tidyr (Version 1.0.2), psych (Version 1.9.12.31), and stats (Version 3.6.2) packages. Geospatial analyses (e.g., geolocation, watershed area calculations, land use distributions) were performed in ArcGIS Desktop (ESRI, Version 10.6.1) using data from the MN Geospatial Commons and the 2016 National Land Cover Database (NLCD; USGS, 2016).[221]

Total neonicotinoid concentrations were defined as the sum of all neonicotinoid concentrations above the MDL in each sample. Concentrations below the MDL were not included in the calculations.

4.3.8 Toxicity calculations

The pesticide toxicity index (PTI) for all samples was calculated following the method of Nowell et al.[222] The PTI was calculated from the additive effects of neonicotinoid concentrations and the taxon-specific toxicity thresholds (eq 4-2 and

Table C-9).

$$\mathrm{PTI_t} = \sum_{\mathrm{i}=1}^{\mathrm{n}} \mathrm{E_i}/\mathrm{TC_{i,t}} \qquad (4-2)$$

where n is the number of detected neonicotinoids, E is the concentration of neonicotinoid i, and $TC_{i,t}$ is the toxicity concentration of neonicotinoid i to the taxonomic

group, t. Values of $TC_{i,t}$ were obtained from the U.S. EPA ECOTOXicology knowledgebase (ECOTOX)[215], U.S. EPA Office of Pesticide Programs (OPP)[223], and the Pesticide Properties DataBase (PPDB).[60] The average of acute LC50s of the mortality or immobility endpoint was used as the TC for each combination of taxon and neonicotinoid. A complete list of the $TC_{i,t}$ values used is in Table C-9.

4.4 Results

4.4.1 Overall detection frequencies

Measured neonicotinoid concentrations are summarized in Table 4-1. At least one neonicotinoid or neonicotinoid transformation product (hereafter referred to as 'neonicotinoids') was detected in 86% of all samples (n = 157) ; 62% contained two or more, 40% contained three or more, and four or more were detected in 18%. The maximum number of neonicotinoids in any sample was five (n = 2; Metropolitan WWTP and Blue Earth River, May); the median number of compounds detected per sample was three. The most frequently detected compounds were imidacloprid (75%), clothianidin (55%), thiamethoxam (43%), and acetamiprid (27%). A significant, positive Spearman's rank correlation (defined as *p*-value < 0.05) was observed between the occurrence of thiamethoxam and clothianidin ($\rho = 0.870$, p-value < 0.001; Figure C-3).

Table 4-1. Summary of measured neonicotinoid concentrations in each type of waterbody

		Imidacloprid		Clothianidin		Acetamiprid		Thiamethoxam	
Rivers and Streams	n	DF (%)	Median (ng/L)	DF (%)	Median (ng/L)	DF (%)	Median (ng/L)	DF (%)	Median (ng/L)
Battle Creek	3	100	2.3	67	0.46	33	< 0.42	33	< 0.12
Bassett Creek	3	100	5.0	100	0.81	33	< 0.42	67	0.34
Fish Creek	3	100	11	100	2.2	33	< 0.42	100	1.8
Minnesota River	3	100	1.6	100	10	33	< 0.42	100	0.97
Kawishiwi River	4	25	< 0.23	25	< 0.42	25	< 0.42	0	< 0.12
Minnehaha Creek	4	75	2.5	75	1.5	50	0.74	75	0.45
Blue Earth River	14	100	1.3	100	17	14	< 0.42	100	3.8
Shingle River	15	100	2.2	47	< 0.42	27	< 0.42	33	< 0.12
Sauk River	4	100	1.5	75	4.6	75	1.5	100	1.3
Snake River	4	100	4.8	100	6.9	25	< 0.42	75	2.1
Zumbro River	4	100	3.3	100	38	25	< 0.42	100	8.0
		Imidacloprid		Clothianidin		Acetamiprid		Thiamethoxam	
Lakes	n	DF (%)	Median (ng/L)	DF (%)	Median (ng/L)	DF (%)	Median (ng/L)	DF (%)	Median (ng/L)
Como	23	74	1.7	39	< 0.42	4	< 0.42	0	< 0.12
Crosby	3	67	0.61	67	1.6	0	< 0.42	33	< 0.12
Gervais	3	100	3.5	33	< 0.42	0	< 0.42	33	< 0.12
Island	3	33	< 0.23	0	< 0.42	0	< 0.42	0	< 0.12
Johanna	3	67	0.85	33	< 0.42	0	< 0.42	0	< 0.12
Josephine	3	67	0.82	0	< 0.42	33	< 0.42	0	< 0.12
Long	3	100	3.6	67	0.77	0	< 0.42	0	< 0.12
Owasso	3	67	0.88	67	0.73	33	< 0.42	0	< 0.12
Silver E.	3	67	0.45	0	< 0.42	0	< 0.42	33	< 0.12
Silver W.	3	67	1.2	0	< 0.42	0	< 0.42	0	< 0.12
Snail	3	67	0.65	67	0.48	0	< 0.42	67	1.4

Table 4-1 continued

Wells	n	Imidacloprid DF (%)	Imidacloprid Median (ng/L)	Clothianidin DF (%)	Clothianidin Median (ng/L)	Acetamiprid DF (%)	Acetamiprid Median (ng/L)	Thiamethoxam DF (%)	Thiamethoxam Median (ng/L)
Cass	6	50	< 0.23	50	< 0.42	17	< 0.42	17	< 0.12
Dodge	6	0	< 0.23	0	< 0.42	0	< 0.42	0	< 0.12
Hennepin	6	83	0.27	83	1.2	67	1.1	83	0.20
Hubbard	6	83	0.25	100	1.2	100	1.4	100	0.22
Olmstead	11	9	<0.23	9	< 0.42	55	0.44	64	0.38

WWTPs[b]	Imidacloprid Concentration (ng/L)	Clothianidin Concentration (ng/L)	Acetamiprid Concentration (ng/L)	Thiamethoxam Concentration (ng/L)
Blue Lake	48	11	< 0.42	< 0.12
Eagles Point	24	2.9	0.48	< 0.12
East Bethel	22	0.67	< 0.42	< 0.12
Empire	13	< 0.42	4.7	< 0.12
Hastings	13	< 0.42	0.64	0.44
Metropolitan	16	32	1.9	1.4
Seneca	29	5.2	< 0.42	< 0.12
St. Croix Valley	12	< 0.42	0.43	< 0.12

[a]detection frequencies are defined as the percentage of measurements > MDL.
[b]each entry is single effluent sample.
n = number of samples. DF = detection frequency.

The median and maximum total neonicotinoid concentration across all samples were 3.0 ng/L and 140 ng/L (Zumbro River, May), respectively. Individual neonicotinoid concentrations ranged from < MDL to 92 ng/L. There were no detections of thiacloprid or any imidacloprid transformation products (Table 4-2). Thiacloprid amide, a transformation product of thiacloprid, was measured > MDL (2.9 ng/L, Table 4-2) in only one sample.

Table 4-2. Method detection limits (MDL), detection frequencies, and median concentrations of neonicotinoids in all samples (n = 157)

Compound	MDL (ng/L)	Detections > MDL (%)	Detections > LRL (%)	Median (ng/L)[a]
Acetamiprid	0.42	27	19	< 0.42
Acetamiprid-N-desmethyl	0.48	5	4	< 0.48
Clothianidin	0.42	55	40	0.52
Imidacloprid	0.23	75	62	1.3
Imidacloprid-olefin	1.7	0	0	< 1.7
Imidacloprid-urea	1.5	0	0	< 1.5
Desnitro-imidacloprid	0.71	0	0	< 0.71
Thiacloprid	0.60	1	0	< 0.60
Thiacloprid amide	0.65	1	1	< 0.65
Thiamethoxam	0.12	43	9	< 0.12
Total neonicotinoid concentration		70	62	3.0

[a]only measurements > MDL were included in the median calculations.

4.4.2 Rivers and Streams

Sixty-one samples were analyzed from 11 rivers and streams (Figure 4-2 and Figure 4-3; Table 4-1). Neonicotinoid concentrations were typically highest during May and decreased thereafter. Total neonicotinoid concentrations ranged from < 0.12 to 140 ng/L (median = 9.3 ng/L). The watershed drainage areas were between 30 and 30,000 km^2

(Table C-2) and included a mixture of predominantly urban (n = 6, including Shingle Creek) and agricultural (n = 4, including Blue Earth River) land use with one predominantly undeveloped watershed of mixed-use forest (Kawishiwi River). The percentage of land dedicated to cultivated crops in agricultural watersheds ranged from 51% (Blue Earth River) to 95% (Snake River).

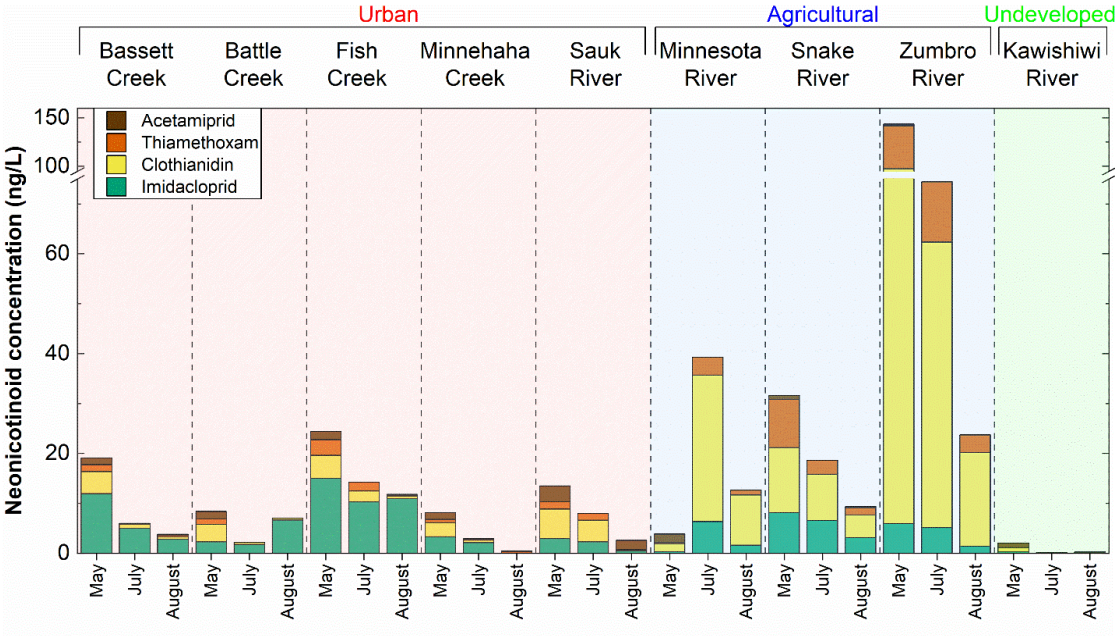

Figure 4-2. Neonicotinoid concentrations in rivers and streams, excluding Shingle Creek and Blue Earth River (see Figure 4-3), during 2019. Colored panels indicate the prevailing land use (red = urban, blue = agricultural, green = undeveloped) of the surrounding watershed. Each column represents one sample.

Clothianidin was the most frequently detected neonicotinoid at both agricultural (100% detection, median concentration = 15 ng/L) and urban (100%, 0.71 ng/L) sampling locations (Table 4-1). The concentrations of imidacloprid, however, were greater than clothianidin in urban-affected watersheds (2.6 ng/L). In all streams, thiamethoxam (0.76 ng/L) and acetamiprid (< 0.42 ng/L) were detected less frequently

and at lower concentrations (Table 4-1). The highest concentration of an individual neonicotinoid was clothianidin (92 ng/L, Zumbro River). The median number of co-occurring neonicotinoids in all samples was three. Only one sample in this study contained a neonicotinoid transformation product (thiacloprid amide, 2.9 ng/L) above the MDL (Blue Earth River, star in Figure 4-3A). Because it was not detected in any quality assurance and control samples, the result was likely not caused by sample contamination or an erroneous detection.

Instantaneous neonicotinoid yields (Figure C-4) were calculated for each of the rivers and streams where continuous discharge measurements were available (calculations in Appendix C). Clothianidin had the highest median yield (20 mg/km^2/d) at agricultural locations and all other neonicotinoids were below 4.0 mg/km^2/d. In urban watersheds, clothianidin (4.2 mg/km^2/d) and imidacloprid (3.4 mg/km^2/d) had the largest median yields while all other compounds were ≤ 1.1 mg/km^2/d.

The increased frequency and total number of sampling events at the Blue Earth River (Figure 4-3A) and Shingle Creek (Figure 4-3B) were used to investigate the temporal variation in neonicotinoids and mitigate potential bias caused by infrequent sampling.[224–227] The characteristic decrease in total neonicotinoid concentration (see Figure 4-3) was observed throughout the season. The increased temporal resolution revealed one or more additional neonicotinoid spikes at each sampling location during July and October (Figure 4-3). A review of stream gauge data[228] and weather records[229] showed that theses spikes corresponded with precipitation-induced pulses in stream flow (Figure 4-3 solid line), thus increasing the neonicotinoid load.

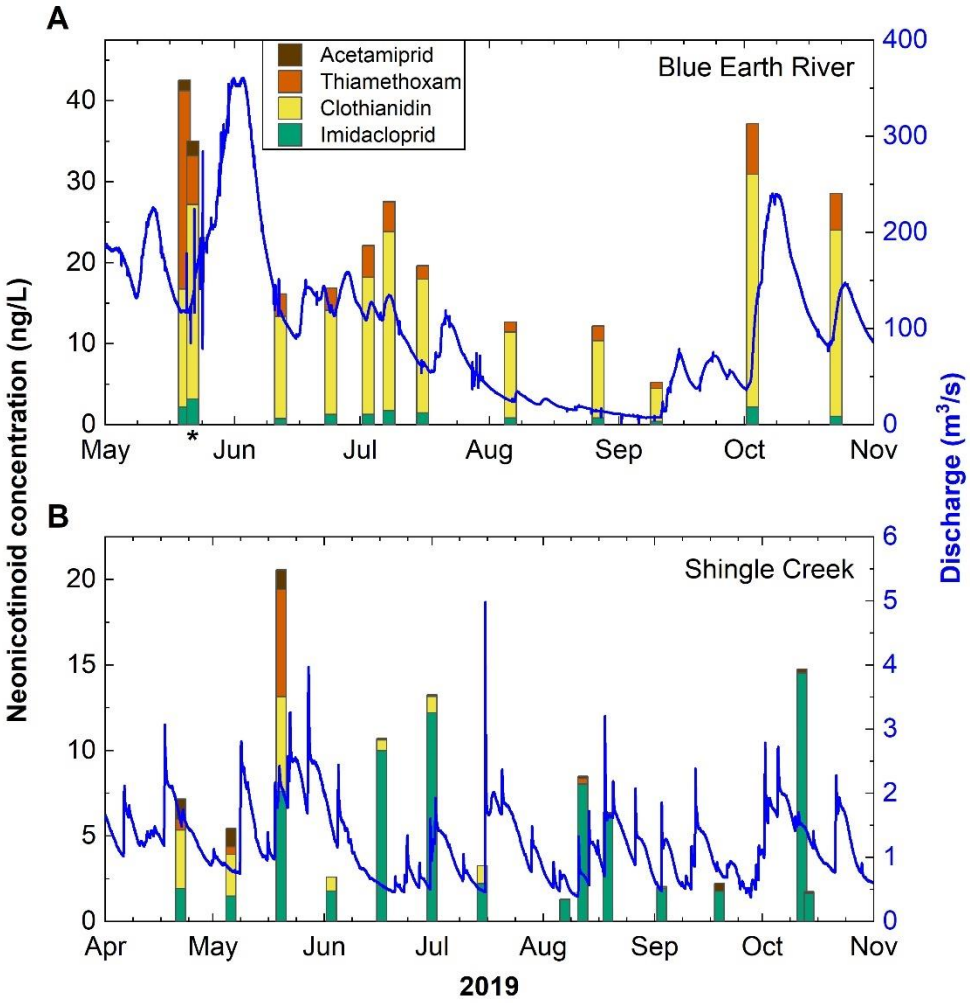

Figure 4-3. Neonicotinoid concentration (left axis, columns) and instantaneous discharge (right axis, solid line) in (A) Blue Earth River (agricultural watershed) and (B) Shingle Creek (urban watershed). * = sample in which thiacloprid amide was detected (2.9 ng/L).

4.4.3 Lakes

Eleven small, shallow lakes (≤ 1.5 km^2 surface area, 39–100% littoral) with small drainage areas (0.5 to 50 km^2, Table C-3) were sampled from urbanized portions (44–91% urban land use) of Ramsey County, MN (Figure 4-4 and Figure C-2). Imidacloprid was the most frequently detected neonicotinoid (72% detection, median = 1.64 ng/L) in all lakes. The other neonicotinoids were detected less frequently (≤ 36%) and at lower

concentrations (Table 4-1). Almost all samples (98%) contained one or more neonicotinoid; the median number of co-occurring neonicotinoids was three.

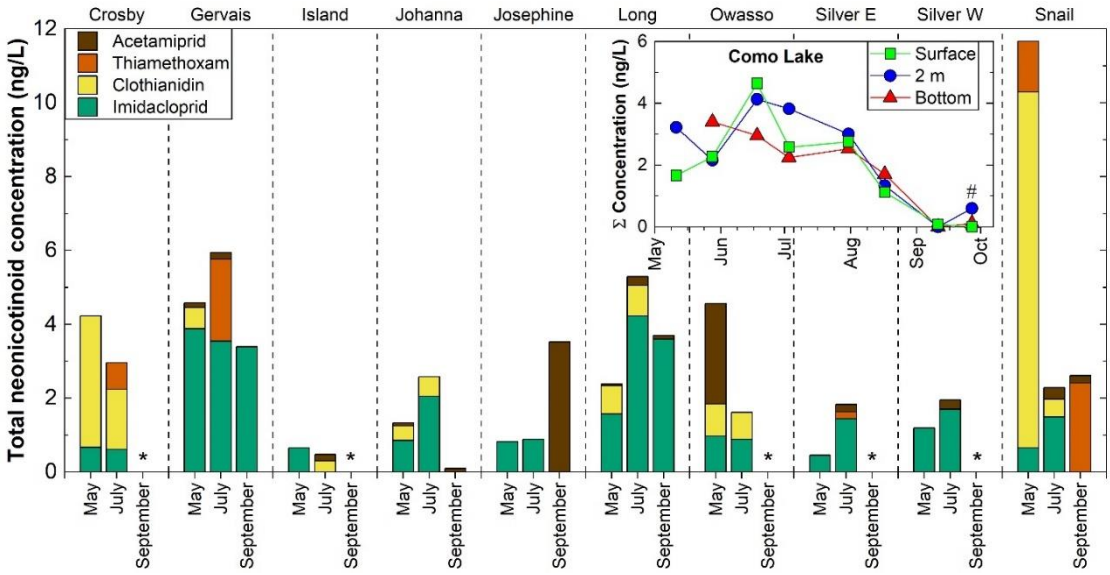

Figure 4-4. (Main panel) Distribution of neonicotinoid concentrations at 10 lakes in Ramsey County, MN during 2019. Water samples were integrated over the top 2 m of each lake. (Inset) Total neonicotinoid concentrations in Como Lake at three depths over time. Total concentrations were mainly composed of imidacloprid. * = No neonicotinoids detected. # = The acetamiprid transformation product, acetamiprid-N-desmethyl, was detected in the bottom water sample at a concentration of 13 ng/L. Because this is the only such detection in all lake samples and owing to its high concentration relative to acetamiprid (< 0.42 ng/L), it is not included in the Figure 4-4 inset.

In half of the 10 lakes sampled once during May, July, and September (Figure 4-4 main panel), neonicotinoid concentrations peaked in July and generally decreased throughout the remainder of the season. No clear patterns emerged in the other lakes and 5 of the lakes had no neonicotinoid concentrations above the MDL in September. Como Lake was sampled on eight separate dates (n = 23 total samples; Figure 4-4 inset) and showed a similar trend in which total neonicotinoid concentrations peaked during mid-

June and decreased thereafter. No significant correlations of concentrations with sampling depth at Como Lake (determined by Spearman rank-analysis) were found (Figure C-5 and Figure C-6). Como Lake is also a shallow lake with a prominent flow-through nature which maintains regular mixing throughout the entire lake.

Ten zooplankton and 38 phytoplankton taxa (Table C-6) in 7 of the lakes were analyzed to determine whether the presence of neonicotinoids affected their taxonomic distributions. Many of these species constitute the foundation of important aquatic food webs and can be an indicator of overall aquatic health.[230] Detailed plankton concentrations along with total neonicotinoid concentrations are provided in Figure C-7 and Figure C-8.

4.4.4 Groundwater

The median and maximum total neonicotinoid concentrations in groundwater wells were 1.4 ng/L and 16 ng/L, respectively (Figure 4-5). At least one neonicotinoid was detected in 74% of wells; two or more were detected in 49%, and four were detected in 26%. The median number of co-occurring neonicotinoids was two. By county, the median total neonicotinoid concentrations were 3.2 ng/L (Hennepin), < 0.12 ng/L (Dodge), 1.3 ng/L (Olmstead), 3.0 ng/L (Hubbard), and 1.3 ng/L (Cass; Table C-1). No detections of thiacloprid or any of the neonicotinoid transformation products occurred in any of the groundwater samples.

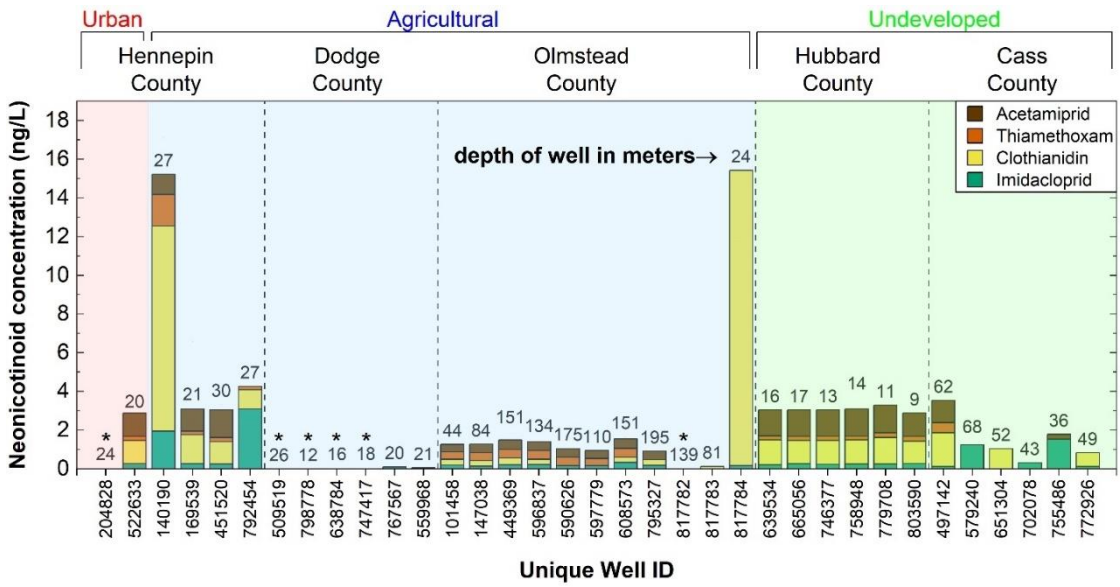

Figure 4-5. Distribution of neonicotinoid concentrations in groundwater wells. Bottom axis labels show the unique Well ID used in the Minnesota Well Index. Upper column labels indicate the depth of each well in meters. * = no neonicotinoids detected.

The predominant type of land use surrounding each sampling location is indicated by the background color in Figure 4-5. Except for Hennepin County, all wells in each county represented the same type of land use: agricultural (Olmstead and Dodge) or undeveloped (Cass and Hubbard). Because drainage areas are not easily determined for groundwater, land use was estimated in the 1 km radius zone surrounding each well. The wells in Hennepin County included both urban (n = 2) and agricultural (n = 4) watersheds. The depth of wells ranged from 11 to 195 m below ground level and are shown by the labels above the columns in Figure 4-5 (see Table C-4).

Hennepin County had the highest concentrations of clothianidin (83% detection, median = 1.2 ng/L; Table 4-1) and acetamiprid (100%, median = 1.1 ng/L). Imidacloprid and thiamethoxam were also frequently detected (83% and 67%, respectively; Table 4-1).

No neonicotinoids were detected > MDL in any of the samples from Dodge County (86–95% agricultural land use). Olmstead County (49–88% agricultural land use) is directly adjacent to Dodge County and also had low neonicotinoid concentrations (Table 4-1). Dodge and Olmstead counties consist of a highly degraded karstic subsurface with rapid groundwater recharge rates as determined from dye tracer studies, radiocarbon dating, and nutrient dynamics.[231]

In predominately undeveloped Hubbard County (all wells were 79–95% undeveloped land use), clothianidin, thiamethoxam, and acetamiprid were detected > MDL in every sample and imidacloprid was detected in 83% of samples (Table 4-1). No neonicotinoids were detected in the quality assurance and control samples from Hubbard County which indicated that the measurements were not attributed to experimental error. Cass County is also largely undeveloped (70–96% undeveloped land use). In the Cass County wells, imidacloprid (50% detection, median 0.22 ng/L) and clothianidin (50%, 0.36 ng/L) were frequently detected. No detections of thiacloprid or any of the neonicotinoid transformation products were made in any of the groundwater samples.

4.4.5 Wastewater treatment plants

Sewersheds (i.e., drainage areas) for the sampled WWTPs range from 45 km^2 (St. Croix Valley) to 1900 km^2 (Metropolitan) with a median area of 230 km^2 (Table C-5). Five of the sewersheds have predominately urban land use (45–73%), two have predominately agricultural land use (59–64%), and one has mostly undeveloped land use

(52%). Two or more neonicotinoids were detected in every sample; seven of the samples contained three neonicotinoids, and one sample contained five (Table 4-1 and Figure 4-6)

Imidacloprid was detected in 100% of samples at concentrations of 12 to 48 ng/L (median 19 ng/L, Figure 4-6A and Table C-1). The acetamiprid transformation product, acetamiprid-N-desmethyl, was also frequently detected (88% detection, median 1.4 ng/L). Clothianidin was the next most abundant neonicotinoid (63% detection, median 1.8 ng/L), followed by acetamiprid (63%, 0.45 ng/L), and thiamethoxam (25%, < 0.12 ng/L). Total neonicotinoid concentrations (median = 26 ng/L, maximum = 61 ng/L) and detection frequencies at WWTPs were higher than rivers, lakes, or groundwater.

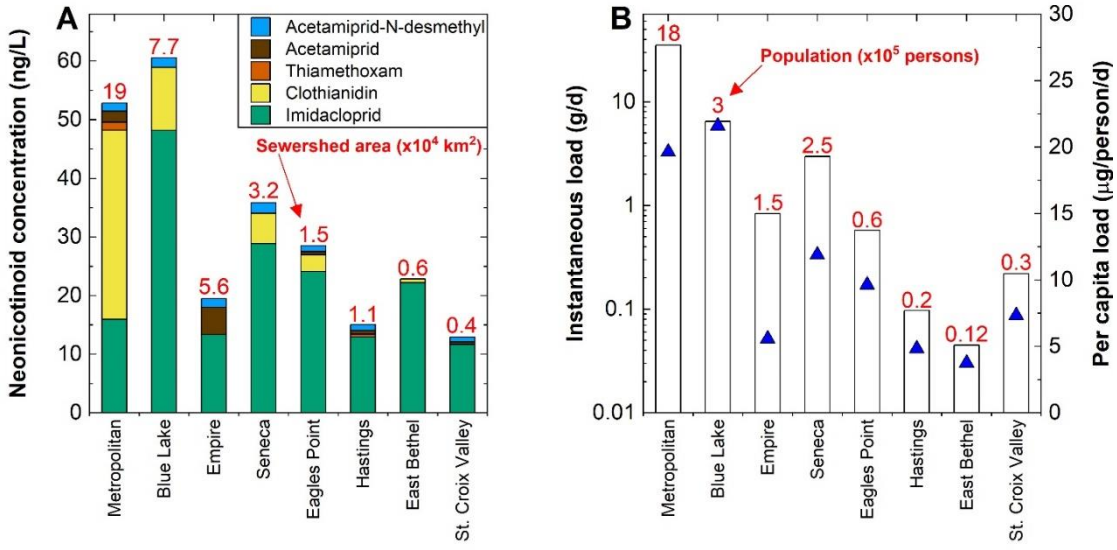

Figure 4-6. Occurrence of neonicotinoids in wastewater treatment plant (WWTP) effluents. (A) Neonicotinoid concentrations (y-axis, columns) and sewershed area (top column labels) of each WWTP. (B) Instantaneous (left y-axis, columns) and per capita (right y-axis, triangles) neonicotinoid loads. Upper column labels indicate the population served by each WWTP. The data in both panels are arranged by decreasing sewershed area, from left to right.

Instantaneous neonicotinoid loads were calculated from the total neonicotinoid concentration and mean discharge at each WWTP (Figure 4-6B left axis, see eq C-3). Loads were highest at the Metropolitan (34 g/d), Blue Lake (6.2 g/d), and Seneca (3.0 g/d) WWTPs and lowest at East Bethel (0.04 g/d) and Hastings (0.10 g/d) WWTPs. Positive Spearman rank-order correlations were determined for neonicotinoid loads with sewershed area ($\rho = 0.905$, *p*-value = 0.002; Figure C-9A) and the population served ($\rho = 0.995$, *p*-value = < 0.001; Figure C-9B). The calculated loads were normalized to the population served by each WWTP to calculate the mean per-capita neonicotinoid load to each plant (eq C-5). The values ranged from 3.4 μg/person/d (East Bethel) to 21 μg/person/d (Blue Lake) as total neonicotinoid concentration (Figure 4-6B right axis). Per-capita loads were positively correlated with the sewershed area of each WWTP ($\rho = 0.714$, *p*-value = 0.05; Figure C-9C).

4.5 Discussion

4.5.1 Effects of land use and watershed characteristics

In lakes and streams, the neonicotinoid concentrations and detection frequencies were related with the type of land use within each watershed (Figure 4-7 and Table 4-3), the drainage area, (Section C.2) and flow conditions (see Section C.9).

Most neonicotinoid products currently registered for non-agricultural uses (pet products, lawn and garden sprays, tree injections) contain imidacloprid; most agricultural products (seed coatings, foliar sprays) consist primarily of clothianidin or thiamethoxam.[33,202] This is observed in the present study by significant correlations of

imidacloprid with urban land use ($\rho = 0.197$, *p*-value = 0.01; Figure C-10A) and of agricultural land use with clothianidin ($\rho = 0.403$, *p*-value < 0.001; Figure C-10B) and thiamethoxam ($\rho = 0.255$, *p*-value = 0.001; Figure C-10B). Imidacloprid (73% detection, median concentration = 1.6 ng/L) and clothianidin (62%, 15 ng/L) were the most frequently detected neonicotinoids in rivers and streams draining agricultural watersheds. It should be noted that clothianidin is also formed from the transformation of thiamethoxam in the environment.[232] The use of thiamethoxam during the last decade has exceeded imidacloprid[218,219] and thus its lower detection frequency in this study could be an artifact of its degradation to clothianidin.

A similar study by Hladik et al.[44] determined a significant relationship between clothianidin and agricultural land use ($\rho = 0.465$, *p*-value 0.003) with measurements from agricultural streams (n = 38) in Iowa, U.S.

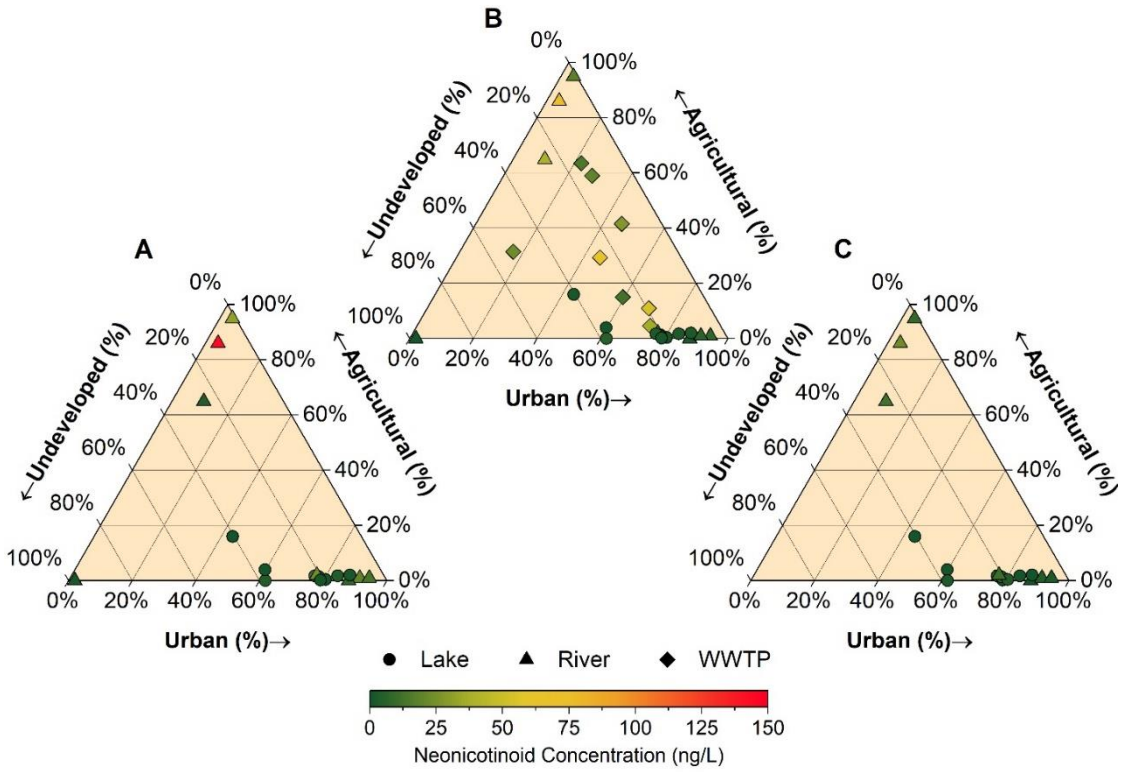

Figure 4-7. Neonicotinoid concentrations as a function of land use and seasonality. Measurements were made during the (A) early (May), (B) middle (July), and (C) late (August–September) 2019 growing season. Triangle vertices correspond to a 100% agricultural (top), undeveloped (bottom left), or urban (bottom right) land use. The color scale indicates the total neonicotinoid concentration in each sample. The type of water body is represented by the symbol shape. Wastewater treatment plants are shown only for panel B because all samples were taken during the mid-growing season (20 to 24 June 2019).

The wide use of neonicotinoids in seed coatings (> 90% of corn and 44–50% of soybeans in the U.S.[32,48]) and their poor incorporation into the targeted crop (2–20% of coating is absorbed by the crop[233,234]) contributes to their frequent observations in streams in agricultural watersheds. The median total neonicotinoid concentration and the median number of neonicotinoids detected in each sample were higher in agricultural, compared to urban or undeveloped, watersheds (Table 4-3). This resulted in a positive correlation

between total neonicotinoid concentrations and agricultural land use ($\rho = 0.549$, *p*-value <0.001; Figure C-10B). In 2016, it was estimated that neonicotinoids were applied to over 98% of the total area of insecticide-treated cropland in North America (540,000 km^2) and, in Minnesota alone, the combined agricultural sales of neonicotinoids exceeded 45,000 kg.[202]

Table 4-3. Summary statistics of neonicotinoid concentrations by predominant land use for the 65 pooled river, stream, lake and WWTP sites.

Land use	n	Median number of neonicotinoids detected	Median total concentration (ng/L)	Maximum total concentration (ng/L; site)	Maximum individual component (ng/L; compound)
Agricultural	48	3	12	140; Zumbro River	92; clothianidin[a]
Urban	92	2	2.9	61; Blue Lake WWTP	48; imidacloprid[b]
Undeveloped	17	2	1.9	3.5; Kawishiwi River	1.8; clothianidin[c]

[a]Zumbro River (May).
[b]Blue Lake WWTP.
[c]Cass County Well ID 497142.
n = number of samples.

In the present study, stronger relationships between drainage area and neonicotinoid concentrations were observed for WWTPs, rivers, and streams than for lakes. Significant, positive correlations occurred between drainage areas and total neonicotinoid concentrations ($\rho = 0.444$, *p*-value < 0.001; Figure C-10C) and the number of neonicotinoids detected ($\rho = 0.428$, *p*-value = 0.002, Figure C-10D). Elsewhere, a meta-analysis by Wolfram et al.[224] used pesticide concentrations from over 600 surface water

samples to develop a model showing that drainage area is inversely correlated with the likelihood that measured neonicotinoid concentrations will exceed regulatory thresholds.

Surface runoff following storm events can increase streamflow and movement of neonicotinoids to the receiving water bodies, especially after the planting of crops in agricultural areas.[41,44,52] The streamflow measurements of the present study revealed significant correlations between total neonicotinoid concentrations and discharge from rivers and streams ($\rho = 0.444$, p-value < 0.001; Figure C-11), WWTPs ($\rho = 0.732$, p-value = 0.037; Figure C-9D), and from Como Lake ($\rho = 0.441$, p-value 0.035; Figure C-5). This trend was also true when each neonicotinoid was considered individually, except for acetamiprid. By establishing streamflow as a driver of neonicotinoid occurrence in flowing systems, these results emphasize the importance of surface water movement on the transport of neonicotinoids.

Como Lake is a heavily engineered system, controlled by several stormwater inlets and one common outlet. Previous data (B. Belden. Capitol Region Watershed District, St. Paul, MN, U.S., personal communication) has shown that the intensive management of Como Lake, in combination with its small size, creates short hydraulic residence times and allows for it to be considered as a continuously flowing system. For example, the 0.2 m^3/s spikes in discharge from Como Lake to create an estimated residence time of < 20 h following large rain events (see Figure C-5). This causes an exchange of approximately all of the total lake volume over a 24 h period. The rapid turnover prohibits well-developed stratification which is observed in the relatively consistent neonicotinoid concentrations at the three depths (Figure 4-4 inset).

All lakes in the present study are located in Ramsey County, Minnesota (area = 440 km^2, < 44% urban, Figure 4-1 and Figure C-1); thus, it was difficult to determine the effects of watershed characteristics on neonicotinoid occurrence. Nevertheless, many of the important factors influencing neonicotinoid occurrence in surface and groundwater (e.g., discharge, land use, drainage area) described here and elsewhere[41,44] were also true for lakes. Imidacloprid was detected most frequently and at higher concentrations than the other compounds (72% detection, median = 1.2 ng/L). These results are still significant because as of 2016, no neonicotinoids had been quantified in any of Minnesota's lakes.[202]

Neonicotinoid concentrations in groundwater were less than the other hydrologic compartments (Figure 4-5). Hydrogeologic variables, such as groundwater recharge rates, water flow paths, and groundwater age, especially in southeastern Minnesota,[231] influence the occurrence of neonicotinoids. For example, despite the abundance of agriculture in Dodge and Olmstead counties, much of the bedrock in the region contains highly degraded karst features and creates rapid groundwater recharge rates.[235] Because of this, the groundwater is quickly discharged thus diluting neonicotinoid concentrations. This is supported by Barry et al.[231] in which a hydrogeologic survey of the region revealed many highly fractured aquifer materials with groundwater flow rates of 1.6 to 4.8 km/d. Other portions of Dodge and Olmstead counties contain carbonate bedrock which is resistant to weathering and prevents the vertical migration of contaminants from surface water to groundwater. The aquifers of Cass, Hubbard, and Hennepin counties are

more defined and have lower groundwater flow rates; these regions therefore have much longer recharge rates with a limited potential to dilute any introduced neonicotinoids.

4.5.2 Temporal patterns in neonicotinoid concentrations

The temporal analysis of neonicotinoids in rivers and streams showed that the occurrence of neonicotinoids is influenced by their period of use before and during the growing season (Figure 4-2 and Figure 4-3). The elevated early-season (May) concentrations, at most sites, both urban and agricultural, were attributed to runoff from spring storms following their application, which mobilized both the current year's neonicotinoids and those remaining from previous seasons.[41,236,237] In agricultural watersheds, the subsequent decreases in concentrations reflect the fact that most neonicotinoids are administered as seed coatings and applied during planting. Any compounds not incorporated into the target crop are quickly removed from the surrounding landscape. In urban environments, neonicotinoids are applied later in the growing season and may be affected by other (bio)chemical transformation processes.

The exception to these seasonal trends in rivers and streams was at the Minnesota River near Judson, MN which had a lower total neonicotinoid concentration in May (3.9 ng/L), followed by a higher concentration in July (39 ng/L). The low concentration was likely caused by delayed planting in response to an abnormally wet spring in southwestern Minnesota during 2019.[238] In addition, the sample collection in July was preceded by a rain event (~2 cm) which caused increased streamflow.[238] Rain events are directly linked to elevated runoff and streamflow which promotes neonicotinoid

mobilization. In the present study, positive relationships between stream discharge and median total neonicotinoid concentrations were observed in rivers and streams (ρ = 0.444, *p*-value < 0.001; Figure C-11).

The number of neonicotinoids detected in each sample did not change (by Spearman rank correlations; Figure C-12) throughout the season. There were also no substantial changes in the relative ratios of individual neonicotinoids. For example, the ratio of imidacloprid to clothianidin in agricultural and urban watersheds over the entire growing season were (mean ± SD) 0.35 ± 0.54 and 4.1 ± 4.9, respectively.

As observed in rivers and streams (Figure 4-2 and Figure 4-3), neonicotinoid concentrations in lakes generally decreased throughout the season (Figure 4-4) but to a lesser extent. This was attributed to the typical application timeline of pesticides in different watersheds. For example, the larger decrease of neonicotinoid concentrations in rivers and streams indicates the influence of agriculture, in which neonicotinoids are primarily applied as seed coatings only during planting. The more consistent neonicotinoid concentrations in lakes, which were all in urbanized watersheds, likely occurred from use on lawns, gardens, and trees applied throughout the growing season. As a result, urban watersheds are more likely to experience chronic neonicotinoid exposure.

4.5.3 Potential toxicity and ecosystem impacts

The aquatic life benchmarks for neonicotinoid exposure to freshwater invertebrates (e.g., midges, scuds, daphnids) range from 10 ng/L to 100,000 ng/L (chronic) and 385

ng/L to > 474,000,000 ng/L (acute).[223] No neonicotinoids in the present study were detected above their lowest species-specific acute benchmark and only 10% of all samples contained one or more compound that exceeded the minimum chronic benchmark. Surface water sampling conducted by the MDA in 2014 found no measurements that exceeded any benchmark value in any sample.[202] While these data suggest that the neonicotinoid concentrations in the present study pose a low risk to aquatic life, previous research has shown that even if neonicotinoid concentrations do not exceed benchmark values, the health of aquatic communities is still negatively affected (e.g., paralysis, impaired mobility, reduced fertility).[216,239] This highlights the importance of the potential sub-lethal chronic effects that contribute to aquatic health metrics.[208,240]

The risks posed by (co)occurring neonicotinoids were further evaluated by calculating the pesticide toxicity index (PTI[222]) of all samples (

Table C-10). Currently available aquatic life benchmarks[60,215,223] indicate that toxicity thresholds for neonicotinoids to most aquatic taxa are exceeded when PTIs are greater than ~0.4 (Figure C-13). Median PTIs in the present study ranged from 10^{-9} to 10^{-5}; individual taxon-specific PTIs decreased in the order of *Daphnia* ($10^{-5.9}$), crustaceans ($10^{-6.0}$), mollusks ($10^{-6.2}$), fishes ($10^{-7.9}$), and macrophytes ($10^{-8.8}$). This suggests that there was a low risk to aquatic life from all observed neonicotinoid concentrations.

There was a strong influence of watershed characteristics on PTIs in all types of waterbodies (Table C-11). Significant positive correlations were found between agricultural land use and all taxon-specific PTIs. Except for crustaceans, positive correlations were observed for PTIs with percent urban land use and drainage area (Table

C-11). Despite lower concentrations in smaller watersheds, however, a meta-analysis of insecticide concentrations in U.S. surface waters (n = 4391)[224] concluded that the risk posed to aquatic organisms by insecticides was disproportionally greater in small watersheds. This was true even when exposed to equal or lesser concentrations.[213]

Only the parent neonicotinoids (imidacloprid, clothianidin, acetamiprid, thiamethoxam, thiacloprid) were considered in the calculations of PTI because toxicity benchmarks have not been established for many of the transformation products. The benchmarks that do exist for the transformation products provide conflicting evidence for their relative toxicities. Some studies[61,62] suggest that neonicotinoid transformation products possess toxicities equal to or greater than the parent compounds, while others indicate that toxicities are several orders of magnitude lower.[208,223] Despite these uncertainties, the common mode of action by all neonicotinoids[203] suggests that the transformation products could create some level of negative impacts to non-target organisms. It is also unclear how co-occurring neonicotinoids impact aquatic organisms. For example, neonicotinoid mixtures have shown to cause interactions, but the effects have been both synergistic and antagonistic.[211,212] Because neonicotinoid-based products often contain mixtures of neonicotinoids or other pesticides,[41,209,210] future research should aim to address this gap in knowledge.

4.5.4 Sources to WWTPs

Because the primary source of water to the WWTPs in this study was through municipal wastewater collection network, it was expected that any surface and

groundwater contributions of neonicotinoids would be minimal. WWTPs had among the highest total (13 to 61 ng/L) and individual (e.g., imidacloprid = 12 to 48 ng/L) neonicotinoid concentrations. This is consistent with reports of elevated neonicotinoid concentrations at other WWTPs. In a study of 13 U.S. WWTPs, year-round detections of imidacloprid occurred at every facility with mean influent and effluent concentrations of 60.5 ng/L and 58.5 ng/L, respectively. This equates to an overall ~3% removal of imidacloprid during the WWTP treatment process.[241] Poor removal has also been observed at numerous other WWTPs worldwide.[242–246] It is estimated that 1000 to 3400 kg of imidacloprid are released from WWTPs in the U.S. each year.[241] In the present study total neonicotinoid loads from rivers and streams (median = 4.1 g/d) were greater than from WWTPs (0.70 g/d). This does indicate, however, that discharge from WWTPs constitutes a significant portion of the neonicotinoid load in rivers and streams.

The type of treatment used at a WWTP can also influence the transformation of neonicotinoids. The transformation product, acetamiprid-N-desmethyl was detected at all WWTPs except East Bethel (Figure 4-6A). East Bethel is the only WWTP that employs advanced membrane filtration coupled to ultraviolet irradiation for disinfection before discharging the effluent to an underlying aquifer. All of the other WWTPs disinfect by chlorination/dechlorination or ultraviolet irradiation and discharge the effluents to surface water. The stricter disinfection process at East Bethel is likely used because of the different environment receiving WWTP discharge. Because many homes rely on aquifers for home water demand, more stringent effluent regulations are required to ensure contaminant limits are met. Similar ranges of acetamiprid-N-desmethyl concentrations in

WWTP effluents to those in this study have been reported elsewhere.[241] Because this compound was not detected in the influent, the authors speculated that it was formed during the treatment process.[241]

Because imidacloprid is the main neonicotinoid used for non-agricultural purposes,[45] it was not surprising that it was the most frequently detected in the largely urban WWTP effluents (Figure 4-6; median = 19 ng/L, maximum = 48 ng/L). It is more difficult to explain the consistent occurrence of clothianidin (median = 1.8 ng/L, maximum = 32 ng/L). The concentration of clothianidin strongly correlates with the sewershed area (ρ = 0.960, *p*-value = < 0.001; Figure C-9B). The larger the sewershed, the more likely it is that the sewer system receives inputs from agricultural land. For example, despite primarily urban land use surrounding the Blue Lake WWTP, the sewershed still contains ~30% agricultural land.

In the Minneapolis-St. Paul Metropolitan Area, the sewershed areas are positively correlated with the population served by the WWTP (ρ = 0.960, *p*-value = < 0.001). The instantaneous neonicotinoid loads and size of population served were used to determine per-capita neonicotinoid yields at each WWTP (Figure 4-6B). The Metropolitan and East Bethel WWTPs had the largest and smallest neonicotinoid loads and serve the largest and smallest populations, respectively. There is a significant correlation between neonicotinoid loads and population size (ρ = 0.995, *p*-value = < 0.001; Figure C-9B). This is reflected in the per-capita yields (Figure 4-6B). There are currently no guidelines to regulate the discharge of neonicotinoids from WWTPs but the measured

concentrations were still substantially below aquatic life benchmarks for neonicotinoids (10^5 to 10^{12} μg/L).[60,215,223]

Several non-agricultural sources introduce neonicotinoids to WWTPs including residues on foods and pets treated with neonicotinoid-containing medications.[247,248] In a survey of two U.S. Congressional cafeterias in Washington, DC, neonicotinoid residues were detected on 100% of the fruit and vegetable samples and, in some cases, exceeded safe consumption levels (Table C-12).[248] A connected study of Chinese markets detected at least one neonicotinoid in 91% of all samples at similar concentrations to those found in the U.S.[248] Tomatoes, apples, and melons, contained the highest neonicotinoid concentrations. For all tested produce, total neonicotinoid concentrations ranged from 0.01 to 100 μg/kg. Pets that have been administered flea and tick treatment products containing neonicotinoids also release neonicotinoids to wastewater collection systems. Craig et al.[249] showed that when a commercial flea control medication was given to dogs at the recommended dose, neonicotinoids were detected on gloves worn by individuals who came into contact with the dogs for up to one month after application at residual concentrations near 100 μg/kg of glove.

4.6 Conclusions

Neonicotinoid concentrations in surface and groundwater throughout the state of Minnesota were similar to those measured in other studies in the midwestern U.S. Neonicotinoids were detected the most frequently and in the highest concentrations at agricultural locations followed by urban and undeveloped regions. Clothianidin was

closely associated with agricultural land cover, whereas imidacloprid was more closely associated with urban land use. The type of waterbody is an important driver of neonicotinoid occurrence. There were consistently high concentrations in WWTP effluents and significantly lower concentrations in the other hydrologic compartments. Low neonicotinoid concentrations in wells in agricultural regions suggest that their occurrence is likely influenced by one or many hydrogeologic variables. Total neonicotinoid concentrations are correlated to drainage area and streamflow. Neonicotinoid concentrations are typically highest following applications in agricultural and urban use and during elevated streamflow conditions following rain events. No samples exceeded aquatic-life benchmarks for selected non-target aquatic taxa, suggesting that direct toxic effects are not expected. Neonicotinoid concentrations in aquatic systems are expected to increase because of their increasing use, as well as their persistence and mobility in the environment. Continued research and monitoring of the neonicotinoid insecticides in waterbodies in Minnesota and beyond is needed.

4.7 Supplemental data

The supplemental data are available in Appendix C.

4.8 Data availability

Data pertaining to this manuscript are deposited in the Data Repository for the University of Minnesota at (http://hdl.handle.net/11299/214867).

Chapter 5. Conclusion and Outlook

Organic chemicals are used in many ways to improve the health and well-being of humans, plants, and animals. Despite the numerous benefits, their development and use often causes significant and unintended harm to ecosystems. This dissertation furthers the understanding of how organic pollutants behave in natural and engineered environments. While some processes degrade or immobilize contaminants, others exacerbate their effects. Moreover, the distribution and fate of pollutants is highly dependent on several important variables such as environmental conditions, land-use patterns, and whether remediation attempts have been made. Here, the occurrence and potential fate of two classes of chemicals, NACs and neonicotinoid insecticides, was investigated to assess their behavior in the environment.

Experiments with NACs supported the knowledge that iron-bearing minerals are effective reductants of NACs. The results also showed that CSIA will continue to be a useful tool to monitor pollutant degradation despite the presence of complex environmental conditions and the use of novel chemicals. The isotope fractionation during DNAN reduction was not affected by natural organic matter, the identity of the iron-bearing mineral, or repeated exposure to DNAN. The only factor that influenced isotopic fractionation was the underlying reaction mechanisms (e.g., abiotic vs. biotic).

Potential remediation strategies also did not affect the isotope enrichment during abiotic reduction. Natural soil and sediment materials were exposed to *in situ* chemical reduction (ISCR) by sodium dithionite before DNAN reduction experiments. The amount of N- and C-isotope fractionation during these studies was identical to that observed for

DNAN reduction by synthetic minerals that were supplemented with aqueous Fe(II). These results were used to make accurate predictions of the extent of pollutant degradation from isotope ratio measurements alone.

Despite the success of CSIA to quantify abiotic pollutant reduction, there are still limitations to its implementation at contaminated field sites. While CSIA has been incorporated into several monitored natural attenuation protocols, the protocols typically focus on biodegradation and do not include abiotic pathways. Moreover, further experiments should consider other chemicals as reductants for ISCR, such as calcium polysulfide.

Land-use patterns were shown to have the greatest impact on the occurrence of neonicotinoid insecticides in Minnesota. The highest concentrations were detected in agricultural settings followed by urban and undeveloped areas, respectively. Land-use also affected the distribution of individual compounds. Clothianidin was the main compound found in agricultural areas while imidacloprid was detected most frequently and in the greatest concentrations in urban areas.

Treated wastewater effluents had the highest neonicotinoid concentrations of all types of types of water body. This suggests that domestic applications and residues on neonicotinoid-treated food contributes significantly to the total environmental load of neonicotinoids. Despite groundwater wells in this research largely residing in agricultural areas, neonicotinoid concentrations were the lowest of all environmental compartments which indicates the potential impacts of subsurface hydrogeology on neonicotinoid distribution.

No neonicotinoids were detected at concentrations exceeding toxicity thresholds for aquatic insects and plants in any of the samples. In addition, there were no correlations between planktonic abundance and neonicotinoid concentrations. Because these results are focused only on lakes within a small geographic region (Ramsey County, MN), future work should continue to explore the spatiotemporal effects on aquatic species by surveying a broader range of locations over longer time frames.

Future work should also seek to improve the existing analytical techniques for neonicotinoid detection to increase the amount of quantifiable analytes and degradation products and their limits of quantification. For example, fipronil is an insecticide that is used in flea and tick medications for pets and has become widespread in surface and groundwaters. The analysis method used in this research was effective at quantifying neonicotinoids but achieved poor results for fipronil and its degradation products. One potential approach to this limitation is the use of direct aqueous injection (DAI). Methods using DAI have recently emerged as alternatives to conventional sample preparation by SPE.[63] The use of DAI coupled to LC-MS/MS is advantageous because it allows for environmental samples to be injected directly onto an LC column without the need for extensive sample cleanup and preconcentration; thus, the necessary labor and capital are reduced because filtration is the only needed sample preparation. This also reduces the amount of contamination that can be introduced during sample preparation and analysis.

The overall result of this dissertation shows that anthropogenic pollutants will continue to become an increasingly important issue for ecosystem health. The research was successful not only in describing where chemicals are likely to occur, but also in

determining the efficacy of remediation strategies and in guiding the development of techniques to accurately monitor their abundance. These contributions are critical to ensuring the protection and preservation of plants, animal, and human health for generations to come.

References

(1) Johnson, M. S.; Eck, W. S.; Lent, E. M. Toxicity of Insensitive Munition (IMX) Formulations and Components. *Propellants, Explos. Pyrotech.* **2017**, *42* (1), 9–16.

(2) Schwarzenbach, R. P.; Gschwend, P. M.; Imboden, D. M. *Environmental Organic Chemistry*, 2nd ed.; John Wiley & Sons, 2005.

(3) Dodard, S. G.; Sarrazin, M.; Hawari, J.; Paquet, L.; Ampleman, G.; Thiboutot, S.; Sunahara, G. I. Ecotoxicological Assessment of a High Energetic and Insensitive Munitions Compound: 2,4-Dinitroanisole (DNAN). *J. Hazard. Mater.* **2013**, *262*, 143–150.

(4) Pichtel, J. Distribution and Fate of Military Explosives and Propellants in Soil: A Review. *Appl. Environ. Soil Sci.* **2012**, *Article ID*, 33.

(5) Hofstetter, T. B.; Heijman, C. G.; Haderlein, S. B.; Holliger, C.; Schwarzenbach, R. P. Complete Reduction of TNT and Other (Poly)Nitroaromatic Compounds under Iron-Reducing Subsurface Conditions. *Environ. Sci. Technol.* **1999**, *33* (9), 1479–1487.

(6) Schroer, H. W.; Langenfeld, K. L.; Li, X.; Lehmler, H. J.; Just, C. L. Biotransformation of 2,4-Dinitroanisole by a Fungal Penicillium Sp. *Biodegradation* **2017**, *28* (1), 95–109.

(7) Indest, K. J.; Hancock, D. E.; Crocker, F. H.; Eberly, J. O.; Jung, C. M.; Blakeney, G. A.; Brame, J.; Chappell, M. A. Biodegradation of Insensitive Munition Formulations IMX101 and IMX104 in Surface Soils. *J. Ind. Microbiol. Biotechnol.* **2017**, *44* (7), 987–995.

(8) Perreault, N. N.; Manno, D.; Halasz, A.; Thiboutot, S.; Ampleman, G.; Hawari, J. Aerobic Biotransformation of 2,4-Dinitroanisole in Soil and Soil Bacillus Sp. *Biodegradation* **2012**, *23*, 287–295.

(9) Salter-Blanc, A. J.; Bylaska, E. J.; Ritchie, J. J.; Tratnyek, P. G. Mechanisms and Kinetics of Alkaline Hydrolysis of the Energetic Nitroaromatic Compounds 2,4,6-Trinitrotoluene (TNT) and 2,4-Dinitroanisole (DNAN). *Environ. Sci. Technol.* **2013**, *47* (13), 6790–6798.

(10) Ou, C.; Zhang, S.; Liu, J.; Shen, J.; Han, W.; Sun, X.; Li, J.; Wang, L. Enhanced Reductive Transformation of 2,4- Dinitroanisole in a Anaerobic System: The Key Role of Zero Valent Iron. *RSC Adv.* **2015**, *5*, 75195–75203.

(11) Khatiwada, R.; Root, R. A.; Abrell, L.; Sierra-Alvarez, R.; Field, J. A.; Chorover, J. Abiotic Reduction of Insensitive Munition Compounds by Sulfate Green Rust. *Environ. Chem.* **2018**, *15* (5), 259–266.

(12) Ulrich, B. A.; Palatucci, M.; Bolotin, J.; Spain, J. C.; Hofstetter, T. B. Different Mechanisms of Alkaline and Enzymatic Hydrolysis of the Insensitive Munition Component 2,4-Dinitroanisole Lead to Identical Products. *Environ. Sci. Technol. Lett.* **2018**, *5* (7), 456–461.

(13) Niedźwiecka, J. B.; Finneran, K. T. Combined Biological and Abiotic Reactions with Iron and Fe(III)-Reducing Microorganisms for Remediation of Explosives and Insensitive Munitions (IM). *Environ. Sci. Water Res. Technol.* **2015**, *1*, 34–39.

(14) Kwon, M. J.; O'Loughlin, E. J.; Antonopoulos, D. A.; Finneran, K. T. Geochemical and Microbiological Processes Contributing to the Transformation of Hexahydro-1,3,5-Trinitro-1,3,5-Triazine (RDX) in Contaminated Aquifer Material. *Chemosphere* **2011**, *84*, 1223–1230.

(15) Fida, T. T.; Palamuru, S.; Pandey, G.; Spain, J. C. Aerobic Biodegradation of 2,4-Dinitroanisole by Nocardioides Sp. Strain JS1661. *Appl. Environ. Microbiol.* **2014**, *80* (24), 7725–7731.

(16) Spain, J. C.; Hughes, J. B.; Knackmuss, H. *Biodegradation of Nitroaromatic Compounds*; Lewis Publishers, Inc.: Boca Raton, 2000.

(17) Olivares, C.; Liang, J.; Abrell, L.; Sierra-Alvarez, R.; Field, J. A. Pathways of Reductive 2,4-Dinitroanisole (DNAN) Biotransformation in Sludge. *Biotechnol. Bioeng.* **2013**, *110* (6), 1595–1604.

(18) Boddu, V. M.; Abburi, K.; Maloney, S. W.; Damavarapu, R. Thermophysical Properties of an Insensitive Munitions Compound, 2,4-Dinitroanisole. *J. Chem. Eng. Data* **2008**, *53* (5), 1120–1125.

(19) Larson, S. L.; Martin, W. A.; Escalon, B. L.; Thompson, M. Dissolution, Sorption, and Kinetics Involved in Systems Containing Explosives, Water, and Soil. *Environ. Sci. Technol.* **2008**, *42* (3), 786–792.

(20) Linker, B. R.; Khatiwada, R.; Pedrial, N.; Abrell, L.; Sierra, R.; Field, J. A.; Chorover, J. Adsorption of Novel Insensitive Munitions Comounds at Clay Mineral and Metal Oxide Surfaces. *Environ. Chem.* **2015**, *12*, 74–84.

(21) Weissmahr, K. W.; Hildenbrand, M.; Schwarzenbach, R. P.; Haderlein, S. B. Laboratory and Field Scale Evaluation of Geochemical Controls on Groundwater Transport of Nitroaromatic Ammunition Residues. *Environ. Sci. Technol.* **1999**, *33* (15), 2593–2600.

(22) Elsner, M.; Zwank, L.; Hunkeler, D.; Schwarzenbach, R. P. A New Concept Linking Observable Stable Isotope Fractionation to Transformation Pathways of Organic Pollutants. *Environ. Sci. Technol.* **2005**, *39* (18), 6896–6916.

(23) Hofstetter, T. B.; Schwarzenbach, P.; Bernasconi, S. M. Assessing Transformation Processes of Organic Compounds Using Stable Isotope Fractionation. *Environ. Sci. Technol.* **2008**, *42* (21), 7737–7743.

(24) Jochmann, M. A.; Schmidt, T. C. *Compound-Specific Stable Isotope Analysis*, 1st ed.; The Royal Society of Chemistry, 2012.

(25) Sessions, A. L. Isotope-Ratio Detection for Gas Chromatography. *J. Sep. Sci.* **2006**, *29* (12), 1946–1961.

(26) Weber, E. J.; Spidle, D. L.; Thorn, K. A. Covalent Binding of Aniline to Humic Substances. 1. Kinetic Studies. *Environ. Sci. Technol.* **1996**, *30* (9), 2755–2763.

(27) Colón, D.; Weber, E. J.; Anderson, J. L. Effect of Natural Organic Matter on the Reduction of Nitroaromatics by Fe(II) Species. *Environ. Sci. Technol.* **2008**, *42* (17), 6538–6543.

(28) Pati, S. G.; Kohler, H.-P. E.; Hofstetter, T. B. Characterization of Substrate, Cosubstrate, and Product Isotope Effects Associated with Enzymatic Oxygenations of Organic Compounds Based on Compound-Specific Isotope Analysis. In *Methods in Enzymology*; Elsevier Inc., 2017; Vol. 596, pp 291–329.

(29) Hofstetter, T. B.; Neumann, A.; Arnold, W. A.; Hartenbach, A. E.; Bolotin, J.; Cramer, C. J.; Schwarzenbach, R. P. Substituent Effects on Nitrogen Isotope Fractionation during Abiotic Reduction of Nitroaromatic Compounds. *Environ. Sci. Technol.* **2008**, *42* (6), 1997–2003.

(30) Hartenbach, A.; Hofstetter, T. B.; Berg, M.; Bolotin, J.; Schwarzenbach, R. P. Using Nitrogen Isotope Fractionation to Assess Abiotic Reduction of Nitroaromatic Compounds. *Environ. Sci. Technol.* **2006**, *40* (24), 7710–7716.

(31) Hartenbach, A. E.; Hofstetter, T. B.; Aeschbacher, M.; Sander, M.; Kim, D.; Strathmann, T. J.; Arnold, W. A.; Cramer, C. J.; Schwarzenbach, R. P. Variability of Nitrogen Isotope Fractionation during the Reduction of Nitroaromatic Compounds with Dissolved Reductants. *Environ. Sci. Technol.* **2008**, *42* (22), 8352–8359.

(32) Douglas, M. R.; Tooker, J. F. Large-Scale Deployment of Seed Treatments Has Driven Rapid Increase in Use of Neonicotinoid Insecticides and Preemptive Pest Management in U.S. Field Crops. *Environ. Sci. Technol.* **2015**, *49* (8), 5088–5097.

(33) Jeschke, P.; Nauen, R.; Schindler, M.; Elbert, A. Overview of the Status and Global Strategy for Neonicotinoids. *J. Agric. Food Chem.* **2011**, *59* (7), 2897–2908.

(34) Nowak, P. *The Value of Neonicotinoids in North American Agriculture: Executive Summary*; 2015.

(35) Bass, C.; Denholm, I.; Williamson, M. S.; Nauen, R. The Global Status of Insect Resistance to Neonicotinoid Insecticides. *Pestic. Biochem. Physiol.* **2015**, *121*, 78–87.

(36) Sánchez-Bayo, F.; Goka, K.; Hayasaka, D. Contamination of the Aquatic Environment with Neonicotinoids and Its Implication for Ecosystems. *Front. Environ. Sci.* **2016**, *4* (71), 1–14.

(37) Roessink, I.; Merga, L. B.; Zweers, H. J.; Van den Brink, P. J. The Neonicotinoid Imidacloprid Shows High Chronic Toxicity to Mayfly Nymphs. *Environ. Toxicol. Chem.* **2013**, *32* (5), 1096–1100.

(38) Silvanima, J.; Woeber, A.; Sunderman-Barnes, S.; Copeland, R.; Sedlacek, C.; Seal, T. A Synoptic Survey of Select Wastewater-Tracer Compounds and the Pesticide Imidacloprid in Florida's Ambient Freshwaters. *Environ. Monit. Assess.* **2018**, *190* (435), 1–22.

(39) Raby, M.; Nowierski, M.; Perlov, D.; Zhao, X.; Hao, C.; Poirier, D. G.; Sibley, P. K. Acute Toxicity of 6 Neonicotinoid Insecticides to Freshwater Invertebrates. *Environ. Toxicol. Chem.* **2018**, *37* (5), 1430–1445.

(40) Beketov, M.; Liess, M. Acute and Delyaed Effects of the Neonicotinoid Thiacloprid on Seven Freshwater Arthropods. *Environ. Toxicol. Chem.* **2008**, *27* (2), 461–470.

(41) Hladik, M. L.; Kolpin, D. W.; Kuivila, K. M. Widespread Occurrence of Neonicotinoid Insecticides in Streams in a High Corn and Soybean Producing Region, USA. *Environ. Pollut.* **2014**, *193*, 189–196.

(42) Klarich, K. L.; Pflug, N. C.; DeWald, E. M.; Hladik, M. L.; Kolpin, D. W.; Cwiertny, D. M.; LeFevre, G. H. Occurrence of Neonicotinoid Insecticides in Finished Drinking Water and Fate during Drinking Water Treatment. *Environ. Sci. Technol. Lett.* **2017**, *4*, 168–173.

(43) Woodward, E. E.; Hladik, M. L.; Kolpin, D. W. Nitrapyrin in Streams: The First Study Documenting Off-Field Transport of a Nitrogen Stabilizer Compound. *Environ. Sci. Technol. Lett.* **2016**, *3* (11), 387–392.

(44) Hladik, M.; Kolpin, D. First National-Scale Reconnaissance of Neonicotinoid Insecticides in Streams across the USA. *Environ. Chem.* **2015**, *13* (1), 12–20.

(45) Jeschke, P.; Nauen, R. Neonicotinoid Insecticides. In *Comprehensive Molecular Insect Science*; Elsevier, 2005; pp 53–105.

(46) Hua, J.; Relyea, R. Chemical Cocktails in Aquatic Systems: Pesticide Effects on the Response and Recovery of >20 Animal Taxa. *Environ. Pollut.* **2014**, *189*, 18–26.

(47) Mitra, A.; Flynn, K. J. Promotion of Harmful Algal Blooms by Zooplankton Predatory Activity. *Biol. Lett.* **2006**, *2* (2), 194–197.

(48) Simon-Delso, N.; Amaral-Rogers, V.; Belzunces, L. P.; Bonmatin, J. M.; Chagnon, M.; Downs, C.; Furlan, L.; Gibbons, D. W.; Giorio, C.; Girolami, V.; et al. Systemic Insecticides (Neonicotinoids and Fipronil): Trends, Uses, Mode of Action and Metabolites. *Environ. Sci. Pollut. Res.* **2015**, *22* (1), 5–34.

(49) Casida, J. E.; Durkin, K. A. Neuroactive Insecticides: Targets, Selectivity, Resistance, and Secondary Effects. *Annu. Rev. Entomol.* **2013**, *58* (1), 99–117.

(50) Sur, R.; Stork, A. Uptake, Translocation and Metabolism of Imidacloprid in Plants. *Bull. Insectology* **2003**, *56* (1), 35–40.

(51) Alford, A.; Krupke, C. H. Translocation of the Neonicotinoid Seed Treatment Clothianidin in Maize. *PLoS One* **2017**, *12* (3), 1–19.

(52) Krupke, C. H.; Hunt, G. J.; Eitzer, B. D.; Andino, G.; Given, K. Multiple Routes of Pesticide Exposure for Honey Bees Living Near Agricultural Fields. *PLoS One* **2012**, *7* (1), e29268.

(53) Lentola, A.; David, A.; Abdul-Sada, A.; Tapparo, A.; Goulson, D.; Hill, E. M. Ornamental Plants on Sale to the Public Are a Significant Source of Pesticide

Residues with Implications for the Health of Pollinating Insects. *Environ. Pollut.* **2017**, *228*, 297–304.

(54) Cowles, R. S. Optimizing Dosage and Preventing Leaching of Imidacloprid for Management of Hemlock Woolly Adelgid in Forests. *For. Ecol. Manage.* **2009**, *257*, 1026–1033.

(55) R. Masoner, J.; W. Kolpin, D.; M. Cozzarelli, I.; B. Barber, L.; S. Burden, D.; T. Foreman, W.; J. Forshay, K.; T. Furlong, E.; F. Groves, J.; L. Hladik, M.; et al. Urban Stormwater: An Overlooked Pathway of Extensive Mixed Contaminants to Surface and Groundwaters in the United States. *Environ. Sci. Technol.* **2019**, *53* (17), 10070–10081.

(56) Sadaria, A. M.; Sutton, R.; Moran, K. D.; Teerlink, J.; Brown, J. V.; Halden, R. U. Passage of Fiproles and Imidacloprid from Urban Pest Control Uses through Wastewater Treatment Plants in Northern California, USA. *Environ. Toxicol. Chem.* **2017**, *36* (6), 1473–1482.

(57) Goulson, D. An Overview of the Environmental Risks Posed by Neonicotinoid Insecticides. *J. Appl. Ecol.* **2013**, *50*, 977–987.

(58) Bonmatin, J. M.; Giorio, C.; Girolami, V.; Goulson, D.; Kreutzweiser, D. P.; Krupke, C.; Liess, M.; Long, E.; Marzaro, M.; Mitchell, E. A.; et al. Environmental Fate and Exposure; Neonicotinoids and Fipronil. *Environ. Sci. Pollut. Res.* **2015**.

(59) Bonmatin, J. M.; Giorio, C.; Girolami, V.; Goulson, D.; Kreutzweiser, D. P.; Krupke, C.; Liess, M.; Long, E.; Marzaro, M.; Mitchell, E. A.; et al. Environmental Fate and Exposure; Neonicotinoids and Fipronil. *Environ. Sci. Pollut. Res.* **2015**, *22*, 35–67.

(60) University of Hertfordshire, Pesticide Properties DataBase https://sitem.herts.ac.uk/aeru/ppdb/en/index.htm (accessed Oct 12, 2019).

(61) Suchail, S.; Debrauwer, L.; Belzunces, L. P. Metabolism of Imidacloprid in Apis Mellifera. *Pest Manag. Sci.* **2004**, *60* (3), 291–296.

(62) Casida, J. E. Neonicotinoid Metabolism: Compounds, Substituents, Pathways, Enzymes, Organisms, and Relevance. *J. Agric. Food Chem.* **2011**, *59* (7), 2923–2931.

(63) Sandstrom, M. W.; Kanagy, L. K.; Anderson, C. A.; Kanagy, C. J. Determination of Pesticides and Pesticide Degradates in Filtered Water by Direct Aqueous-Injection Liquid Chromatography-Tandem Mass Spectrometry. In *Laboratory Analysis*; U.S. Geological Survey: Reston, VA, 2015.

(64) Hladik, M. L.; Calhoun, D. *Analysis of the Herbicide Diuron, Three Diuron Degradates, and Six Neonicotinoid Insecticides in Water — Method Details and Application to Two Georgia Streams*; Reston, VA, 2012.

(65) Klarich, K. L.; Pflug, N. C.; DeWald, E. M.; Hladik, M. L.; Kolpin, D. W.; Cwiertny, D. M.; LeFevre, G. H. Occurrence of Neonicotinoid Insecticides in Finished Drinking Water and Fate during Drinking Water Treatment. *Environ. Sci. Technol. Lett.* **2017**, *4* (5), 168–173.

(66) Klarich Wong, Kathryn L. T. Webb, D.; R. Nagorzanski, M.; W. Kolpin, D.; L. Hladik, M.; M. Cwiertny, D.; H. LeFevre, G. Chlorinated Byproducts of Neonicotinoids and Their Metabolites: An Unrecognized Human Exposure Potential? *Environ. Sci. Technol. Technol. Lett.* **2019**, *6* (2), 98–105.

(67) Thompson, D. A.; Lehmler, H.-J.; Kolpin, D.; Hladik, M. L.; Vargo, J.; Schilling, K.; LeFevre, G. H.; Peeples, T.; Poch, M. C.; LaDuca, L. E.; et al. A Critical Review on the Potential Impacts of Neonicotinoid Insecticide Use: Current Knowledge of Environmental Fate, Toxicity and Implications for Human Health. *Environ. Sci. Process. Impacts* **2020**, *22*, 1315–1346.

(68) Trzcinski, W.; Cudzilo, S.; Dyjak, S.; Nita, M. A Comparison of the Sensitivity and Performance Characteristics of Melt-Pour Explosives with TNT and DNAN Binder. *Cent. Eur. J. Energ. Mater.* **2014**, *11* (3), 443–455.

(69) Davies, P. J. P. J.; Provatas, A. *Characterization of 2,4-Dinitroanisole: An Ingredient for Use in Low Sensitivity Melt Cast Formulations*; DSTO-TR-1904, Edinburgh, South Australia, 2006; Vol. DSTO-TR-19.

(70) Albright, R. D. *Cleanup of Chemical and Explosive Munitions - Locating, Identifying Contaminants, and Planning for Environmental Remediation of Land and Sea Military Ranges and Ordnance Dumpsites*, 2nd ed.; William Andrew: Norwich, NY, USA, 2012.

(71) Sviatenko, L. K.; Kinney, C.; Gorb, L.; Hill, F. C.; Bednar, A. J.; Okovytyy, S.; Leszczynski, J. Comprehensive Investigations of Kinetics of Alkaline Hydrolysis of TNT (2,4,6-Trinitrotoluene), DNT (2,4-Dinitrotoluene), and DNAN (2,4-Dinitroanisole). *Environ. Sci. Technol.* **2014**, *48* (17), 10465–10474.

(72) Schroer, H. W.; Li, X.; Lehmler, H. J.; Just, C. L. Metabolism and Photolysis of 2,4-Dinitroanisole in Arabidopsis. *Environ. Sci. Technol.* **2017**, *51* (23), 13714–13722.

(73) Halasz, A.; Hawari, J.; Perreault, N. N. New Insights into the Photochemical Degradation of the Insensitive Munition Formulation IMX-101 in Water. *Environ. Sci. Technol.* **2018**, *52* (2), 589–596.

(74) Ahn, S. C.; Cha, D. K.; Kim, B. J.; Oh, S.-Y. Detoxification of PAX-21 Ammunitions Wastewater by Zero-Valent Iron for Microbial Reduction of Perchlorate. *J. Hazard. Mater.* **2011**, *192* (2), 909–914.

(75) Hawari, J.; Monteil-Rivera, F.; Perreault, N. N.; Halasz, A.; Paquet, L.; Radovic-Hrapovic, Z.; Deschamps, S.; Thiboutot, S.; Ampleman, G. Environmental Fate of 2,4-Dinitroanisole (DNAN) and Its Reduced Products. *Chemosphere* **2015**, *119*, 16–23.

(76) Klausen, J. J.; Tröber, S. P.; Haderlein, S. B.; Schwarzenbach, R. P.; Troeber, S. P.; Haderlein, S. B.; Schwarzenbach, R. P. Reduction of Substituted Nitrobenzenes by Fe(II) in Aqueous Mineral Suspensions. *Environ. Sci. Technol.* **1995**, *29* (9), 2396–2404.

(77) Elsner, M.; Schwarzenbach, R. P.; Haderlein, S. B. Reactivity of Fe(II)-Bearing Minerals toward Reductive Transformation of Organic Contaminants. *Environ. Sci. Technol.* **2004**, *38* (3), 799–807.

(78) Colón, D.; Weber, E. J.; Anderson, J. L. QSAR Study of the Reduction of Nitroaromatics by Fe(II) Species. *Environ. Sci. Technol.* **2006**, *40* (16), 4976–4982.

(79) Crocker, F. H.; Indest, K. J.; Fredrickson, H. L. Biodegradation of the Cyclic Nitramine Explosives RDX, HMX, and CL-20. *Appl. Microbiol. Biotechnol.* **2006**, *73* (2), 274–290.

(80) Larese-Casanova, P.; Scherer, M. M. Abiotic Transformation of Hexahydro-1,3,5-Triazine (RDX) by Green Rust. *Environ. Sci. Technol.* **2008**, *42* (11), 3795–3981.

(81) Niedźwiecka, J. B.; Drew, S. R.; Schlautman, M. A.; Millerick, K. A.; Grubbs, E.; Tharayil, N.; Finneran, K. T. Iron and Electron Shuttle Mediated (Bio)Degradation of 2,4-Dinitroanisole (DNAN). *Environ. Sci. Technol.* **2017**, *51* (18), 10729–10735.

(82) Olivares, C.; Sierra-Alvarez, R.; Abrell, L.; Chorover, J.; Field, J.; Khatiwada, R. (Bio)Transformation of 2,4-Dinitroanisole (DNAN) in Soils. *J. Hazard. Mater.* **2016**, *304*, 214–221.

(83) Barrows, S. E.; Cramer, C. J.; Truhlar, D. G.; Elovitz, M. S.; Weber, E. J. Factors Controlling Regioselectivity in the Reduction of Polynitroaromatics in Aqueous Solution. *Environ. Sci. Technol.* **1996**, *30* (10), 3028–3038.

(84) Wijker, R. S.; Bolotin, J.; Nishino, S. F.; Spain, J. C.; Hofstetter, T. B.; S. Wijker, R.; Bolotin, J.; F. Nishino, S.; C. Spain, J.; B. Hofstetter, T. Using Compound-Specific Isotope Analysis to Assess Biodegradation of Nitroaromatic Explosives in the Subsurface. *Environ. Sci. Technol.* **2013**, *47* (13), 6872–6883.

(85) Elsner, M. Stable Isotope Fractionation to Investigate Natural Transformation Mechanisms of Organic Contaminants: Principles, Prospects and Limitations. *J. Environ. Monit.* **2010**, *12* (11), 2005–2031.

(86) Elsner, M.; Jochmann, M. A.; Hofstetter, T. B.; Hunkeler, D.; Bernstein, A.; Schmidt, T. C.; Schimmelmann, A. Current Challenges in Compound-Specific Stable Isotope Analysis of Environmental Organic Contaminants. *Anal. Bioanal. Chem.* **2012**, *403* (9), 2471–2491.

(87) Hofstetter, T. B.; Bolotin, J.; Pati, S. G.; Skarpeli-Liati, M.; Spahr, S.; Wijker, R. S. Isotope Effects as New Proxies for Organic Pollutant Transformation. *Chim. Int. J. Chem.* **2014**, *68* (11), 788–792.

(88) Gorski, C. A.; Nurmi, J. T.; Tratnyek, P. G.; Hofstetter, T. B.; Scherer, M. M. Redox Behavior of Magnetite: Implications for Contaminant Reduction. *Environ. Sci. Technol.* **2010**, *44* (1), 55–60.

(89) Tobler, N. B.; Hofstetter, T. B.; Straub, K. L.; Fontana, D.; Schwarzenbach, R. P. Iron-Mediated Microbial Oxidation and Abiotic Reduction of Organic

Contaminants under Anoxic Conditions. *Environ. Sci. Technol.* **2007**, *41* (22), 7765–7772.

(90) Gorski, C. A.; Edwards, R.; Sander, M.; Hofstetter, T. B.; Stewart, S. M. Thermodynamic Characterization of Iron Oxide–Aqueous Fe(II) Redox Couples. *Environ. Sci. Technol.* **2016**, *50* (16), 8538–8547.

(91) Stewart, S. M.; Hofstetter, T. B.; Joshi, P.; Gorski, C. A. Linking Thermodynamics to Pollutant Reduction Kinetics by Fe2+ Bound Toiron Oxides. *Environ. Sci. Technol.* **2018**, *52* (10), 5600–5609.

(92) Daugherty, E. E.; Gilbert, B.; Nico, P. S.; Borch, T. Complexation and Redox Buffering of Iron(II) by Dissolved Organic Matter. *Environ. Sci. Technol.* **2017**, *51* (19), 11096–11104.

(93) Vindedahl, A. M.; Strehlau, J. H.; Arnold, W. A.; Penn, R. L. Organic Matter and Iron Oxide Nanoparticles: Aggregation, Interactions, and Reactivity. *Environ. Sci. Nano* **2016**, *3*, 494–505.

(94) Vindedahl, A. M.; Arnold, W. A.; Penn, R. L. Impact of Pahokee Peat Humic Acid and Buffer Identity on Goethite Aggregation and Reactivity. *Environ. Sci. Nano* **2015**, *2* (5), 509–517.

(95) Vindedahl, A. M.; Stemig, M. S.; Arnold, W. A.; Penn, R. L. Character of Humic Substances as a Predictor for Goethite Nanoparticle Reactivity and Aggregation. *Environ. Sci. Technol.* **2016**, *50* (3), 1200–1208.

(96) Strehlau, J. H.; Stemig, M. S.; Penn, R. L.; Arnold, W. A. Facet-Dependent Oxidative Goethite Growth as a Function of Aqueous Solution Conditions. *Environ. Sci. Technol.* **2016**, *50* (19), 10406–10412.

(97) Chun, C. L.; Penn, R. L.; Arnold, W. A. Kinetic and Microscopic Studies of Reductive Transformations of Organic Contaminants on Goethite. *Environ. Sci. Technol.* **2006**, *40* (10), 3299–3304.

(98) Hofstetter, T. B.; Spain, J. C.; Nishino, S. F.; Bolotin, J.; Schwarzenbach, R. P.; B. Hofstetter, T.; C. Spain, J.; F. Nishino, S.; Bolotin, J.; P. Schwarzenbach, R. Identifying Competing Aerobic Nitrobenzene Biodegradation Pathways by Compound-Specific Isotope Analysis. *Environ. Sci. Technol.* **2008**, *42* (13), 4764–4770.

(99) Wijker, R. S.; Zeyer, J.; Hofstetter, T. B. Isotope Fractionation Associated with the Simultaneous Biodegradation of Multiple Nitrophenol Isomers by Pseudomonas Putida B2. *Environ. Sci. Process. Impacts* **2017**, *19* (5), 775–784.

(100) Butler, E. C.; Hayes, K. F. Effects of Solution Composition and PH on the Reductive Dechlorination of Hexachloroethane by Iron Sulfide. *Environ. Sci. Technol.* **1998**, *32*, 1276–1284.

(101) Anschutz, A. J.; Penn, R. L. Reduction of Crystalline Iron(III) Oxyhydroxides Using Hydroquinone: Influence of Phase and Particle Size. *Geochem. Trans.* **2005**, *6* (3), 60–66.

(102) Schwertmann, U.; Cornell, R. M. Magnetite. In *Iron Oxides in the Laboratory: Preparation and Characterization*; Wiley-VCH Verlag GmbH: Weinheim, Germany, 2000; pp 135–140.

(103) Viollier, E.; Inglett, P. W.; Hunter, K.; Roychoudhury, A. N.; Van Cappellen, P. The Ferrozine Method Revisited: Fe(II)/Fe(III) Determination in Natural Waters. *Appl. Geochemistry* **2000**, *15* (6), 785–790.

(104) Bourdoiseau, J. A.; Jeannin, M.; Rémazeilles, C.; Sabot, R.; Refait, P. The Transformation of Mackinawite into Greigite Studied by Raman Spectroscopy. *J. Raman Spectrosc.* **2011**, *42* (3), 496–504.

(105) Brunauer, S.; Emmett, P. H.; Teller, E. Gases in Multimolecular Layers. *J. Am. Chem. Soc.* **1938**, *60* (1), 309–319.

(106) Berg, M.; Bolotin, J.; Hofstetter, T. B. Compound-Specific Nitrogen and Carbon Isotope Analysis of Nitroaromatic Compounds in Aqueous Samples Using Solid-Phase Microextraction Coupled to GC/IRMS. *Anal. Chem.* **2007**, *79* (6), 2386–2393.

(107) Kremser, A.; Jochmann, M. A.; Schmidt, T. C. PAL SPME Arrow - Evaluation of a Novel Solid-Phase Microextraction Device for Freely Dissolved PAHs in Water. *Anal. Bioanal. Chem.* **2016**, *408* (3), 943–952.

(108) Spahr, S.; Huntscha, S.; Bolotin, J.; Maier, M. P.; Elsner, M.; Hollender, J.; Hofstetter, T. B. Compound-Specific Isotope Analysis of Benzotriazole and Its Derivatives. *Anal. Bioanal. Chem.* **2013**, *405* (9), 2843–2856.

(109) Spahr, S.; Bolotin, J.; Schleucher, J.; Ehlers, I.; von Gunten, U.; Hofstetter, T. B. Compound-Specific Carbon, Nitrogen, and Hydrogen Isotope Analysis of N - Nitrosodimethylamine in Aqueous Solutions. *Anal. Chem.* **2015**, *87* (5), 2916–2924.

(110) Meckenstock, R. U.; Morasch, B.; Griebler, C.; Richnow, H. H. Stable Isotope Fractionation Analysis as a Tool to Monitor Biodegradation in Contaminated Acquifers. *J. Contam. Hydrol.* **2004**, *75* (3–4), 215–255.

(111) Scott, K. M.; Lu, X.; Cavanaugh, C. M.; Liu, J. S. Optimal Methods for Estimating Kinetic Isotope Effects from Different Forms of the Rayleigh Distillation Equation. *Geochim. Cosmochim. Acta* **2004**, *68* (3), 433–442.

(112) Zuman, P.; Shah, B. Addition, Reduction, and Oxidation Reactions of Nitrosobenzene. *Chem. Rev.* **1994**, *94*, 1621–1641.

(113) Wallace, G. C.; Sander, M.; Chin, Y.-P. P.; Arnold, W. A. Quantifying the Electron Donating Capacities of Sulfide and Dissolved Organic Matter in Sediment Pore Waters of Wetlands. *Environ. Sci. Process. Impacts* **2017**, *19* (5), 758–767.

(114) Lan, Y.; Elwood Madden, A. S.; Butler, E. C. Transformation of Mackinawite to Greigite by Trichloroethylene and Tetrachloroethylene. *Environ. Sci. Process. Impacts* **2016**, *18* (10), 1266–1273.

(115) Tobiszewski, M.; Namieśnik, J. Abiotic Degradation of Chlorinated Ethanes and Ethenes in Water. *Environ. Sci. Pollut. Res.* **2012**, *19* (6), 1994–2006.

(116) Hunkeler, D.; Meckenstock, R. U.; Lollar, B. S.; Schmidt, T. C.; Wilson, J. T. *A Guide for Assessing Biodegradation and Source Identification of Organic Ground Water Contaminants Using Compound Specific Isotope Analysis (CSIA)*; Oklahoma, USA, 2008.

(117) Bernstein, A.; Adar, E.; Ronen, Z.; Lowag, H.; Stichler, W.; Meckenstock, R. U. Quantifying RDX Biodegradation in Groundwater Using Δ15N Isotope Analysis. *J. Contam. Hydrol.* **2010**, *111*, 25–35.

(118) Van Breukelen, B. M. Extending the Rayleigh Equation to Allow Competing Isotope Fractionating Pathways to Improve Quantification of Biodegradation. *Environ. Sci. Technol.* **2007**, *41* (11), 4004–4010.

(119) Tobler, N. B.; Hofstetter, T. B. Carbon and Hydrogenisotope Toluene Oxidation by Geobacter Metallireducens with Different Fe(III) Phases as Terminal Electron Acceptors. *Environ. Sci. Technol.* **2008**, *42* (21), 7786–7792.

(120) Pati, S. G.; Kohler, H. P. E.; Bolotin, J.; Parales, R. E.; Hofstetter, T. B. Isotope Effects of Enzymatic Dioxygenation of Nitrobenzene and 2-Nitrotoluene by Nitrobenzene Dioxygenase. *Environ. Sci. Technol.* **2014**, *48* (18), 10750–10759.

(121) Wijker, R. S.; Pati, S. G.; Zeyer, J.; Hofstetter, T. B. Enzyme Kinetics of Different Types of Flavin-Dependent Monooxygenases Determine the Observable Contaminant Stable Isotope Fractionation. *Environ. Sci. Technol. Lett.* **2015**, *2* (11), 329–334.

(122) Pati, S. G.; Kohler, H.-P. E.; Pabis, A.; Paneth, P.; Parales, R. E.; Hofstetter, T. B. Substrate and Enzyme Specificity of the Kinetic Isotope Effects Associated with the Dioxygenation of Nitroaromatic Contaminants. *Environ. Sci. Technol.* **2016**, *50* (13), 6708–6716.

(123) Mancini, S. A.; Hirschorn, S. K.; Elsner, M.; Lacrampe-Couloume, G.; Sleep, B. E.; Edwards, E. A.; Sherwood Lollar, B. Effects of Trace Element Concentration on Enzyme Controlled Stable Isotope Fractionation during Aerobic Biodegradation of Toluene. *Environ. Sci. Technol.* **2006**, *40* (24), 7675–7681.

(124) Ferrey, M. L.; Wilkin, R. T.; Ford, R. G.; Wilson, J. T. Nonbiological Removal of Cis-Dichloroethylene and 1,1-Dichloroethylene in Aquifer Sediment Containing Magnetite. *Environ. Sci. Technol.* **2004**, *38* (6), 1746–1752.

(125) Hofstetter, T. B.; Neumann, A.; Schwarzenbach, R. P. Reduction of Nitroaromatic Compounds by Fe (II) Species Associated with Iron-Rich Smectites. *Environ. Sci. Technol.* **2006**, *40* (1), 235–242.

(126) Hofstetter, T. B.; Schwarzenbach, R. P.; Haderlein, S. B. Reactivity of Fe(II) Species Associated with Clay Minerals. *Environ. Sci. Technol.* **2003**, *37* (3), 519–528.

(127) Schaefer, C. E.; Ho, P.; Berns, E.; Werth, C. Mechanisms for Abiotic Dechlorination of Trichloroethene by Ferrous Minerals under Oxic and Anoxic Conditions in Natural Sediments. *Environ. Sci. Technol.* **2018**, *52* (23), 13747–13755.

(128) Simpanen, S.; Dahl, M.; Gerlach, M.; Mikkonen, A.; Malk, V.; Mikola, J.; Romantschuk, M. Biostimulation Proved to Be the Most Efficient Method in the Comparison of in Situ Soil Remediation Treatments after a Simulated Oil Spill Accident. *Environ. Sci. Pollut. Res.* **2016**, *23* (24), 25024–25038.

(129) McGuire, T. M.; Adamson, D. T.; Burcham, M. S.; Bedient, P. B.; Newell, C. J. Evaluation of Long-Term Performance and Sustained Treatment at Enhanced Anaerobic Bioremediation Sites. *Groundw. Monit. Remediat.* **2016**, *36* (2), 32–44.

(130) Wu, Y.-J.; Liu, P.-W. G.; Hsu, Y.-S.; Whang, L.-M.; Lin, T.-F.; Hung, W.-N.; Cho, K.-C. Application of Molecular Biological Tools for Monitoring Efficiency of Trichloroethylene Remediation. *Chemosphere* **2019**, *233*, 697–704.

(131) Schaefer, C. E.; Lavorgna, G. M.; Haluska, A. A.; Annable, M. D. Long-Term Impacts on Groundwater and Reductive Dechlorination Following Bioremediation in a Highly Characterized Trichloroethene DNAPL Source Area. *Groundw. Monit. Remediat.* **2018**, *38* (3), 65–74.

(132) Amonette, J. E.; Szecsody, J. E.; Schaef, H. T.; Templeton, J. C.; Gorby, Y. A.; Fruchter, J. S. *Abiotic Reduction of Aquifer Materials by Dithionite: A Promising in-Situ Remediation Technology*; Richland, WA, USA, 1994.

(133) Fruchter, J. S. J. S.; Cole, C. R. C. R.; Williams, M. D. M. D.; Vermeul, V. R.; Amonette, J. E. J. E.; Szecsody, J. E.; Istok, J. D.; Humphrey, M. D. Creation of a Subsurface Permeable Treatment Zone for Aqueous Chromate Contamination Using In Situ Redox Manipulation. *Groundw. Monit. Remediat.* **2000**, *20* (2), 66–77.

(134) Graham, M. C.; Farmer, J. G.; Anderson, P.; Paterson, E.; Hillier, S.; Lumsdon, D. G.; Bewley, R. J. F. Calcium Polysulfide Remediation of Hexavalent Chromium Contamination from Chromite Ore Processing Residue. *Sci. Total Environ.* **2006**, *364* (1–3), 32–44.

(135) Fan, D.; O'Brien Johnson, G.; G. Tratnyek, P.; L. Johnson, R. Sulfidation of Nano Zerovalent Iron (NZVI) for Improved Selectivity During In-Situ Chemical Reduction (ISCR). *Environ. Sci. Technol.* **2016**, *50* (17), 9558–9565.

(136) Han, Y.; Yan, W. Reductive Dechlorination of Trichloroethene by Zero-Valent Iron Nanoparticles: Reactivity Enhancement through Sulfidation Treatment. *Environ. Sci. Technol.* **2016**, *50* (23), 12992–13001.

(137) D. Ludwig, R.; Su, C.; R. Lee, T.; T. Wilkin, R.; D. Acree, S.; R. Ross, R.; Keeley, A. In Situ Chemical Reduction of Cr(VI) in Groundwater Using a Combination of Ferrous Sulfate and Sodium Dithionite: A Field Investigation. *Environ. Sci. Technol.* **2007**, *41* (15), 5299–5305.

(138) Dresel, P. E.; Wellman, D. M.; Cantrell, K. J.; Truex, M. T. Review: Technical and Policy Challenges in Deep Vadose Zone Remediation of Metals and Radionuclides. *Environ. Sci. Technol.* **2011**, *45* (10), 4207–4216.

(139) Szecsody, J. E.; Fruchter, J. S.; Williams, M. D.; Vermeul, V. R.; Sklarew, D. In Situ Chemical Reduction of Aquifer Sediments: Enhancement of Reactive Iron

Phases and TCE Dechlorination. *Environ. Sci. Technol.* **2004**, *38* (17), 4656–4663.

(140) McKelvie, J. R.; Mackay, D. M.; de Sieyes, N. R.; Lacrampe-Couloume, G.; Sherwood Lollar, B. Quantifying MTBE Biodegradation in the Vandenberg Air Force Base Ethanol Release Study Using Stable Carbon Isotopes. *J. Contam. Hydrol.* **2007**, *94* (3–4), 157–165.

(141) Chartrand, M.; Passeport, E.; Rose, C.; Lacrampe-Couloume, G.; Bidleman, T. F.; Jantunen, L. M.; Sherwood Lollar, B. Compound Specific Isotope Analysis of Hexachlorocyclohexane Isomers: A Method for Source Fingerprinting and Field Investigation of in Situ Biodegradation. *Rapid Commun. Mass Spectrom.* **2015**, *29* (6), 505–514.

(142) Bosma, T. N. P.; Middeldorp, P. J. M.; Schraa, G.; Zehnder, A. J. B. Mass Transfer Limitation of Biotransformation: Quantifying Bioavailability. *Environ. Sci. Technol.* **1997**, *31* (1), 248–252.

(143) Torrent, J.; Schwertmann, U.; Barron, V. The Reductive Dissolution of Synthetic Goethite and Hematite in Dithionite. *Clay Miner.* **1987**, *22* (3), 329–337.

(144) Yang, L.; I. Steefel, C.; A. Marcus, M.; R. Bargar, J. Kinetics of Fe(II)-Catalyzed Transformation of 6-Line Ferrihydrite under Anaerobic Flow Conditions. *Environ. Sci. Technol.* **2010**, *44* (14), 5469–5475.

(145) Amstaetter, K.; Borch, T.; Larese-Casanova, P.; Kappler, A. Redox Transformation of Arsenic by Fe(II)-Activated Goethite (α-FeOOH). *Environ. Sci. Technol.* **2009**, *44* (1), 102–108.

(146) Sherwood Lollar, B.; Slater, G. F.; Sleep, B.; Witt, M.; Klecka, G. M.; Harkness, M.; Spivack, J. Stable Carbon Isotope Evidence for Intrinsic Bioremediation of Tetrachloroethene and Trichloroethene at Area 6, Dover Air Force Base. *Environ. Sci. Technol.* **2000**, *35* (2), 261–269.

(147) Thullner, M.; Richnow, H. H.; Fischer, A. Characterization and Quantification of in Situ Biodegradation of Groundwater Contaminants Using Stable Isotope Fractionation Analysis: Advantages and Limitations. In *Environmental and Regional Air Pollution*; Nova Science Publishers, 2009.

(148) Alvarez-Zaldívar, P.; Centler, F.; Maier, U.; Thullner, M.; Imfeld, G. Biogeochemical Modelling of in Situ Biodegradation and Stable Isotope Fractionation of Intermediate Chloroethenes in a Horizontal Subsurface Flow Wetland. *Ecol. Eng.* **2016**, *90*, 170–179.

(149) Schmidt, T. C.; Zwank, L.; Elsner, M.; Berg, M.; Meckenstock, R. U.; Haderlein, S. B. Compound-Specific Stable Isotope Analysis of Organic Contaminants in Natural Environments: A Critical Review of the State of the Art, Prospects, and Future Challenges. *Anal. Bioanal. Chem.* **2004**, *378* (2), 283–300.

(150) Sherwood Lollar, B.; Slater, G.; Ahad, J.; Sleep, B.; Spivack, J.; Brennan, M.; MacKenzie, P. Contrasting Carbon Isotope Fractionation during Biodegradation or Trichloroethylene and Toluene: Implications for Intrinsic Bioremediation. *Org. Geochem.* **1999**, *30*, 813–820.

(151) Aeppli, C.; B. Hofstetter, T.; I. F. Amaral, H.; Kipfer, R.; P. Schwarzenbach, R.; Berg, M. Quantifying In Situ Transformation Rates of Chlorinated Ethenes by Combining Compound-Specific Stable Isotope Analysis, Groundwater Dating, And Carbon Isotope Mass Balances. *Environ. Sci. Technol.* **2010**, *44* (10), 3705–3711.

(152) Berens, M. J.; Ulrich, B. A.; Strehlau, J. H.; Hofstetter, T. B.; Arnold, W. A. Mineral Identity, Natural Organic Matter, and Repeated Contaminant Exposures Do Not Affect the Carbon and Nitrogen Isotope Fractionation of 2,4-Dinitroanisole during Abiotic Reduction. *Environ. Sci. Process. Impacts* **2018**, *21*, 51–62.

(153) Boparai, H. K.; Comfort, S. D.; Shea, P. J.; Szecsody, J. E. Remediating Explosive-Contaminated Groundwater by in Situ Redox Manipulation (ISRM) of Aquifer Sediments. *Chemosphere* **2008**, *71* (5), 933–941.

(154) He, F.; Zhao, D.; Paul, C. Field Assessment of Carboxymethyl Cellulose Stabilized Iron Nanoparticles for in Situ Destruction of Chlorinated Solvents in Source Zones. *Water Res.* **2010**, *44* (7), 2360–2370.

(155) Istok, J. D.; Amonette, J. E.; Cole, C. R.; Fruchter, J. S.; Humphrey, M. D.; Szecsody, J. E.; Teel, S. S.; Vermeul, V. R.; Williams, M. D.; Yabusaki, S. B. In Situ Redox Manipulation by Dithionite Injection: Intermediate-Scale Laboratory Experiments. *Ground Water* **1999**, *37*, 884–889.

(156) Hocking, G.; Givens, M. A.; Thurman, C. M.; Lacko, C. M. Installation of Permeable Reactive Barrier at Tinker Air Force Base, Oklahoma City, Oklahoma. In *5th International Conference on Remediation of Chlorinated and Recalcitrant Compounds*; Monterey, CA, 2006.

(157) Voelz, J.; Arnold, W. A.; Penn, R. L. Redox-Induced Nucleation and Growth of Goethite on Synthetic Hematite Nanoparticles. *Am. Mineral.* **2018**, *103*, 1021–1029.

(158) Strehlau, J. H.; Berens, M. J.; Arnold, W. A. Mineralogy and Buffer Identity Effects on RDX Kinetics and Intermediates during Reaction with Natural and Synthetic Magnetite. *Chemosphere* **2018**, *213*, 602–609.

(159) Cornell, R. M.; Giovanoli, R. Acid Dissolution of Hematites of Different Morphologies. *Clay Miner.* **1993**, *28* (2), 223–232.

(160) Cornell, R. M.; Giovanoli, R. Acid Dissolution of Akaganeite and Lepidocrocite: The Effect on Crystal Morphology. *Clays Clay Miner.* **1988**, *36* (5), 385–390.

(161) Sumner, M. E.; Miller, W. P. Cation Exchange Capacity and Exchange Coefficients. In *Methods of Soil Analysis Part 3 - Chemical Methods*; 1996; pp 1201–1229.

(162) Schimmelmann, A.; Albertino, A.; Sauer, P. E.; Qi, H.; Molinie, R.; Mesnard, F. Nicotine, Acetanilide and Urea Multi-Level 2H-, 13C- and 15N-Abundance Reference Materials for Continuous-Flow Isotope Ratio Mass Spectrometry. *Rapid Commun. Mass Spectrom.* **2009**, *23* (22), 3513–3521.

(163) Ojeda, A. S.; Phillips, E.; Mancini, S. A.; Sherwood Lollar, B. Sources of Uncertainty in Biotransformation Mechanistic Interpretations and Remediation Studies Using CSIA. *Anal. Chem.* **2019**, *91* (14), 9147–9153.

(164) G. B. Williams, A.; M. Scherer, M. Spectroscopic Evidence for Fe(II)−Fe(III) Electron Transfer at the Iron Oxide−Water Interface. *Environ. Sci. Technol.* **2004**, *38* (18), 4782–4790.

(165) Amonette, J. E.; Workman, D. J.; Kennedy, D. W.; Fruchter, J. S.; Gorby, Y. A. Dechlorination of Carbon Tetrachloride by Fe(II) Associated with Goethite. *Environ. Sci. Technol.* **2000**, *34* (21), 4606–4613.

(166) Fan, D.; J. Bradley, M.; W. Hinkle, A.; L. Johnson, R.; G. Tratnyek, P. Chemical Reactivity Probes for Assessing Abiotic Natural Attenuation by Reducing Iron Minerals. *Environ. Sci. Technol.* **2016**, *50* (4), 1868–1876.

(167) Voelz, J. L.; Johnson, N. W.; Chun, C. L.; Arnold, W. A.; Penn, R. L. Quantitative Dissolution of Environmentally Accessible Iron Residing in Iron-Rich Minerals: A Review. *ACS Earth Sp. Chem.* **2019**, *3* (8), 1371–1392.

(168) Essington, M. E. *Soil and Water Chemistry: An Integrative Approach*, 2nd ed.; CRC Press, 2015.

(169) Guo, H.; Barnard, A. S. Naturally Occurring Iron Oxide Nanoparticles: Morphology, Surface Chemistry and Environmental Stability. *J. Mater. Chem. A* **2013**, *1* (January 2013), 27–42.

(170) Schwertmann, U.; Cornell, R. M. *Iron Oxides in the Laboratory: Preparation and Characterization*, 2nd ed.; Wiley-VCH: Weinheim, 2000.

(171) Strehlau, J. H.; Toner, B. M.; Arnold, W. A.; Penn, R. L. Accessible Reactive Surface Area and Abiotic Redox Reactivity of Iron Oxyhydroxides in Acidic Brines. *Geochim. Cosmochim. Acta* **2017**, *197*, 345–355.

(172) James, B. R.; Brose, D. A. Oxidation-Reduction Phenomena. In *Handbook of Soil Science: Properties and Processes*; CRC Press: Boca Raton, FL, 2012; pp 14-1-14–24.

(173) Gorski, C. A.; Scherer, M. M. Influence of Magnetite Stoichiometry on FeII Uptake and Nitrobenzene Reduction. *Environ. Sci. Technol.* **2009**, *43* (10), 3675–3680.

(174) Haggstrom, L.; Annersten, H.; Ericsson, T.; Wappling, R.; Karner, W.; Bjarman, S. Magnetic Dipolar and Electric Quadrupolar Effects on the Mossbauer Spectra of Magnetite above the Verwey Transition. *Hyperfine Interact.* **1977**, *5* (1), 201–214.

(175) Vandenberghe, R. E.; Hus, J. J.; De Grave, E. Evidence from Mössbauer Spectroscopy of Neo-Formation of Magnetite/Maghemite in the Soils of Loess/Paleosol Sequences in China. *Hyperfine Interact.* **1998**, *117* (1/4), 359–369.

(176) Wehrli, B.; Sulzberger, B.; Stumm, W. Redox Processes Catalyzed by Hydrous Oxide Surfaces. *Chem. Geol.* **1989**, *78* (3–4), 167–179.

(177) Torrent, J.; Barron, V. Iron Oxides in Relation to the Colour of Mediterranean Soils. In *Applied Study of Cultural Heritage and Clays*; 2003; pp 377–386.

(178) Lovley, D. R.; Coates, J. D.; Blunt-Harris, E. L.; Phillips, E. J. P.; Woodward, J. C. Humic Substances as Electron Acceptors for Microbial Respiration. *Nature* **1996**, *382*, 445–448.

(179) Scott, D. T.; McKnight, D. M.; Blunt-Harris, E. L.; Kolesar, S. E.; Lovley, D. R. Quinone Moieties Act as Electron Acceptors in the Reduction of Humic Substances by Humics-Reducing Microorganisms. *Environ. Sci. Technol.* **1998**, *32* (19), 2984–2989.

(180) Lovley, D. R.; Fraga, J. L.; Coates, J. D.; Blunt-Harris, E. L. Humics as an Electron Donor for Anaerobic Respiration. *Environ. Microbiol.* **1999**, *1* (1), 89–98.

(181) Ratasuk, N.; A. Nanny, M. Characterization and Quantification of Reversible Redox Sites in Humic Substances. *Environ. Sci. Technol.* **2007**, *41* (22), 7844–7850.

(182) Dunnivant, F. M.; Schwarzenbach, R. P.; Macalady, D. L. Reduction of Substituted Nitrobenzenes in Aqueous Solutions Containing Natural Organic Matter. *Environ. Sci. Technol.* **1992**, *26* (11), 2133–2141.

(183) Deiana, S.; Gessa, C.; Manunza, B.; Rausa, R.; Solinas, V. Iron(III) Reduction by Natural Humic Acids: A Potentiometric and Spectroscopic Study. *Eur. J. Soil Sci.* **1995**, *46* (1), 103–108.

(184) Beyer, M. E.; Bond, A. M.; McLaughlin, R. J. W. Simultaneous Polarographic Determination of Ferrous, Ferric, and Total Iron in Standard Rocks. *Anal. Chem.* **2002**, *47* (3), 479–482.

(185) Haese, R. R.; Wallmann, K.; Dahmke, A.; Kretzmann, U.; Müller, P. J.; Schulz, H. D. Iron Species Determination to Investigate Early Diagenetic Reactivity in Marine Sediments. *Geochim. Cosmochim. Acta* **1997**, *61* (1), 63–72.

(186) Neumann, A.; Hofstetter, T. B.; Lüssi, M.; Cirpka, O. A.; Petit, S.; Schwarzenbach, R. P.; B. Hofstetter, T.; Lüssi, M.; A. Cirpka, O.; Petit, S.; et al. Assessing the Redox Reactivity of Structural Iron in Smectites Using Nitroaromatic Compounds As Kinetic Probes. *Environ. Sci. Technol.* **2008**, *42* (22), 8381–8387.

(187) Erickson, A. J.; Gulliver, J. S.; Arnold, W. A.; Brekke, C.; Bredal, M. Abiotic Capture of Stormwater Nitrates with Granular Activated Carbon. *Environ. Eng. Sci.* **2016**, *33* (5), 354–363.

(188) Simon, R.; Colón, D.; L. Tebes-Stevens, C.; J. Weber, E. Effect of Redox Zonation on the Reductive Transformation of P-Cyanonitrobenzene in a Laboratory Sediment Column. *Environ. Sci. Technol.* **2000**, *34* (17), 3617–3622.

(189) Freeze, R. A.; Cherry, J. A. *Groundwater*, 1st ed.; Prentice Hall, 1979.

(190) Gulliver, J. S. *Introduction to Chemical Transport in the Environment*; Cambridge University Press: Cambridge, 2007.

(191) Haderlein, S. B.; Weissmahr, K. W.; Schwarzenbach, R. P. Specific Adsorption of Nitroaromatic Explosives and Pesticides to Clay Minerals. *Environ. Sci. Technol.* **1996**, *30* (2), 612–622.

(192) Arthur, J. D.; Mark, N. W.; Taylor, S.; Šimunek, J.; Brusseau, M. L.; Dontsova, K. M. Batch Soil Adsorption and Column Transport Studies of 2,4-Dinitroanisole (DNAN) in Soils. *J. Contam. Hydrol.* **2017**, *199*, 14–23.

(193) B. Haderlein, S.; P. Schwarzenbach, R. Adsorption of Substituted Nitrobenzenes and Nitrophenols to Mineral Surfaces. *Environ. Sci. Technol.* **1993**, *27* (2), 316–326.

(194) Abe, Y.; Hunkeler, D. Does the Rayleigh Equation Apply to Evaluate Field Isotope Data in Contaminant Hydrogeology? *Environ. Sci. Technol.* **2006**, *40* (5), 1588–1596.

(195) Thullner, M.; Centler, F.; Richnow, H. H.; Fischer, A. Quantification of Organic Pollutant Degradation in Contaminated Aquifers Using Compound Specific Stable Isotope Analysis - Review of Recent Developments. *Org. Geochem.* **2012**, *42* (12), 1440–1460.

(196) Chiogna, G.; Eberhardt, C.; Grathwohl, P.; A. Cirpka, O.; Rolle, M. Evidence of Compound-Dependent Hydrodynamic and Mechanical Transverse Dispersion by Multitracer Laboratory Experiments. *Environ. Sci. Technol.* **2009**, *44* (2), 688–693.

(197) Fischer, A.; Theuerkorn, K.; Stelzer, N.; Gehre, M.; Thullner, M.; H. Richnow, H. Applicability of Stable Isotope Fractionation Analysis for the Characterization of Benzene Biodegradation in a BTEX-Contaminated Aquifer. *Environ. Sci. Technol.* **2007**, *41* (10), 3689–3696.

(198) Thullner, M.; Fischer, A.; Richnow, H. H.; Wick, L. Y. Influence of Mass Transfer on Stable Isotope Fractionation. *Applied Microbiology and Biotechnology*. Springer January 11, 2013, pp 441–452.

(199) Tsitonaki, A.; Petri, B.; Crimi, M.; Mosbk, H.; Siegrist, R. L.; Bjerg, P. L. In Situ Chemical Oxidation of Contaminated Soil and Groundwater Using Persulfate: A Review. *Crit. Rev. Environ. Sci. Technol.* **2010**, *40* (1), 55–91.

(200) Sheets, L. P.; Li, A. A.; Minnema, D. J.; Collier, R. H.; Creek, M. R.; Peffer, R. C. A Critical Review of Neonicotinoid Insecticides for Developmental Neurotoxicity. *Crit. Rev. Toxicol.* **2016**, *46* (2), 153–190.

(201) Buszewski, B.; Bukowska, M.; Ligor, M.; Staneczko-Baranowska, I. A Holistic Study of Neonicotinoids Neuroactive Insecticides—Properties, Applications, Occurrence, and Analysis. *Environ. Sci. Pollut. Res.* **2019**, *26*, 34723–34740.

(202) Minnesota Department of Agriculture, *Review of Neonicotinoid Use, Registration, and Insect Pollinator Impacts in Minnesota*; St. Paul, MN, 2016.

(203) Matsuda, K.; Buckingham, S. D.; Kleier, D.; Rauh, J. J.; Grauso, M.; Sattelle, D. B.; Buckingham, S. D. Neonicotinoids: Insecticides Acting on Insect Nicotinic Acetylcholine Receptors. *Trends Pharmacol. Sci.* **2001**, *22* (11), 573–580.

(204) Tomizawa, M.; Casida, J. E. Neonicotinoid Insecticide Toxicology: Mechanisms of Selective Action. *Annu. Rev. Pharmacol. Toxicol.* **2005**, *45*, 247–268.

(205) Schaafsma, A.; Limay-Rios, V.; Xue, Y.; Smith, J.; Baute, T. Field-Scale Examination of Neonicotinoid Insecticide Persistence in Soil as a Result of Seed Treatment Use in Commercial Maize (Corn) Fields in Southwestern Ontario. *Environ. Toxicol. Chem.* **2016**, *35* (2), 295–302.

(206) Todey, S. A.; Fallon, A. M.; Arnold, W. A. Neonicotinoid Insecticide Hydrolysis and Photolysis: Rates and Residual Toxicity. *Environ. Toxicol. Chem.* **2018**, *37* (11), 2797–2809.

(207) Hladik, M. L.; Bradbury, S.; Schulte, L. A.; Helmers, M.; Witte, C.; Kolpin, D. W.; Garrett, J. D.; Harris, M. Neonicotinoid Insecticide Removal by Prairie Strips in Row-Cropped Watersheds with Historical Seed Coating Use. *Agric. Ecosyst. Environ.* **2017**, *241*, 160–167.

(208) Morrissey, C. A.; Mineau, P.; Devries, J. H.; Sanchez-Bayo, F.; Liess, M.; Cavallaro, M. C.; Liber, K. Neonicotinoid Contamination of Global Surface Waters and Associated Risk to Aquatic Invertebrates: A Review. *Environ. Int.* **2015**, *74*, 291–303.

(209) Main, A. R.; Headley, J. V.; Peru, K. M.; Michel, N. L.; Cessna, A. J.; Morrissey, C. A. Widespread Use and Frequent Detection of Neonicotinoid Insecticides in Wetlands of Canada's Prairie Pothole Region. *PLoS One* **2014**, *9* (3), 1–12.

(210) Sánchez-Bayo, F.; Hyne, R. V. Detection and Analysis of Neonicotinoids in River Waters - Development of a Passive Sampler for Three Commonly Used Insecticides. *Chemosphere* **2014**, *99*, 143–151.

(211) Deneer, J. W. Toxicity of Mixtures of Pesticides in Aquatic Systems. *Pest Manag. Sci.* **2000**, *56* (6), 516–520.

(212) Warne, M. S. J.; Hawker, D. W. The Number of Components in a Mixture Determines Whether Synergistic and Antagonistic or Additive Toxicity Predominate: The Funnel Hypothesis. *Ecotoxicology and Environmental Safety*. 1995, pp 23–28.

(213) Schulz, R. Field Studies on Exposure, Effects, and Risk Mitigation of Aquatic Nonpoint-Source Insecticide Pollution: A Review. *J. Environ. Qual.* **2004**, *33* (2), 419–448.

(214) Schäfer, R. B.; Carsten von der Ohe, P.; Rasmussen, J.; J. Kefford, B.; Beketov, M. A.; Schulz, R.; Liess, M. Thresholds for the Effects of Pesticides on Invertebrate Communities and Leaf Breakdown in Stream Ecosystems. *Environ. Sci. Technol.* **2012**, *46* (9), 5134–5142.

(215) U.S. Environmental Protection Agency, ECOTOX knowledgebase version 5 https://cfpub.epa.gov/ecotox/ (accessed Feb 4, 2020).

(216) Gibbons, D.; Morrissey, C.; Mineau, P. A Review of the Direct and Indirect Effects of Neonicotinoids and Fipronil on Vertebrate Wildlife. *Environ. Sci. Pollut. Res. Int.* **2015**, *22* (1), 103–118.

(217) U.S. Census Bureau, State Area Measurements and Internal Point Coordinates https://www.census.gov/geographies/reference-files/2010/geo/state-area.html (accessed Nov 3, 2020).

(218) Wieben, C. M. Estimated Annual Agricultural Pesticide Use for Counties of the Conterminous United States, 2013-2017: U.S. Geological Survey Data Release. **2019**.

(219) U.S. Department of Agriculture, National Agricultural Statistics Service report https://www.nass.usda.gov/index.php (accessed Dec 3, 2020).

(220) U.S. Environmental Protection Agency. *Definition and Procedure for the Determination of the Method Detection Limit, Revision 2*; 2016.

(221) Yang, L.; Jin, S.; Danielson, P.; Homer, C.; Gass, L.; Bender, S. M.; Case, A.; Costello, C.; Dewitz, J.; Fry, J.; et al. A New Generation of the United States National Land Cover Database: Requirements, Research Priorities, Design, and Implementation Strategies. *ISPRS J. Photogramm. Remote Sens.* **2018**, *146*, 108–123.

(222) Nowell, L. H.; Norman, J. E.; Moran, P. W.; Martin, J. D.; Stone, W. W. Pesticide Toxicity Index-a Tool for Assessing Potential Toxicity of Pesticide Mixtures to Freshwater Aquatic Organisms. *Sci. Total Environ.* **2014**, *476–477*, 144–157.

(223) U.S. Environmental Protection Agency, Office of Pesticide Programs https://www.epa.gov/pesticides (accessed Jan 5, 2020).

(224) Wolfram, J.; Stehle, S.; Bub, S.; Petschick, L. L.; Schulz, R. Insecticide Risk in US Surface Waters: Drivers and Spatiotemporal Modeling. *Environ. Sci. Technol.* **2019**, *53* (20), 12071–12080.

(225) Stehle, S.; Schulz, R. Agricultural Insecticides Threaten Surface Waters at the Global Scale. In *Natural Academy of Sciences of the United States of America*; 2015; pp 5750–5755.

(226) Spycher, S.; Mangold, S.; Doppler, T.; Junghans, M.; Wittmer, I.; Stamm, C.; Singer, H. Pesticide Risks in Small Streams—How to Get as Close as Possible to the Stress Imposed on Aquatic Organisms. *Environ. Sci. Technol.* **2018**, *52* (8), 4526–4535.

(227) Stehle, S.; Knäbel, A.; Schulz, R. Probabilistic Risk Assessment of Insecticide Concentrations in Agricultural Surface Waters: A Critical Appraisal. *Environ. Monit. Assess.* **2013**, *185* (8), 6295–6310.

(228) U.S. Geological Survey, Current Conditions for the Nation https://waterdata.usgs.gov/nwis/uv?

(229) National Oceanic and Atmospheric Administration, NOWData - NOAA Online Weather Data https://w2.weather.gov/climate/xmacis.php?wfo=mpx (accessed Jan 6, 2020).

(230) Hladik, M. L.; Main, A. R.; Goulson, D. Environmental Risks and Challenges Associated with Neonicotinoid Insecticides. *Environ. Sci. Technol.* **2018**, *52*, 3329–3335.

(231) Barry, J.; Miller, T.; Steenberg, J.; Runkel, A.; Kuehner, K.; Alexander, E. C. Combining High Resolution Spring Monitoring, Dye Tracing, Watershed Analysis, and Outcrop and Borehole Observations to Characterize the Galena Karst, Southeast Minnesota, USA. In *16th Sinkhole Conference*; University of South Florida Libraries, 2020.

(232) Nauen, R.; Ebbinghaus-Kintscher, U.; Salgado, V. L.; Kaussmann, M. Thiamethoxam Is a Neonicotinoid Precursor Converted to Clothianidin in Insects and Plants. *Pestic. Biochem. Physiol.* **2003**, *76* (2), 55–69.

(233) Sánchez-Bayo, F. The Trouble with Neonicotinoids. *Science Magazine*. 2014, pp 806–807.

(234) Nuyttens, D.; Devarrewaere, W.; Verboven, P.; Foqué, D. Pesticide-Laden Dust Emission and Drift from Treated Seeds during Seed Drilling: A Review. *Pest Manag. Sci.* **2013**, *69* (5), 564–575.

(235) Steenberg, J. R. *C-50, Geologic Atlas of Dodge County, Minnesota*; 2019.

(236) Thurman, E. M.; Goolsby, D. A.; Meyer, M. T.; Mills, M. S.; Pomes, M. L.; Kolpin, D. W. A Reconnaissance Study of Herbicides and Their Metabolites in Surface Water of the Midwestern United States Using Immunoassay and Gas Chromatography/Mass Spectrometry. *Environ. Sci. Technol.* **2002**, *26* (12), 2440–2447.

(237) Hladik, M. L.; Corsi, S. R.; Kolpin, D. W.; Baldwin, A. K.; Blackwell, B. R.; Cavallin, J. E. Year-Round Presence of Neonicotinoid Insecticides in Tributaries to the Great Lakes, USA. *Environ. Pollut.* **2018**, *235*, 1022–1029.

(238) National Weather Service, Twin Cities Forecast Office https://www.weather.gov/mpx/ (accessed Jan 6, 2020).

(239) Schepker, T. J.; Webb, E. B.; Tillitt, D.; LaGrange, T. Neonicotinoid Insecticide Concentrations in Agricultural Wetlands and Associations with Aquatic Invertebrate Communities. *Agric. Ecosyst. Environ.* **2020**, *287*, 106678.

(240) Cavallaro, M. C.; Liber, K.; Headley, J. V.; Peru, K. M.; Morrissey, C. A. Community-Level and Phenological Responses of Emerging Aquatic Insects Exposed to 3 Neonicotinoid Insecticides: An in Situ Wetland Limnocorral Approach. *Environ. Toxicol. Chem.* **2018**, *37* (9), 2401–2412.

(241) Sadaria, A. M.; Supowit, S. D.; Halden, R. U. Mass Balance Assessment for Six Neonicotinoid Insecticides during Conventional Wastewater and Wetland Treatment: Nationwide Reconnaissance in United States Wastewater. *Environ. Sci. Technol.* **2016**, *50* (12), 6199–6206.

(242) Hope, B. K.; Pillsbury, L.; Boling, B. A State-Wide Survey in Oregon (USA) of Trace Metals and Organic Chemicals in Municipal Effluent. *Sci. Total Environ.* **2012**, *417–418*, 263–272.

(243) Qi, W.; Singer, H.; Berg, M.; Müller, B.; Pernet-Coudrier, B.; Liu, H.; Qu, J. Elimination of Polar Micropollutants and Anthropogenic Markers by Wastewater Treatment in Beijing, China. *Chemosphere* **2015**, *119*, 1054–1061.

(244) Heeb, F.; Singer, H.; Pernet-Coudrier, B.; Qi, W.; Liu, H.; Longrée, P.; Müller, B.; Berg, M. Organic Micropollutants in Rivers Downstream of the Megacity Beijing: Sources and Mass Fluxes in a Large-Scale Wastewater Irrigation System. *Environ. Sci. Technol.* **2012**, *46* (16), 8680–8688.

(245) Campo, J.; Masia, A.; Blasco, C.; Pico, Y. Occurrence and Removal Efficiency of Pesticides in Sewage Treatment Plants of Four Mediterranean River Basins. *J. Hazard. Mater.* **2013**, *263*, 146–157.

(246) Masia, A.; Campo, J.; Vazques-Roig, P.; Blasco, C.; Pico, Y. Screening of Currently Used Pesticides in Water, Sediments and Biota of the Guadalquivir River Basin (Spain). *J. Hazard. Mater.* **2013**, *263* (1), 95–104.

(247) Chen, M.; Tao, L.; McLean, J.; Lu, C. Quantitative Analysis of Neonicotinoid Insecticide Residues in Foods: Implication for Dietary Exposures. *J. Agric. Food Chem.* **2014**, *62* (26), 6082–6090.

(248) Lu, C.; Chang, C.-H.; Palmer, C.; Zhao, M.; Zhang, Q. Neonicotinoid Residues in Fruits and Vegetables: An Integrated Dietary Exposure Assessment Approach. *Environ. Sci. Technol.* **2018**, *52* (5), 3175–3184.

(249) Craig, M. S.; Gupta, R. C.; Candery, T. D.; Britton, D. A. Human Exposure to Imidacloprid from Dogs Treated with Advantage®. *Toxicol. Mech. Methods* **2005**, *15* (4), 287–291.

(250) Melander, L.; Saunders, W. H. *Reaction Rates of Isotopic Molecules*; John Wiley & Sons: New York, 1980.

(251) Kreft, A.; Zuber, A. On the Physical Meaning of the Dispersion Equation and Its Solutions for Different Initial and Boundary Conditions. *Chem. Eng. Sci.* **1978**, *33*, 1471–1480.

(252) U.S. Geological Survey, USGS Water Data for USA https://waterdata.usgs.gov/nwis? (accessed Oct 5, 2020).

(253) Minnesota Department of Agriculture, Surface Water Pesticide Water Quality Monitoring https://www.mda.state.mn.us/pesticide-fertilizer/surface-water-pesticide-water-quality-monitoring (accessed Nov 5, 2020).

(254) Vermillion Community College, Watershed Science Program https://www.vcc.edu/programs-degrees/natural-resource-water-management/watershed-science/ (accessed Oct 8, 2019).

(255) Minnesota Pollution Control Agency, Watershed pollutant load monitoring https://www.pca.state.mn.us/water/watershed-pollutant-load-monitoring (accessed Nov 5, 2020).

(256) International Water Institute https://iwinst.org/ (accessed Nov 5, 2019).

(257) Manske, J. *Quality Assurance and Procedures Manual For the Ramsey County Lake Management Laboratory Ramsey County Public Works*; Arden Hills, MN, 2019.

(258) Minnesota Department of Natural Resources, LakeFinder https://www.dnr.state.mn.us/lakefind/index.html (accessed Dec 2, 2020).

(259) Minnesota Department of Natural Resources, County Geologic Atlas Program https://www.dnr.state.mn.us/waters/groundwater_section/mapping/index.html (accessed Nov 5, 2020).

(260) Minnesota Department of Health, MN Well Index https://www.health.state.mn.us/communities/environment/water/mwi/index.html (accessed Oct 5, 2020).

(261) Metropolitan Council Environmental Services, Water and Wastewater https://metrocouncil.org/Wastewater-Water.aspx (accessed Nov 5, 2020).

(262) Agrawal, J. P. *High Energy Materials: Propellants, Explosives and Pyrotechnics*; Wiley-VCH: Weinheim, 2010.

(263) Spalding, R. F.; Fulton, J. W. Groundwater Munition Residues and Nitrate near Grand Island, Nebraska, U.S.A. *J. Contam. Hydrol.* **1988**, *2*, 139–153.

(264) Paquet, L.; Monteil-Rivera, F.; Hatzinger, P. B.; Fuller, M. E.; Hawari, J. Analysis of the Key Intermediates of RDX (Hexahydro-1,3,5-Trinitro-1,3,5-Triazine) in Groundwater: Occurrence, Stability and Preservation. *J. Environ. Monit.* **2011**, *13*, 2304–2311.

(265) Jenkins, T. F.; Hewitt, A. D.; Grant, C. L.; Thiboutot, S.; Ampleman, G.; Walsh, M. E.; Ranney, T. A.; Ramsey, C. A.; Palazzo, A. J.; Pennington, J. C. Identity and Distribution of Residues of Energetic Compounds at Army Live-Fire Training Ranges. *Chemosphere* **2006**, *63* (8), 1280–1290.

(266) Lapointe, M.-C.; Martel, R.; Diaz, E. A Conceptual Model of Fate and Transport Processes for RDX Deposited to Surface Soils of North American Active Demolition Sites. *J. Environ. Qual.* **2017**, *46*, 1444–1454.

(267) U.S. Environmental Protection Agency. *2012 Edition of the Drinking Water Standards and Health Advisories*; 2012.

(268) Etnier, E. L. Water Quality Criteria for Hexahydro-1,3,5-Trinitro-1,3,5-Triazine (RDX). *Regul. Toxicol. Pharmacol.* **1989**, *9*, 147–157.

(269) Sheremata, T. W.; Halasz, A.; Paquet, L.; Thiboutot, S.; Ampleman, G.; Hawari, J. The Fate of the Cyclic Nitramine Explosive RDX in Natural Soil. *Environ. Sci. Technol.* **2001**, *35* (6), 1037–1040.

(270) Williams, A. G. B.; Gregory, K. B.; Parkin, G. F.; Scherer, M. M. Hexahydro-1,3,5-Trinitro-1,3,5-Triazine Transformation by Biologically Reduced Ferrihydrite: Evolution of Fe Mineralogy, Surface Area, and Reaction Rates. *Environ. Sci. Technol.* **2005**, *39* (14), 5183–5189.

(271) Danielsen, K. M.; Hayes, K. F. PH Dependence of Carbon Tetrachloride Reductive Dechlorination by Magnetite. *Environ. Sci. Technol.* **2004**, *38* (18), 4745–4752.

(272) Alessi, D. S.; Grundl, T. Reduction of 2,4,6-Trinitrotoluene and Hexahydro-1,3,5-Trinitro-1,3,5-Triazine by Hydroxyl-Complexed Fe(II). *J. Environ. Eng.* **2008**, *134* (12), 937–943.

(273) Gregory, K. B.; Larese-Casanova, P.; Parkin, G. F.; Scherer. Michelle F. Abiotic Transformation of Hexahydro-1,3,5-Trinitro-1,3,5-Triazine by FeII Bound to Nagnetite. *Environ. Sci. Technol.* **2004**, *38* (5), 1408–1414.

(274) Hawari, J.; Halasz, A.; Sheremata, T.; Beaudet, S.; Groom, C.; Paquet, L.; Rhofir, C.; Ampleman, G.; Thiboutot, S. Characterization of Metabolites during Biodegradation of Hexahydro-1,3,5-Trinitro-1,3,5-Triazine (RDX) with Municipal Anaerobic Sludge. *Appl. Environ. Microbiol.* **2000**, *66*, 2652–2657.

(275) Kim, D.; Strathmann, T. J. Role of Organically Complexed Iron(II) Species in the Reductive Transformation of RDX in Anoxic Environments. *Environ. Sci. Technol.* **2007**, *41* (4), 1257–1264.

(276) Kwon, M. J.; Finneran, K. T. Hexahydro-1,3,5-Trinitro-1,3,5-Triazine (RDX) Reduction Is Concurrently Mediated by Direct Electron Transfer from Hydroquinones and Resulting Biogenic Fe(II) Formed During Electron Shuttle-Amended Biodegradation. *Environ. Eng. Sci.* **2009**, *26* (5), 961–971.

(277) Kwon, M. J.; Finneran, K. T. Biotransformation Products and Mineralization Potential for Hexahydro-1,3,5-Trinitro-1,3,5-Triazine (RDX) in Abiotic versus Biological Degradation Pathways with Anthraquinone-2,6-Disulfonate (AQDS) and Geobacter Metallireducens. *Biodegradation* **2008**, *19* (5), 705–715.

(278) Wiedemeier, T. H.; Wilson, B. H.; Ferrey, M. L.; Wilson, J. T. Efficacy of an In-Well Sonde to Determine Magnetic Susceptibility of Aquifer Sediment. *Groundw. Monit. Remediat.* **2017**, *37* (2), 25–34.

(279) Just, C. L. Face and Phytophotolysis of RDX in Reed Canary Grass (Phalaris Arundinacea), University of Iowa, 2001.

(280) U.S. Environmental Protection Agency. *EPA/600/R-01/025*; Washington D.C., 2001.

(281) Stookey, L. L. Ferrozine - A New Spectrophotometric Reagent for Iron. *Anal. Chem.* **1970**, *42*, 779–781.

(282) Pan, X.; Zhang, B.; Cox, S. B.; Anderson, T. A.; Cobb, G. P. Determination of N-Nitroso Derivatives of Hexahydro-1,3,5-Trinitro-1,3,5-Triazine (RDX) in Soils by Pressurized Liquid Extraction and Liquid Chromatography–Electrospray Ionization Mass Spectrometry. *J. Chromatogr. A* **2006**, *1107* (1–2), 2–8.

(283) Gorski, C. A.; Handler, R. M.; Beard, B. L.; Pasakarnis, T.; Johnson, C. M.; Scherer, M. M. Fe Atom Exchange between Aqueous Fe2+ and Magnetite. *Environ. Sci. Technol.* **2012**, *46* (22), 12399–12407.

(284) Gorski, C. A.; Scherer, M. M. Influence of Magnetite Stoichiometry on Fe(II) Uptake and Nitrobenzene Reduction. *Environ. Sci. Technol.* **2009**, *43*, 3675–3680.

(285) Oh, S.-Y.; Chiu, P. C.; Cha, D. K. Reductive Transformation of 2,4,6-Trinitrotoluene, Hexahydro-1,3,5-Trinitro-1,3,5-Triazine and Nitroglycerin by Pyrite and Magnetite. *J. Hazard. Mater.* **2008**, *158*, 652–655.

(286) Stemig, A. M.; Do, T. A.; Yuwono, V. M.; Arnold, W. A.; Penn, R. L. Goethite Nanoparticle Aggregation: Effects of Buffers, Metal Ions, and 4-Chloronitrobenzene Reduction. *Environ. Sci. Nano* **2014**, *1* (5), 478–487.

(287) Buchholz, A.; Laskov, C.; Haderlein, S. B. Effects of Zwitterionic Buffers on Sorption of Ferrous Iron at Goethite and Its Oxidation by CCl4. *Environ. Sci. Technol.* **2011**, *45* (8), 3355–3360.

(288) He, C.; He, D.; Collins, R. N.; Garg, S.; Mu, Y.; Waite, T. D. Effects of Good's Buffers and PH on the Structural Transformation of Zero Valent Iron and the Oxidative Degradation of Contaminants. *Environ. Sci. Technol.* **2018**, *52* (3), 1393–1403.

(289) Danielsen, K. M.; Gland, J. L.; Hayes, K. F. Influence of Amine Buffers on Carbon Tetrachloride Reductive Dechlorination by the Iron Oxide Magnetite. *Environ. Sci. Technol.* **2005**, *39* (3), 756–763.

(290) Strehlau, J. H.; Schultz, J. D.; Vindedahl, A. M.; Arnold, W. A.; Penn, R. L. Effect of Nonreactive Kaolinite on 4-Chloronitrobenzene Reduction by Fe(II) in Goethite-Kaolinite Heterogeneous Suspensions. *Environ. Sci. Nano* **2017**, *4* (2), 325–334.

(291) Hinshelwood, C. N. *The Kinetics of Chemical Change*; Clarendon Press: Oxford, 1940.

(292) Hougen, O. A.; Watson, K. M. Solid Catalysts and Reaction Rates. *Ind. Eng. Chem.* **1943**, *35* (5), 529–541.

Appendix A. Supporting Information for Chapter 2

Mineral Identity, Natural Organic Matter, and Repeated Contaminant Exposures do not Affect the Carbon and Nitrogen Isotope Fractionation of 2,4-Dinitroanisole during Abiotic Reduction

A.1 Chemical Sources and Analytical Methods

A.1.1 Materials

All aqueous solutions were prepared in ultrapure Milli-Q water (18.2 MΩ•cm) that was first deoxygenated by bubbling with N_2 gas (99.99%, Matheson) for at least 2 h. $Na_2S•9H_2O$ (≥98%), $Fe(NO_3)_3•9H_2O$ (≥98%), methanol (ACS grade), $NaHCO_3$ (ACS grade), $FeSO_4•7H_2O$ (ACS grade), KNO_3 (≥99%), and HCl (trace metals grade) were purchased from Sigma. $FeCl_2•6H_2O$ (ACS grade), HCl (ACS grade), NaOH (ACS grade), KOH (ACS grade), H_2SO_4 (ACS grade), acetonitrile (HPLC grade), ferrozine (B-(2-pyridyl)-5,6-bis(4-sulfophenyl)-1,2,4-triazine disodium salt hydrate, >98%), and NaCl (ACS grade) were purchased from Fisher. All glassware, cuvettes, stir bars, and Nalgene bottles were soaked in 0.1 M oxalic acid (pH 3.5) for at least 2 days and rinsed with ultrapure water prior to use to remove any residual iron. Elliot Soil Humic Acid (ESHA, Cat. No. 4S102H) was purchased from the International Humic Substances Society (IHSS) in St. Paul, MN. Elemental composition was performed by the IHSS and characterized the ESHA sample as 7.62% (w/w) water, 0.44% (w/w) ash, and 59.51% (w/w) C. Solutions containing ESHA were prepared to 5 mg/L as organic carbon.

A.1.2 Ferrozine Assay for Determining Fe(II) Content

The Fe(II) content was determined by the method of Viollier et al.[103] Aliquots from the batch reactors were filtered with a 0.2 μm PTFE syringe filter. To measure the Fe(II) content, 0.10 mL of reaction filtrate was transferred to a clean, dry polystyrene cuvette with 2.70 mL deoxygenated, ultrapure water and 0.20 mL of a 5 g/L aqueous ferrozine solution. Each sample was capped, mixed by inversion, and the absorbance was measured at 562 nm using a Shimadzu UV-1601PC UV-Vis spectrophotometer. A five-point calibration curve was constructed by producing serial dilutions from 0.0–0.005 mM Fe(II) in ultrapure water. A ferrozine/ultrapure water solution was used as the blank. The Fe(III) content of a sample can also be quantified by the ferrozine assay by using hydroxylamine hydrochloride to reduce the Fe(III) to Fe(II). The difference between the measurements with and without hydroxylamine give the Fe(III) value.

A.1.3 HPLC Method

Aqueous DNAN, MENA, and DAAN concentrations were quantified by an Agilent Technologies 1200 Series HPLC equipped with a photodiode array and an Inertsil ODS-3 column (4.6 × 250 mm, 5 μm particle size). The mobile phase (60 % acetonitrile/40 % ultrapure water) was operated at a flow rate of 1.00 mL/min. The injection volume was 20 μL. A five-point calibration curve was produced for DNAN from 0.01–0.2 mM. The typical retention times with this method were approximately 4.2 min, 5.8 min, and 7.0 min for DAAN, MENA, and DNAN, respectively. The detection wavelength was 230 nm.

A.2 Mineral Synthesis and Analysis

A.2.1 Mineral Synthesis Procedures

The mackinawite synthesis method was adapted from Butler and Hayes.[100] One-hundred and twenty (120) mL of 1.1 M $Na_2S•9H_2O$ were added to 200 mL of 0.57 M $FeCl_2•6H_2O$ and stirred for 3 days. The particle suspension was then equally divided into two dialysis bags (Spectrum Laboratories Inc., molecular weight cut off = 2000 g/mol) and placed in fresh, deoxygenated, ultrapure water three times per day for three days. Following dialysis, the mineral suspensions were combined and stored in a 500 mL Nalgene bottle. The particle density in suspension was determined as 33.3 g/L.

The goethite synthesis method was adapted from Anschutz and Penn.[101] First, a ferrihydrite suspension was produced by adding 1 L of 0.48 M $NaHCO_3$ dropwise to 1.0 L of 0.40 M $Fe(NO_3)_3•9H_2O$ with constant stirring. The resulting suspension was transferred to 250 mL Nalgene bottles and microwaved in 30 s intervals until boiling occurred with venting and shaking between each interval. Once boiling was achieved, the suspensions were submersed in an ice bath until the suspension temperature reached 20 °C and then transferred into dialysis bags and placed in fresh, deoxygenated, ultrapure water three times per day for three days. Following dialysis, the pH of the suspension was adjusted to 12 with 5 M NaOH and aged at 90 °C for 72 h. Approximately 400 mL of the supernatant were discarded to concentrate the goethite particles after aging. The counter-ions in the goethite suspension were removed by dialysis according to the previously described method.[101] The particle density in suspension was determined as 10 g/L.

The magnetite synthesis method was adapted from Schwertmann and Cornell.[102] An $FeSO_4$ solution was prepared by dissolving 40 g of $FeSO_4 \cdot 7H_2O$ in 280 mL of ultrapure water in a 0.5 L separation flask. A KNO_3/KOH solution was prepared by first dissolving 3.23 g of KNO_3 in 120 mL of ultrapure water in a 250 mL beaker. Slowly, 22.4 g of KOH were then added to the KNO_3 solution. The separation flask was placed in a 90 °C water bath and allowed to equilibrate with constant stirring. Both the separation flask and 250 mL beaker were covered with aluminum foil and bubbled under N_2. The KNO_3/KOH solution was then transferred to a buret and added to the $FeSO_4$ solution by piercing the foil above the $FeSO_4$ with the buret tip and adding dropwise. Once all the solution had been added and a black precipitate had formed, the solution was allowed to continue stirring for 45 min under constant N_2 bubbling. The solution was then cooled and transferred to an anaerobic glovebag. The particles were washed three times by centrifugation, dried, and stored in the glovebag.

A.2.2 Mineral Characterization Methods

X-Ray diffraction (XRD) patterns were collected using a PANanalytical X'Pert Pro X-ray diffractometer equipped with a cobalt source (1.79 Å) and an X'Celerator detector. Patterns were collected from 20° to 80° 2θ over 60 min and compared to powder diffraction files (PDF) No. 29-0713 (goethite), No. 19-0629 (magnetite), and No. 15-0037 (mackinawite). Prior to analysis, each mineral suspension was washed three times via centrifugation with ultrapure water to remove any salts, dried, and finely ground

using a mortar and pestle. XRD patterns of the as-synthesized minerals are provided in Figure A-1.

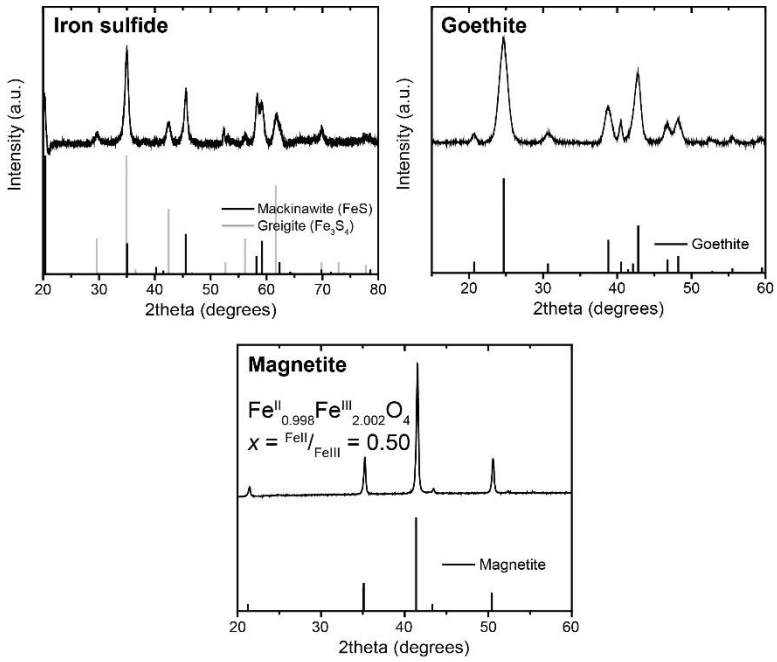

Figure A-1. XRD patterns for synthetic iron sulfide (mackinawite), goethite, and magnetite.

Surface areas were determined by nitrogen adsorption analyses and calculated using the Brunauer-Emmett-Teller (BET) adsorption model.[105] Measurements were performed between 0 and 0.3 P/P_0 using a Quantachrome Autosorb iQ analyzer. Samples were outgassed at 100 °C for 12 h prior to analysis.

Mass loading experiments were performed to determine mass of particles per suspension volume for goethite and mackinawite. Five total aliquots (0.1–0.5 mL) of each suspension were added to separate weigh boats of known mass and dried at room

temperature until no liquid remained. Particle densities were then calculated by fitting the mass of dried solid against aliquot volume with a linear regression model.

A.3 Control Experiments for DNAN Transformation Kinetics

A control experiment was performed to determine if DNAN transformation occurs in the absence of a mineral phase. Reactors were prepared in triplicate with bicarbonate buffer (10 mM, pH 7), Fe(II) (1 mM), and DNAN (0.2 mM). The results (Figure A-2) revealed that no DNAN transformation occurred without an associated mineral phase after 21 days.

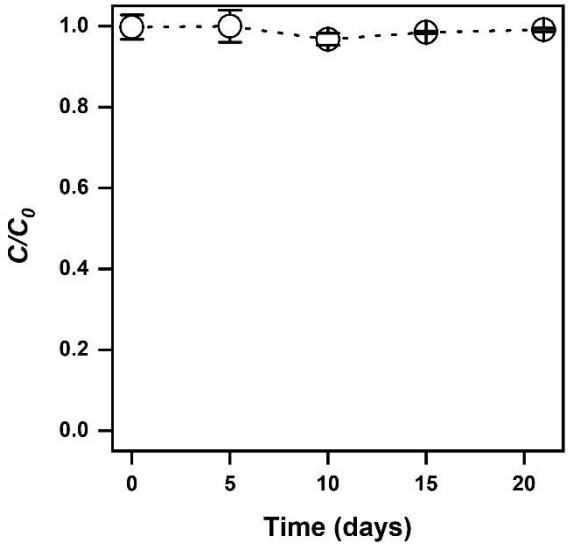

Figure A-2. Control experiment for DNAN transformation without an added mineral. No DNAN transformation was observed in the control reactor with aqueous Fe(II) as compared to systems containing an Fe-bearing mineral (see Figure 2-1). Reactors were prepared according to the methods described in the main text. Error bars represent standard deviations in triplicate reactors.

A.4 CSIA Data Analysis

A.4.1 Calculation of Isotope Fractionation Parameters

Carbon and nitrogen isotope signatures, $\delta^{13}C$ and $\delta^{15}N$, were calculated according to eq. A-1 from $^{13}C/^{12}C$ and $^{15}N/^{14}N$ measurements performed using SPME coupled to GC/IRMS.[106,108]

$$\delta^{h}E = \frac{R(^{h}E/^{l}E)_{sample}}{R(^{h}E/^{l}E)_{reference}} - 1 \qquad (A-1)$$

where $R(^{h}E/^{l}E)_{sample}$ and $R(^{h}E/^{l}E)_{reference}$ are the ratios of the heavy (h) and light (l) isotopes of the element, E. Isotope enrichment factors for DNAN were then derived from log-linear regression of eq. 1-1 (see main text). Carbon and nitrogen apparent kinetic isotope effects, ^{13}C-AKIE and ^{15}N-AKIE, were then calculated according to eq. 1-2 (see main text)[23] where $z = 1$ for ^{13}C-AKIE and $z = 2$ for ^{15}N-AKIE. It should be noted that values of ε_E obtained from eq. 1-1 are bulk enrichment values whereas values used to calculate ^{h}E-AKIEs from eq. 1-2 are specific for the reactive position (i.e., $\varepsilon_{\text{reactive position}}$). The differences in these values account for intermolecular and intramolecular competition which can lead to "isotopic dilution" and subsequent decreases in observed fractionation values. For simplicity, we did not make this distinction in the main text but ε_E values provided in the main text are for $\varepsilon_{\text{reactive position}}$. See refs 9 and 10 for a detailed description of how this correction is made.[22,250]

A.4.2 Detailed Carbon Fractionation Results

In the main text (Figure 2-3) all isotope fractionation results are plotted together, for simplicity, because minimal fractionation was observed across all sample sets. Here, values of $\delta^{15}N$ and $\delta^{13}C$ vs. C/C_0 (Figure A-3) are provided separately for each combination of reaction condition and mineral type.

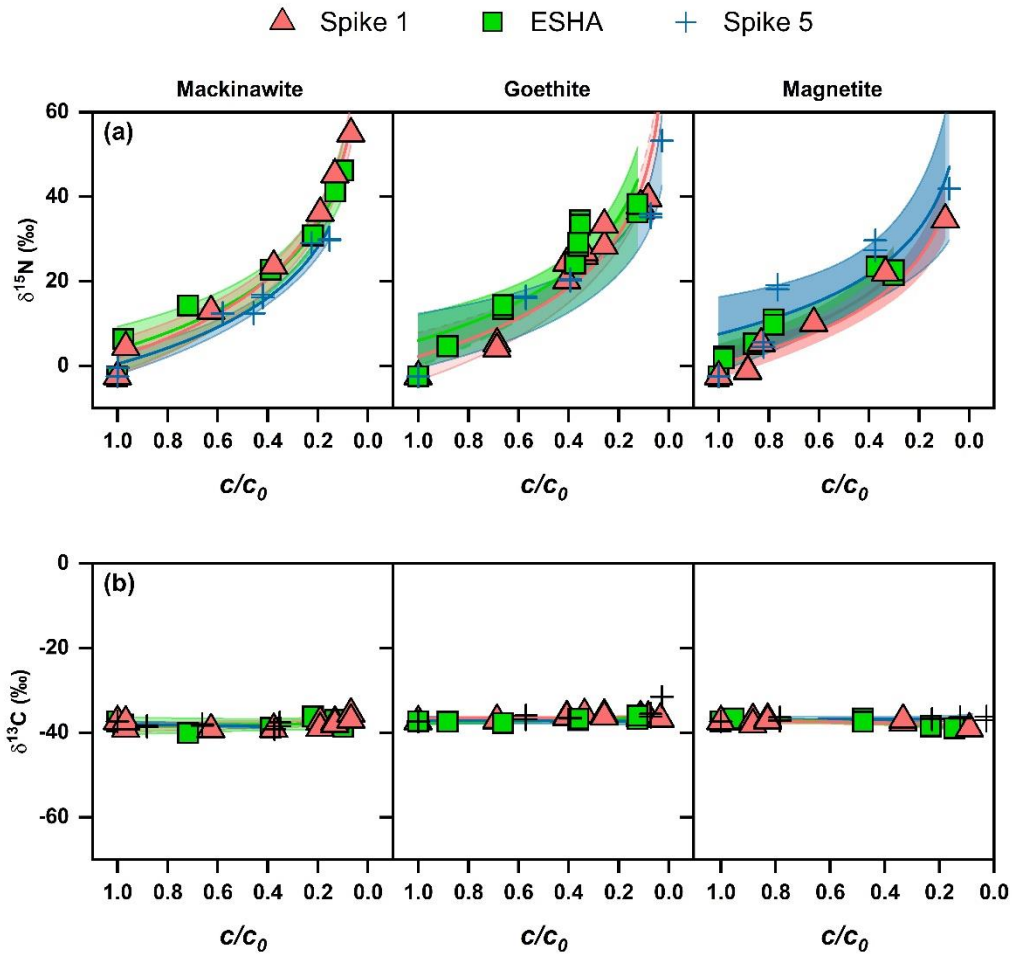

Figure A-3. Complete (a) N and (b) C isotope fractionation results for abiotic reduction of DNAN calculated using nonlinear regression analyses of eq. 1-1. All shaded regions represent 95% confidence intervals for each data set.

A.4.3 Decreased Enrichment Factors during Repeated Contaminant Exposure

A general trend of slightly reduced N fractionation was observed over 5 sequential DNAN spikes (Figure A-4). Several factors may contribute to this result and we hypothesize the observed effects to be caused by the evolution of mineral surfaces. For example, Chun et al.[97] observed the oxidative growth of goethite nanoparticles during the reduction of 4-chloronitrobenzene in sequential-spike batch reactions containing Fe(II)/goethite, similar to those in the present study. Even though particle growth had occurred, the newly formed surfaces displayed marked increases in roughness leading to decreased mineral reactivity and negligible (even decreases on some facets) changes in surface area. Losses in reactivity were attributed to a lower Fe(II) uptake capacity of the roughened surfaces (approximately 16% decrease over five spikes). In addition, changes in mineral morphology may inhibit proton and electron transfer reactions that occur prior to the initial N—O bond cleavage. These transfer reactions typically elicit isotope effects that are minute in comparison to N—O bond cleavage but may be diminished over multiple contaminant reductions as the mineral evolves resulting in decreased total isotope enrichment.[31] The trends in reductive pathways ($\varepsilon_N \approx$ -19 to -9 ‰ and $\varepsilon_C \approx$ -0.1 to -1.5 ‰), however, are still easily distinguished from oxidation (ε_N = -2.7 ± 0.4 ‰ , ε_C = -6.0 ± 0.5 ‰ and ε_N = -3.2 to -2.5 ‰ , ε_C = -3.7 to 2.8 ‰ for alkaline hydrolysis and biodegradation, respectively).[12]

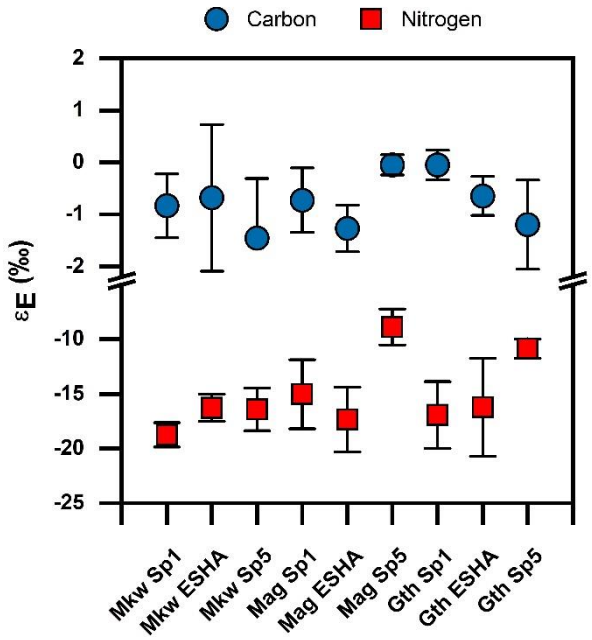

Figure A-4. Carbon and nitrogen isotope enrichment factors (ε_E) in mackinawite (Mkw), magnetite (Mag), and goethite (Gth) suspensions derived using log-linear regression of eq. 1-1. Error bars represent the 95% confidence intervals.

A.4.4 Two-Dimensional Isotope Analysis

In the main text (Figure 2-5), the results of two-dimensional CSIA are provided with all reduction data combined. These same data are presented in (Figure A-5) with the reduction data separated by mineral type to indicate that isotope fractionation in each mineral suspension followed the same trend.

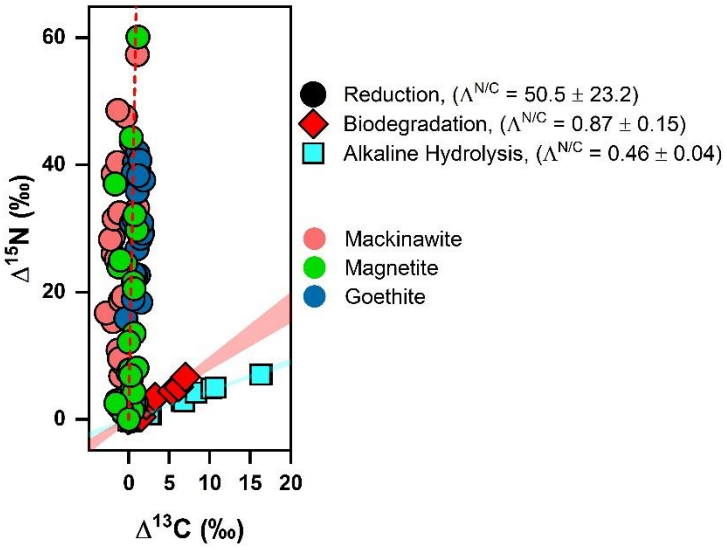

Figure A-5. Two-dimensional isotope fractionation for reductive and oxidative DNAN transformation pathways. Isotope fractionation observed during abiotic reduction (circles) is shown with respect to the mineral type and compared to alkaline hydrolysis (squares), and biodegradation (diamonds). Alkaline hydrolysis and biodegradation data were reproduced with permission from Ulrich et al.[12]

Appendix B. Supporting Information for Chapter 3

Assessment of 2,4-dinitroanisole transformation using compound-specific isotope analysis after in situ chemical reduction of iron oxides

B.1 Chemicals

Methanol (ACS grade), $NaHCO_3$ (ACS grade), and HCl (trace metals grade) were purchased from Sigma. 2,4-Dintroanisole (DNAN,98%) was purchased from Alfa Aesar. $FeCl_2 \cdot 6H_2O$ (ACS grade), HCl (37%, ACS grade), NaOH (50% in H_2O), H_2SO_4 (ACS grade), acetonitrile (HPLC grade), ferrozine (B-(2-pyridyl)-5,6-bis(4-sulfophenyl)-1,2,4-triazine disodium salt hydrate, >98%), and NaCl (ACS grade) were purchased from Fisher. The DNAN transformation products 2-amino-4-nitroaniline (2-ANAN, 98%), 4-amino-2-nitroaniline (4-ANAN, 97%), and 2,4-diaminoanisole (DAAN, ≥98%) were purchased from Fisher.

All glassware, cuvettes, stir bars, and Nalgene bottles were soaked in 0.1 M oxalic acid (pH 3.5) for at least 2 days and rinsed with ultrapure water prior to use to remove any residual iron.

B.2 Additional details of mineral characterization

X-Ray diffraction (XRD) patterns were collected using a PANanalytical X'Pert Pro X-ray diffractometer equipped with a cobalt source (1.79 Å) and an X'Celerator detector. Scans were performed from 20° to 60° 2θ over 60 min and compared to powder diffraction files (PDF) No. 29-0713 (goethite), No. 33-0664 (hematite), No. 19-0629 (magnetite), and No. 46-1045 (quartz). Before analysis, each mineral was washed three

times via centrifugation with ultrapure water to remove any salts, dried, and finely ground using a mortar and pestle. The relevant chemical properties of all materials are provided in Table B-1. All collected XRD patterns are shown in Figure B-1.

Table B-1. Chemical properties of natural materials and the synthetic analogs* used in this study. Mineral phases were determined by X-ray diffraction (XRD).

sample	reactive iron phase	bulk mineral phase	total Fe % (w/w)	Fe(II)/Fe(III)
TCAAP	magnetite (Fe_3O_4)	quartz (SiO_2)	3.03[c]	<LOD
TCAAP extract[a]	magnetite (Fe_3O_4)	quartz (SiO_2)	6.9	0.1
magnetite*[a]	magnetite (Fe_3O_4)	n.d.[b]	72[d]	0.5
Tinker AFB	hematite (Fe_2O_3)	quartz (SiO_2)	2.04[c]	<LOD
hematite*	hematite (Fe_2O_3)	n.d.[b]	70[d]	<LOD

[a]data obtained from Strehlau et al.[158]
[b]none detected.
[c]Determined by ICP-OES.
[d]estimated from structural formulas of pure minerals.

B.3 Analytical methods

B.3.1 Ferrozine assay

The Fe(II) content was determined by the method of Viollier et al.[103] Aliquots from the batch reactors were extracted and filtered as described in the previous sections. To measure the Fe(II) content, 0.10 mL of reaction filtrate was transferred to clean, dry polystyrene cuvette with 2.70 mL deoxygenated, ultrapure water and 0.20 mL of a 5 g/L aqueous ferrozine solution. Each sample was capped, mixed by inversion, and the absorbance was measured at 562 nm using a Shimadzu UV-1601PC UV-Vis spectrophotometer. A five-point calibration curve was constructed by producing serial

dilutions from 0.0–0.005 mM Fe(II) in ultrapure water. A ferrozine/ultrapure water solution was used as the blank. The Fe(III) content of a sample can also be quantified by the ferrozine assay as in the case of determining magnetite stoichiometry.

B.3.2 HPLC-DAD

Aqueous DNAN, MENA, iMENA, and DAAN concentrations were quantified with an Agilent Technologies 1200 Series HPLC equipped with an diode array detector (DAD) and an Inertsil ODS-3 column (4.6 × 250 mm, 5 µm particle size). All analytes were detected at a wavelength of 230 nm. The mobile phase (60 % acetonitrile/40 % ultrapure water) was operated at a flow rate of 1.00 mL/min. The injection volume was 20 µL. A five-point calibration curve was produced for DNAN from 10–200 µM. The typical retention times with this method were approximately 3.1, 4.3, 5.7 min and 7.0 min for DAAN, iMENA, MENA, and DNAN, respectively.

B.3.3 SPME

Extraction of aqueous samples for compound specific isotope analysis (CSIA) was performed via online SPME carried out using a PAL autosampler equipped with a PAL SPME Arrow Tool and a Heatex Stirrer. All samples were initially diluted with 10 mM phosphate buffer (pH=7) to obtain concentrations within a range of linear response, and sodium chloride (200 g/L) was added to maximize extraction efficiency. Following equilibration at 50 °C for 10 min, the SPME Arrow was immersed in the sample for 70 minutes at 50 °C (600 RPM stir rate), and then DNAN was thermally desorbed from the arrow in an injector equipped with a deactivated liner (270 °C, 6 minutes).

B.3.4 GC/IRMS

DNAN $^{15}N/^{14}N$ and $^{13}C/^{12}C$ isotope ratios were determined using a Trace GC (Thermo Electron Corp.) coupled to an isotope ration mass spectrometer (IRMS; DeltaPLUS XL, Thermo Electron Corp.) via a combustion interface (GC Combustion III, Thermo) equipped with a Ni/Pt reactor. The GC contained an Rtx-5MS capillary column (0.32 mm ID, 1 µm film thickness, 30 m length) and was operated in splitless mode (splitless time 6 minutes, purge flow 50 ml/min) with the following temperature program: 50 °C for 1 minute, ramp 10 °C/min to 250 °C, hold for 5 minutes. During $\delta^{15}N$ analysis a liquid nitrogen trap was used to trap CO_2 produced from combustion. The self-made oxidation reactor was operated as described previously.[108] Method quantification limits (MQLs) for $\delta^{13}C$ and $\delta^{15}N$ signatures according to the moving mean procedure were 0.2 µM and 1 µM, respectively.[109]

Analytes were measured against standard laboratory gases that were introduced at the beginning of each run (CO_2 and N_2 for C and N isotope ratio measurements, respectively). Subsets of six samples were bracketed with DNAN standards in duplicate or triplicate to allow correction for any drift in signal observed during each run. The $\delta^{13}C$ and $\delta^{15}N$ values for the solid DNAN standard were determined to be -37.38 ± 0.01‰ and -2.48 ± 0.06‰, respectively, by EA/IRMS.

B.4 Electron balance calculations

B.4.1 Batch experiments

The total amount of electrons transferred from Fe-bearing materials to DNAN in batch reactors was calculated according to eq B-1.

$$\text{total electrons transferred} = (6c_{MENA} + 6c_{iMENA} + 12c_{DAAN}) * V_R \qquad (B-1)$$

where V_R is the reactor volume (35 mL) and the analyte concentrations (c) are those at the endpoint of batch experiments.

B.4.2 Column experiments

In column experiments, the cumulative amount of electrons transferred were calculated by integrating the concentration measurements shown in Figure B-2c-d according to eq B-2.

$$\text{total electrons transferred} = \int_0^V (6c_{MENA} + 6c_{iMENA} + 12c_{DAAN})\text{dV} \qquad (B-2)$$

where c is the measured analyte concentration at the column outlet and V is the volume of DNAN solution introduced to the column.

B.5 Additional sediment column details

The physical properties of packed sediment columns are provided in Table B-2. The calculation of dispersion coefficients (D) in columns was adapted from Kreft and Zuber[251] as shown in eq B-3.

$$\frac{c}{c_0} = \frac{1}{2}\text{erfc}\left(\frac{L - uz}{\sqrt{4Dz}}\right) + \frac{1}{2}\exp\left(\frac{uL}{D}\right)\text{erfc}\left(\frac{L+uz}{\sqrt{4Dz}}\right) \qquad (B-3)$$

where c/c_0 is the normalized DNAN concentration at the column outlet relative to the input level, u is the mean flow velocity in the column, L is the column height, and z is the vertical displacement in the column. Because our measurements were made at the column outlet, L was equal to z in all cases. Fitting was performed using the Levenberg-Marquardt algorithm in Origin Version 2019b (OriginLab Corporation).

Table B-2. Physical parameters of columns. Mean diffusion coefficients (D) determined from the nonreactive tracer were small and slightly greater for Tinker AFB (2.53 (± 0.12) x 10^{-4} cm^2 s^{-1}) than TCAAP (2.37 (± 0.22) x 10^{-4} cm^2 s^{-1}) columns. Similarly, large values of Pe (> 40) and uninhibited breakthrough of the nonreactive tracer (~1 PV) indicated convection-dominated regimes without preferential flow. All columns were 2.5 cm I.D. by 10 cm in length.

						before		after	
type	column no.	mass (g)	ρ_p (g/mL)	ρ_b (g/mL)	PV (mL)	φ	D (cm^2/s)	φ	D (cm^2/s)
TCAAP	1	47.7	2.64	1.59	11.9	0.40	$2.69x10^{-4}$	0.41	$2.69x10^{-4}$
	2	32.2	2.60	1.64	9.0	0.46	$2.35x10^{-4}$	0.46	$2.35x10^{-4}$
	3	40.2	2.76	1.64	10.0	0.41	$2.11x10^{-4}$	0.43	$2.11x10^{-4}$
Tinker	1	27.5	2.68	1.70	11.5	0.37	$2.48x10^{-4}$	0.37	$2.48x10^{-4}$
AFB	2	30.2	2.72	1.72	10.5	0.49	$2.41x10^{-4}$	0.50	$2.41x10^{-4}$
	3	33.1	2.70	1.68	10.7	0.48	$2.70x10^{-4}$	0.49	$2.70x10^{-4}$

B.6 CSIA data processing

Carbon and nitrogen isotope signatures ($\delta^{13}C$, $\delta^{15}N$) were calculated according to eq B-4 from measured $^{13}C/^{12}C$ and $^{15}N/^{14}N$ values.[106,108]

$$\delta^{h}E = \left(\frac{^{h}E/\ ^{l}E_{sample}}{^{h}E/\ ^{l}E_{reference}} - 1 \right) * 1000‰ \qquad (B-4)$$

where $^{h}E/^{l}E_{sample}$ and $^{h}E/^{l}E_{reference}$ are the ratios of the heavy (h) and light (l) isotopes of the element, E.

The correlation of N and C isotope fractionation ($\Lambda^{N/C}$) was determined using both simple linear regression and by the York model as described by Ojeda et al.[163] Linear regression analyses were performed in R (Version R-3.6.2) with RStudio (Version 1.2.5033) and the 'rgr' and 'IsoplotR' packages. The method and example R script are provided in the supporting information of Ojeda et al.[163]

B.7 Additional CSIA results

Bulk carbon and nitrogen isotope enrichment factors (ε_C and ε_N) and AKIEs were calculated from all experiments (Table B-3). The values were obtained from experiments for DNAN reduction with untreated materials receiving a constant supply of 1 mM dissolved Fe(II). The predictions made by applying the Rayleigh fractionation equation (eq 3-4) to our results are shown in Table B-4. Details of the calculations are provided in the main text.

Table B-3. Bulk N and C isotope enrichment factors (ε_E) and AKIEs in batch reaction for DNAN reduction. All errors represent 95% confidence intervals. These values correspond to the data presented in Figure 3-3 in the main text.

material	ε_N (‰)	^{15}N-AKIE (-)	ε_C (‰)	^{13}C-AKIE (-)
Tinker AFB				
untreated + Fe(II)	-11.1 ± 4.3	1.023 ± 0.009	-0.7 ± 0.1	1.0007 ± 0.0002
reduced	-9.9 ± 3.8	1.020 ± 0.008	-0.2 ± 0.1	1.0002 ± 0.0002
hematite	-21.2 ± 3.3	1.044 ± 0.007	-0.3 ± 0.4	1.0003 ± 0.0008
TCAAP				
untreated + Fe(II)	-21.5 ± 2.6	1.045 ± 0.005	-0.8 ± 1.0	1.0008 ± 0.0020
reduced	-15.8± 4.3	1.033 ± 0.009	-0.3 ± 0.2	1.0003 ± 0.0004
magnetite	-13.2 ± 1.7	1.027 ± 0.003	-0.7 ± 0.3	1.0007 ± 0.0006
goethite[a]	-16.9 ± 3.0	1.035 ± 0.003	-0.1 ± 0.3	1.0000 ± 0.0003
mackinawite[a]	-18.8 ± 1.4	1.039 ± 0.001	-0.8 ± 0.6	1.0008 ± 0.0008

[a]data obtained from Berens et al.[152]

Table B-4. Estimated values of predicted vs measured DNAN transformation in sediment columns. All errors represent 95% confidence intervals.

material	measured (c/c_o)	$\delta^{15}N$ (‰)	predicted (c/c_o)	error (c/c_o)
TCAAP	0.98	-1.94 ± 0.16	0.96± 0.010	0.02
	0.97	-1.52 ± 0.11	0.94 ± 0.007	0.03
	0.83	3.51 ± 0.15	0.67 ± 0.007	0.16
	0.50	9.59 ± 0.02	0.45 ± 0.001	0.04
	0.24	14.28 ± 0.16	0.33 ± 0.003	0.09
	0.15	16.64 ± 0.13	0.28 ± 0.002	0.13
	0.14	15.06 ± 0.43	0.31 ± 0.009	0.18
Tinker AFB	1.00	-2.22 ± 0.08	0.98 ± 0.005	0.02
	0.98	-1.20 ± 0.11	0.92 ± 0.007	0.06
	0.94	-1.04 0.91	0.91 ± 0.008	0.03
	0.41	8.47 ± 0.18	0.48 ± 0.006	0.07
	0.19	14.82 ± 0.11	0.32 ± 0.002	0.13
	0.16	11.95 ± 0.12	0.38 ± 0.003	0.22

B.8 Additional figures.

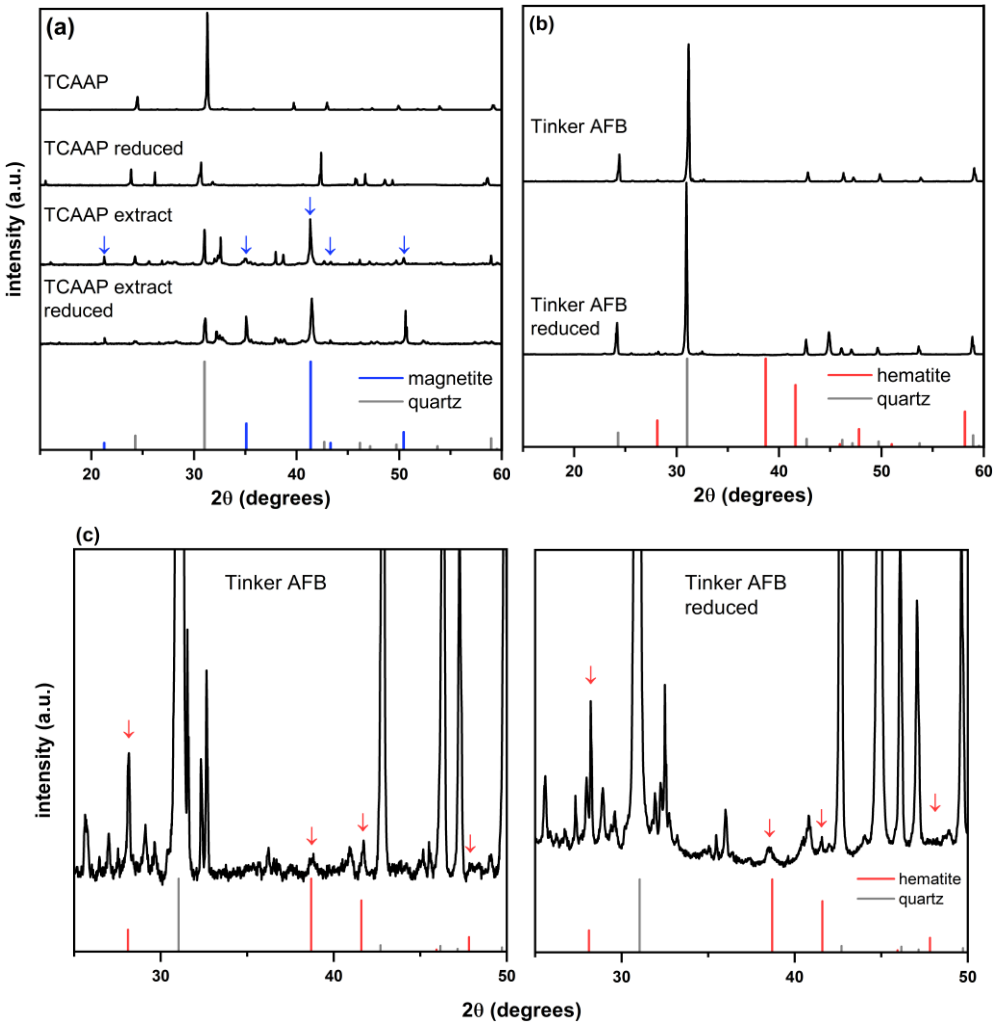

Figure B-1. X-ray diffraction patterns of native and dithionite-reduced minerals used in this study. Both the bulk TCAAP material (a, top two patterns) and the magnetic extract (a, bottom two patterns) indicated that magnetite was the dominant iron-bearing mineral phase. (b) Hematite was the dominant iron phase in Tinker AFB sediment. Because of the strong quartz signal in Tinker AFB patterns, an enlarged subsection is provided in (c). These data reveal that negligible phase transformation occurred during ISCR and suggest that the primary effects of the treatment on the underlying mineralogy was the (re)generation of surface Fe(II).

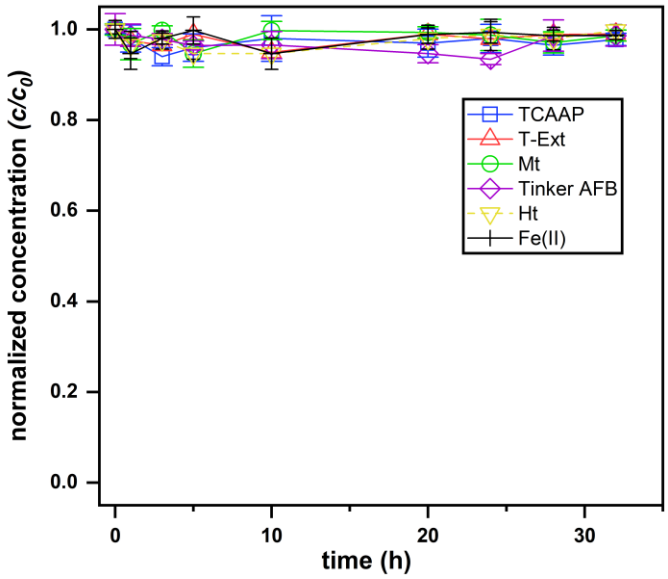

Figure B-2. Control experiments for DNAN removal in suspensions of untreated minerals and dissolved Fe(II) without a mineral present. No reduction was observed over 32 h. Reactors remained on the rotator for three weeks with no detectable concentration loss (data not shown).

Scheme B-1. Reductive transformation mechanism of DNAN to form 2/4-ANAN and DAAN. Each nitro-group transformation to form an amino-group requires the transfer of 6 electrons and 6 protons.

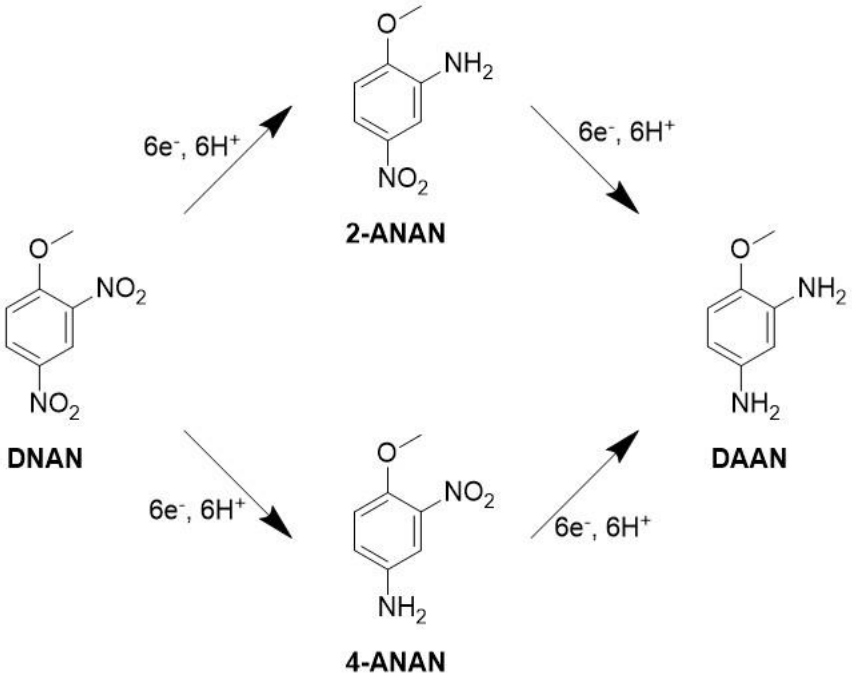

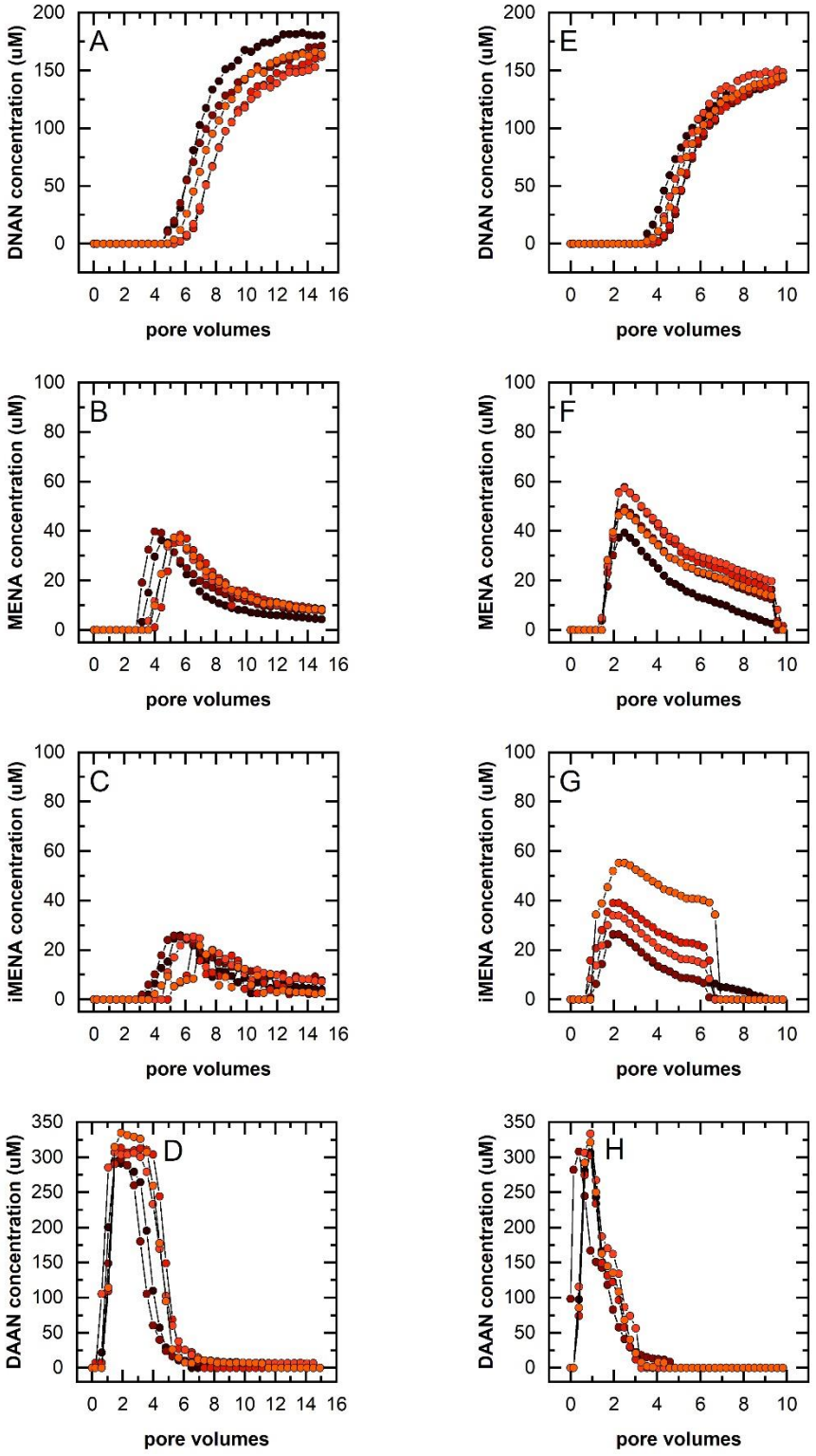
A
DNAN concentration (uM)
pore volumes
B
MENA concentration (uM)
pore volumes
C
iMENA concentration (uM)
pore volumes
D
DAAN concentration (uM)
pore volumes
E
DNAN concentration (uM)
pore volumes
F
MENA concentration (uM)
pore volumes
G
iMENA concentration (uM)
pore volumes
H
DAAN concentration (uM)
pore volumes

Figure B-3. Breakthrough curves for 200 μM DNAN in (A-D) TCAAP and (E-H) Tinker AFB sediment columns following five sequential cycles of dithionite exposure and DNAN reduction. These are the data from Figure 3-2 expanded to show each individual cycle.

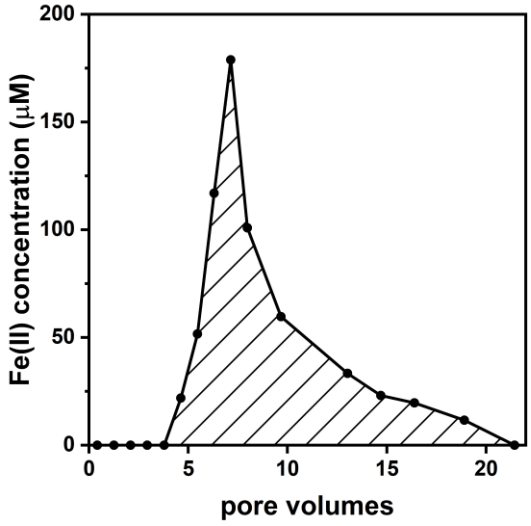

Figure B-4. Representative concentration profile of Fe(II) detected in column effluents during dithionite treatment.

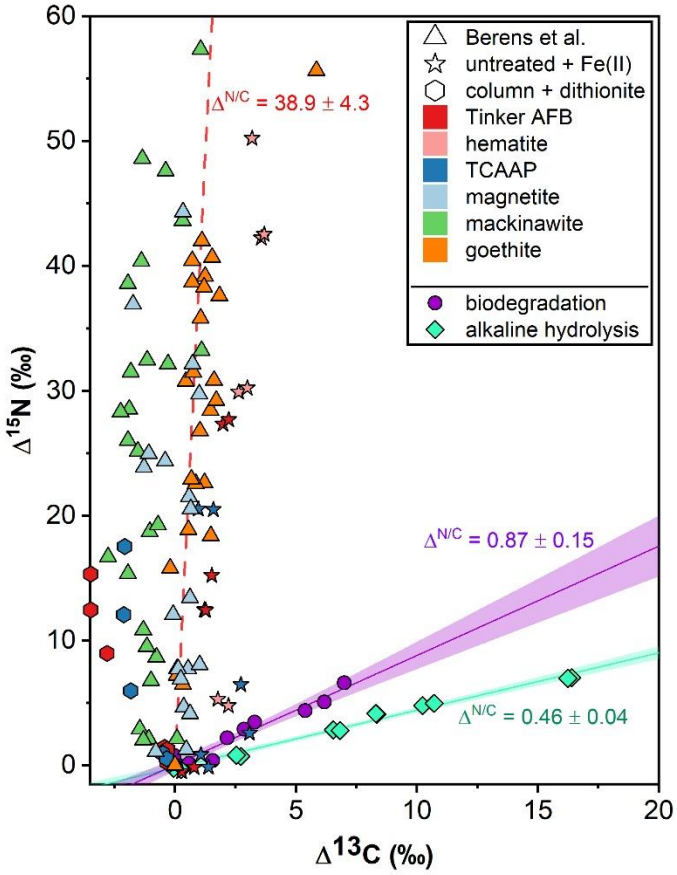

Figure B-5. Dual-element (N vs C) isotope analysis to indicate multiple potential DNAN transformation pathways. Data from the present study for abiotic reduction by untreated minerals + Fe(II) (stars) and from columns receiving ISCR (hexagons) are shown. The observations from our previous work[152] is also provided (triangles). The dotted line represents the fit from linear regression by the York method as described by Ojeda et al.[163] The isotope fractionation observed during biodegradation (circles) and alkaline hydrolysis (diamonds) are provided for reference. The latter data sets were reproduced with permission from Ulrich et al.[12] Shaded portions represent the 95% confidence intervals from nonlinear regression analysis.

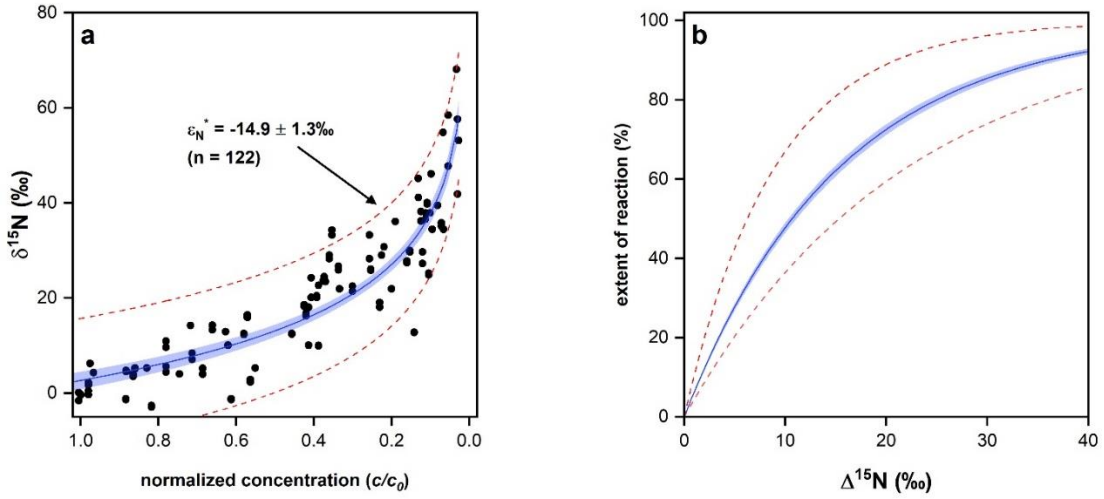

Figure B-6. $\delta^{15}N$ vs c/c_0 values were combined from all batch experiments to evaluate consistencies in fractionation and calculate the associated ε_N* value. Theoretical plot relating the extent of DNAN transformation to measured $\delta^{15}N$ values using eq 3-4.

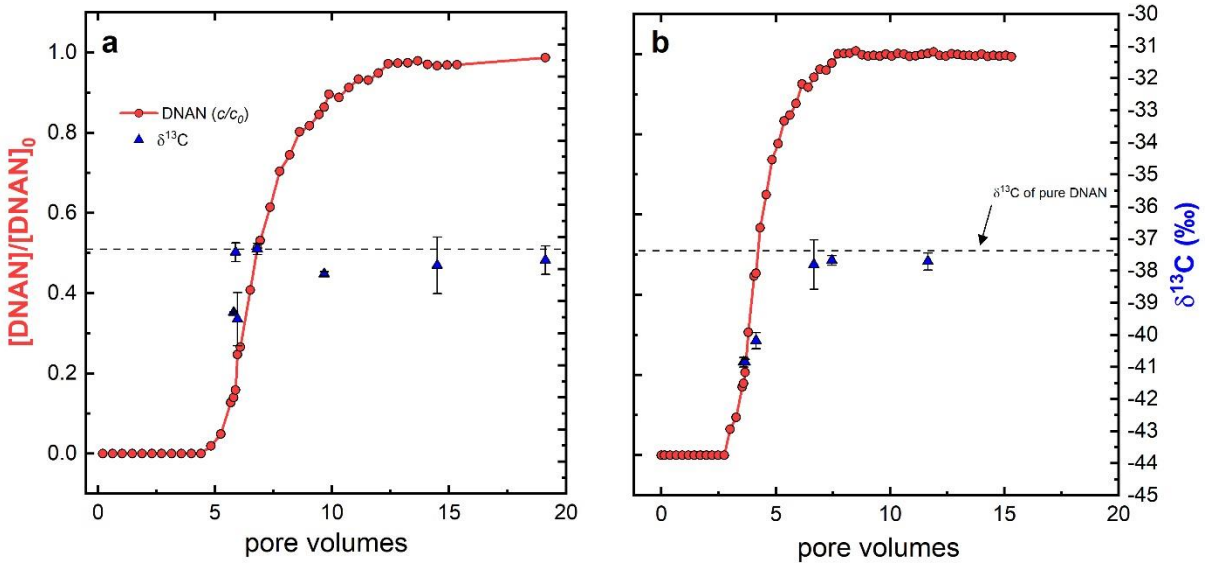

Figure B-7. Extent of DNAN conversion ([DNAN]/[DNAN]$_0$, circles) and C isotope signatures ($\delta^{13}C$, triangles) measured at the breakthrough front during column experiments with dithionite-reduced (a) TCAAP and (b) Tinker AFB materials. Concentration data represent the average of five sequential breakthrough experiments. Error bars in $\delta^{13}C$ values indicate the standard deviations from triplicate measurements.

Appendix C. Supporting Information for Chapter 4

Neonicotinoid Insecticides in Surface Water, Groundwater, and Wastewater across Land Use Gradients and Potential Effects

C.1 Chemicals and Materials

C.1.1 Neonicotinoid Standards.

All of the neonicotinoid analytical standards are summarized in Table C-1. All compounds were used as received and dissolved in Optima™ grade acetonitrile.

Table C-1. List of neonicotinoid analytical standards.

Compound	CAS Number	Source	Purity
Imidacloprid	138261-41-3	Supelco	≥ 98.0%
Clothianidin	210880-92-5	Supelco	≥ 98.0%
Thiamethoxam	153719-23-4	Supelco	≥ 98.0%
Acetamiprid	190604-92-3	Supelco	≥ 98.0%
Thiacloprid	111988-49-9	Supelco	≥ 98.0%
Desnitro-Imidacloprid	127202-53-3	Supelco	≥ 99.0%
Imidacloprid-Urea	120868-66-8	ChemService, Inc.	≥ 98.0%
Imidacloprid-Olefin	115086-54-9	Supelco	≥ 99.0%
Acetamiprid-N-Desmethyl	190604-92-3	Supelco	≥ 99.0%
Thiacloprid Amide	676288-91-4	Supelco	≥ 98.0%
^{13}C-caffeine	78072-66-9	Sigma-Aldrich	≥ 99%
Imidacloprid-d_4	1015855-75-0	Supelco	≥ 99.0%
Clothianidin-d_3	1262776-24-8	Supelco	≥ 97.0%

C.1.2 Bottle Cleaning

One-liter polycarbonate sample bottles were manually cleaned with an anionic detergent solution (Alconox, Alconox, Inc.) and rinsed with deionized water. The bottles were then soaked overnight in a 10% hydrochloric acid bath, rinsed with ultrapure water

(≥18.2 MΩ·cm, Milli-Q, MilliporeSigma) sterilized in an autoclave for 30 min, and air-dried in a fume hood. The bottles then remained sealed until sample collection.

C.2 Detailed Sampling Locations

Water samples for the present study were collected from four different classes of waterbodies: rivers and streams (Table C-2), lakes (Table C-3), groundwater wells (Table C-4), and wastewater treatment plant (WWTP) effluents (Table C-5).

Table C-2. Detailed summary of river and stream sampling locations in the present study.

Site Name	Latitude (WGS1984)	Longitude (WGS1984)	Predominant Land Use	Partner	Drainage Area (km^2)[a]	USGS ID	Sampling Method
Battle Creek below McKnight Road in St. Paul, MN	44.93863	-93.0327	Urban	MDA	26	05331050	Dipper pole from bank
Bassett Creek	44.97825	-93.2994	Urban	MDA	55	NA[b]	Van Dorn from bridge or dipper pole from bank
Fish Creek	44.89965	-93.0074	Urban	MDA	120	NA[b]	Dipper pole from bank
Minnesota River at Judson, MN	44.20285	-94.19371	Agricultural	MDA	29,000	05317500	Weighted bucket from bridge
Kawishiwi River near Ely, MN	47.81777	-91.78419	Undeveloped	VCC	2,200	05126210	Dipper pole from bank
Minnehaha Creek at Hiawatha Ave	44.91935	-93.22539	Urban	MDA	460	05289800	Van Dorn from bridge or dipper pole from bank
Blue Earth River near Rapidan, MN	44.09785	-94.10881	Agricultural	MDA	6,240	05320000	Dipper pole from bridge
Shingle Creek at Queen Ave	45.05176	-93.31007	Urban	None[c]	73	05288705	Wading

Table C-2. Continued.

Sauk River at Mississippi River	45.59348	-94.17756	Urban	MPCA	2,670	05270500	Weighted bucket from bridge
Snake River near Alvarado, MN	48.41597	-97.10723	Agricultural	IWI	800	05086000	Dipper pole from bank
Zumbro River, N Fork near Wanamingo, MN	44.31425	-92.81269	Agricultural	MDA	274	05373720	Van Dorn from bridge

[a]Drainage areas obtained from USGS Water Data for USA[252]
[b]NA = sampling locations not near a USGS gage station; streamflow measurements were not made for these locations
[c]Shingle Creek samples were collected by the author (M.J.B.)
MDA = Minnesota Department of Agriculture[253]; VCC = Vermillion Community College[254]; MPCA = Minnesota Pollution Control Agency[255]; IWI = International Water Institute[256]

Table C-3. Detailed summary of lake sampling locations in the present study. Samples were collected with the Ramsey County Environmental Services, Lakes Management division.[257] All lakes are within predominantly urban watersheds.

Lake name	Latitude (WGS1984)	Longitude (WGS1984)	Total area (km^2)[a]	Littoral area (%)[a]	Shore line (km)[a]	Max depth (m)[a]	Drainage Area (km^2)[a]
Como	44.98148	-93.14070	0.29	96%	2.8	4.7	6.9
Crosby	44.90673	-93.14928	0.28	68%	2.7	5.8	6.2
Gervais	45.01907	-93.07159	0.95	39%	5.3	12.5	3.6
Island	45.05512	-93.13651	0.24	100%	4.3	3.4	0.15
Johanna	45.04200	-93.17238	0.86	45%	4.8	13.1	11.3
Josephine	45.03517	-93.15177	0.47	70%	2.7	13.4	3.5
Long	45.07734	-93.20249	0.70	64%	6.3	9.1	52.6
Owasso	45.04080	-93.12354	1.52	78%	9.1	11.3	8.8
Silver E.	45.03002	-92.98606	0.31	93%	3.1	5.5	1.8
Silver W.	45.04669	-93.22614	0.29	88%	3.3	14.3	2.0
Snail	45.07130	-93.12265	0.64	82%	3.9	9.1	3.9

[a]Determined by the Minnesota DNR Fisheries office[258]

Table C-4. Detailed summary of groundwater well sampling locations in the present study. All samples were collected as part of the Minnesota Department of Natural Resources (MN DNR) County Geologic Atlas (CGA) program.[259]

County	Well ID[a]	Latitude (WGS1984)	Longitude (WGS1984)	Predominant Land Use	Elevation (m)[b]	Depth below ground level (m)[b]
Hennepin	140190	45.12013	-93.52294	Agricultural	285.0	27.1
	169539	45.15311	-93.47905	Agricultural	281.0	21.0
	204828	45.07333	-93.42610	Urban	274.3	24.4
	451520	45.17377	-93.58975	Agricultural	289.9	29.6
	522366	45.21375	-93.43960	Urban	266.7	19.5
	792454	45.16702	-93.42994	Agricultural	276.5	26.5
Hubbard	639534	46.82113	-95.09770	Undeveloped	442.9	16.2
	665056	47.35147	-95.04264	Undeveloped	442.3	17.1
	746377	47.38615	-95.07917	Undeveloped	434.6	13.4
	758948	46.98724	-95.10803	Undeveloped	448.7	14.0
	779708	47.20406	-94.99038	Undeveloped	434.9	10.7
	803590	46.99657	-94.97645	Undeveloped	440.4	9.10
Dodge	509519	44.03865	-92.84006	Agricultural	386.5	61.9
	798778	43.88036	-92.87124	Agricultural	389.2	67.7
	638784	44.1692	-92.95193	Agricultural	369.4	52.4
	747417	44.08884	-92.88624	Agricultural	375.8	42.7
	767567	44.08629	-92.99974	Agricultural	375.5	36.0
	559968	44.00242	-92.98499	Agricultural	391.6	48.8
Cass	497142	46.88994	-94.48171	Undeveloped	424.0	25.9
	579240	47.18267	-93.86270	Undeveloped	395.3	12.2
	651304	47.11607	-94.04029	Undeveloped	399.9	16.5
	702078	46.82803	-94.54613	Undeveloped	405.7	18.3
	755486	46.44423	-94.68315	Undeveloped	393.5	19.8
	772926	46.62896	-94.56382	Undeveloped	449.7	20.7
Olmstead	101458	43.85804	-92.66529	Agricultural	399.9	43.6
	147038	43.97870	-92.27487	Agricultural	394.1	83.8
	449369	44.10068	-92.49045	Agricultural	338.6	151.2
	506837	44.13490	-92.63928	Agricultural	364.2	134.1
	590626	43.86520	-92.13538	Agricultural	344.7	175.3
	597779	43.93759	-92.62272	Agricultural	378.8	109.7
	608573	44.17565	-92.66196	Agricultural	337.4	150.9
	795327	44.11901	-92.34073	Agricultural	345.0	195.1
	817782	43.95826	-92.28838	Agricultural	382.5	138.7
	817783	43.95826	-92.28838	Agricultural	382.5	80.8
	817784	43.95826	-92.28838	Agricultural	382.5	24.4

[a]Unique Well ID values used in the Minnesota Well Index[260]

[b]Elevation and depth measurements were made by the MN DNR CGA sampling team[259]

Table C-5. Description of wastewater treatment plants. Samples were collected by Metropolitan Council Environmental Services (MCES).[261]

Name	Latitude (WGS1984)	Longitude (WGS1984)	Predominant Land Use	Mean Discharge (MGD)	Sewershed Area (km^2)[a]	Population Served[a]	Discharge Point
Blue Lake	44.79756	-93.43028	Urban	27	768.0	300000	Minnesota River
Eagles Point	44.78892	-92.91999	Urban	4.8	153.3	60000	Mississippi River
East Bethel	45.30904	-93.24293	Undeveloped	0.47[a]	59.4	12000	Groundwater
Empire	44.66668	-93.10865	Agricultural	10.7	561.4	150000	Mississippi River
Hastings	44.74573	-92.85074	Agricultural	1.7	109.0	20000	Mississippi River
Metropolitan	44.92775	-93.04530	Urban	172	1888.8	1800000	Mississippi River
Seneca	44.82962	-93.20737	Urban	21.9	316.5	250000	Minnesota River
St. Croix Valley	45.04061	-92.79345	Urban	3.5	44.5	30000	St. Croix River

[a]Determined by MCES[261]
Mean discharge estimates were not available for East Bethel. The maximum capacity was used.
MGD = millions of gallons per day.

C.3 Plankton Sampling

Zooplankton samples were collected into a Dolphin plankton bucket (74 μm, Dolphin) by vertical tow (~1 m/s) through the epilimnion to the surface using a net (30 μm width, 80 μm mesh) equipped with a length-calibrated rope. The depth of the epilimnion varied by lake and season and was determined as the depth which DO is less than 0.5 mg/L. Samples were transferred into plastic pouches (Whirl-Pak) and preserved with a 2% Lugol's solution. Two-meter (2 m) composite samples from the top 2 m of the water column were taken for phytoplankton enumeration. These samples were preserved in an HDPE bottle with a 1% Lugol's solution.

Samples of planktonic assemblages were collected from Como Lake (n = 11) and Crosby Lake (n = 10) and Island, Johanna, Josephine, Long, Silver W., and Silver E. Lakes (n = 8) between April and September 2019. The three most detected phytoplankton genera were *Cryptomonas* (73% detection, median = 269 cells/mL), *Oscillatoria* (61%, 3700 cells/mL), and *Artabaena* (58%, 430 cells/mL); *Aphanizomemnon* was found at the highest concentrations but only in three samples (5%, 25000 cells/mL; Figure C-7). *Naupli* (100%, 13 counts/L) and *Cyclopoid* (98%, 10 counts/L) were the most common zooplankton genera; Naupli was also the most abundant (Figure C-8). The Shannon-Wiener Diversity Index of each sample was calculating with the vegan (Version 2.5-6) package in R to quantify the taxonomic distribution of each plankton community.

Table C-6. Summary of plankton taxonomic groups surveyed in the present study. Samples were collected by the Ramsey County Environmental Services, Lakes Management division.[257]

	Plankton Taxonomic Group		
Phytoplankton	*Actinastrum*	*Dinobryon*	*Quadrigula*
	Anabaena	*Elakototrhix*	*Radiococcus*
	Ankistrodesmus	*Euglena*	*Scenedesmus*
	Aphanizomenon	*Fragilaria*	*Staurastrum*
	Aphanocapsa	*Gloeocapsa*	*Stephanodiscus*
	Asterionella	*Gomphosphaeria*	*Stylosphaeribium*
	Ceratium	*Haemetococcus*	*Tetraedron*
	Chlamydomonas	*Mallomonas*	*Ulothrix*
	Chloroccum	*Melosira*	
	Coelastrum	*Microcystis*	
	Cosmarium	*Navicula*	
	Crucigenia	*Oocystis*	
	Cryptomonas	*Oscillatoria*	
	Cyclotella	*Phacus*	
	Glenodinium	*Pediastrum*	
Zooplankton	*Cyclopoid*	*Daphnia*	*Diaphnosoma*
	Calanoid	*Bosmina*	*Leptodora*
	Naupli	*Chydorus*	
	Rotifers	*Ceriodaphnia*	

C.4 Details of LC-MS/MS Analysis Method

Table C-7. Details of neonicotinoid analytes and multiple reaction monitoring (MRM) parameters.

Compound	Exact mass	Parent mass (m/z)	Product ion mass (m/z)	Collision energy (V)	RT (min)
Imidacloprid	256.060127	256.04	209.05	14	10.93
			175.05	25	
Clothianidin	249.008723	250.02	131.94	18	10.44
			169.05	15	
Thiamethoxam	291.019288	292.07	211.05	14	9.08
			181.09	20	
Acetamiprid	222.067224	223.10	126.01	18	11.88
			56.07	15	
Thiacloprid	252.023645	253.06	126.13	22	13.57
			90.08	38	
Desnitro-Imidacloprid	210.067224	211.11	126.06	24	10.91
			90.14	38	
Imidacloprid-Urea	211.05124	212.08	128.09	18	9.55
			99.11	22	
Imidacloprid-Olefin	253.036652	254.07	205.15	15	8.85
			171.18	20	
Acetamiprid-N-Desmethyl	208.051574	209.11	126.06	20	10.67
			90.14	35	
Thiacloprid Amide	270.03421	271.07	254.19	12	9.98
			228.1	15	
^{13}C-caffeine[a]	197.09044	198.12	140.07	22	7.22
			112.07	26	
Imidacloprid-d_4[b]	259.077409	260.04	213.05	14	10.94
			179.05	25	
Clothianidin-d_3[b]	252.027554	253.02	172.05	15	10.36
			131.94	18	

[a]Internal standard added to each sample
[b]Analytical surrogate added to each sample

C.5 Quality Assurance

C.5.1 Sampling sequence.

All sample sequences analyzed by LC-MS/MS were set up as follows: The sequences were bracketed at the beginning and end by a sequence of 7 calibration standards with individual neonicotinoid concentrations from 0.1 to 300 μg/L, in order of increasing concentration. After the initial set of calibration standards, a solvent blank was injected to assess carryover and background noise. Five experimental samples were then analyzed followed by another solvent blank and an injection of the lowest calibration standard for continued calibration verification. The pattern of 5 samples, 1 solvent blank, and 1 verification injection was repeated for the whole sequence. A typical sample sequence contained approximately 100 injections.

C.5.2 Calculation of RPD

The relative percent difference (RPD) was defined as the difference in the calculated concentration between an initial and a duplicate sample (eq C-1). Each duplicate sample was collected immediately after the initial sample and processed through the same extraction and analysis methods. The initial sample was used for the data analysis; the duplicate sample was only used to calculate the RPD.

$$\mathrm{RPD}(\%) = \frac{c_{\mathrm{sample}} - c_{\mathrm{duplicate}}}{\left(c_{\mathrm{sample}} + c_{\mathrm{duplicate}}\right)/2} \times 100\% \qquad (C-1)$$

Table C-8. Chemical information and results of quality assurance and control for all neonicotinoids. Descriptions of MDLs (eq C-1) and LRLs are provided in the main text. The MDLs are reproduced in Table 4-1.

Compound	Molecular formula	MDL (ng L^{-1})	LRL (ng L^{-1})	RPD (%)
Acetamiprid	$C_9H_9ClN_4$	0.42	0.84	11 ± 8
Acetamiprid-N-Desmethyl	$C_9H_9ClN_4$	0.48	0.95	16 ± 9
Clothianidin	$C_6H_8ClN_5O_2S$	0.42	0.84	12 ± 5
Imidacloprid	$C_9H_{10}ClN_5O_2$	0.23	0.45	16 ± 4
Imidacloprid-Olefin	$C_9H_8ClN_5O_2$	1.70	3.40	NA
Imidacloprid-Urea	$C_9H_{10}ClN_3O$	1.52	3.04	NA
Desnitro-Imidacloprid	$C_9H_{11}ClN_4$	0.71	1.42	NA
Thiacloprid	$C_{10}H_9ClN_4S$	0.60	1.20	25 ± 18
Thiacloprid-Amide	$C_{10}H_{11}ClN_4OS$	0.65	1.29	20 ± 12
Thiamethoxam	$C_8H_{10}ClN_5O_3S$	0.12	0.23	19 ± 13

[a]NA = all measurements in samples and replicates were < MDL

C.5.3 Calculation of Recovery in Spiked Samples

Two liters of sample were collected during random sampling events to assess the recovery in spiked water samples. Samples were prepared by adding 10 ng from a stock solution containing 10 μg/L of each neonicotinoid to 1 L of the water samples or Optima-grade water. The spiked samples and the remaining 1 L of water were then processed through the entire analytical procedure outlined in the main text. The percent recoveries of the spiked samples were calculated according to eq C-2.

$$\text{Recovery}(\%) = \frac{c_{\text{spiked}} - c_{sample}}{c_{expected}} \times 100\% \qquad (C-2)$$

where c_{spiked} and c_{sample} are the neonicotinoid concentrations in the water samples with and without the neonicotinoid spike, respectively, and $c_{expected}$ is the expected neonicotinoid concentration in the spiked sample.

C.6 Calculation of Neonicotinoid Toxicity

The calculation of the pesticide toxicity index (PTI) is outlined in the main text and uses the values provided in

Table C-9. The calculated PTIs for five major taxonomic groups of aquatic species is provided in

Table C-10.

Table C-9. Taxon-specific toxicity concentrations ($TC_{i,t}$) for each combination of neonicotinoid, *i*, and taxonomic group, *t*. Concentrations are the average of acute LC50s of the mortality or immobility endpoint for each combination of taxon and neonicotinoid.

	Taxon-specific toxicity concentrations (mg L^{-1} a.i.)[a]				
	Crustaceans	Fish	Molluscs	*Daphnia*	Plants
Acetamiprid	0.08	14.43	n.d.	49.8[b]	19.2
Clothianidin	15.6	104.2[b]	2.09	0.5	9.7
Imidacloprid	0.076	186.9	2.32	40.5	1.2
Thiacloprid	5.23	30.2	ND	85.1[b]	0.92
Thiamethoxam	8.05	125[b]	6.20	100[b]	20

[a]all values obtained from the U.S. EPA ECOTOX database[215] unless otherwise noted
[b]obtained from the Pesticide Properties DataBase (PPDB)[60]
a.i. = active ingredient. ND = no data

Table C-10. Median and maximum pesticide toxicity indexes (PTIs) for five major aquatic taxa in each type of waterbody and land-use type. All samples from the present study are included in the PTI calculations.

		log(PTI)									
		Crustaceans		Molluscs		Fish		*Daphnia*		Plants	
	n	Med	Max	Med	Max	Med	Max	Med	Max	Med	Max
Total	157	-6.0	-4.9	-6.2	-4.3	-7.9	-5.9	-5.9	-4.7	-8.8	-7.4
Lakes	53	-5.9	-5.4	-6.3	-5.3	-8.1	-7.0	-6.3	-4.7	-8.9	-8.4
Rivers	61	-5.8	-4.9	-5.5	-4.3	-7.2	-5.9	-5.1	-3.7	-8.5	-7.8
Wells	35	-7.0	-5.3	-6.3	-5.1	-8.0	-6.8	-6.2	-4.5	-9.4	-8.5
WWTP	8	-5.5	-5.3	-5.7	-4.8	-7.4	-6.5	-5.4	-4.2	-7.8	-7.4
Agricultural	48	-5.9	-4.9	-5.2	-4.3	-6.9	-5.9	-4.7	-3.7	-8.6	-7.8
Undeveloped	17	-7.0	-6.8	-6.2	-4.0	-7.9	-7.7	-5.7	-5.5	-9.4	-8.9
Urban	92	-6.0	-4.9	-6.2	-4.8	-8.0	-6.5	-6.1	-4.2	-8.7	-7.4

Table C-11. Spearman rank correlation coefficients of PTIs for five major aquatic taxa with drainage area and each type of land-use. Drainage area correlations do not include groundwater samples (n = 35). All samples from the present study were included in the calculations for each land-use type.

		Crustacean		Molluscs		Fish		*Daphnia*		Aquatic Plants	
Parameter	n	ρ	*p*-value	ρ	*p*-value	ρ	*p*-value	ρ	*p*-value	ρ	*p*-value
Drainage area	122	0.211	0.298	0.622	<0.001*	0.650	<0.001*	0.636	<0.001*	0.411	<0.001*
Agricultural	42	0.448	<0.001*	0.542	<0.001*	0.486	<0.001*	0.484	<0.001*	0.539	<0.001*
Urban	107	-0.089	0.300	-0.246	0.003*	-0.325	<0.001*	-0.250	0.002*	0.249	0.003*
Undeveloped	16	0.016	0.855	0.077	0.360	0.144	0.090	0.104	0.198	-0.373	<0.001*

*p-value < 0.05

C.7 Hydrologic Calculations

C.7.1 Loads and yields

The instantaneous loads of neonicotinoid for all WWTPs and the set of rivers and streams that have measured streamflow were made by multiplying the neonicotinoid concentration in each sample by the streamflow at the time of sampling (eq C-3).

$$\text{neonicotinoid load (g/d)} = Q \times c_i \times \text{conversion factors} \qquad (C-3)$$

where Q is the instantaneous discharge (m^3/s) and c_i is the concentration (ng/L) of the neonicotinoids. For rivers and streams, the instantaneous yields were calculated by dividing the loads by the drainage area (eq C-4). Per-capita loads at WWTPs were calculated by dividing the neonicotinoid loads by the population served by each plant (eq C-5).

$$\text{neonicotinoid yield } \left(\mu g/km^2/d\right) = \frac{\text{neonicotinoid load } (\mu g/d)}{\text{drainage area } (km^2)} \qquad (C-4)$$

$$\text{per-capita load } \left(\mu g/\text{person}/d\right) = \frac{\text{neonicotinoid load } (\mu g/d)}{\text{population (people)}} \qquad (C-5)$$

C.7.2 Calculation of lake turnover

The average flow rate of water through Como Lake was determined from continuous measurements made at the outlet of Como Lake near the southeast corner of the lake. The hydraulic residence time of the lake was calculated by dividing the volume of the lake by the instantaneous discharge at the lake outlet. The fraction of total lake volume exchanged during and after a rain event was calculated by first integrating a plot of lake discharge (y-axis) versus time (x-axis) for a given period with elevated discharge. The value of the integral was then divided by the total lake volume (eq C-6).

$$\text{fraction of turnover} = \frac{\int_{t_0}^{t_f} Q \, dt}{V} \qquad (C-6)$$

where t_0 and t_f (in s) are the initial and final times of the elevated discharge period, Q is the instantaneous discharge (m^3/s), and V is the total lake volume (~580,000 m^3).

C.8 Neonicotinoid safe consumption guidelines

Table C-12. Human safe consumption levels.[60]

Compound	Acceptable daily intake (mg/kg-b.w./d)[a]
Acetamiprid	0.025
Clothianidin	0.097
Imidacloprid	0.060
Thiacloprid	0.010
Thiamethoxam	0.026

[a]b.w. = body weight

C.9 Additional Figures

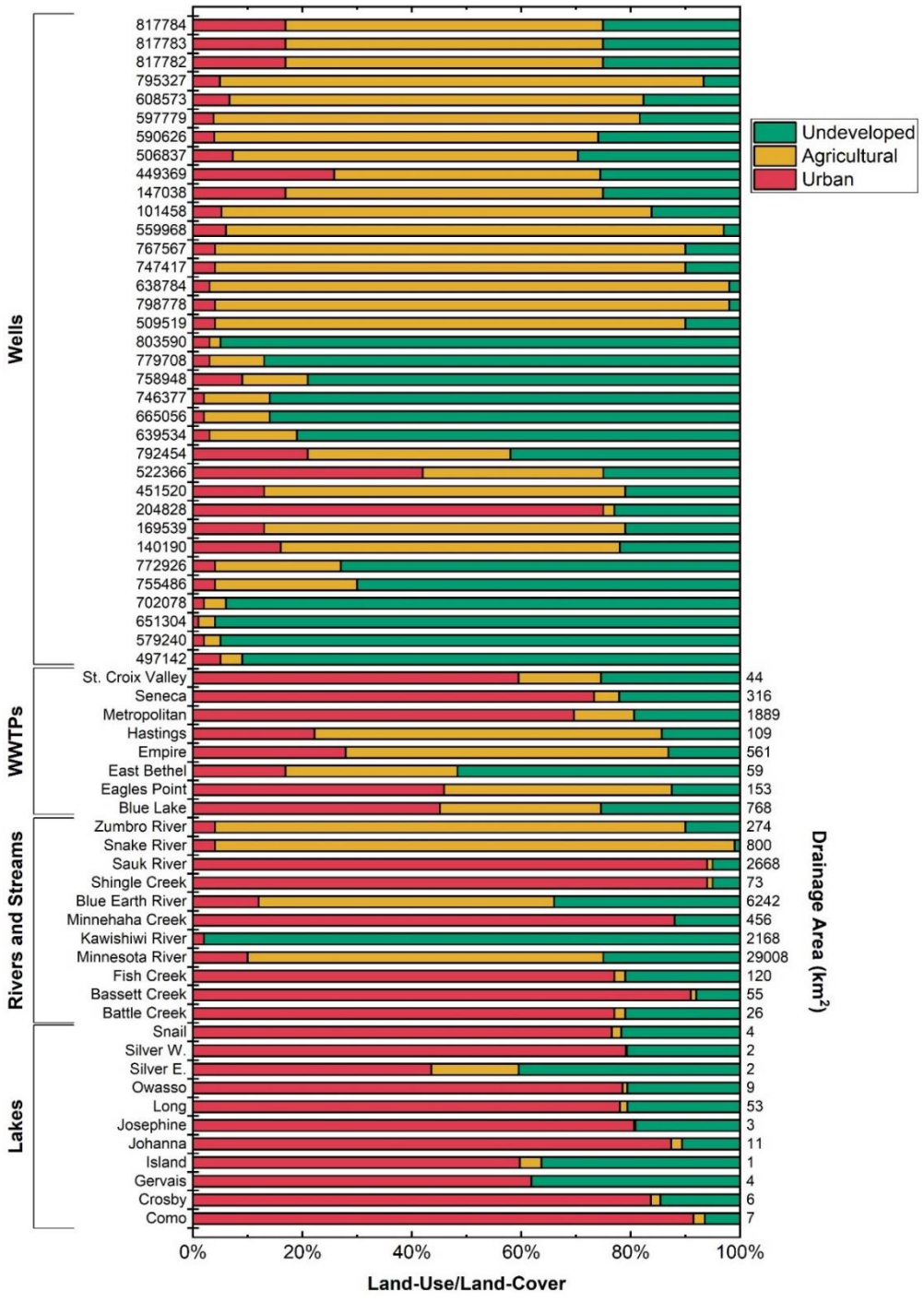

Figure C-1. Land use distribution and drainage areas for all sampling locations in this study.

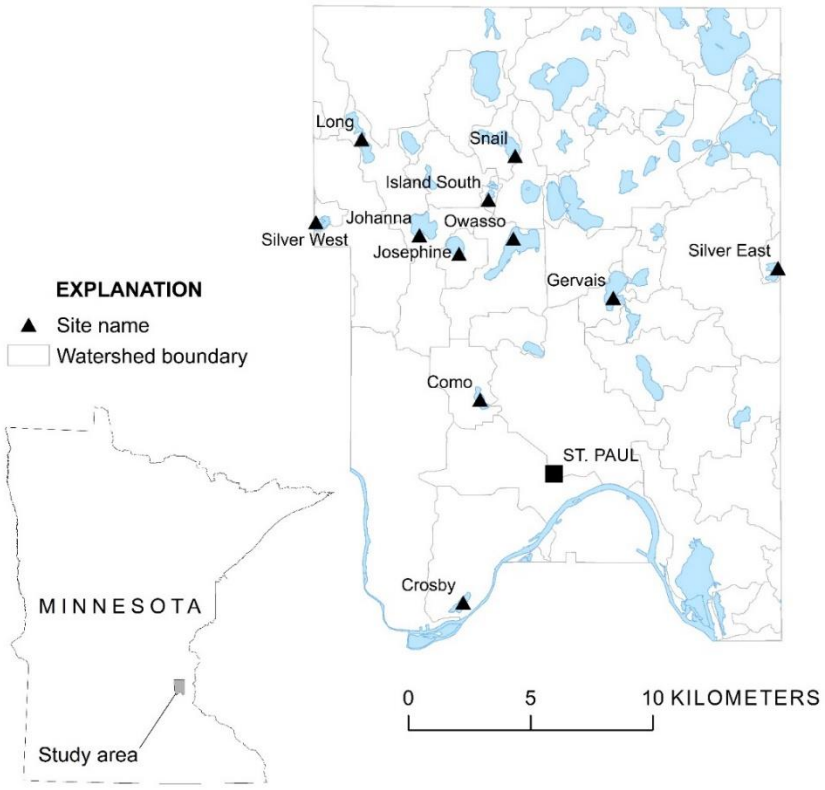

Figure C-2. Detailed map of the lakes surveyed for the present study. The zoomed in portion on the right shows the outline of Ramsey County, MN with the solid lines denoting watershed boundaries.

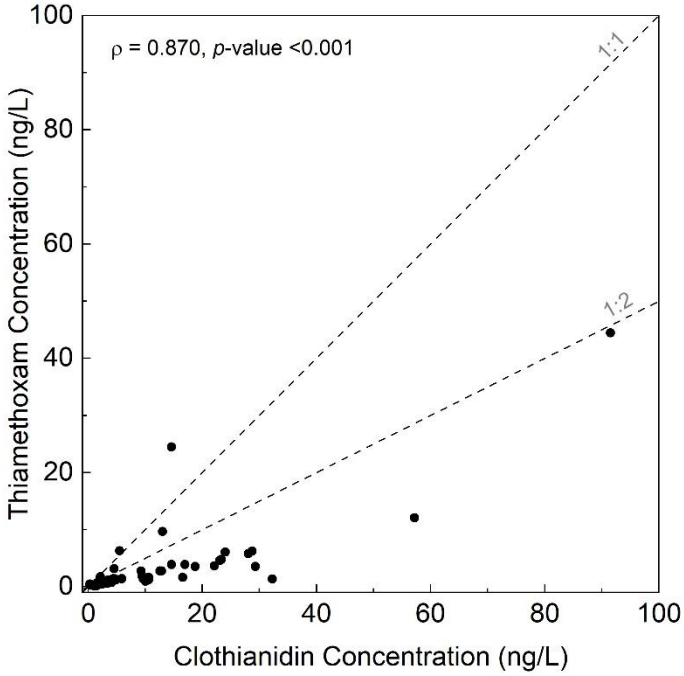

Figure C-3. Thiamethoxam versus clothianidin concentrations in all samples. The ρ and *p*-values determined from Spearman's rank correlation analyses are provided in each plot. The dotted lines indicate a 1:1 and 1:2 relationship and are provided to guide the reader's eye.

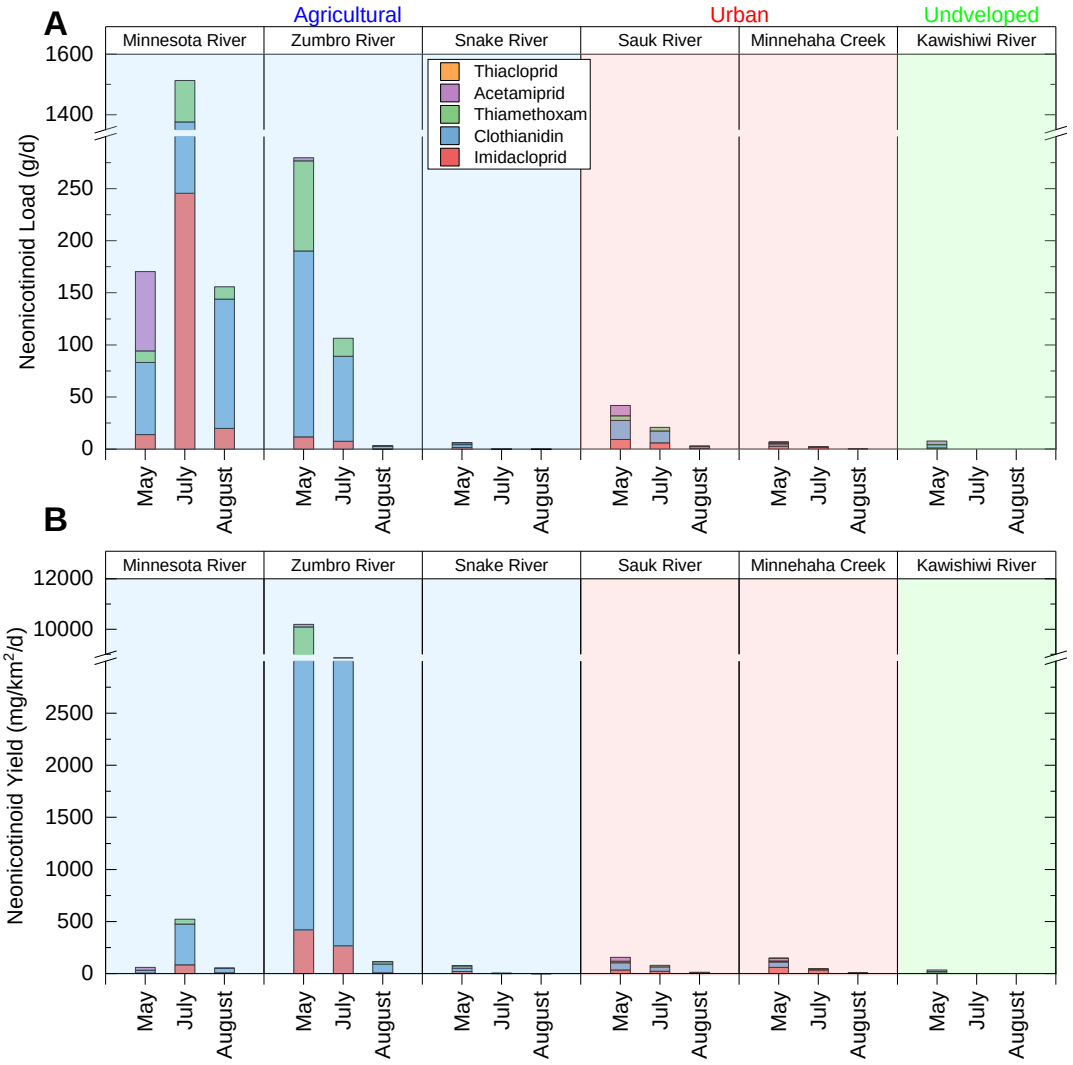

Figure C-4. Instantaneous neonicotinoid (A) loads and (B) yields for each of the rivers and streams where continuous discharge measurements were made.

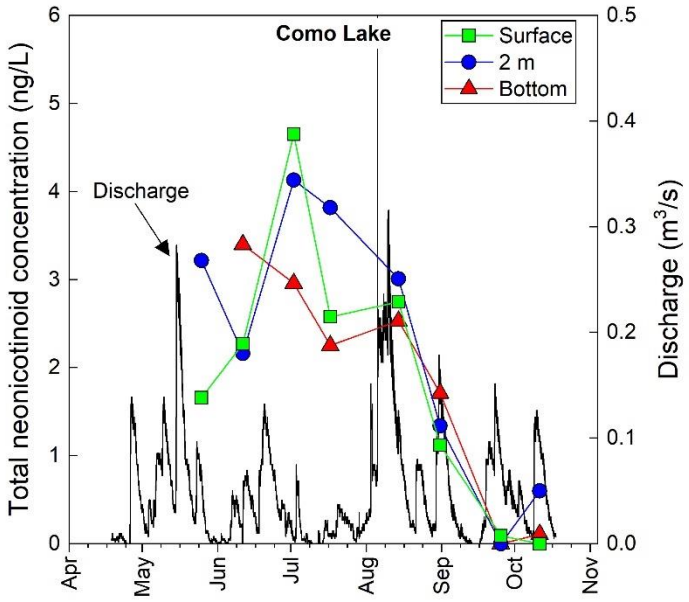

Figure C-5. Total neonicotinoid concentration (left y-axis) at three different depths and instantaneous discharge measurements (right y-axis) from Como Lake during 2019.

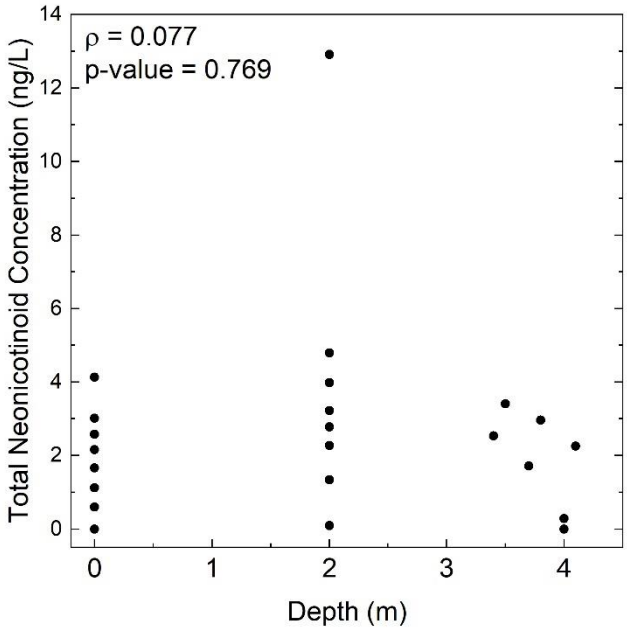

Figure C-6. Total neonicotinoid concentration versus depth at Lake Como. There was no significant correlation between these parameters.

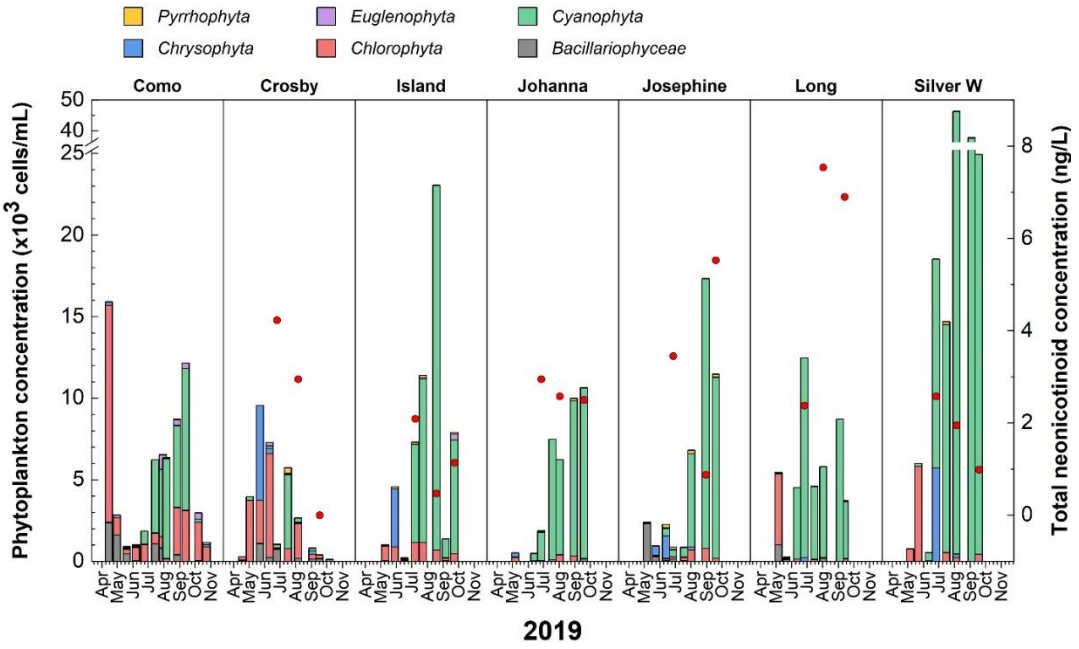

Figure C-7. Total phytoplankton (columns, left y-axis) and neonicotinoid concentrations (circles, right y-axis) measured in 7 Ramsey County lakes during 2019.

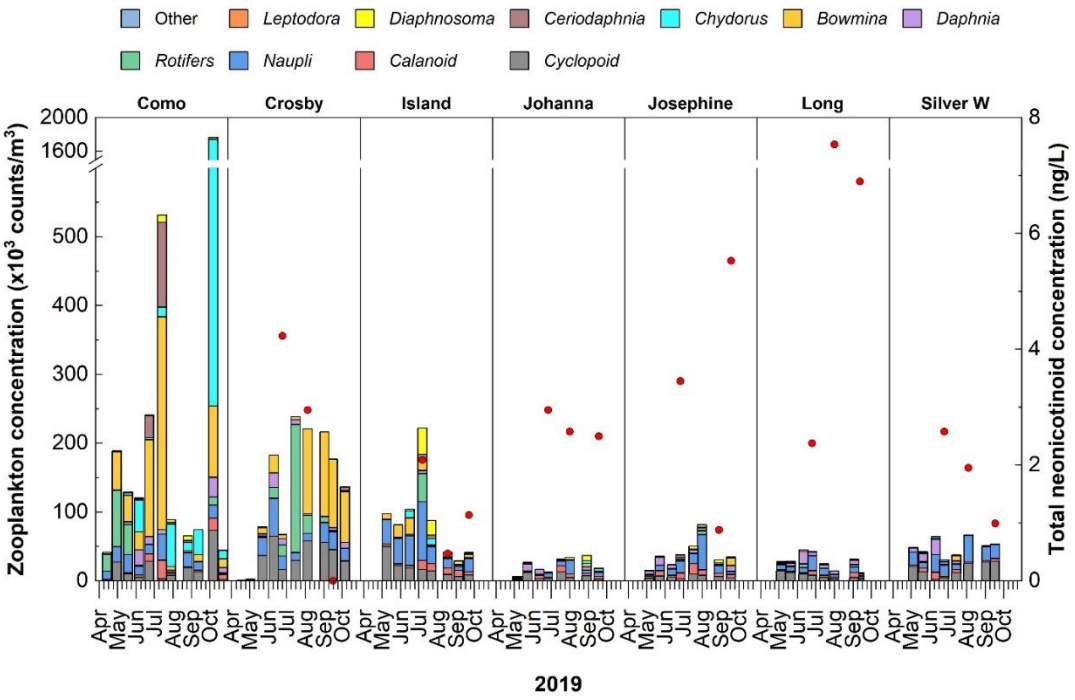

Figure C-8. Total zooplankton (columns, left y-axis) and neonicotinoid concentrations (circles, right y-axis) measured in 7 Ramsey County lakes during 2019.

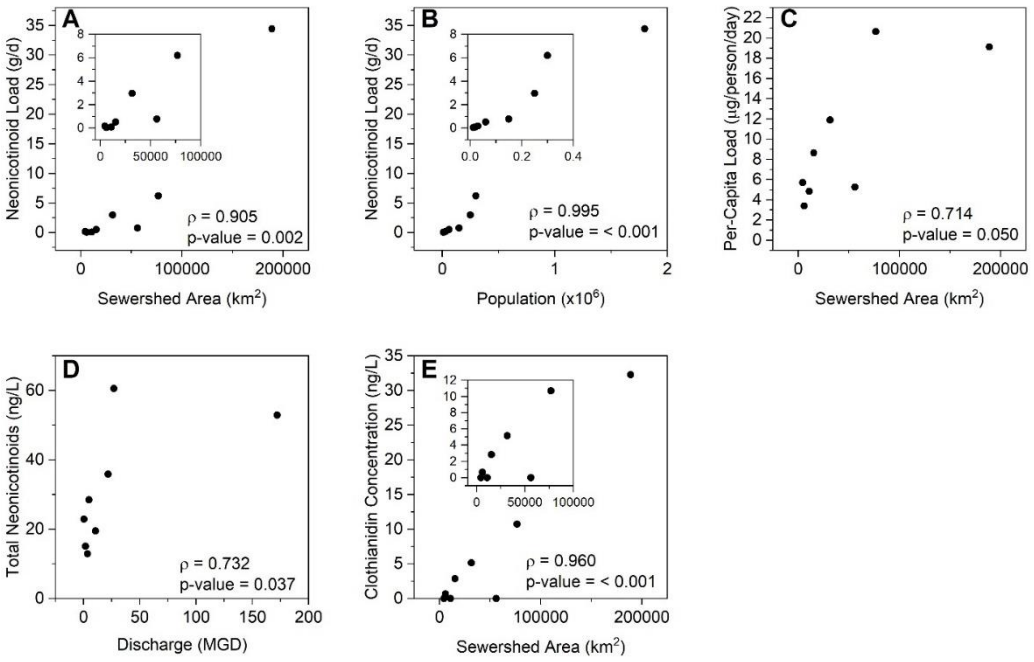

Figure C-9. Correlations for data collected from all WWTPs. The ρ and *p*-values determined from Spearman's rank correlation analyses are provided in each plot. The Metropolitan WWTP has a much greater sewershed area and population served than the other WWTPs. The results without the Metropolitan WWTP are provided in each of the figure insets. Total neonicotinoid load versus (A) sewershed area (inset values, ρ = 0.857, *p*-value = 0.024) and (B) population size (inset values, ρ = 0.990, *p*-value = < 0.001). (C) Per-capita total neonicotinoid load versus sewershed area, (D) Total neonicotinoid load versus mean WWTP discharge (MGD = millions of gallons per day), and (E) clothianidin concentration vs sewershed area (inset values, ρ = 0.556, *p*-value = 0.195).

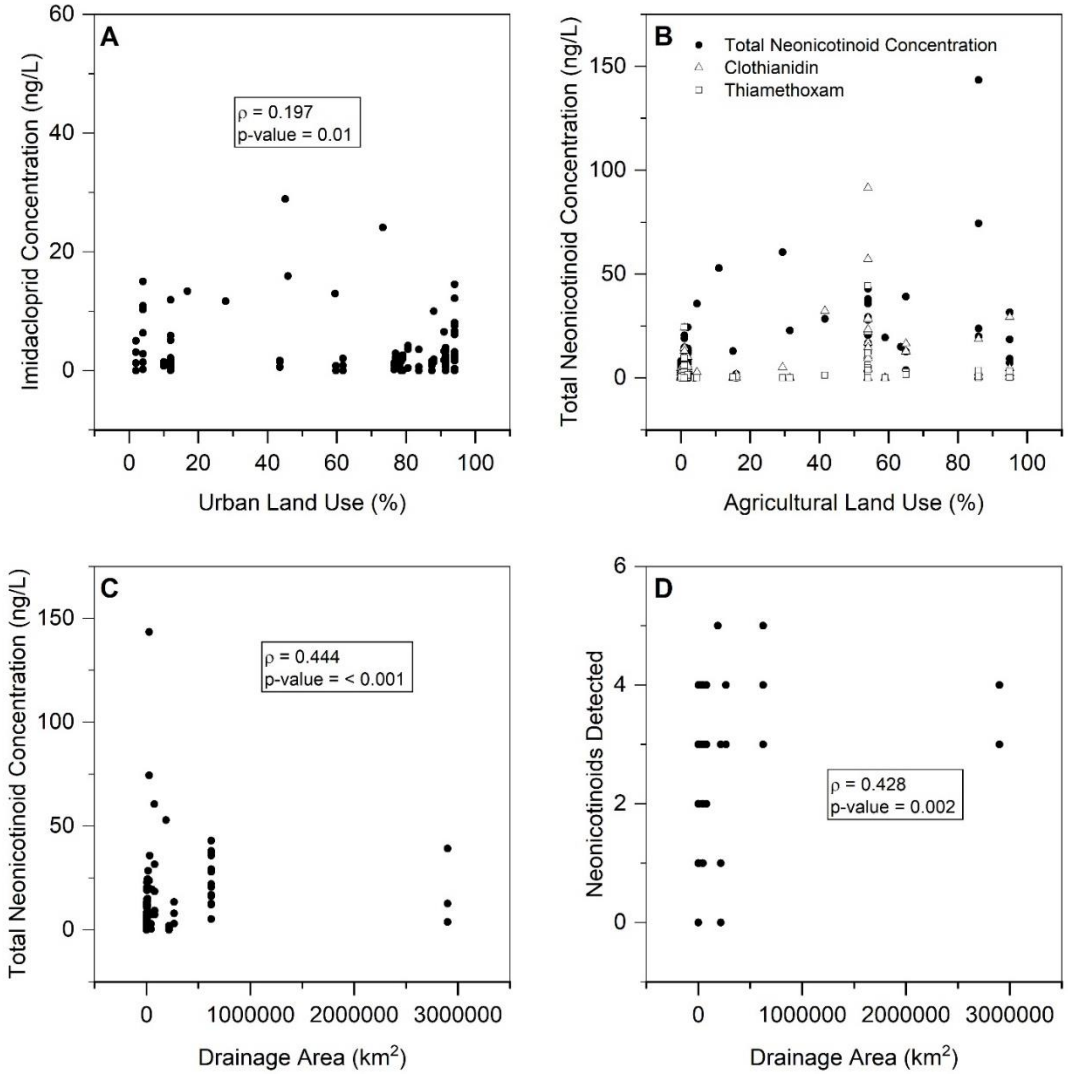

Figure C-10. Correlations for data collected from all sampling locations. The ρ and p-values determined from Spearman's rank correlation analyses are provided in each plot. (A) Imidacloprid concentration versus urban land use (a significant correlation, p-value < 0 .05). (B) Percent agricultural land use versus concentrations of total neonicotinoids (ρ = 0.549, p-value < 0.001), clothianidin (ρ = 0.403, p-value < 0.001), and thiamethoxam (ρ = 0.255, p-value = 0.001). Drainage area versus (C) total neonicotinoid concentrations and (D) the number of neonicotinoids detected.

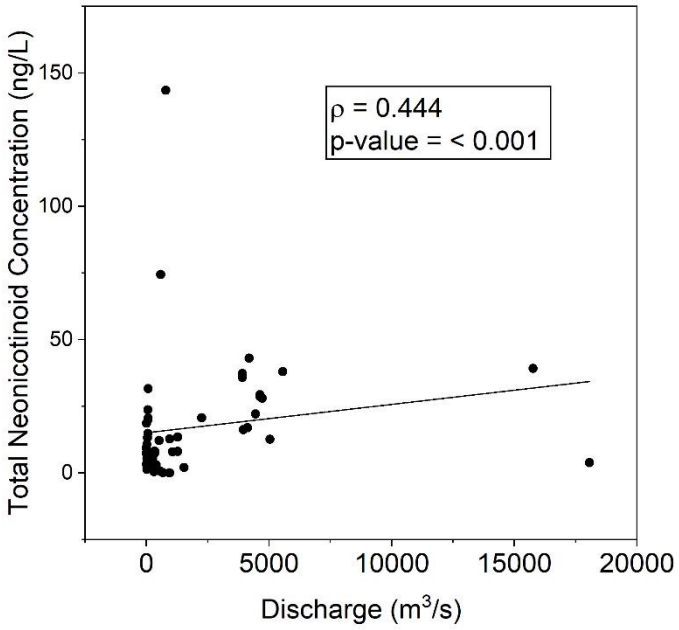

Figure C-11. Total neonicotinoid concentration versus discharge for all rivers and streams where continuous discharge measurements were made.

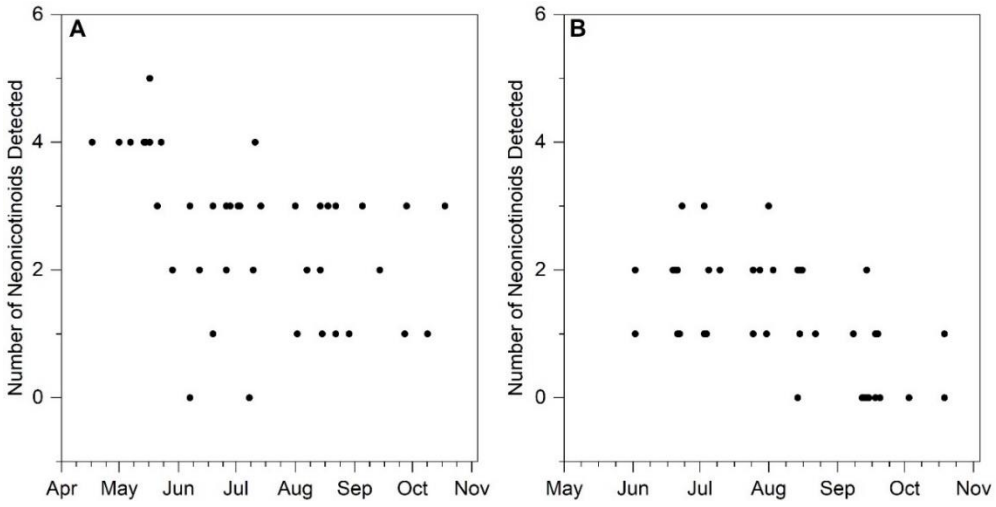

Figure C-12. Total number of neonicotinoids detected in water samples from (A) rivers and streams and (B) lakes. No significant Spearman's rank correlations (p-value < 0.05) were observed.

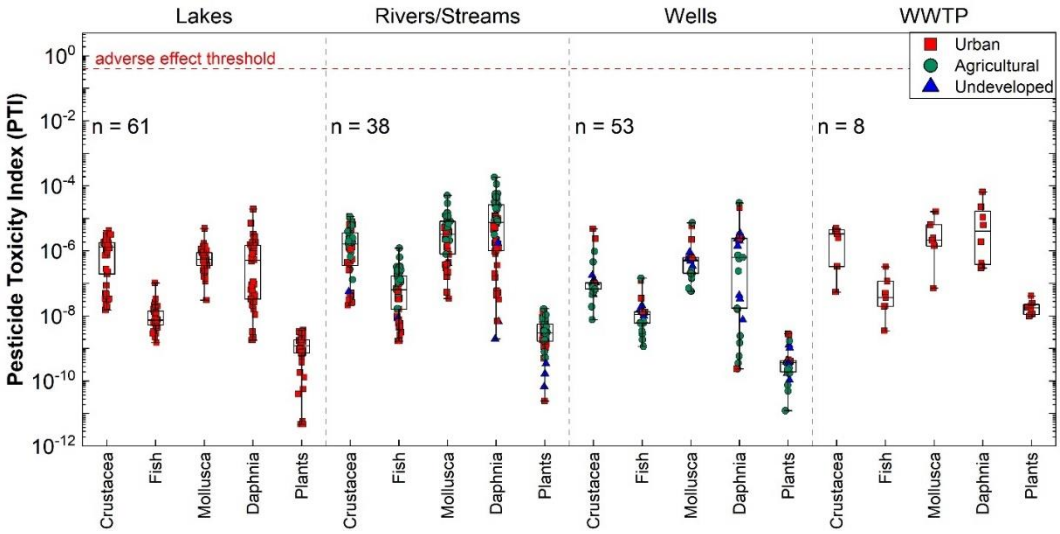

Figure C-13. Pesticide toxicity indexes (PTIs) for 5 taxonomic group of aquatic organisms separated by the type of waterbody. Each point indicates one individual sample. Box plots represent the median, 25th percentile, and 75th percentile and minimum and maximum values are shown by the whiskers.

Appendix D. Mineralogy and buffer identity effects on RDX kinetics and intermediates during reaction with natural and synthetic magnetite

This chapter has been published in the journal *Chemosphere* and is reproduced with permission.

Strehlau, J.H.; Berens, M.J.; Arnold, W.A. *Chemosphere*. **2018**, *213*, 602–609. doi: 10.1016/J.CHEMOSPHERE.2018.09.139

D.1 Overview

Hexahydro-1,3,5-trinitro-1,3,5-triazine (RDX) is known to undergo reduction mediated by ferrous iron in the presence of minerals, including magnetite. Idealized laboratory conditions may not provide representative reaction kinetics or pathways compared to field conditions. The effects of magnetite mineral morphology, the aquifer material matrix, the presence of aqueous Fe(II), and the buffer identity on RDX reduction kinetics and intermediate formation are investigated in this work. Reactions in bicarbonate buffer were substantially slower than those performed in 3-(N-morpholino)propanesulfonic acid (MOPS) buffer, and the presence of quartz and clays in magnetite-containing aquifer material resulted in slower reaction kinetics and production of additional iron oxide phases. Buffer identity also changed the rate controlling step and reaction product distribution. Conditions as close to those expected in field systems are necessary to evaluate the reaction rates and pathways of RDX in reduced groundwater systems.

D.2 Introduction

High explosive materials, including hexahydro-1,3,5-trinitro-1,3,5-triazine (RDX), have been historically used for both military and commercial practices[262]. Improper

disposal, incomplete detonations, and accidental spills have led to detection in groundwater systems, especially near military bases and ammunition plants.[263–266] Because RDX is associated with negative impacts and risk to both plant and human health,[267,268] remediation strategies and outcomes are of concern. RDX does not sorb strongly to soil,[269] thus the biotic and abiotic chemical transformations in groundwater systems are generally studied from both laboratory and field approaches. For example, it has been demonstrated that both Fe(II)-containing minerals and Fe(II) adsorbed on Fe(III)-containing minerals are efficient reductants for highly oxidized molecules such as explosives.[5,76,270] Magnetite (Fe_3O_4) is a mixed-valent iron oxide, containing both structural Fe(II) and Fe(III) and is reported to be capable of both directly donating electrons from mineral-bound Fe(II) as well as mediating electron transfer from aqueous Fe(II) via adsorption and subsequent interfacial electron transfer[77,88,271]. Magnetite is also naturally occurring and has been detected in aquifer materials near ammunition plants or detonation ranges, and it has been proposed to be responsible for abiotic contaminant reduction in groundwater[124].

Microcosm experiments have allowed researchers to identify several possible RDX degradation pathways that result in a variety of intermediates and products produced under reducing conditions, including hexahydro-1-nitroso-3,5-dinitro-1,3,5-triazine (MNX), hexahydro-1,3-dinitroso-5-nitro-1,3,5-triazine (DNX), hexahydro-1,3,5-trinitroso-1,3,5-triazine (TNX) via reduction, and other N- and C-containing products from hydrolysis or biodegradation (Figure D-6[14,80,270,272–277]). While data from laboratory microcosm experiments can serve as predictors for the environmental fate of RDX, it is important to emphasize the significant impact that environmental or solutions conditions

may have on natural attenuation of contaminants. These variables not only affect the rate of contaminant degradation but also the degradation products, evolving mineralogy, and solution chemistry. RDX reduction is influenced by various factors, including mineral composition and aqueous Fe(II) concentration. Reduced iron has been shown to be important in RDX reduction, with bio-reduced minerals producing nitroso intermediates (predominantly MNX) in a system where pH was controlled with 3-(N-morpholino)propanesulfonic acid (MOPS) buffer [270]. Complexed iron in solutions containing Good's buffers (AMPSO 100mM pH 8.5–9.25;[272] 25 mM MES pH 5–6.25, 25 mM MOPS pH 6.6–7.5, 25 mM EPPS pH 7.6–8.6[275]) also reduces RDX, MNX, DNX, and TNX, but ring cleavage is the proposed reaction pathway for both RDX and the nitroso intermediates. RDX is also reduced in natural sediments under iron reducing conditions[14,276] and by quinone electron shuttles[277] in simulated groundwater (bicarbonate buffer), with minimal MNX production. Greater yields of MNX were seen with Fe(II)/goethite as the reductant.[14] Clearly, the identities of the reductant and other factors will influence the conclusions drawn regarding RDX fate in the environment.

In this work, abiotic reduction of RDX by both synthetic and natural magnetite was explored to examine the effects of mineral morphology, the aquifer material matrix, the presence of aqueous Fe(II), and the buffer identity on RDX reduction kinetics and intermediate formation. To better predict natural attenuation processes in the field, the reactivity of naturally sourced magnetite was compared to synthetic magnetite, offering insight into the influences that natural systems have on microcosm observations. To simulate iron reducing conditions without the complicating factors/competing reaction pathways of a biologically active system, the reactors were amended with ferrous iron.

Aquifer material was collected from the Twin Cities Army Ammunition Plant (TCAAP) in Arden Hills, MN, where it is known that magnetite is present.[124] While RDX has not been detected in TCAAP groundwater, the site has faced concerns with groundwater contamination from chlorinated solvents in the 1980s and from 1,4-dioxane in recent years,[278] and it provides a material where natural attenuation of oxidized groundwater contaminants is occurring.[124] Comparing natural and synthetic materials and different solutions conditions allows assessment of not only how different conditions affect the rates and products of abiotic RDX reduction, but also the testing necessary to assess the potential for natural attenuation to be a viable component of groundwater remediation strategies.

D.3 Experimental

D.3.1 Materials

Aquifer material within the saturated zone was collected from the south central area of TCAAP by sonic drilling, near the location of the previous study by Ferrey et al. (2004).[124] Material collected between 44 and 54 m below the surface was separated by depth into four 5-gallon buckets and sealed for transportation back to the laboratory. Material at each depth (100 – 500 g) was dried in a glove bag (Coy, 95% N_2/5% H_2) for use in batch experiments and for material characterization. The magnetic extract of the aquifer material (noted in this paper as "TCAAP extract") was collected by weighing 5.00 ± 0.05 g of the dried 44 m aquifer material in a weigh boat with a neodymium magnet held to the exterior side. The weigh boat was then gently rotated, allowing particles to magnetically adhere to the side. This extraction process was repeated on the

loose material 10 – 20 times, until 0.170 ± 0.005 g magnetic extract was obtained. Repeated trials showed that this was the maximum reproducible amount of extractable magnetic material that could be obtained. All steps to collect the magnetic material were performed within the glovebag.

Synthetic magnetite nanoparticles were prepared by oxidation of an Fe(II) solution as described by Schwertmann and Cornell (detailed in Section D.8).[170] The Supplementary Material for Appendix D is provided in Section D.8. RDX was synthesized with several safety precautions by nitration of hexamethylenetetramine (HMTA) as detailed in the Section D.8.[279] It should be highlighted that the procedure emphasizes the use of purum p.a. > 99% fuming nitric acid (Sigma Aldrich). Less pure fuming nitric acid was used in early attempts and resulted in a violent, exothermic reaction, as described in the Section D.8. We emphasize the importance of reagent choice and purity for reproducibility and safety in this procedure.

D.4 Batch experiments

Batch reactors were prepared in 40 mL serum bottles inside the anaerobic glove bag. The buffer, prepared in ultrapure water (Milli-Q, 18.2 MΩ cm), was either bicarbonate buffer, prepared by adding 0.42 g $NaHCO_3$ (Sigma Aldrich, ACS) to 0.5 L deoxygenated ultrapure water and adjusting to pH 7 using 1 M H_2SO_4 (Fisher, ACS), or MOPS buffer, prepared by adding 2.62 g or 0.52 g MOPS (Sigma Aldrich, 99.5%) to 0.25 L deoxygenated water and adjusting to pH 7 using 5 M NaOH (Fisher, ACS). A stock solution of aqueous Fe(II) containing 175 mM $FeCl_2 \cdot 4\ H_2O$ (Fisher, ≥ 98%) in ultrapure

water with 3% 1 M HCl was stored in the glove bag and remade after one week of storage.

Reactors were prepared at approximately the same total Fe loading (0.73 – 0.89 g/L depending on mineralogy and depth collected) by adding either 5.00 ± 0.05 g TCAAP aquifer material, 0.170 ± 0.005 g TCAAP extract, or 0.030 ± 0.005 g synthetic magnetite with 34.6 mL of buffer. For reactors containing aqueous Fe(II), 34.4 mL buffer and 0.2 mL of Fe(II) stock solution were added. Reactors were crimp capped and rotated 21 – 24 h in the glove bag. A previous study found the reductive capacity of TCAAP aquifer material to be primarily controlled by magnetite-mediated abiotic reduction.[124] This observation was supported by monitoring conducted by the EPA in which transformation products consistent with biotic reduction were minor products.[280] To this end, no additional steps were taken to control potential competition from biotic pathways in our experiments. After equilibration, reactions were initiated by adding 0.4 mL of 17.5 mM synthetic RDX stock solution (in 1:1 acetonitrile:methanol). In additional experiments, the effect of initial concentration of RDX was assessed by changing the volume of spiked stock solution. Reactors were mixed end-over-end on a Glas-Col rotator at 40 rpm. Samples were taken by withdrawing 1 mL and filtering through a 0.2 μm Nylon syringe filter (Captiva) into amber glass HPLC vials. Aqueous Fe(II) concentration and pH were also measured with each sample. Aqueous Fe(II) concentration was quantified by adding 0.1 mL of the HPLC filtrate to a polystyrene cuvette with 0.2 mL of 5 g/L ferrozine (Sigma Aldrich, 97%) in water and 2.7 mL ultrapure water. Absorbance was measured at 562 nm using a Shimadzu UV-1601PC spectrophotometer.[281] Aqueous Fe(II) concentration in the reactor was calculated from absorbance using a five-point calibration

curve (0.05 – 0.005 mM $FeCl_2 \cdot 7H_2O$) and readjusted back to 1 mM with the appropriate volume of Fe(II) stock solution at each sampling point throughout the experiment. Experiments to assess the reactivity of the intermediate TNX (AccuStandard, 99.8%) were prepared identically, except that they were spiked with a stock of TNX. In selected experiments the reactor was spiked first with RDX, and after RDX and all nitroso-intermediates had degraded, TNX was added. All batch experiments were performed at room temperature (21–23 °C).

RDX degradation was monitored by high pressure liquid chromatography (HPLC) using an Agilent 1200 system with ZORBAX Eclipse Plus C-18 column (4.6 mm × 250 mm, 5 µm). Operating conditions included a mobile phase of 40:60 acetonitrile:ultrapure water, 1 mL/min flow rate, 230 nm detection wavelength, and 10 µL injection volume. RDX was quantified by a five-point calibration curve (0.01 – 0.2 mM RDX). Analytical standards of RDX and TNX (AccuStandard) were used to identify corresponding peaks (9.1 min and 6.2 min, respectively). Additional peaks were present at 8.1 min and 6.9 min, which are assumed to be MNX and DNX based on their retention times located between RDX and TNX, similar to other works.[269,282] Reaction rate constants were reported from pseudo-first order kinetics and errors were 95% confidence intervals for reactions performed either in duplicate for reactors involving TCAAP aquifer sediment materials or in triplicate for reactors involving synthetic magnetite.

D.5 Mineral characterization

Mineral characterization by X-ray diffraction (XRD), scanning electron microscopy (SEM), and transmission electron microscopy (TEM). X-ray diffraction (XRD) was

performed on a PANalytical X'Pert Pro X-ray diffractometer (Co source, 1.79 Å) with an X'Celerator detector, collecting patterns 15 – 60 °2θ over 40 min. Patterns were compared to powder diffraction files for quartz (#046-1045), magnetite (#019-0629), and goethite (#029-0713). Scanning electron microscopy (SEM) micrographs were collected using a JEOL 6500 field emission gun microscope at 5 – 10 kV with elemental mapping collected by energy-dispersive X-ray spectroscopy using a Thermo Scientific Noran system. Samples were uncoated and prepared on carbon tape. Transmission electron microscopy (TEM) was performed on a FEI Tecnai T12 microscope with a LaB_6 electron source (120 kV) and Gatan charge-coupled device (CCD) camera. Samples were prepared by suspending a small amount (< 1 mg) of dried sample in 1 mL ultrapure water, sonicating 15 s, diluting 10 μL of that suspension to 1 mL, and air drying a drop of dilute suspension on a 200 mesh holey carbon coated copper grid (SPI Supplies).

Stoichiometry (Fe(II)/Fe(III) ratio) of the synthetic magnetite and the magnetic TCAAP extract was quantified by acid digestion in 3 M HCl (Fisher, TraceMetal) for 7 d and then processed by the method of Viollier et al. (2000)[103] using ferrozine (Aldrich, 97%), hydroxylamine (Acros, 97%), and ammonium acetate (Macron, ACS) in polystyrene cuvettes. Absorbance was measured as described above. Fe percent (w/w) of TCAAP aquifer material collected at each of the four depths was quantified by inductively coupled plasma-atomic emission spectrometry (ICP-AES) by Pace Analytical, Minneapolis, MN and adjusted by percent moisture.

D.6 Results and discussion

D.6.1 Natural and synthetic magnetite

TCAAP aquifer material, TCAAP magnetic extract, and synthetic magnetite differed in both purity and particle size. Aquifer material collected from the south-central area of TCAAP (location shown in Figure D-1a) was primarily a mixture of sand and silt, with quartz the only detectable mineral by XRD (Figure D-1b). A simple magnetic extraction on dried material revealed a significant amount of magnetite in the aquifer matrix. Although the extract was observably darker in color (inset pictures in Figure D-1b), extraction did not yield pure magnetite and both quartz and clay minerals were still detectable by XRD. Because of quartz and other mineral impurities in the extract, percent magnetite in the whole aquifer material was instead estimated using ICP-AES analyses, which resulted in 0.51 – 0.62% total Fe (w/w) depending on depth collected. Although this value does not directly correspond to magnetite, it is similar to the reported ~ 0.3% magnetite determined through magnetic susceptibility by Ferrey et al. (2004).[124] The TCAAP extract was 6.9% iron, with an Fe(II)/Fe(III) ratio of 0.1. This supports the XRD results that the magnetic extract is not comprised of iron oxides alone and indicates that the magnetite stoichiometry is below the ideal 0.5 value. Magnetite synthesis yielded pure magnetite nanoparticles with no secondary phases detected by XRD. Fe(II)/Fe(III) stoichiometry was determined to be 0.50 ($Fe(II)_{1.00}Fe(III)_{2.00}O_4$) by acid digestion, hydroxylamine reduction, and ferrozine colorimetry. A second magnetite synthesis was performed to check the reproducibility of this result and yielded magnetite with a stoichiometry of 0.49, although these magnetite nanoparticles were not further used in this study.

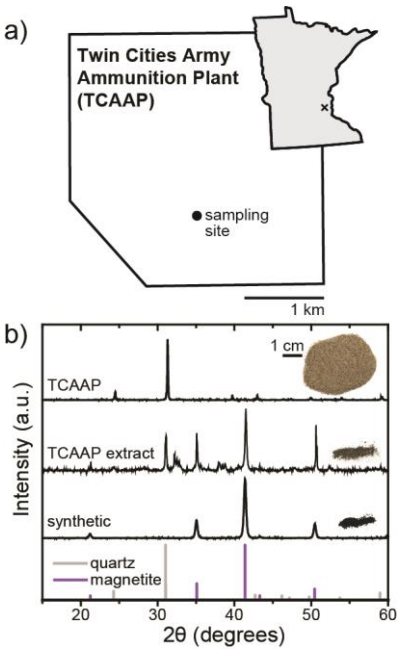

Figure D-1. a) Location of the Twin Cities Army Ammunition Plant in Minnesota, USA and the site of core sampling for batch experiments. b) XRD patterns of unreacted materials. Magnetite sources from top to bottom: aquifer material, aquifer magnetic extract, and synthetic magnetite. Inset images are photo representations of each source of magnetite.

D.6.2 Variables affecting magnetite reactivity towards RDX

Several factors contributed to varying observed rate constants for RDX reduction in the presence of magnetite. All tested conditions and corresponding pseudo-first order rate constants are outlined in Table D-1. Variables that resulted in significant differences in rate constants included the presence of aqueous Fe(II), buffer identity, magnetite source, and presence of nonreactive minerals, evidence that experimental parameters are critical considerations when using microcosm experiments as predictors for natural environments.

Table D-1. Reaction conditions and pseudo-first order rate constants (k_{obs}) for RDX reduction

Source	Collection depth (m)	Fe (% w/w)	Total mineral mass (g)	Fe loading (g/L)	Buffer[a]	[Fe(II)] (mM)	k_{obs} (h^{-1})[b]	k_{Fe} (L g^{-1} h^{-1})[c]
TCAAP	44	0.62	5.00 ± 0.05	0.89	Bicarbonate	0	ND[d]	ND
TCAAP	44	0.62	5.00 ± 0.05	0.89	Bicarbonate	1	1.8 (± 0.4) ×10^{-3}	2.0 ± (0.4) ×10^{-3}
TCAAP	48	0.62	5.00 ± 0.05	0.89	Bicarbonate	1	5.8 (± 1.8) ×10^{-4}	6.5 ± (2.0) ×10^{-4}
TCAAP	51	0.51	5.00 ± 0.05	0.73	Bicarbonate	1	1.3 (± 0.1) ×10^{-3}	1.8 ± (0.1) ×10^{-3}
TCAAP	54	0.56	5.00 ± 0.05	0.80	Bicarbonate	1	1.3 (± 0.2) ×10^{-3}	1.6 ± (0.3) ×10^{-3}
TCAAP extract	44	6.9	0.170 ± 0.005	0.34	Bicarbonate	0	ND	ND
TCAAP extract	44	6.9	0.170 ± 0.005	0.34	Bicarbonate	1	4.5 (± 0.3) ×10^{-3}	1.3 ± (0.1) ×10^{-2}
Synthetic	NA[e]	72.4	0.030 ± 0.005	0.62	Bicarbonate	0	ND	ND
Synthetic	NA	72.4	0.030 ± 0.005	0.62	Bicarbonate	1	8.9 (± 1.2) ×10^{-2}	1.4 ± (0.2) ×10^{-1}
Synthetic	NA	72.4	0.030 ± 0.005	0.62	50 mM MOPS	0	ND	ND
Synthetic	NA	72.4	0.030 ± 0.005	0.62	50 mM MOPS	1	5.4 (± 0.9) ×10^{-1}	8.7 ± (1.5) ×10^{-1}
Synthetic	NA	72.4	0.030 ± 0.005	0.62	10 mM MOPS	1	3.3 (± 0.5) ×10^{-1}	5.3 ± (0.8) ×10^{-1}
None	NA	NA	0	0	Bicarbonate	0	ND	ND
None	NA	NA	0	0	Bicarbonate	1	ND	ND

[a] 10 mM bicarbonate and MOPS at pH 7

[b] Errors are 95% confidence intervals. All R^2 values of for the linear fits to lnC versus time data are > 0.95.

[c] k_{obs} normalized by the Fe loading (g/L) from the added mineral.

[d] ND = RDX loss was not detected within 21 days of sampling.

[e] NA = Not applicable

D.6.3 Solution variables

No degradation of RDX was observed in bicarbonate buffer alone or with aqueous Fe(II). The greatest variable across all experimental conditions with minerals was whether aqueous Fe(II) was present. No reaction was detected over 21 d in reactors with mineral phases that did not contain aqueous Fe(II). This indicates no biodegradation of RDX. Magnetite has structural Fe(II), suggesting that the direct transfer of electrons from mineral to oxidized groundwater contaminants is possible. While it is expected that aqueous Fe(II) would increase contaminant reduction rate through adsorption and electron delocalization within the mineral, a review of current literature found variability in the extent of direct electron transfer from magnetite to contaminant in the absence of aqueous Fe(II).[173,283] Researchers have noted quantifiable $–NO_2$ reduction rates for nitroaromatic compounds and RDX over time-scales of minutes or days by magnetite alone, with magnetite stoichiometry controlling reaction rate.[88,284,285] Others did not detect $–NO_2$ reduction by magnetite under similar conditions, even after weeks of sampling,[76,273] and the results in Table D-1 support this latter finding. One study detected loss of RDX in magnetite suspensions but noted that sorption on the mineral may be influencing RDX concentration.[285] The synthetic magnetite used in our study had a stoichiometry of 0.50, suggesting that a substoichiometric Fe(II)/Fe(III) ratio was not controlling reaction rate. Possible variations of the minerals, including how they were synthesized, their surface and chemistry, and residual aqueous Fe(II) may explain the widespread differences in the literature regarding observed synthetic magnetite reactivity. Thus, interpretations of magnetite reactivity based on literature data must include careful

consideration of material preparation and experimental conditions. These discrepancies warrant future review of the physical and chemical properties of magnetite that drive its reactivity toward oxidized molecules in the presence and absence of aqueous Fe(II).

Buffer identity also affected RDX reduction rates by adsorbed Fe(II) on synthetic magnetite, with pseudo-first order rate constants nearly one order of magnitude faster in 50 mM MOPS buffer than in 10 mM bicarbonate buffer at similar pH. An experiment with 10 mM MOPS was also performed to normalize ionic strength to that of bicarbonate buffered reactions. These results revealed similar pseudo-first order rate constants to reactions containing 50 mM MOPS, thus supporting our observation that significant rate constant increases are due to buffer identity, and not ionic strength. Aqueous Fe(II) concentration after equilibration with synthetic magnetite in each buffer was comparable, with aqueous Fe(II) concentration decreasing from 1 mM to 0.76 ± 0.01 mM in bicarbonate buffer and 0.71 ± 0.01 mM in MOPS, so the effect is not related to amount of Fe(II) associated with the mineral surface. While aggregate size was not monitored here, qualitative observations of magnetite particles noted faster settling in bicarbonate buffer (settled in under 24 h) than in MOPS buffer (still suspended after 3 d). These results with magnetite support that aggregate size, which is influenced by buffer identity and associated with the amount of accessible reactive surface area,[286] affects observed reaction rates of mineral-mediated redox reactions. Buffer identity has significant effects on observed reaction rates for mineral-mediated redox reactions by adsorbed Fe(II) on goethite (α-FeOOH),[94] which has been attributed to larger aggregate sizes in bicarbonate buffer than in MOPS buffer more so than amount of adsorbed Fe(II). MOPS buffer has

been shown to alter redox reactions at the goethite surface[287] and the corrosion process of zero-valent iron.[288] It has also been shown that Good's buffers affect both the kinetics and reaction pathways of carbon tetrachloride in the presence of magnetite.[289] Thus, buffers should not be considered passive, and bicarbonate or other environmentally relevant buffers may better predict reaction rates in environmental systems.

D.6.4 Magnetite source and composition

Comparisons between synthetic magnetite and magnetite in natural aquifer material revealed not only the importance of mineral size and morphology but also the effects that nonreactive minerals have on mineral-mediated natural attenuation processes. Although surface area was not quantified for natural TCAAP magnetite, general particle sizes (50 – 100 μm for natural magnetite and 0.05 – 0.1 μm for synthetic magnetite) from SEM and TEM micrographs (Figure D-2) provided evidence of higher specific surface area for synthetic magnetite, making surface area the most likely explanation for the differences in rate constants between synthetic and natural magnetite. This is supported by the fact that normalization of the rate constants by the amount of iron present in the minerals (k_{Fe} in Table D-1) provides the same overall trends in rate constant. Furthermore, extracting the magnetic portion of TCAAP aquifer material led to faster RDX degradation rates in comparison to whole aquifer material. The loadings (5.00 g and 0.17 g) were chosen such that the total amount of Fe in the two sets of experiments were approximately equal (assuming that the magnetic extract contains all of the iron present), and in actuality, less Fe was present in the extract given that other minerals were also collected along with the

magnetic material. In natural TCAAP sediment, the observed reactions rates of RDX were significantly decreased. Potential reasons are loss of accessible reactive surface sites either through heteroaggregation and subsequent blocking of reactive surface sites on the magnetite particles or through competitive Fe(II) adsorption to less reactive surfaces.[290] During these experiments, TCAAP aquifer material reactions required approximately three times more aqueous Fe(II) addition to maintain an equilibrium aqueous 1 mM Fe(II) concentration at each sampling point as compared to TCAAP magnetic extract, indicating that competitive Fe(II) adsorption to, and reaction on, less reactive surfaces was occurring. Given that the aqueous concentration was maintained at 1 mM Fe(II), we suspect aggregation and blocking of sites limits reaction on the magnetite.

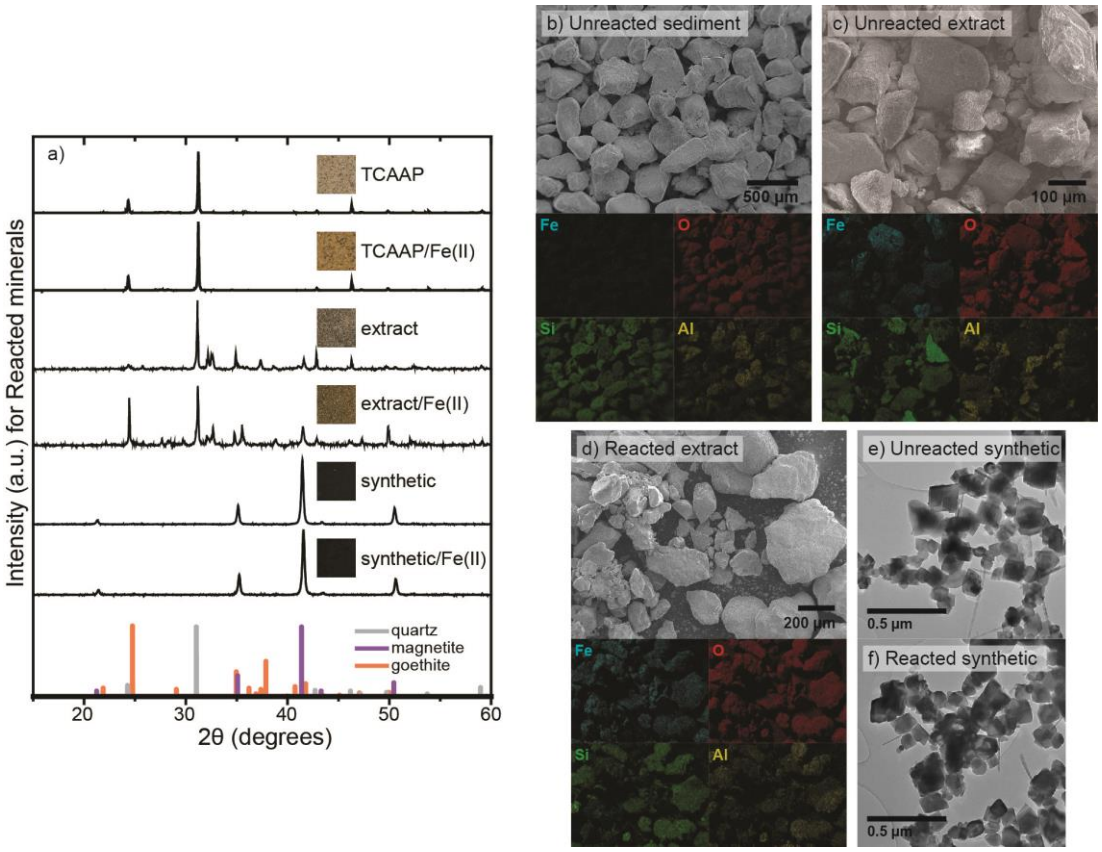

Figure D-2. a) XRD patterns of minerals collected and washed anaerobically following reaction with 0.2 µM RDX in 10 mM bicarbonate buffer at pH 7. Inset images are photo representations of each sample. b-d) Representative SEM micrographs and corresponding elemental mapping by EDS for unreacted TCAAP aquifer material, unreacted TCAAP magnetic extract, and TCAAP magnetic extract with Fe(II) reacted with RDX in the presence of aqueous Fe(II). Micrographs only pertain to material collected at a depth of 44 m. e-f) Representative TEM micrographs for synthetic magnetite particles either unreacted or reacted with RDX in the presence of aqueous Fe(II). For reactions, buffer identity was 10 mM bicarbonate buffer at pH 7.

Mineral characterization data, including XRD patterns and elemental mapping in SEM micrographs (Figure D-2), of the reacted minerals supported competitive Fe(II) adsorption through detection of oxidized iron oxides, such as goethite, in the TCAAP extract following several anaerobic washes and removal from the anaerobic glove bag.

The XRD pattern for reacted TCAAP extract with Fe(II) revealed goethite production, which was not observed in the pattern of reacted synthetic magnetite with Fe(II). Both the TCAAP aquifer material and the extract with Fe(II) present also had a notable orange color after washing (inset images in Figure D-2a). In the SEM element maps, Fe and O were detected on all grains in reacted TCAAP extract + Fe(II) where only select grains contained exclusively Fe and O in the unreacted material, providing evidence of a layer of iron oxide on all grains including clays and quartz. Thus, it is likely that, at the very least, adsorption of Fe(II) on other minerals led to reaction occurring on other surfaces, contributing to the slower RDX reduction rate observed with TCAAP sediment, and reaction did not exclusively occur on the magnetite. Because of the large abundance of these other materials, Fe(II) is adsorbed to these less reactive surfaces, and the reaction with Fe(II) occurring on quartz or clays (leading to the formation of goethite) is slower than the reaction on magnetite, as shown by the normalized rate constants in Table D-1. Good's buffers are also known to lead to higher reaction rates than carbonate buffer with goethite,[286] and thus the effect of the buffer effect on rate could be due to effects on both magnetite and goethite surfaces.[287,289] It is interesting that reactions on these other surfaces also appear to occur in the TCAAP extract, where a larger fraction of magnetite is present initially. Further *in situ* imaging would be necessary to quantify any impact of heteroaggregation on limited reaction of the magnetite particles.

D.6.5 Influence of buffer identity on reaction intermediates

Buffer identity not only affected observed rate constants for RDX degradation but also the quantity of intermediates detected. Three nitroso derivatives of RDX were detected during abiotic RDX reduction and peak areas for RDX, MNX, DNX, and TNX are provided in Figure D-3.

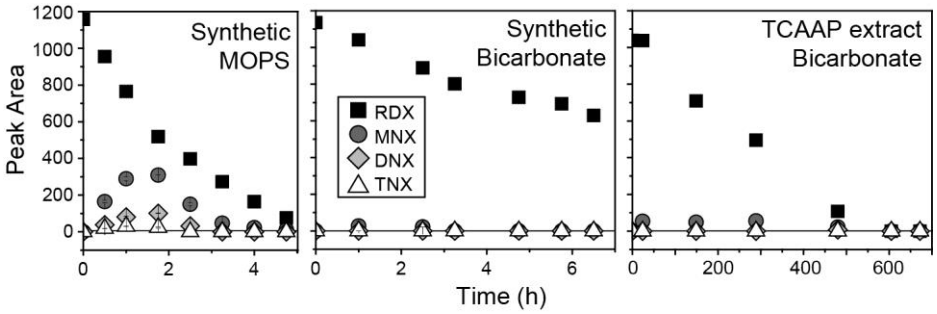

Figure D-3. Peak area of RDX and nitroso derivatives MNX, DNX, and TNX over reaction time with different magnetite sources (either synthetic or TCAAP extract) and different buffers (either 50 mM MOPS pH 7 or 10 mM bicarbonate pH 7).

The accumulation of all three nitroso derivatives was significantly greater in reactions containing MOPS buffer as compared to similar reactions containing bicarbonate buffer. The products in MOPS buffer are similar to those observed previously with MOPS in the presence of minerals,[270,273] and additional products observed in other studies include formaldehyde, NH_4^+, and N_2O.[80,273] The accumulation of nitroso compounds could be due to 1) slower reaction of the intermediates in the presence of MOPS buffer, 2) competition for reactive sites between RDX and the intermediates, or 3) an alteration in the reaction pathway caused by the different buffers. To evaluate these possibilities, TNX was introduced to and quantified for reactors

containing synthetic magnetite and aqueous Fe(II) in either MOPS or bicarbonate buffer. No degradation of TNX in MOPS or bicarbonate buffer alone was observed. In the experiments containing synthetic magnetite, Fe(II), and bicarbonate buffer, TNX would degrade slowly for 4+ hours, whereas in MOPS buffer, there was a sudden disappearance (Figure D-4). Pre-exposure to RDX shortened, but did not eliminate, this induction period for both buffers, indicating that alteration of the magnetite surface is required for TNX reaction. While these data point to additional complexities in the reaction pathways, it does not appear that slower reaction rates of intermediates in the MOPS buffer is a viable explanation for the differences seen in Figure D-3.

.

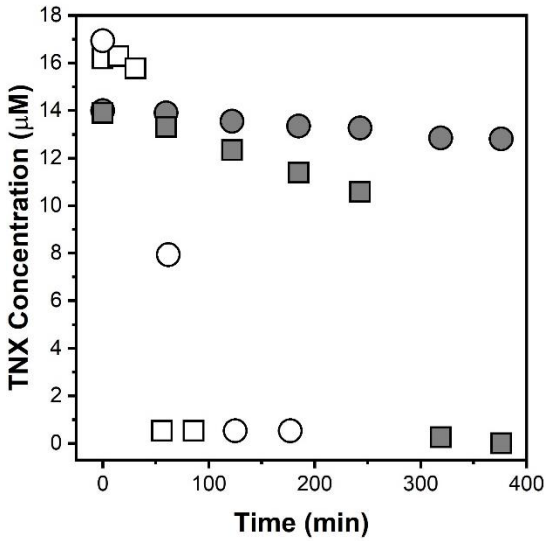

Figure D-4. Reaction of TNX with Fe(II)/synthetic magnetite bicarbonate buffer (circles) and in MOPS buffer (squares). Closed symbols indicate experiments in which batch reactions were performed following the standard procedure described above. Open symbols indicate experiments where reactors were pre-exposed to RDX and allowed to react to completion before initiating experiments with TNX.

Results from varying the initial concentration of RDX are shown in Figure D-5. According to Langmuir-Hinshelwood-Hougen-Watson (LHHW) kinetics,[291,292] a linear relationship between reaction rate and initial concentration is indicative of adsorption to the surface being the rate limiting step, and a plateau in reaction rate is reached when reaction is the rate limiting step. The data demonstrate that adsorption is rate limiting in MOPS buffer (Figure D-5a) and reaction is rate limiting in carbonate buffer (Figure D-5b). The aggregation of particles is greater in the bicarbonate buffer meaning fewer reactive sites are available[94,286] which could be partially responsible for the lower overall rates of reaction in the bicarbonate buffered reactors. The site availability does not drive whether a reaction is adsorption or reaction limited in LHHW kinetics, but we cannot rule out that the plateau in rate versus concentration has not been reached in the MOPS buffered system due to a weaker binding of RDX to the surface. The concentration range tested, however, is already beyond that expected in most contaminated groundwater systems. Thus, we conclude there is likely a difference in rate limiting step between the two buffers.

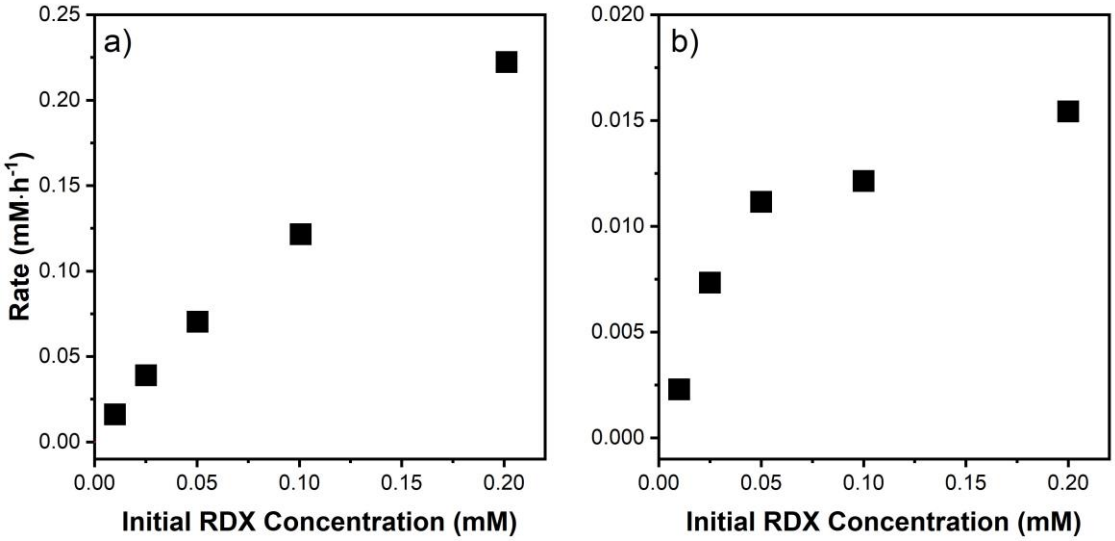

Figure D-5. Initial reaction rate ($k_{obs}C_0$) as a function of initial RDX concentration in either a) 50 mM MOPS or b)10 mM bicarbonate at pH 7. Note the difference in scales for the y-axes.

If the rate is adsorption limited, reactive surface sites for both RDX and intermediates would be available. On the other hand, intermediates should accumulate in the reaction limited system, especially if intermediates desorb before reacting further and if the intermediates are less reactive than the parent compound. From the results above with TNX, it is unclear whether TNX reacts more slowly than RDX, but TNX reactivity is obviously not straightforward.

Given that the rate limiting step for RDX degradation varies depending on buffer identity, the most likely explanation for the different reaction intermediate profiles is that the buffer identity affects the reaction pathway of RDX, with intermediate products other than MNX, DNX, and TNX forming in bicarbonate buffer. This suggests that Good's buffers affect reaction pathways of not only chlorinated solvents,[287,289] but also

nitramines. In the TCAAP material and the extract, the pathways of reaction may be altered by the buffer on both the original magnetite present and the goethite formed. Evaluating results from previous studies including various mineral surfaces performed in Good's buffers (MNX, DNX, TNX produced in high yield),[270,273] those in carbonate buffer or simulated groundwater (low yield of MNX, DNX, TNX),[14,276] and taking into account that ring cleavage products dominated in systems with Good's buffers and complexed iron,[275] it appears that the combination of Good's buffers with mineral surfaces gives both kinetics and product distributions that may not match those likely to be found in the field.

The results of the work have important implications for the assessment of the reactivity of RDX with iron oxide minerals and of the importance of abiotic reduction at sites for which natural attenuation is part of the remediation strategy. The data presented here further highlight the significance of solution variables and mineral characteristics when relying on microcosm experiments for predicting natural attenuation of groundwater contaminants. Given that aqueous Fe(II) was necessary for RDX degradation in the presence of magnetite for our experiments, and that there is much variability in literature about the reaction between oxidized organic molecules and magnetite in the absence of aqueous Fe(II), it is not yet clear whether the presence of aqueous Fe(II) is necessary for reaction of oxidized groundwater contaminants in sediments containing magnetite. In addition, the use of synthetic magnetite, while ideal for controlling mineralogy and decreasing experiment times, will not always correspond to results using natural magnetite-containing sediments. Even with the consideration of

varying size and morphology, nonreactive minerals such as clays and quartz will affect contaminant degradation rates indirectly through competition for dissolved Fe(II). Finally, comparisons of RDX degradation rates and reaction pathway under similar conditions with the exception of buffer identity revealed that buffer choice and concentration may also affect assessment of both reaction kinetics and pathways. Here, bicarbonate buffer at low concentration, which is representative of typical groundwater chemistry, slowed reaction rates, changed the rate limiting step, and led to variable detection and accumulation of certain intermediates compared to MOPS buffer, which would have large impacts on predicting RDX degradation pathways in natural systems. In combination, these results indicate that while idealized and controllable laboratory conditions are useful in assessing reactions that may occur, conditions as close to those expected in field systems are necessary to evaluate the reaction rates and pathways of RDX in reduced groundwater systems.

D.7 Acknowledgements

We thank Michael LeFrancois and Lindsey Kenyon (Arcadis), Mary Lee (Minnesota Army National Guard), Roger Walton (U.S. Army Environmental Command), and Amy Hadiaris (Minnesota Pollution Control Agency) for assistance with TCAAP aquifer material collection. Drilling was performed under the Army's Installation Restoration Program (IRP), a subset of the Defense Environmental Restoration Program. We also thank Thomas Webber (University of Minnesota) for SEM imaging and EDS mapping and R. Lee Penn for access to the XRD.

This work was supported by the Strategic Environmental Research and Development Program (SERDP) as part of project ER 2618. Parts of this work were carried out in the Characterization Facility, University of Minnesota, which receives partial support from the National Science Foundation through the MRSEC program.

The authors declare no competing interests.

D.8 Supplementary Material for Appendix D

D.8.1 Synthesis of magnetite nanoparticles

In an Erlenmeyer flask, 140 mL of ultrapure water (Milli-Q, 18.2 MΩ cm) was bubbled under N_2 for 30 min and equilibrated to 90 °C in a water bath. Under constant flow of N_2 and magnetic stirring, 20 g $FeSO_4 \cdot 7\ H_2O$ (Fisher, ACS) was added to the flask and then 60 mL of a deoxygenated solution containing 1.62 g KNO_3 (Sigma Aldrich, ACS) and 11.2 g KOH (Mallinckrodt, ACS) was added dropwise. After complete addition, the black suspension was stirred an additional 45 min at 90 °C, cooled to 40 °C, poured into a 250 mL Nalgene bottle, and transferred to the glove bag, where the particles were washed three times with water and dried. The magnetite synthesis method was adapted from Schwertmann and Cornell, 2000.[170]

D.8.2 RDX synthesis

To a two-necked 100 mL round bottom flask in a circulating water bath at 5 °C, 20 g of fuming nitric acid (Sigma Aldrich, purum p.a., > 99%) was carefully added and magnetically stirred. A thermometer to directly measure reaction temperature was set in the flask side neck. Once the nitric acid was at 5 °C, 1.2 g HMTA (Sigma Aldrich, ACS) was slowly added in small increments. During HMTA addition, the temperature was carefully maintained at 5 – 10 °C, slowing if the temperature neared 10 °C. To prevent significant heat production, the addition was performed over at least 1 h and HMTA accumulation in the flask neck was avoided. After complete HMTA addition, the solution was stirred at 15 – 20 °C for 3.5 h and then carefully poured into a 100 mL beaker

containing 30 mL of ultrapure water and ice made from 10 mL of ultrapure water. The white precipitate was recovered by Büchner filtration through a 70 mm Whatman 44 glass fiber filter and washed with deionized water, 5% sodium carbonate, and water until the pH of the filtrate was neutral. The precipitate was air dried in the hood for 20 h on the filter, portioned into five 20 mL scintillation vials, and dissolved in 15 mL of 1:1 acetonitrile (Sigma Aldrich, HPLC) and methanol (Sigma Aldrich, HPLC). The synthesis yielded pure RDX (25 – 50% yield) with no detectable byproducts as characterized by liquid chromatography using an Agilent 1200 system with ZORBAX Eclipse Plus C-18 column (4.6 mm × 250 mm, 5 µm) and a 40:60 acetonitrile:ultrapure water mobile phase, 1 mL/min flow rate, 230 nm detection wavelength, and 10 µL injection volume. The entire procedure was performed in a well-ventilated hood behind a blast shield and hood sash, and full PPE with Sol-Vex acid resistant gloves were worn. It is important to note that the purity of fuming nitric acid was important, and attempts using > 90% red fuming nitric acid were unsuccessful and resulted in a violent, highly exothermic reaction when small amounts of HMTA were added. The RDX synthesis method was adapted from Just, 2001.[279]

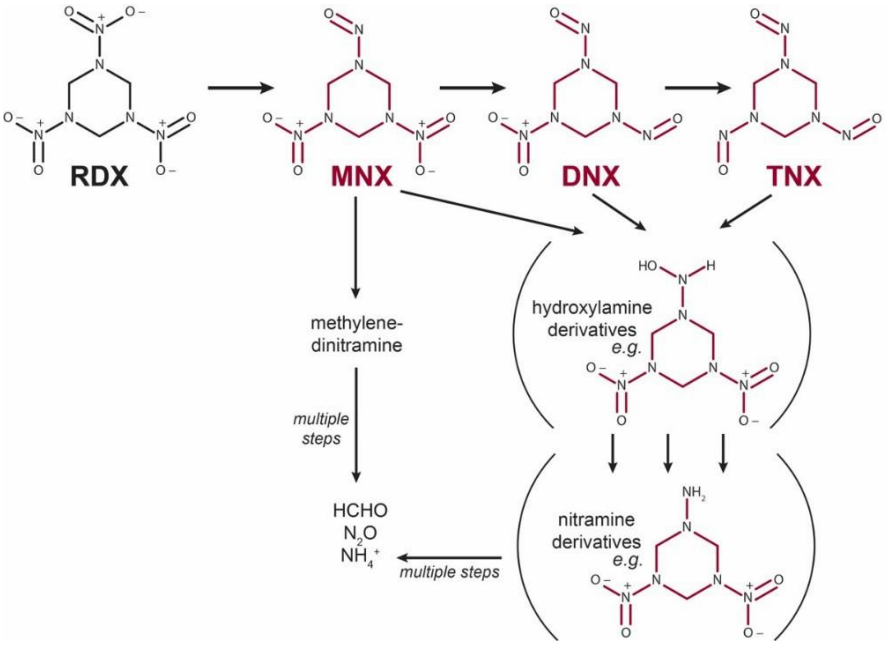

Figure D-6. Pathway of abiotic nitro-reduction of RDX. Nitroso-intermediates (MNX, DNX, TNX) are generated during sequential reduction of nitro-moieties. The remaining structures indicate further N-moiety reduction and ring-cleavage products. Adapted from Larese-Casanova and Scherer, 2008.[80]